# Geology of the Kidd Creek Deep Orebodies – Mine D, Western Abitibi Subprovince, Canada

A thesis submitted to the

Faculty of Graduate and Postdoctoral Studies

In partial fulfillment of the requirements for the

Master of Science Degree in Earth Sciences

Department of Earth Sciences

Faculty of Science

University of Ottawa

**Abstract**

The giant Kidd Creek Mine is an Archean Cu-Zn-Ag deposit in the Abitibi Greenstone belt, located in the Superior Province of Canada and is one of the largest known base metal massive sulfide mines in the world with a tonnage of 170.7 Mt (Past production, Resource and Reserve). The massive sulfides in Mine D comprise a number of ore lenses that are interpreted to be the downplunge continuation of the Central orebody from the upper mine. These are referred to as the West, Main, and South lenses. The massive sulfides overlie a silicified rhyolitic unit at the top of a mixed assemblage of rhyolite flows, volcaniclastic sediments and ultramafic flows. The sheared nature of the fragmental units in the hanging wall of the deposit, at depth, illustrates the greater deformation that has occurred than in the upper mine. Metal zonation and the distribution of Cu stringer mineralization suggest that the West and Main lenses may be part of a single massive sulfide body (Main orebody) that has been structurally dismembered. The South Lens is a detached body, separated by late faults. The large Cu stringer zone beneath the West and Main lenses has a thickness of up to 150 metres, and is much broader and structurally remobilized in Mine D partially due to a newly identified series of vertically trending offset faults, that extends along the entire length of the massive sulfide bodies. A number of features of the North, Central and South orebodies in the upper part of the mine (e.g., Se-rich halo around Cu-rich zones) have been recognized in Mine D and provide an important framework for correlating the deep orebodies with the upper levels of the mine. Drilling below the current mine levels indicates that the massive sulfide and Cu stringer zones continue below 10,200 feet (3109 m) and highlight the remarkable continuity of the deposit downplunge with no end in sight.

Two main ore suites have been recognized in the upper part of the mine and in Mine D: a low-temperature, polymetallic assemblage of Zn, Ag, Pb, Cd, Sn, Sb, As, Hg, ±Tl, ±W,

and a higher-temperature suite of Cu, Co, As, Bi, Se, In, ±Ni. More than 25 different ore minerals and ore-related gangue minerals are present, including Co-As-sulfides, Cu-Sn-sulfides, Ag-minerals, and selenides. The massive ores consist mainly of pyrite, pyrrhotite, sphalerite, magnetite and chalcopyrite, together with minor galena, tetrahedrite, arsenopyrite, and native silver with a quartz and siderite gangue. Despite the high Ag content of the ores, the majority of the massive sulfides are remarkably Au poor except for a local gold zone that has been recognized in the deep mine in association with high-temperature mineralization. The trace elements in the ores exhibit strong zonation and diverse mineralogy. Spectacular albite porphyroblasts, up to 1 cm in size occur in the most Cu-rich ores of Mine D which are coincident with the peak of regional metamorphism and likely represent higher metamorphic or hydrothermal temperatures. Overall the orebodies have remained remarkably similar downplunge. However, unlike the upper part of the mine, pyrrhotite is dominantly hexagonal, only tetrahedrite was observed as the dominant sulfosalt, and magnetite occurs as both blebby porphyroblasts and as abundant intergrowths with sphalerite-chalcopyrite ores and siderite. These characteristics suggest that the deep mine has been subjected to higher metamorphic temperatures, possibly related to depth of burial, and that the original hydrothermal fluids may of had a lower $H_2S/CO_2$ and/or higher temperatures.

## Acknowledgments

There were many people who have helped me through this, albeit longer than anticipated thesis of whom I am thankful. I extremely grateful to Mark Hannington for the inception this project in the first place, helping me through its early stages, supporting my decision to seek full time employment during its course, and helping me stick with it near then end when it seems there is no end in sight. His perpetual enthusiasm was a source of strength to see this project through. I would also like to extend my sincere thanks to Sandy Sheperd for always helping me in my absence from the university and for always having time for a chat.

I would also like to thank the past and present personnel at Kidd Operations, specifically Pete Calloway, Benoit Drolet, Greg Cooper, Dave Counter, Pierre Noel, Ron Lafond, Celeste Andrews and Claude Breton for their support, aid and guidance and putting up with my perpetual ramblings and crazy theories throughout this project. They have made my time at Kidd Creek and extremely educational and enjoyable experience. Kidd Operations also provided geological information such as drill core and access to geochemical data such as ASSAY and ICP presented in this paper.

I would also like to thank my family and friends for their never-ending support, guidance and always believing in me. Finally, I am indebted to Kaitlin Taylor for her patience, her unwavering support and for always being there for me when I needed her whether for encouragement or simply telling me what I really needed to hear.

## Table of Contents

## List of Figures

## List of Tables

# Chapter 1. Geological Setting of the Kidd Creek Deposit and Mine D

## *1.1 Introduction*

The giant Kidd Creek Mine is an Archean Cu-Zn-Ag deposit in the Abitibi Greenstone belt (Figure 1.1), located in the Superior Province of Canada, and is one of the largest known volcanogenic massive sulfide (VMS) deposits in the world, with total past production of 148.3 Mt. The total resource of Mine D is estimated at 34.7 Mt at 2.09% Cu, 5.20% Zn, 54 g/t Ag, and 0.15% Pb. The upper part of the mine consisted of three main orebodies accessed in the former open pit (from surface to 800 ft level), the No. 1 Mine (800 to 2500 ft level), the No. 2 Mine (2600 to 4600 ft level), and the No. 3 Mine (4700 to 6800 ft level). The North and South orebodies extended from surface to a depth of 3,400 feet (1036 m); the Central orebody has been traced to the deepest levels of the mine as the Main orebody (>9,800 feet or >2987 m) (Figure 1.4), where it is split into the West and Main lenses. A Cu stringer zone underlies the Main Lens (above 8000 ft level) and the West Lens (below 8000 ft level) and can be traced from surface to the bottom of Mine D. The mine stratigraphy is remarkably continuous down plunge but is complicated by faulting and several stages of folding. Previous studies of the Kidd Creek deposit (Hannington et al., 1999) documented the major ore zones of the No. 1, No. 2 and No. 3 mines from the 2400 to 4700 levels and provide a benchmark for understanding the new ore zones being developed in Mine D.

The ore lenses in Mine D are interpreted to be the downplunge continuation of the Central orebody (Figure 1.4). Below 6800 ft (2072 m), these are referred to as the Main, West, and South lenses. The massive sulfides overlie a silicified rhyolitic unit at the top of a

mixed assemblage of rhyolite flows, volcaniclastic sediments and ultramafic flows. The sheared nature of the fragmental units in the hanging wall of the deposit, at depth, illustrates the greater deformation that has occurred compared to the upper mine. Metal zonation and the distribution of Cu-stringer mineralization suggest that the West and Main lenses were part of a single massive sulfide body that has been cut by a series of near vertical offset faults. The South Lens also may be a detached body, separated by late faults. The large Cu-stringer zone beneath the Main orebody has a thickness of ~30 metres and is much broader and structurally remobilized in Mine D partially due to the offset faults, but extends along the entire length of the massive sulfide bodies. Drilling below the current mine levels indicates that both the massive sulfide and Cu-stringer zones continue below 10,200 feet (3109 metres). A number of features of the North, Central and South orebodies in the upper part of the mine (e.g., Se-rich halo around Cu-rich zones) have been recognized in Mine D and provide an important framework for correlating the deep orebodies with the upper levels of the mine.

A number of questions have been addressed. Are the deep orebodies of Kidd Creek a part of the same hydrothermal system that was responsible for Mine 1 and 2? If so, it would suggest that this is among the largest contiguous hydrothermal upflow zones known in the geological record. What are the major controls on the down-plunge continuity of the deposit? The prevailing hypothesis is that the Central Orebody extended from surface to the bottom of Mine D, and the deep orebodies are the same, chemically and mineralogically, having been affected only by a higher degree of metamorphism. The approach to address these questions included detailed mapping and sampling of the deep orebodies to compare the structure, mineralogy, and geochemistry with the upper parts of the mine.

### *1.2 Regional Geology*

The Giant Kidd Creek deposit is hosted by the Kidd-Munro Assemblage, a dominantly mafic to ultramafic volcanic package with local felsic volcanic rocks (Ayer et al. 2005; Berger, 2011). The volcanic strata have been overturned (near vertical) and form east-west trending folds formed by regional north-south compression during the Kenoran Orogeny at 2700 Ma (Bleeker, 1999; Figure 1.2). Regionally, the E-W trend of the volcanic rocks likely reflects an original linear arrangement of rifts or arc-like assemblages (Ludden et al., 1986; Barrie and Davis, 1990; Jackson and Fyon, 1991). Felsic volcanism in the Kidd-Munro Assemblage occurred mainly between 2716.5±1.0 and 2714.8±0.7 Ma (Bleeker, and van Breemen, 2011). The rhyolites at Kidd Creek have a maximum age of 2717±2 Ma and are similar in age to felsic volcanic rocks over 60 km to the east, indicating a regional widespread felsic magmatic event. Supracrustal rocks of the region are intruded by late Archean tonalite-trondhjemite-granodiorite plutons. The largest of these in the Timmins area are the Goundhog River tonalite and the Kenogamissi batholith, located ~100 km south of Kidd Creek. Part of these intrusions may have been coeval with felsic volcanism in the Kidd-Munro Assemblage (Bleeker, 1999). Although tholeiitic basalts are the dominant rock type, there are anomalous concentrations of komatiites, such as those at the historic Pyke hill outcrop in Munro Township (Pyke et al., 1973), as well as in the Kidd Creek Volcanic Complex. The southern margin of the Kidd-Munro Assemblage is bound by Porcupine Group sediments that are juxtaposed against the mine stratigraphy along an unconformity or thrust fault (Bleeker, 1999). These metasediments separate the Kidd-Munro volcanic rocks from the Porcupine camp in Timmins.

### *1.3 Local Geology*

The Kidd Creek Orebody is located within the Kidd Creek Volcanic Complex which is a strongly deformed package of felsic volcanic rocks, epiclastic rocks, basalts and komatiites. The deposit is hosted by high-silica rhyolite that is underlain by komatiitic flows and overlain by tholeiitic basalts. Thin sedimentary units, including interflow graphitic argillites, are associated with the sulfides and record a break in volcanism during which the massive sulfide deposits were formed.

Large-scale folds to the northeast and west of the mine form the Kidd West basin and the Kidd 66 basin, respectively (Figure 1.3). These structures are large synforms that contain abundant basaltic flows, mafic breccias and minor interflow sediments that comprise the stratigraphic hanging wall of the mine. Minor interflow felsic volcanic and sedimentary rocks occur outside the mine, including the North rhyolite, Chance rhyolite, and Carnegie rhyolite, all of which contain graphitic argillite and minor sulfide. The Chance deposit, in the Chance rhyolite, contains 176,900 tonnes of Zn-Pb-Ag sulfides that are considered to be broadly coeval with the Kidd Creek deposit (Figure 1.3). At Kidd Creek, the volcanic complex is floored by ultramafic flows intercalated with minor rhyolite (Bleeker, 1999). The deep footwall of the deposit is cut off by a major thrust fault or unconformity which juxtaposes younger Porcupine group sediments against the mine stratigraphy. As a result, we do not know what underlies the komatiites.

The Kidd Creek deposit is located in an anomalous S-shaped fold structure that plunges steeply to the northwest. It sits at the top of a locally thickened pile of massive rhyolite, which is about 300 m thick at the location of the mine. The upper part of the mine

stratigraphy is intruded by a gabbroic sill, the base of which is an important marker for unravelling the Kidd Creek mine fold.

Three ore lenses were first exploited in the open pit: the North orebody, the Central orebody and the South orebody. These lenses plunge steeply along a major $F_2$ fold structure. The orebodies present at depth in the mine are the Main and West lenses (Main orebody), the South Lens, the Greywacke Lens (extension of the Triangle orebody) and the Northwest Lens. The Cu-rich stringer zone at the stratigraphic base of the deposit is consistent from surface to the bottom of the deepest drillholes in Mine D (Figure 1.4). The rhyolites exhibit abundant pervasive sericitization and intense silicification. There is also abundant chlorite, albite and tourmaline associated with the hydrothermal upflow zones of the main orebodies. All rocks in the mine, including the alteration, have been metamorphosed to greenschist facies.

The massive sulfide orebodies have been cut by five groups of faults: Gouge-type faults that generally dip 65° to the northeast, Offset faults that strike both approximately North-South and East-West and are near vertical, South-dipping faults that dip 70°-85° to the south-southwest, North-dipping faults, and other faults and shears with variable strikes and dips. The most significant faults at depth in the mine are the East-West trending Offset faults (Offset Fault 1 and Offset Fault 2), which control the location of mineralization at different elevations in the mine and the N-S Offset Fault. These faults displace the ore zones 100s of vertical metres. South-dipping faults have segmented many of the ore lenses and are responsible for a significant amount of ongoing seismic activity at the mine (e.g., North M Fault).

The most significant faults in the upper mine were the South-dipping faults which had a similar trend to many regional structures (Montreal River Fault). Although the N-S Offset fault in the deep mine is similar to these South-dipping faults in the way that it cuts and displaces the orebody, its strike and dip does not align with the same regional structures. There are, however, less pervasive N-S trending structures identified throughout the Kidd-Munro Assemblage, which may be analogous to the N-S Offset fault. It would have been a flat lying structure in the original stratigraphy. The Offset 1 and Offset 2 faults in Mine D are roughly East-West trending vertical structures that would have also been vertical in the original stratigraphy. They are similar in strike and dip to the East-West Shear in the upper mine which may have been an important ore-controlling structure for the South Orebody in the upper mine (Hannington et al., 1999).

### *1.4 Geology of Mine D*

Detailed geology maps were produced of 7000, 7500, 8000, 8600, 9000, and 9500 levels (Figure 1.5 to 1.10). These figures are a compilation of many years of work by the Kidd Creek Geology, Exploration and Survey departments. The geological information was produced using a combination of exploration, primary ore definition, and definition diamond drilling and underground development mapping. The development contours were produced from ongoing work by the Survey department. Lithological contacts, ore outlines and faults were first wire-framed using drill-hole information and then updated as development mapping became available. Faults that are continuous across multiple elevations of drill-hole intercepts and/or development mapping are labelled as Major Faults. The development

mapping shows lithological contacts, ore contacts, approximate lithological abundances, mapped faults and shears, joints, quartz-filled fractures, quartz and Cu-rich veins, and schistosity. All of these data exist in the mine database on their respective layers and may be imported for any level in the mine. These diagrams effectively show the stratigraphic cross-section across the orebody, downplunge. A close up of development mapping through the gabbro, felsic volcanic rocks, and massive sulfides is provided in (Figure 1.11) to show the level of detail in underground mapping included in the level plans.

The geology of Mine D (6900 to 9600 levels or 2103 m to 2926 m) consists of structurally complex massive sulfide lenses, deposited within felsic volcaniclastic rocks perched on top of intensely silicified rhyolite, which in turn sits on talc-carbonate-altered komatiites. The immediate hanging wall of the felsic volcaniclastic rocks is occupied by a gabbroic sill complex, which extends all the way from surface. The gabbro is locally interlayered with weakly quartz-phyric rhyolite similar to the Quartz Porphyry of the upper mine. At depth in the mine, felsic volcaniclastic rocks of the mine sequence extend past the southern termination of the gabbro sill and locally contain altered Quartz Porphyry, silicified black argillites and other altered felsic rocks (Figure 1.9). This likely represents the top of the volcanic pile before the gabbro sill was intruded. A gabbro window to the southeast of the termination of the gabbro sill reappears at 6800 level due to the southward migration of the contact with the Porcupine greywacke as well as South-dipping faults and the East-West Shear from the upper mine. A similar window of gabbro was present to the east of the South Orebody in the upper mine but was cut out at 3600 level by the East-West Shear. There are two sets of shallowly dipping (originally subvertical) dykes which crosscut the ore zones of Mine D. The first, at ~8600 level (Figure 1.8), looks very much like the gabbro sill in the

immediate hanging wall and is relatively undeformed and unaltered. The second, at ~9400 level (Figure 1.10), appears to be more intermediate in composition but is structurally complex and cannot be easily connected between development mapping and drill-hole intercepts.

The top of the mine stratigraphy consists of intermediate pillowed volcanics. There is a small exposure of graphitic sediment between 7000 and 8000 level (Figure 1.5 and Figure 1.6), stratigraphically below the South Lens that is structurally bound by the intersection of several strong faults. At all levels the southern extent of the mine is cut off by a thrust fault or unconformity which juxtaposes Porcupine group sediments against the mine stratigraphy. This contact on 9000 level exists as a paper thin line (Figure 1.9). A quartz porphyry with abundant quartz-feldspar phenocrysts exists immediately south of a sliver of the Porcupine group sediments followed by talc-altered komatiites (Figure 1.9). The geology at the southern end of the mine at depth is unknown due to lack of diamond drill-hole information.

The West and Main lenses are the dominant bodies and are interpreted to be structurally offset sections of the same massive sulfide body (the Main orebody). The South Lens is a structurally complex group of smaller massive sulfide bodies that lie stratigraphically above the West and Mains lenses. The Greywacke Lens is stratigraphically above the South Lens and is located in felsic volcaniclastic rocks at the southern termination of the gabbro sill. The southward migration of the greywacke thrust fault or unconformity which reopened ore hosting stratigraphy (Figure 1.4) is responsible for the reoccurrence of the SOB at 5200 level as the South and Greywacke lenses in Mine D. The Northwest Lens is predominantly a pyrite-pyrrhotite lens that is controlled by the vertical Offset faults.

The main differences between Mine D and the upper parts of the mine are the almost complete lack of graphitic argillites within the ore zones, the presence of the western talc-altered graphitic zone between the gabbro sill and the intermediate pillowed volcanics, the sheared nature of the fragmental units illustrating the greater deformation than in the upper part of the mine, the presence of near vertical offset faults that were not recognized in the upper mine, a less compact Cu-rich stringer zone due to faulting, the lack of a significant chalcopyrite-rich South Lens.

### *1.5 Methodology*

Samples of diamond drill-hole core were chosen based on availability and distribution. Many of the available holes higher in Mine D were too steep to give a representative distribution of samples at different levels. Each of the sampled drillholes were relogged, paying close attention to mineralogy, metal zonation, and textures. Four inch samples were taken to represent the ore types in each hole and prepared for polished sections. The remainder of the core was crushed and pulverized using a tungsten-carbide chipper and a Cr-steel mill and puck. To complement the 4-inch samples, assay pulps (1.5 m pulverized mine samples) were also retrieved corresponding to each 4-inch sample interval, where available.

Minor and trace elements were analyzed by a combination of INAA (instrumental neutron activation analysis), ICP-MS (inductively coupled plasma – mass spectrometry), and ICP-OES (inductively coupled plasma – optical emission spectrometry) at Activation Laboratories, Ancaster, Ontario. Data reported for: Zn, Cu, Pb, Mn, Tl, Sn, Cd, Ga, Ge, In,

Bi, Te, Co, Ni, Mo, Ba, Rb, Sr, Li, B, Cs, Be, La, Nd, Sm, Eu, Tb, Yb, Pr, Gd, Dy, Er, Tm, Y, Ta, Nb, Th, U, W, V, and Ho were determined by ICP-MS. Si, Al, K, Ca, Mg, P, Ti, and S were determined by ICP-OES. Fe, Na, Au, Ag, As, Sb, Se, Ir, Br, Lu, Hf, and Sc were determined by INAA. For the most part, data are reported for those methods with the lowest detection limits. For ICP-MS/OES, a combination of sodium peroxide fusion followed by multi-acid digestion was used to dissolve the samples. A minimum of 10 certified reference materials were used for the required analytes, all prepared by sodium peroxide fusion. Samples were analyzed using a Varian 735ES ICP or a Thermo 6500 ICAP and Perkin Elmer Sciex ELAN 6000, 6100 or 9000 ICP/MS. For INAA, a 30 g aliquot was encapsulated in a polyethylene vial and irradiated with an internal standard at a thermal neutron flux of 7x10 $^{12n}$ cm-2 s-1. After a 7-day delay to allow Na-24 to decay, the samples are counted on a high purity Ge detector with resolution of better than 1.7 KeV for the 1332 KeV Co-60 photopeak. The decay-corrected activities are compared to a calibration developed from multiple certified international reference materials. Mercury was analyzed by a cold vapour technique in which 0.5 g of sample was digested with aqua regia and Hg (II) is reduced to mercury vapour using stannous chloride. Argon bubbled through the solution in a closed reaction system was used to liberate and transport the Hg atoms into an absorption cell (a Perkins Elmer FIMS Flow Injection Mercury System) where they were determined by the absorption of light at 253.nm. Infrared absorption analysis was used to determine $CO_2$. A 0.2 g sample is thermally decomposed in a resistance furnace in a pure nitrogen environment at 1000°C, directly releasing $CO_2$; water is removed in a moisture trap prior to the detection of carbon dioxide in the IR cell. The carbon dioxide absorbs IR energy at a precise wavelength within the IR spectrum; all other IR energy is prevented from reaching the IR detector by a narrow bandpass filter. Quantitative analyses were carried out by wavelength dispersive X-

ray spectrometry (WDS) using a JEOL JXA-8230 Electron Probe at the University of Ottawa. A JEOL JEE-420 Carbon Coater was used to initially carbon coat the polished sections. A JEOL JSM-6610LV SEM was also used to find probe targets. The ore minerals were analyzed using 20.0 keV accelerating voltage with a 20 nA beam, a counting time of 10 seconds and ZAF correction method.

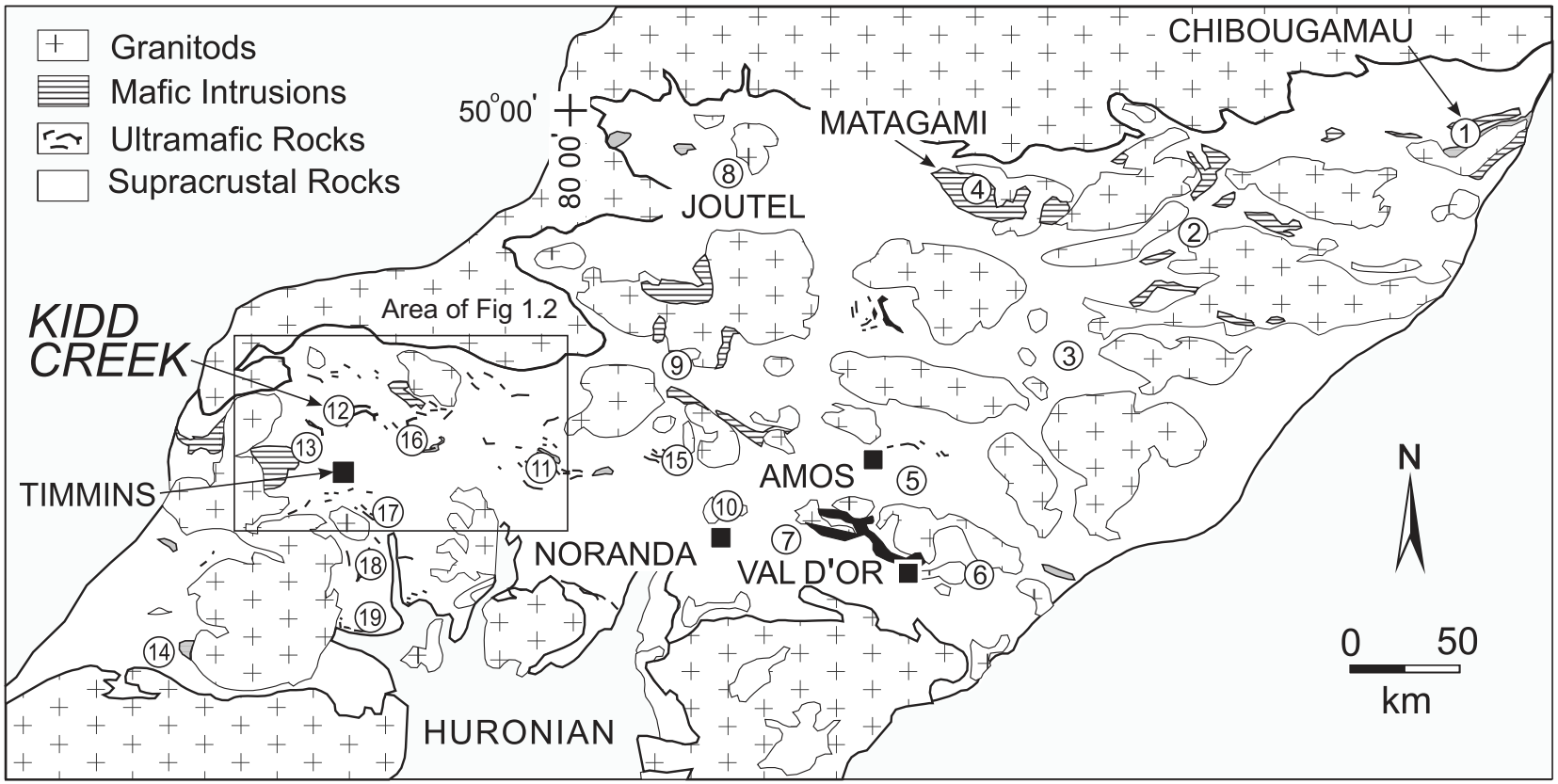


Cu-Zn Deposits and Districts:

1. Chibougamau
2. Desmaraisville
3. Quevillon
4. Matagami
5. Amos-Barraute
6. Val d'Or
7. Bousquet
8. Joutel
9. Normetal
10. Noranda
11. Munro Township
12. Kidd Creek
13. Kamiskotia
14. Swayze

Ni Deposits:

15. Dumont
16. Dundonald
17. Shaw Dome
18. Texmont
19. Sothman

Figure 1.1 Geological map of the Archean Abitibi Greenstone Belt showing the distribution of Cu-Zn Deposits and Districts (Hannington, 2010).

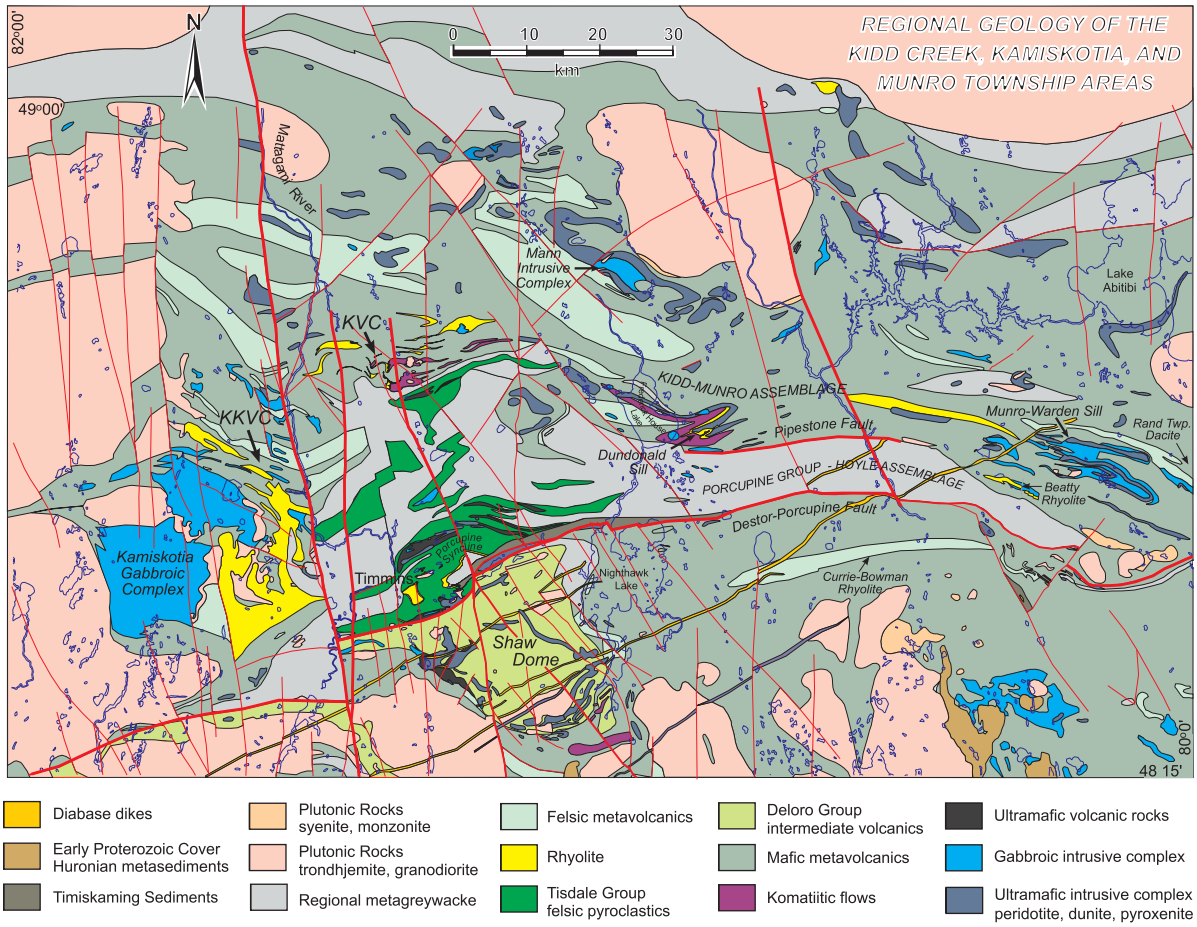


Figure 1.2 Geological Map of the region surrounding the Kidd Volcanic Complex (KVC). The Kamiskotia Volcanic Complex is shown as KKVC (Hannington, 2010).

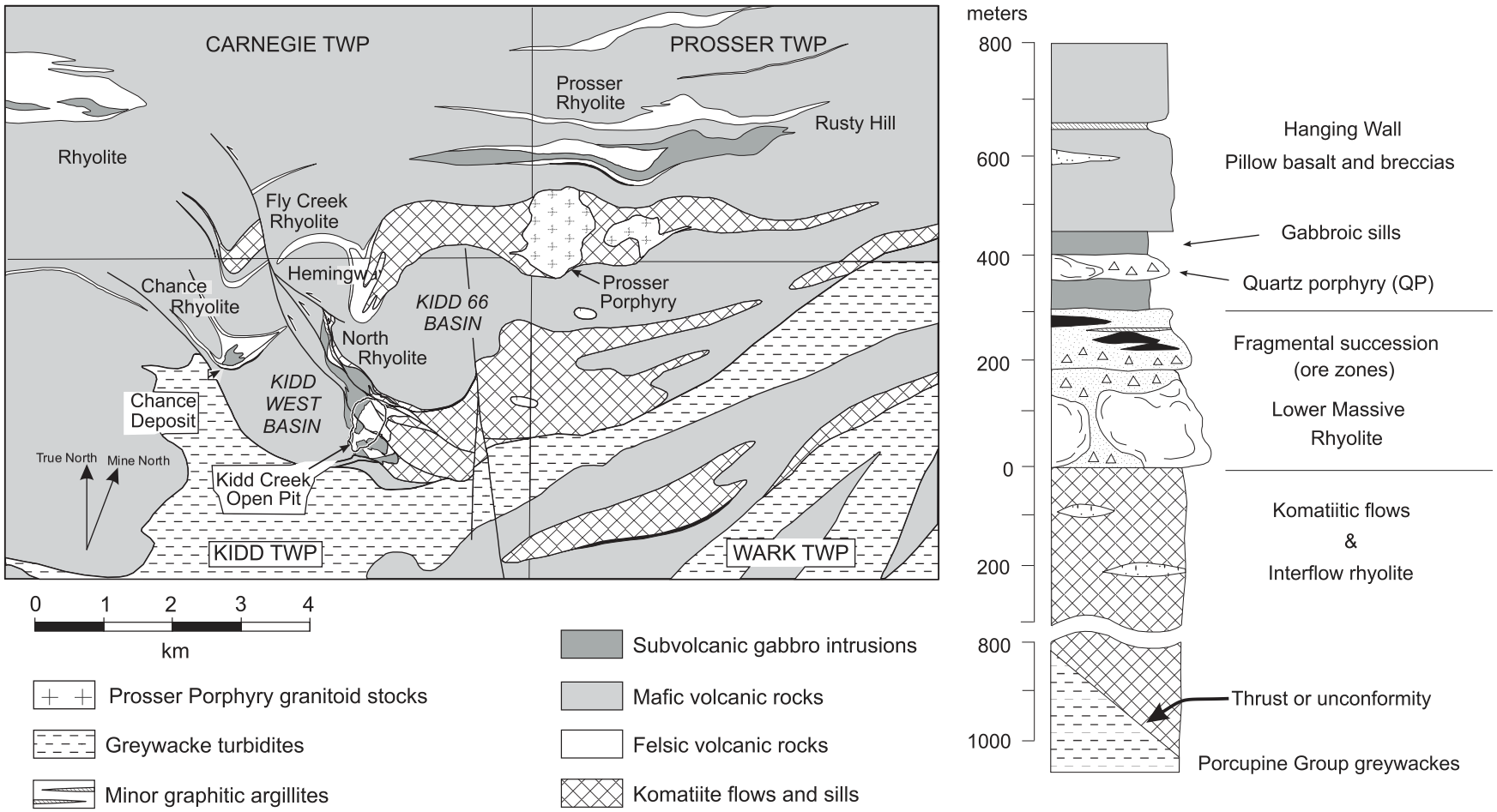


Figure 1.3 Geologic setting of the Kidd Creek mine based on surficial geology and drill core. The orebodies are contained within an S-shaped fold structure which plunges steeply to the North (Hannington, 2010). Mine North is 20 East of True North.

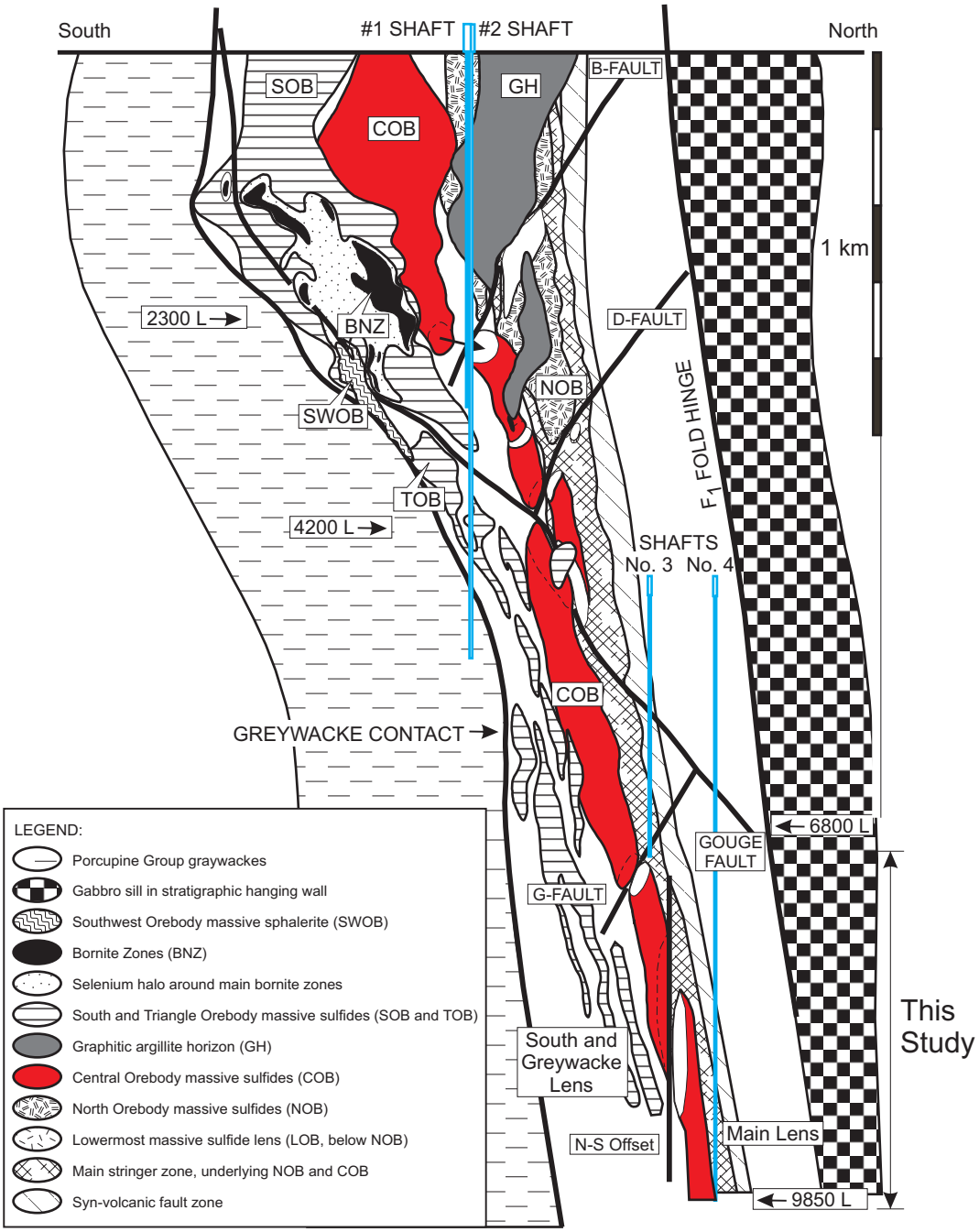


Figure 1.4 Fold-restored long section of the mine looking west. All orebodies are placed in their relative stratigraphic positions (modified with permission from Bleeker., 1999).

Figure 1.5  Map of the 7000 level showing a portion of the Kidd Creek mine dominated by the West and Main lenses (Central orebody) the South Lens and the Greywacke Lens (Triangle orebody). The West and Main Lens are structurally offset pods of the same massive sulfide body. A rare occurrence of black argillite beneath the South Lens may be a reoccurrence of the Triangle orebody in the upper mine. Purple lines are major faults. Minor faults, joints, quartz veins and Cp stringers are mapped in the drifts.

Figure 1.6  Map of the 7500 level showing a portion of the Kidd Creek mine dominated by the West and Main lenses (Central orebody), the South Lens and the Greywacke Lens (Triangle orebody). This is very similar to 7000 level, but the black argillite has migrated northwards relative to the South Lens. Purple lines are major faults. Minor faults, joints, quartz veins and Cp stringers are mapped in the drifts.

Figure 1.7  Map of the 8000 level showing a portion of the Kidd Creek mine dominated by the West and Main lenses (Central orebody), the South Lens and the Greywacke Lens (Triangle orebody). The black argillite has been cut out of the stratigraphy and the N-S Offset has nearly moved through the West-Main Lens. The Greywacke Lens is beginning to disappear. Purple lines are major faults. Minor faults, joints, quartz veins and Cp stringers are mapped in the drifts.

Figure 1.8  Map of the 8600 level showing a portion of the Kidd Creek mine dominated by the West and Main lenses (Central orebody), and the South Lens. The Greywacke Lens has essentially disappeared. The West-Main Lens has migrated through the N-S Offset and Offset Fault yielding a typical mound of massive sulfide. The Cu-rich Stringer zone has also grown in size on the North side of the Offset Fault. Purple lines are major faults. Minor faults, joints, quartz veins and Cp stringers are mapped in the drifts.

Figure 1.9  Map of the 9000 level showing a portion of the Kidd Creek mine dominated by the West and Main lenses (Central orebody), and the South Lens. This is very similar to 8600 level but the Cu-rich stringer zone is being constrained by the presence of massive rhyolite. It is also spread out, likely due to the Offset 2 Fault displacing the zone. Purple lines are major faults. Minor faults, joints, quartz veins and Cp stringers are mapped in the drifts.

Figure 1.10  Map of the 9500 level showing a portion of the Kidd Creek mine dominated by the West and Main lenses (Central orebody), and the South Lens. The Dip of West-Main Lens has decreased once it became bound between the Offset and Offset 2 Faults. Black argillites are present between the mafic volcanics and the gabbro and within the mafic volcanics which may represent another horizon. Purple lines are major faults. Minor faults, joints, quartz veins and Cp stringers are mapped in the drifts.

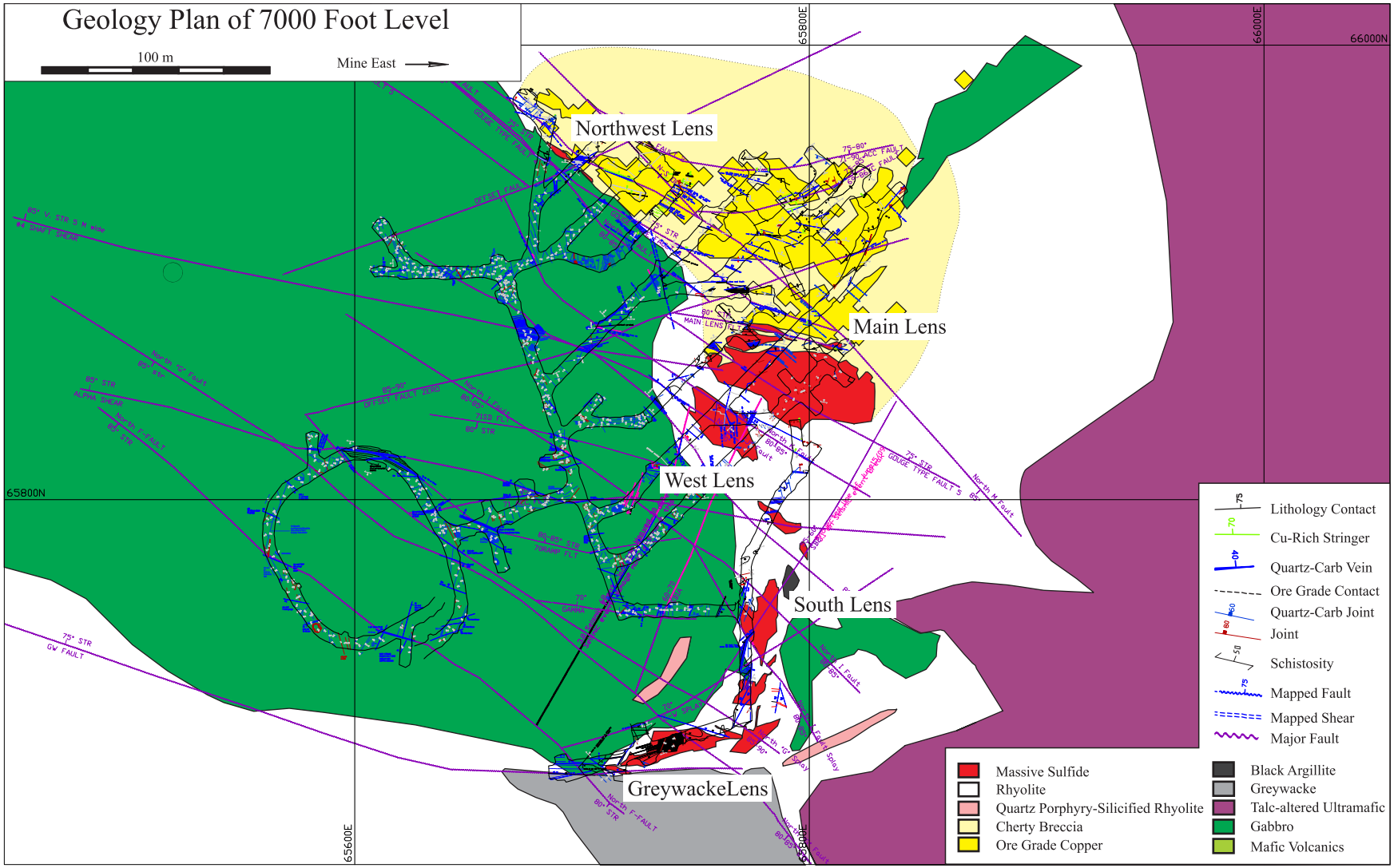
Geology Plan of 7000 Foot Level
100 m
Mine East
Northwest Lens
Main Lens
West Lens
South Lens
GreywackeLens
65800E
66000E
66000N
65800N
65600E
65600E
Lithology Contact
Cu-Rich Stringer
Quartz-Carb Vein
Ore Grade Contact
Quartz-Carb Joint
Joint
Schistosity
Mapped Fault
Mapped Shear
Major Fault
Massive Sulfide
Rhyolite
Quartz Porphyry-Silicified Rhyolite
Cherty Breccia
Ore Grade Copper
Black Argillite
Greywacke
Talc-altered Ultramafic
Gabbro
Mafic Volcanics

Figure 1.5

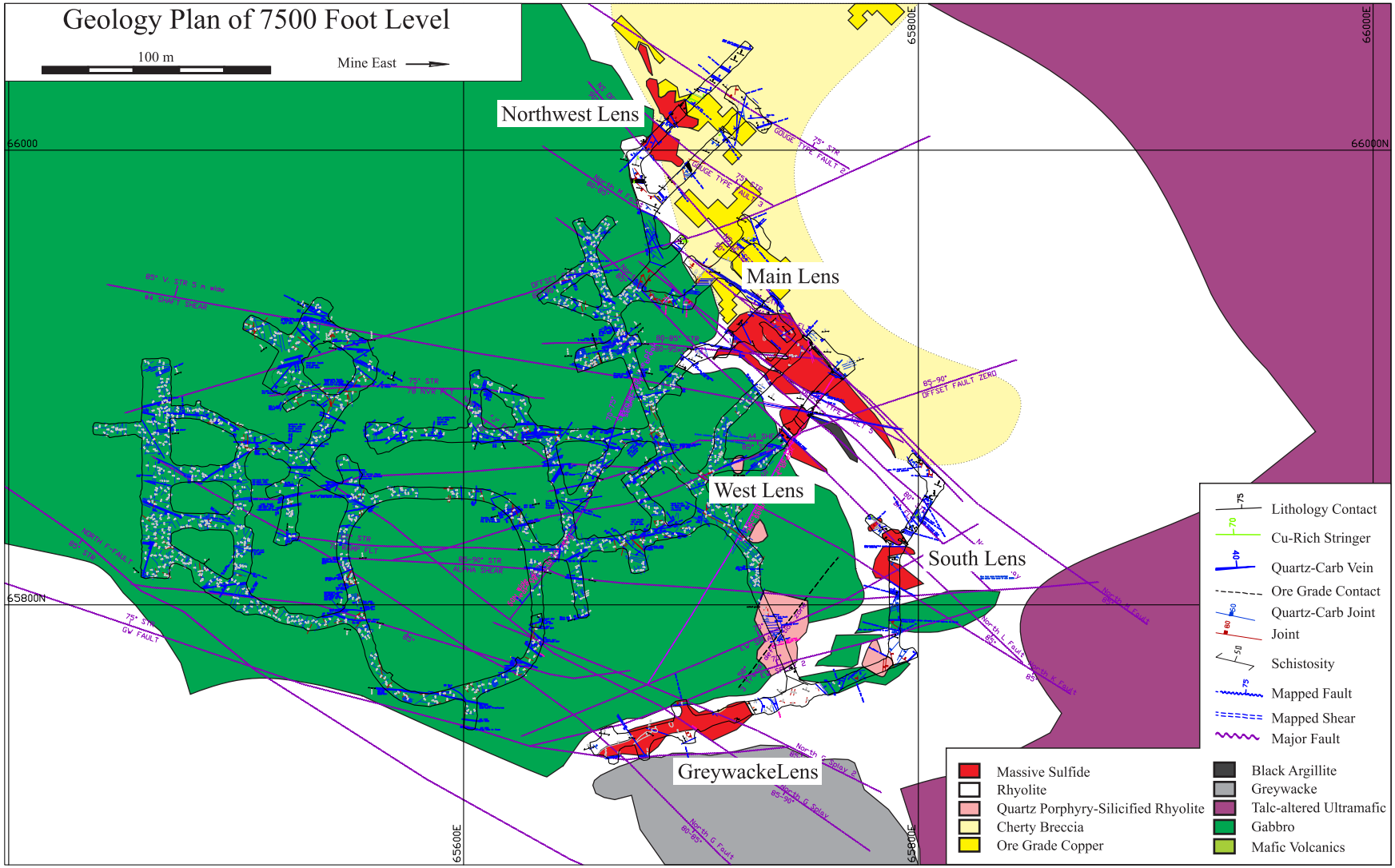
Geology Plan of 7500 Foot Level
100 m
Mine East
Northwest Lens
Main Lens
West Lens
South Lens
GreywackeLens
66000
66000N
65800E
65800N
65600E
Lithology Contact
Cu-Rich Stringer
Quartz-Carb Vein
Ore Grade Contact
Quartz-Carb Joint
Joint
Schistosity
Mapped Fault
Mapped Shear
Major Fault
Massive Sulfide
Rhyolite
Quartz Porphyry-Silicified Rhyolite
Cherty Breccia
Ore Grade Copper
Black Argillite
Greywacke
Talc-altered Ultramafic
Gabbro
Mafic Volcanics

Figure 1.6

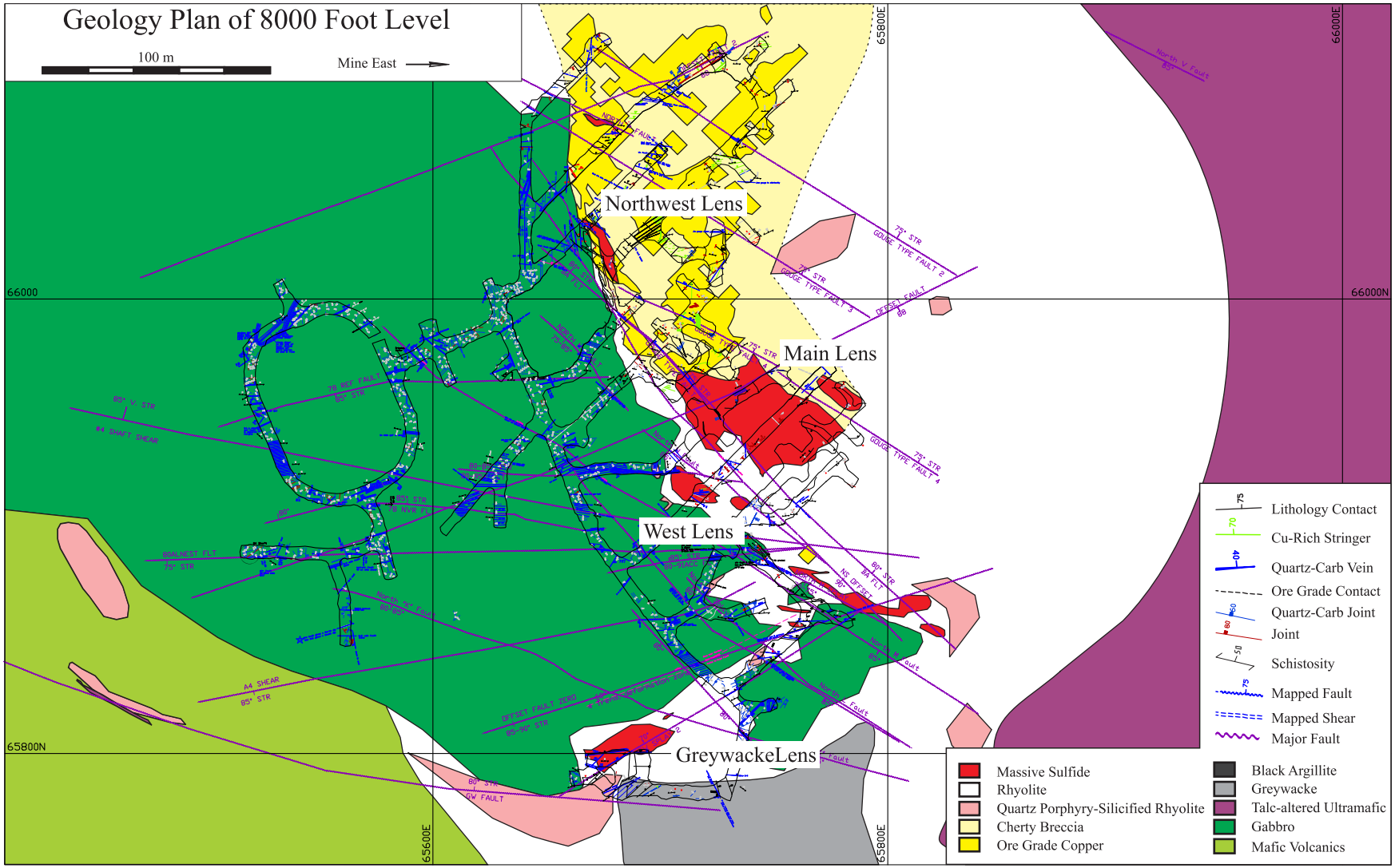
Geology Plan of 8000 Foot Level
100 m
Mine East
Northwest Lens
Main Lens
West Lens
GreywackeLens
66000
66000N
65800N
65600E
65800E
66000E
Lithology Contact
Cu-Rich Stringer
Quartz-Carb Vein
Ore Grade Contact
Quartz-Carb Joint
Joint
Schistosity
Mapped Fault
Mapped Shear
Major Fault
Massive Sulfide
Rhyolite
Quartz Porphyry-Silicified Rhyolite
Cherty Breccia
Ore Grade Copper
Black Argillite
Greywacke
Talc-altered Ultramafic
Gabbro
Mafic Volcanics

Figure 1.7

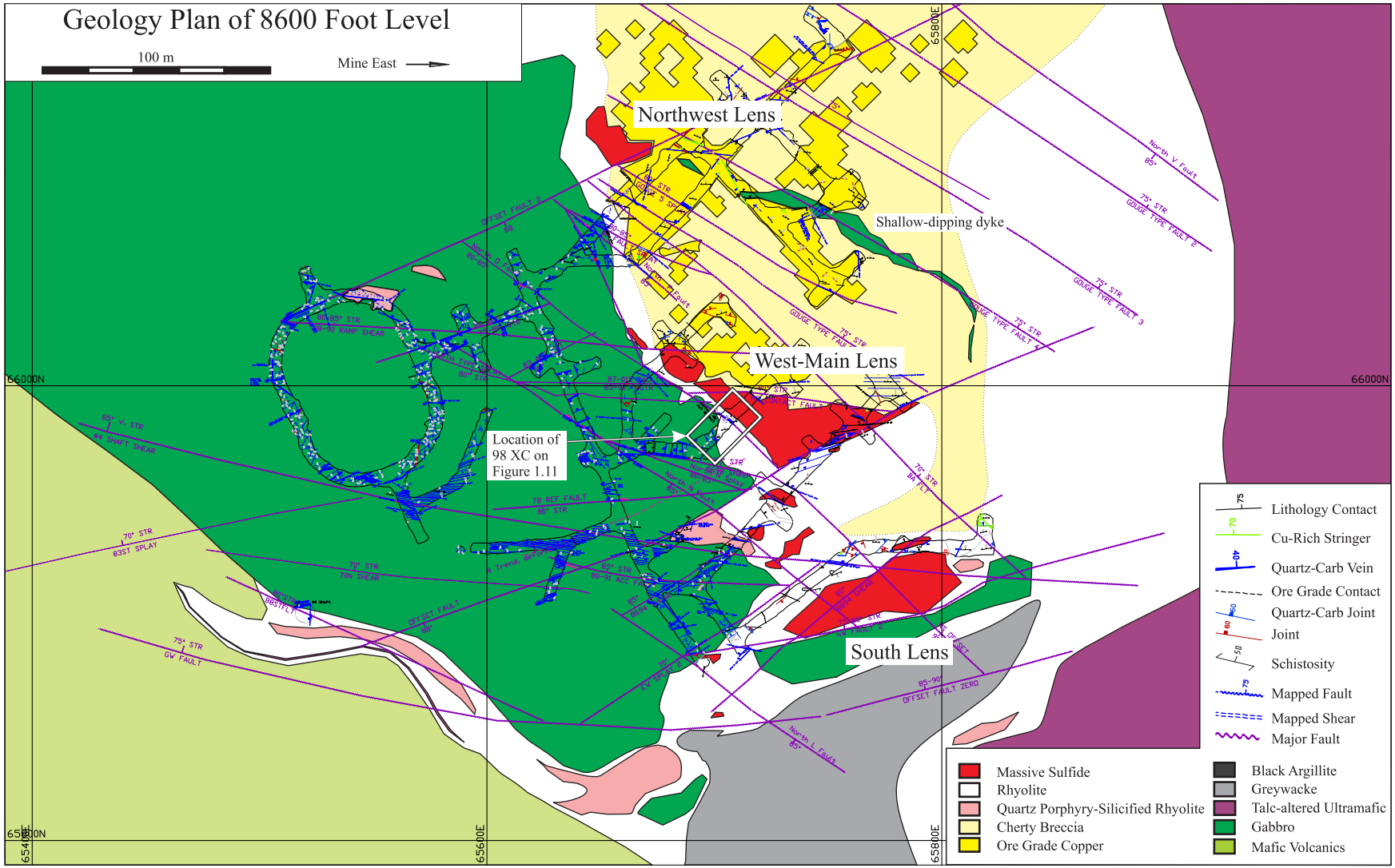
Geology Plan of 8600 Foot Level
100 m
Mine East
Northwest Lens
Shallow-dipping dyke
West-Main Lens
South Lens
Location of 98 XC on Figure 1.11
66000N
65800E
65600E
65400E
Lithology Contact
Cu-Rich Stringer
Quartz-Carb Vein
Ore Grade Contact
Quartz-Carb Joint
Joint
Schistosity
Mapped Fault
Mapped Shear
Major Fault
Massive Sulfide
Rhyolite
Quartz Porphyry-Silicified Rhyolite
Cherty Breccia
Ore Grade Copper
Black Argillite
Greywacke
Talc-altered Ultramafic
Gabbro
Mafic Volcanics

Figure 1.8

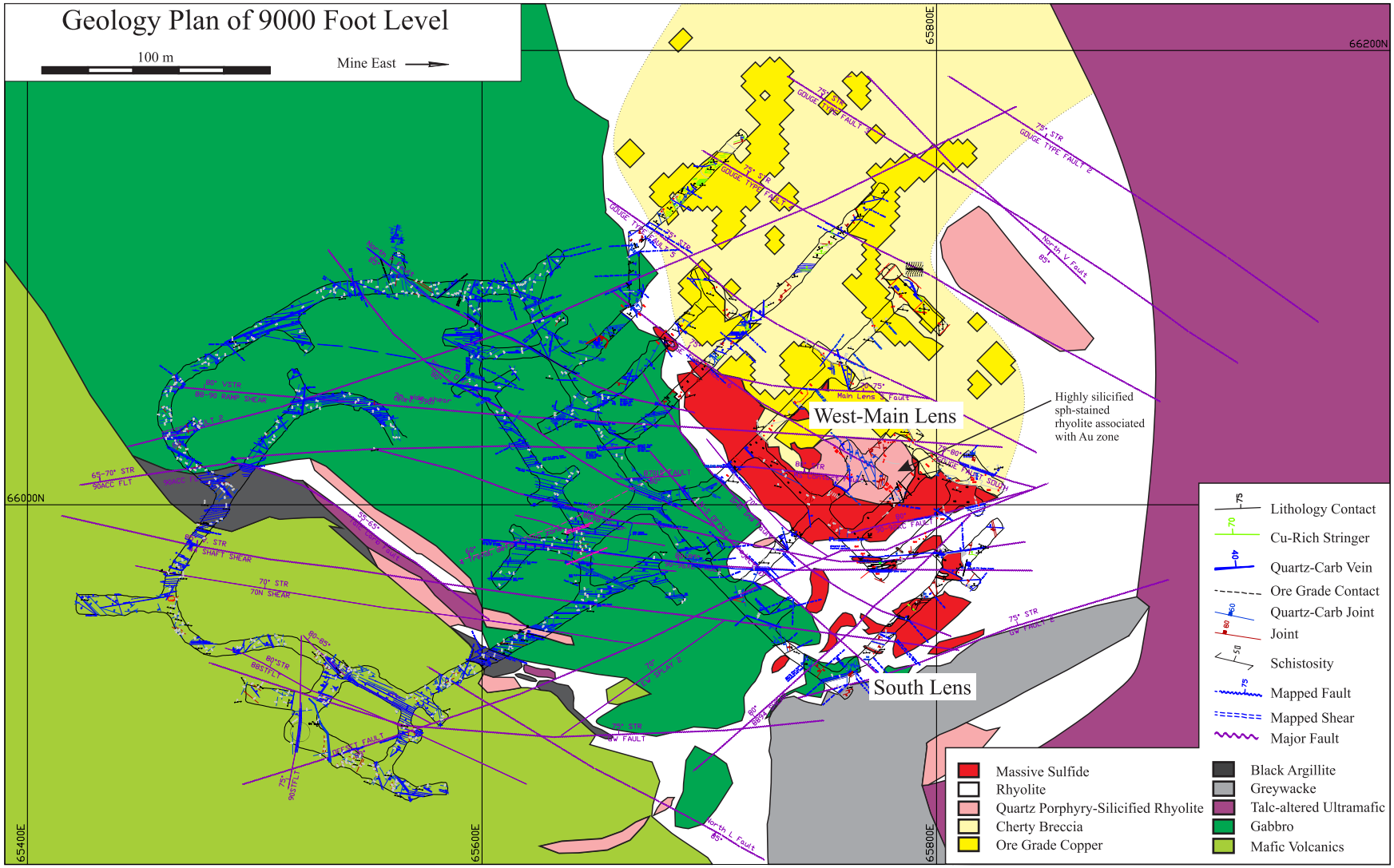
Geology Plan of 9000 Foot Level
100 m
Mine East
65800E
66200N
66000N
65400E
65600E
65800E
West-Main Lens
South Lens
Highly silicified sph-stained rhyolite associated with Au zone
Lithology Contact
Cu-Rich Stringer
Quartz-Carb Vein
Ore Grade Contact
Quartz-Carb Joint
Joint
Schistosity
Mapped Fault
Mapped Shear
Major Fault
Massive Sulfide
Rhyolite
Quartz Porphyry-Silicified Rhyolite
Cherty Breccia
Ore Grade Copper
Black Argillite
Greywacke
Talc-altered Ultramafic
Gabbro
Mafic Volcanics

Figure 1.9

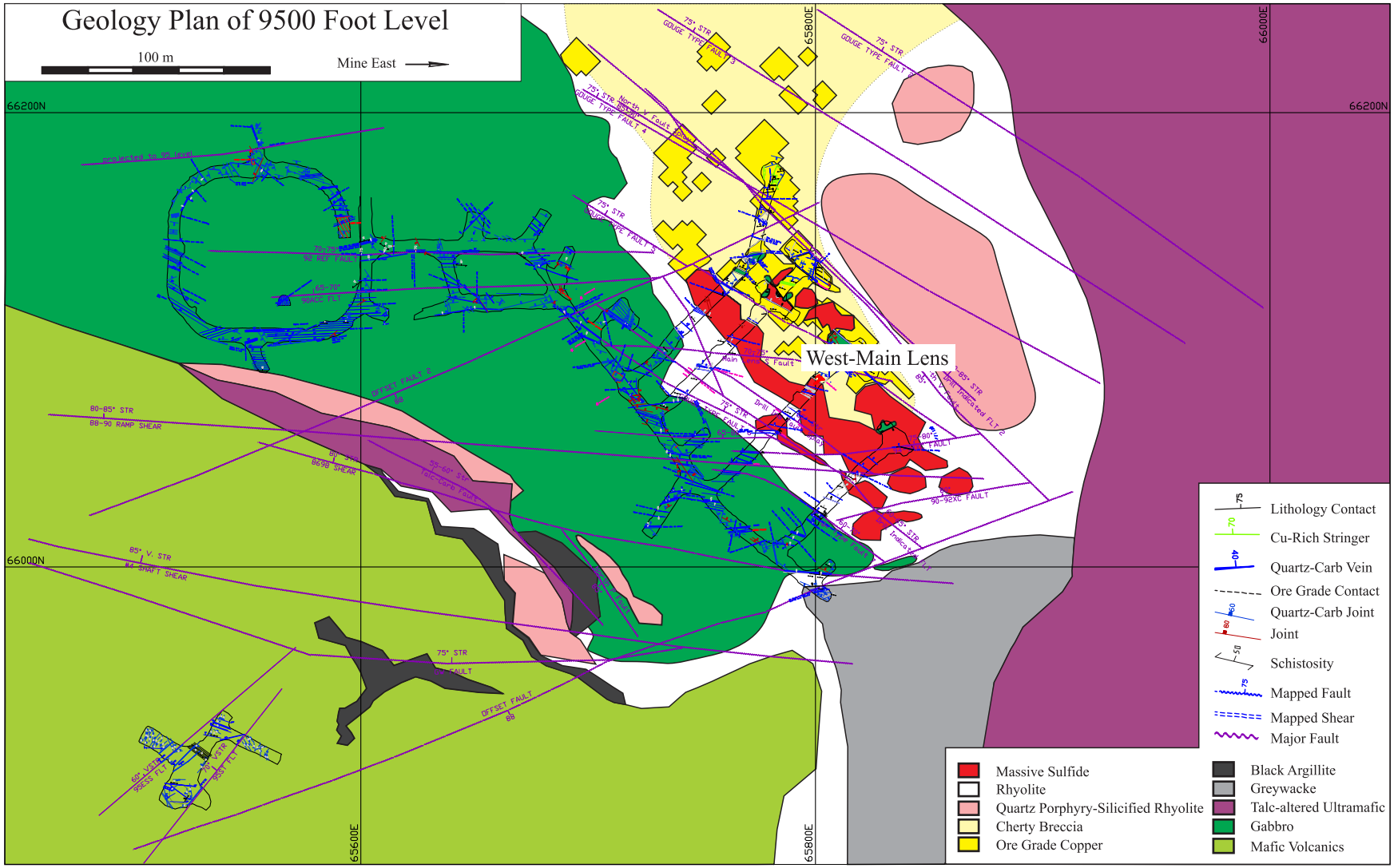
Geology Plan of 9500 Foot Level
100 m
Mine East
66200N
66000N
65600E
65800E
66000E
West-Main Lens
Lithology Contact
Cu-Rich Stringer
Quartz-Carb Vein
Ore Grade Contact
Quartz-Carb Joint
Joint
Schistosity
Mapped Fault
Mapped Shear
Major Fault
Massive Sulfide
Rhyolite
Quartz Porphyry-Silicified Rhyolite
Cherty Breccia
Ore Grade Copper
Black Argillite
Greywacke
Talc-altered Ultramafic
Gabbro
Mafic Volcanics

Figure 1.10

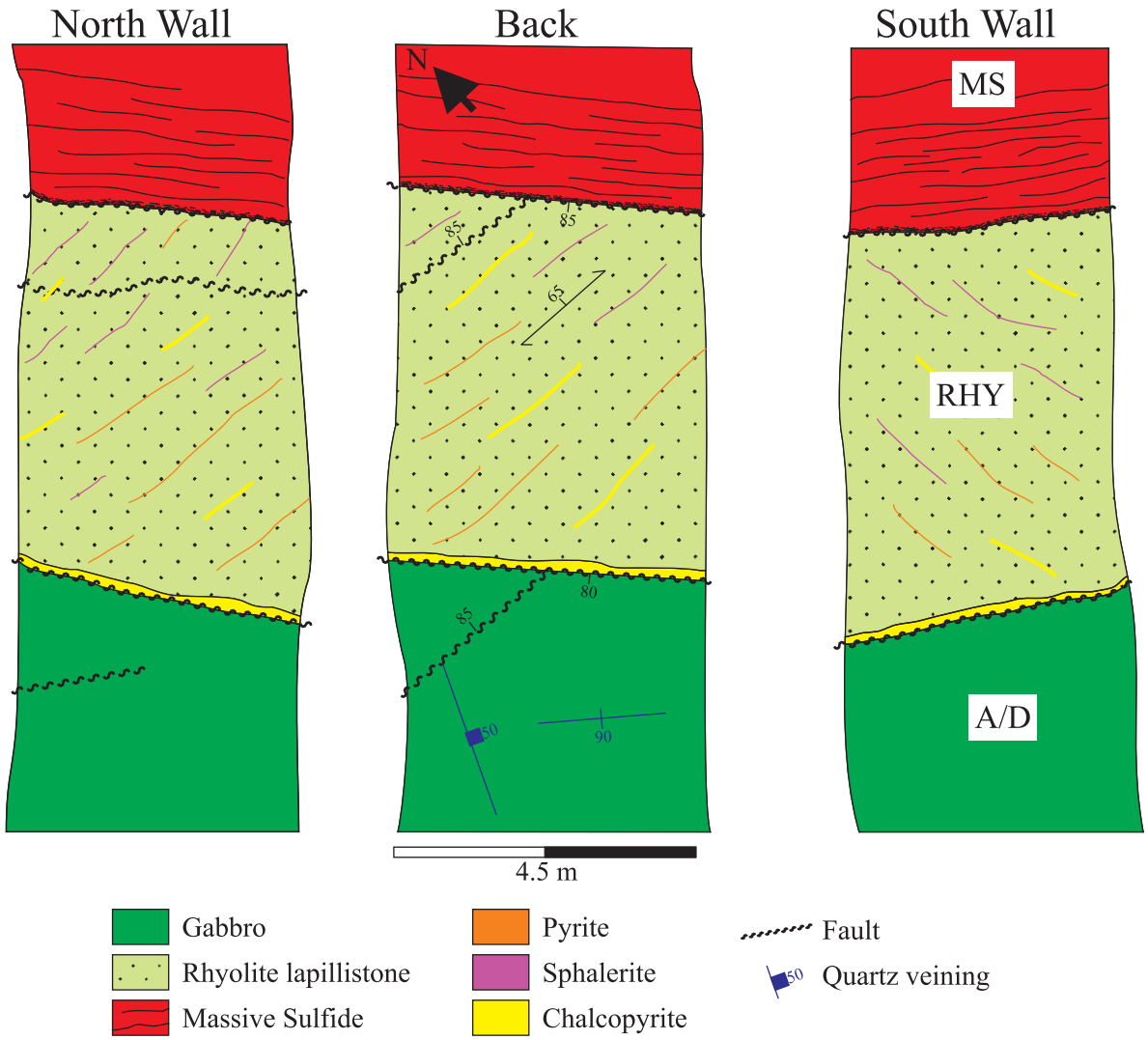


Figure 1.11 Map of an ore exposure in the 98 crosscut on 8300 Level. Faulted contacts between the gabbro sill (A/D), the rhyolite lapillistone, and the massive sulfides. The gabbro contains many quartz-carbonate veins and joints. A pervasive 30 cm chalcopyrite stringer has been remobilized into the faulted contact between the gabbro and the rhyolite. The rhyolite contains heavy sericite alteration along schistocity with bands of pyrite, sphalerite staining and few chalcopyrite stringers. The faulted contact between the rhyolite and the massive sulfides, which are predominantly pyrite and sphalerite with minor chalcopyrite, contains 3-5 cm of gouge. The massive sulfides are also strongly sheared up to several metres away from the contact. Two East-West steeply dipping faults were also seen terminating against the faults.

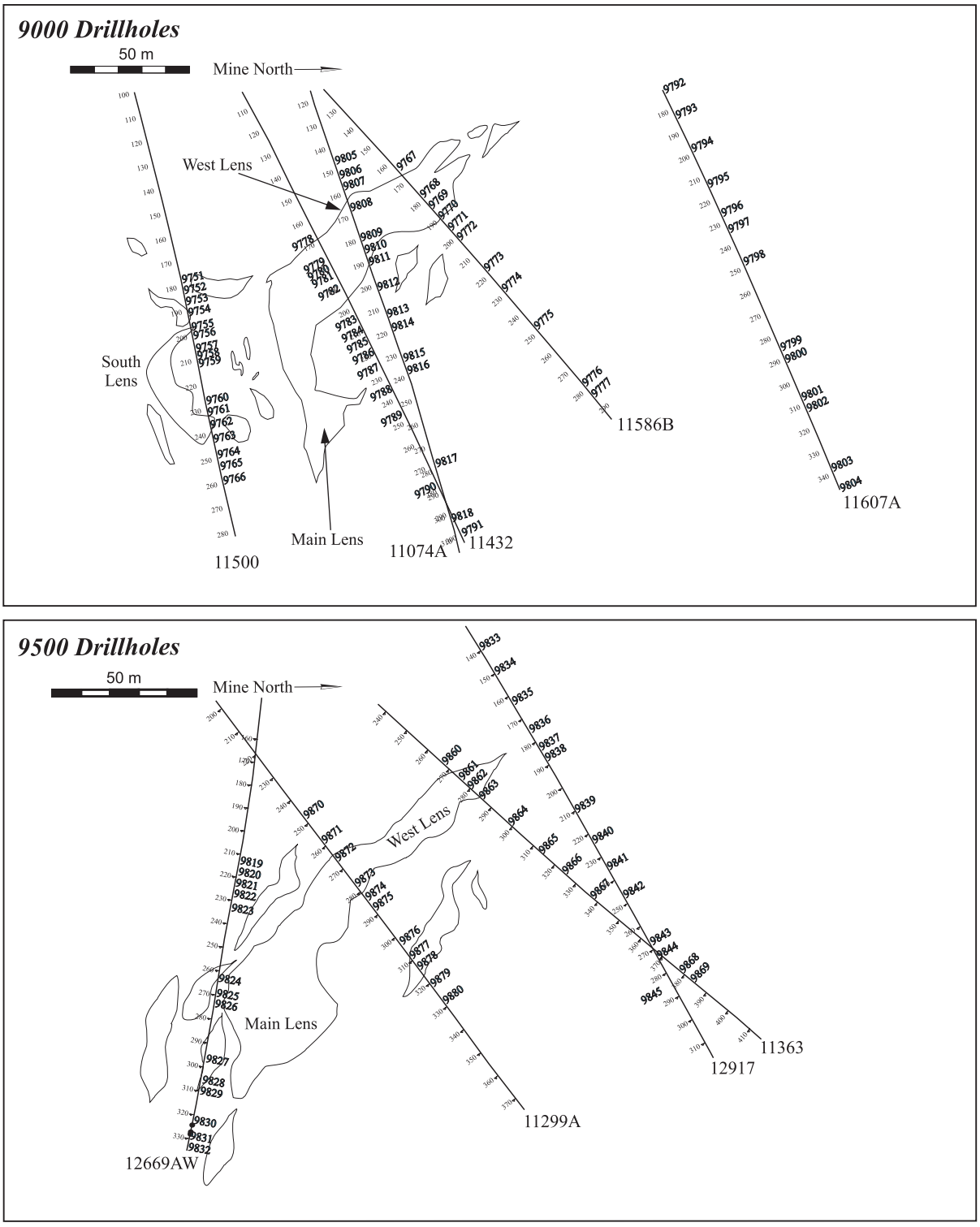


Figure 1.12 Diamond Drill-hole and sample locations at the 9000 and 9500 levels.

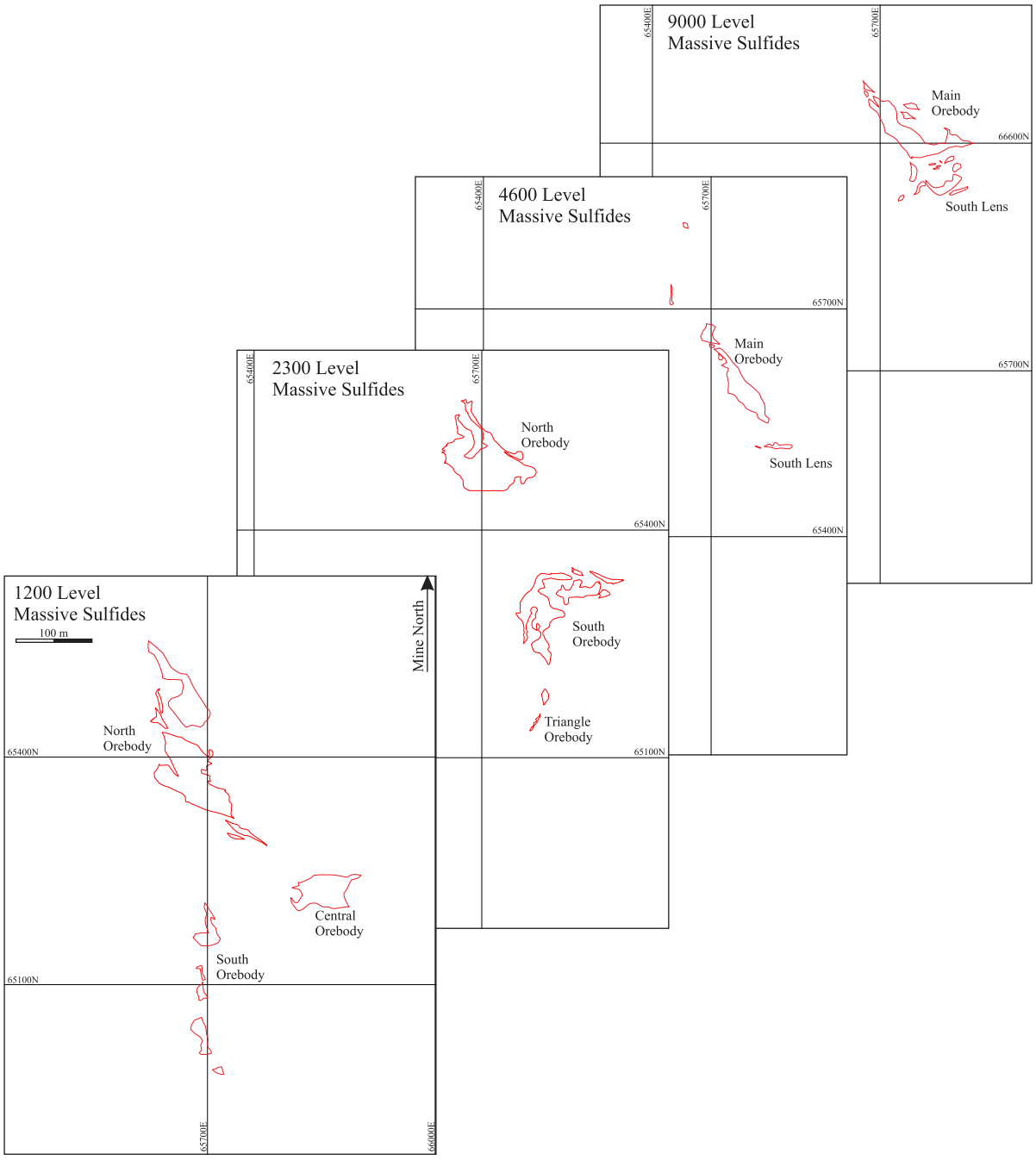


Figure 1.13 Representative cross sections of 1200, 2300, 4600, and 9000 levels showing the relative sizes of the massive sulfide bodies.

# Chapter 2. Description of the Ore Lenses in Mine D

## *2.1 West and Main Lenses*

The Main Lens, which is interpreted to be a downplunge extension of the Central orebody from the upper mine, is the largest lens in Mine 3. It is up to 50 m thick and is composed of massive pyrite and pyrrhotite with zones of massive sphalerite and lesser chalcopyrite. It is thickest in Mine 3 around the 6000 level and decreases in size downplunge where it is split by the N-S Offset into the Main lens and a structurally offset portion, West Lens. At 8600 level, the N-S Offset has completely migrated through the massive sulfides which have left the West Lens as the dominant massive sulfide body with a thickness of 35 m (Figure 2.1). The main host rock is tuffaceous rhyolite that overlies highly silicified massive rhyolite immediately below the massive sulfides.

In Mine 3, the stratigraphic top of the massive sulfide lens comprises heterolithic fragmental ore grading into massive sphalerite ore and finally to massive sphalerite-chalcopyrite ore (see below) at the stratigraphic base of the lens (Table 3.1 and 3.2). Cu-rich stringers underlie the massive sulfides. In Mine D, the Main Lens consists of massive sphalerite, chalcopyrite and pyrrhotite. A zone of semi-massive pyrrhotite-chalcopyrite commonly occurs immediately below the Main Lens in the cherty breccia and grades into a conformable Cu-rich stringer zone that is interpreted to have been the main upflow zone of the deposit.

Heterolithic fragmental ores are important at the stratigraphic top of the West Lens and Main Lens and contain abundant galena and Ag-rich tetrahedrite. These ores grade into massive sphalerite (both pyrite and pyrrhotite-rich) and finally to massive sphalerite-

chalcopyrite-pyrrhotite ore at the base of the lenses (Table 3.1 and 3.2). The massive sulfides are hosted by tuffaceous rhyolite and typically lie stratigraphically above a zone of massive silicified rhyolite. Semi-massive sulfides consisting of chalcopyrite, pyrrhotite and pyrite stockwork occur locally below the zone of massive silicified rhyolite. All of these sulfides lie above a conformable zone of Cu-rich stringers associated with intense chlorite alteration and minor tourmaline.

The presence of similar mineralization in the West and Main lenses is consistent with the interpretation that the West lens is a faulted portion of the Main Lens. The heterolithic fragmental ore belongs to the epiclastic deposits that accumulated on top of the massive sulfide lenses along the length of the orebody (Figure 2.2). Sphalerite clast-rich ore in the West and Main lenses consists of sphalerite clasts up to metres in scale but generally up to 10 cm in size. Other clasts consist of pyrite and felsic lapilli. Many of the clasts are sheared and elongated which makes their original characteristics hard to identify compared to similar ore in the upper part of the mine. The proportion of heterolithic fragmental ore is also much smaller than in the upper part of the mine where the main orebodies were overlain by thick deposits of epiclastic material.

The bulk of the massive sulfides which occur beneath the fragmental ores in the West and Main lenses consist of pyrite-pyrrhotite, pyrite-sphalerite ore, and pyrrhotite-sphalerite ore with minor stringer sphalerite (Figure 2.2). The sphalerite-rich ores contain galena, Ag-tetrahedrite (Figure 2.3A) and cassiterite (Table 3.1 and 3.2) and closely resemble the pyrite-sphalerite ores from the North Orebody in the upper mine.

Massive sphalerite ore occurs beneath the pyrite-sphalerite zones towards the margins of the West and Main Lenses (Figure 2.2 and Figure 2.3D). Locally, it consists of an aggregate of many massive sphalerite clasts with bands of pyrite. This ore type typically contains abundant fine-grained cassiterite and also commonly exhibits replacement by chalcopyrite, similar to that in the North Orebody in the upper mine.

Sphalerite-chalcopyrite ores occur at the base of the West and Main lenses, dependant on depth (Figure 2.2). The chalcopyrite forms stringers in the massive sulfides, locally overprinting the massive sphalerite and pyrrhotite (Figure 2.4C). The sphalerite exhibits abundant chalcopyrite disease and is extensively replaced by chalcopyrite and pyrrhotite. In contrast to the upper mine, the distinction between massive sphalerite and massive chalcopyrite ores is less clear, as sphalerite and chalcopyrite are commonly both present in abundance. The only massive chalcopyrite in Mine D appears to be related to structural remobilization.

### *2.2 Copper Stringer Zone*

The Cu-stringer zone is interpreted to have been the main feeder zone of the deposit, possibly along a graben-bounding fault extending from surface to the bottom of the mine (Figure 3.7: Bleeker, 1999; Hannington et al, 1999). The zone consists primarily of chalcopyrite stringers up to 1m wide containing up to 20 wt% Cu (Figure 2.4D). In some locations, chalcopyrite has been structurally remobilized into massive chalcopyrite veins. Stringer pyrrhotite and chlorite are also commonly associated with the chalcopyrite. Sericite and sphalerite staining (Figure 2.3E) occur in silicified rhyolite at the margins of the stringer

zone. The distribution of the Cu stringers in the deep mine is now mainly controlled by a series of E-W trending sub-vertical offset faults that may have been part of the original upflow zone. The stringer zone has also been displaced by a combination of the E-W trending Offset fault and the Northwest-Southeast trending South-dipping faults (such as the North M e.g., Figure 2.1).

If only ore grade material is considered (greater than 2% Cu equivalent), it is evident that there is somewhat more contained copper at the 4600 level than 9000 level (ratio of approximately 1.28:1). However, the Cu-rich stringer zone on 4600 is very compact, with little low-grade material between the high-grade zones, whereas on 9000 the stringer zone is broader with abundant low-grade material between the high-grade zones. If these low grade zones are included, 9000 level has approximately the same overall contained copper.

### *2.3 South Lens*

The South Lens is a sphalerite-rich orebody perched on highly silicified rhyolite that consists of massive pyrite-pyrrhotite-sphalerite ore and massive sphalerite ore with locally remobilized chalcopyrite stringers (Figure 2.2), similar to the West and Main Lenses (Table 3.1 and 3.2). It is interpreted to be either a stacked lens stratigraphically above the Main and West lenses or a structural offset from the Main Lens. Graphitic argillites are present in the footwall of the South Lens between 7000 and 8000 level (Figure 1.5 and 1.6), implying that it is a separate orebody, as in the upper part of the mine. The South Orebody was very large in the upper mine but decreased in size downplunge and was cut out of the stratigraphy around the 4000 level by the northward migration of the greywacke contact and the southern

migration of the North B fault (Figure 1.4). In Mine No.3 the greywacke contact retreats towards the South and the South Lens reappears at 4900 Level. Unlike in the upper mine, the South Lens is located in an intensely sheared area, which has dismembered the lens into many discrete elongated panels that are difficult to piece back together. No significant Cu-rich stringer zone occurs below any part of the South Lens. This is a major difference from the upper mine, where the Cu-rich tail of the South Lens contained the bornite zone and selenium halo (Hannington et al., 1999). "Bornite-zone like" mineralogy has been intersected in a diamond drill hole to the southeast (including a Se-rich halo: Figure 4.1), but no other traces of bornite ore have been found. The main part of the South Lens is most Cu-rich on its west side, which contrasts with the metal zoning in the other lenses.

### *2.4 Greywacke Lens (Triangle orebody)*

The Triangle orebody, which is referred to as the Greywacke Lens in Mine D, was another orebody near the South Orebody in the upper mine (Figure 1.6). It was present in Mine No.1 and No.2, but was cut out of the stratigraphy at approximately 4400 level by the North C fault. It has reappeared below 5600 level, most likely due to the southward migration of the greywacke contact (Figure 1.4). In Mine D, the Greywacke Lens is located near the termination of the gabbro sill and is bound by a series of major offset faults. It has higher copper grades (up to 10 wt% Cu) than the South Lens but still contains abundant sphalerite and consists mostly of massive sphalerite-chalcopyrite ore (Figure 2.2). The sphalerite within this orebody is very coarse, dark, and truly massive, with little to no pyrite

or pyrrhotite. This ore type closely resembles the Triangle orebody of the upper mine (Table 3.1 and 3.2).

### *2.5 Northwest Lens*

The Northwest Lens is located to the north of the Main and West lenses. It consists of pyrite and pyrrhotite and has no recognized ore potential (Figure 2.3C). Although chalcopyrite stringers are found beneath the lens, there is rarely any copper or zinc mineralization within the massive pyrite and pyrrhotite (Figure 2.2). This lens is discontinuous, and its position appears to be controlled by the vertical offset faults (Figure 2.1) suggesting that it was structurally emplaced on top of Cu-rich stringers (Table 3.1 and 3.2).

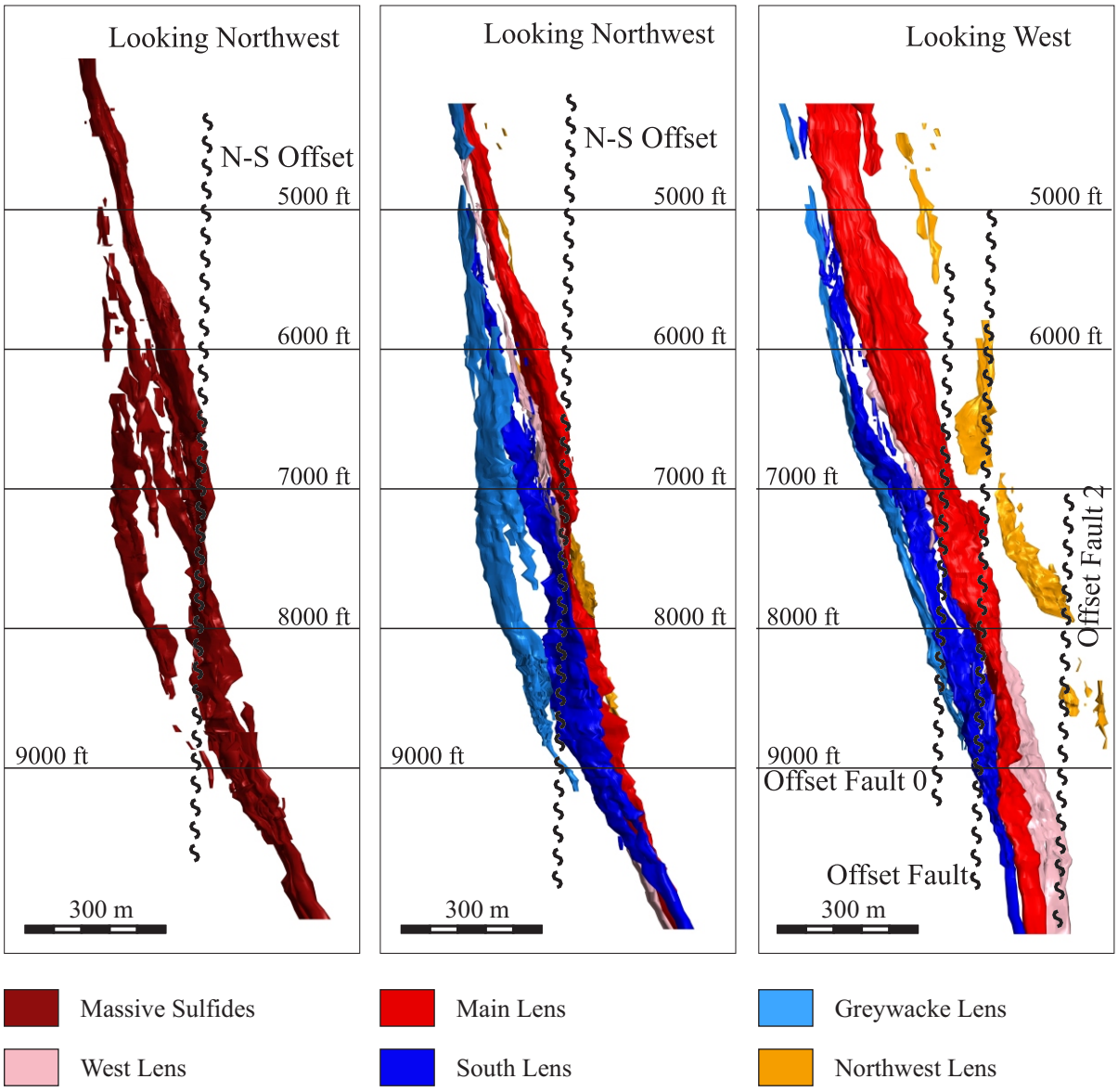


Figure 2.1 Long sections of ore zones in Mine 3 and Mine # from 4600 ft level to 9600 ft level (A). Section looking Northwest showing the displacement of the N-S Offset Fault in massive sulfides. (B). Section looking Northwest showing ore zones (note: Cu-rich stringer is not represented). (C). Section looking West showing the displacements of the roughly E-W trending Offset Fault series.

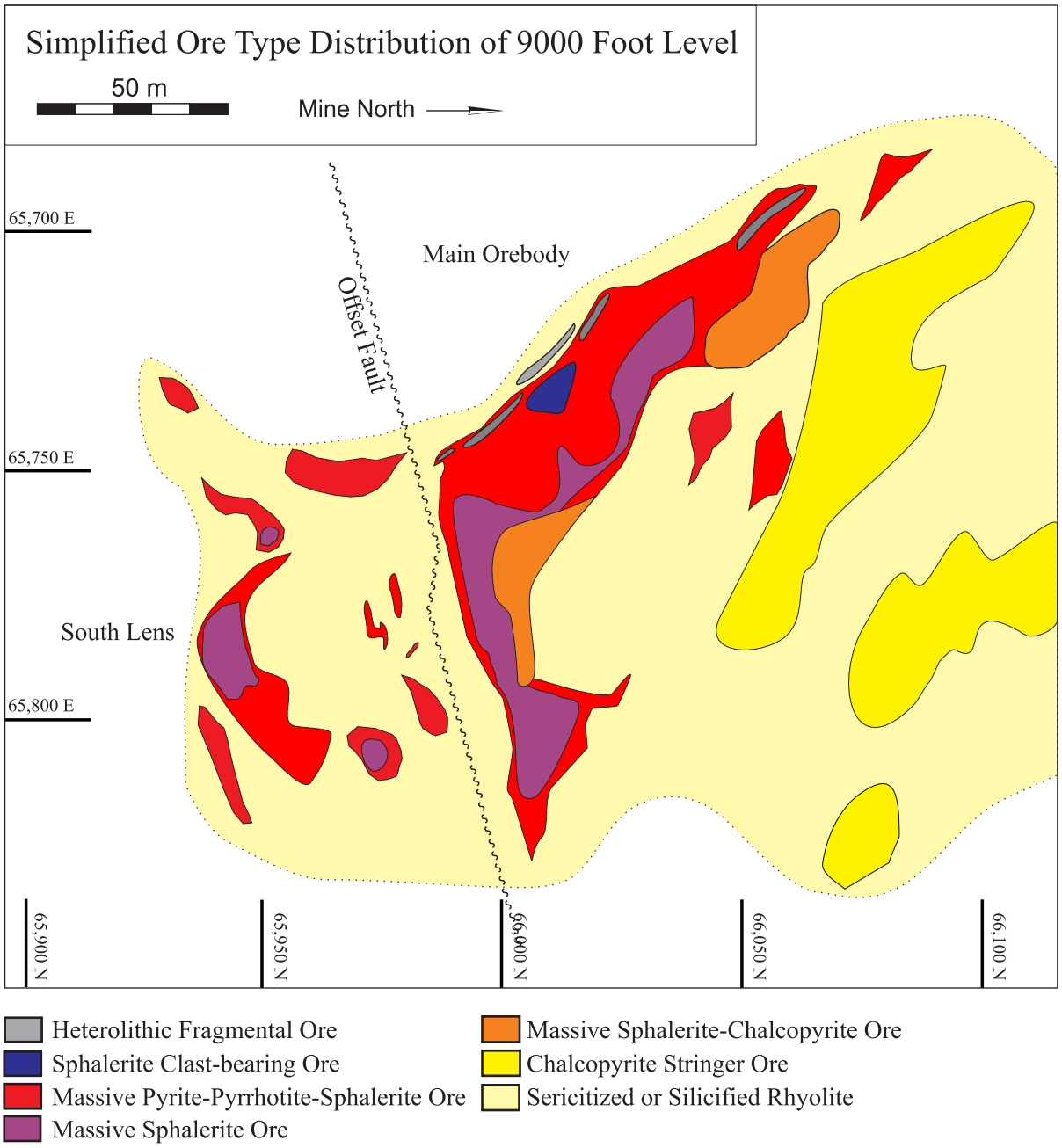


Figure 2.2 Schematic illustration of the distribution of different ore types in the Main Orebody and South Lens of the 9000 foot level.

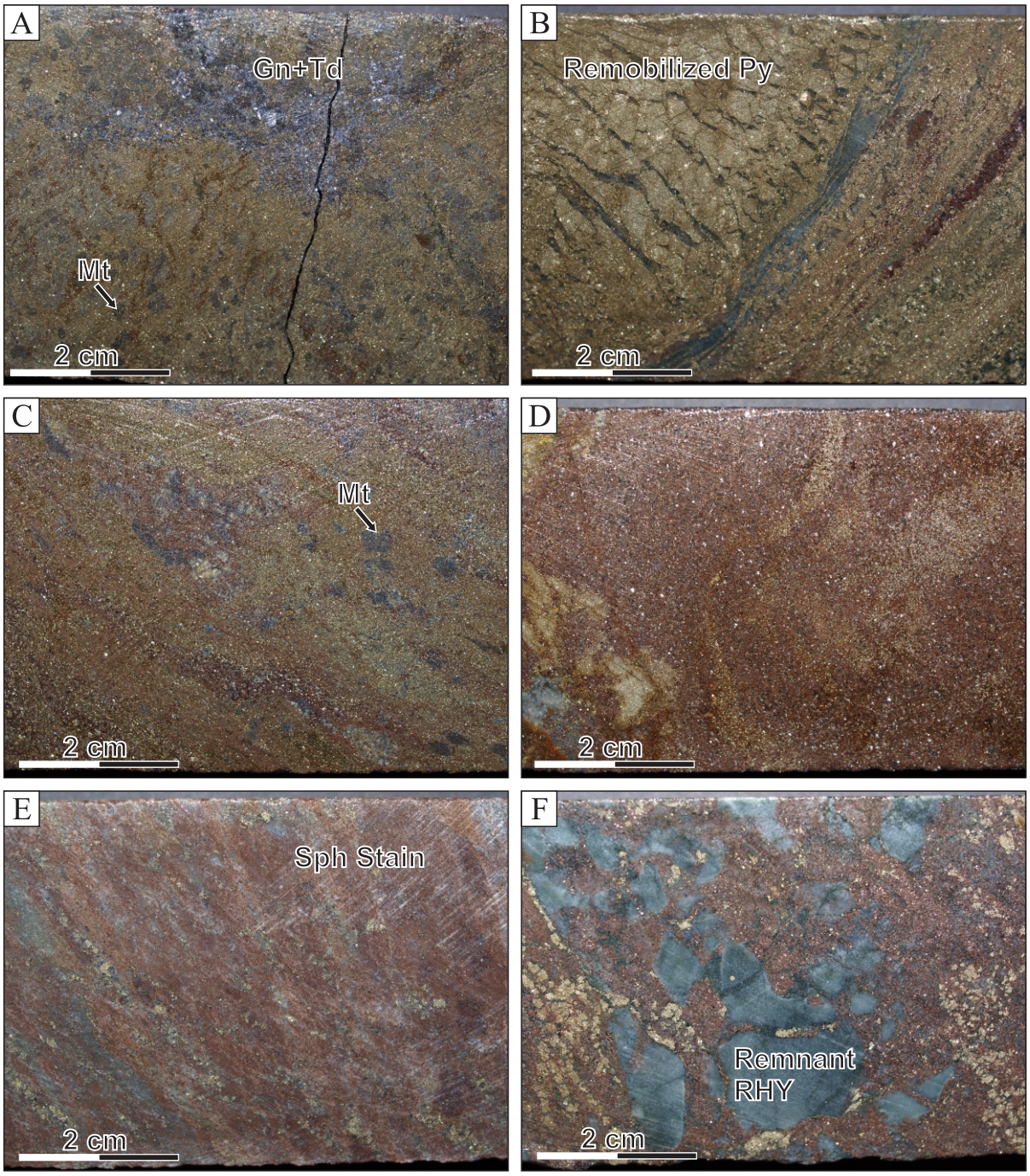


Figure 2.3 Representative photographs of diamond drill cores or ore types in Mine D. All core is NQ core which has a diameter of 4.76 cm. A) Massive pyrite ore containing galena, magnetite blebs and wispy sphalerite; KCD209781. B) Massive pyrite-sphalerite ore with abundant remobilized pyrite; KCD209872. C) Fine-grained massive pyrite-sphalerite ore with magnetite blebs; KCD209782. D) Massive sphalerite with wisps of pyrite; KCD209815. E) Sphalerite staining with minor pyrite; KCD209818. F) Sphalerite stringer with minor pyrite growing between brecciated host rhyolite; KCD209813.

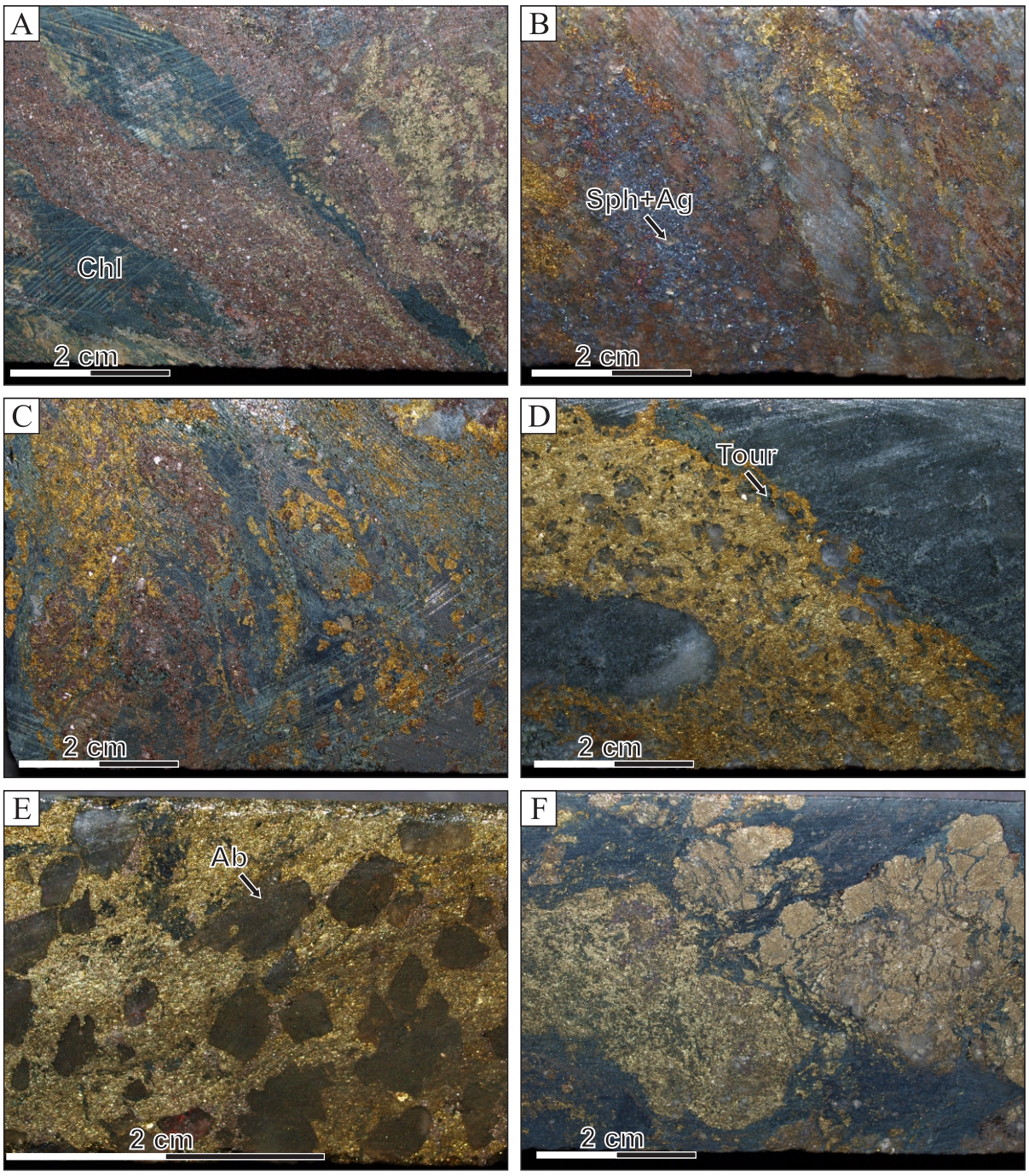


Figure 2.4 Representative photographs of diamond drill cores or ore types in Mine D. All core is NQ core which has a diameter of 4.76 cm. A) Massive pyrite-sphalerite in a heavily chloritic matrix; KCD209784. B) Sphalerite-chalcopyrite stringer in a high grade silver zone; KCD209873. C) Massive sphalerite-chalcopyrite in a heavily chloritic matrix; KCD209785. D) Chalcopyrite stringer with associated pyrrhotite and tourmaline; KCD209795. E) Chalcopyrite with large albite porphyroblasts. This core has been quartered; KCD209796. F) Remnant nodular pyrite in a rich chloritic matrix with fine-grained chalcopyrite and pyrite; KCD209810.

Table 2.1 Tonnage and Grades in Mine D

| Ore Zone | Tonnes (Mt) | Cu (%) | Zn (%) | Pb (%) | Ag (g/t) |
|---|---|---|---|---|---|
| West Lens | 5.1 | 1.3 | 7.7 | 0.5 | 150 |
| Main Lens | 6.4 | 1.1 | 10.0 | 0.1 | 52 |
| South Lens | 5.4 | 1.3 | 8.2 | 0.1 | 32 |
| Greywacke Lens | 2.1 | 3.0 | 10 | 0.3 | 94 |
| Northwest Lens | 0.6 | 1.4 | 2.5 | <0.1 | 10 |
| Cu-Rich Stringer Zone | 13.3 | 3.24 | 0.6 | <0.1 | 30 |

Data are from the bottom of 6800 to 10200 ft.
Cu-rich Stringer Zone data is for total Copper within the stringer envelope.

Table 2.2 Distribution of Ore Types in the main lenses of Mine D

| West and Main Lens | South Lens | Greywacke Lens | Northwest Lens | Cu-rich Stringer |
|---|---|---|---|---|
| Heterolithic fragmental ore | Sphalerite staining and stringers | Massive sphalerite-pyrite ore | Massive pyrite | Cu stringer mineralization |
| Sphalerite clast-rich breccias | Massive sphalerite-pyrite ore | Massive sphalerite-pyrrhotite ore | Massive sphalerite-chalcopyrite ore | Sphalerite staining and stringers |
| Sphalerite staining and stringers | Massive sphalerite-pyrrhotite ore | Massive sphalerite-chalcopyrite ore | Cu-stringer mineralization | |
| Massive pyrite | Massive sphalerite-chalcopyrite ore | | | |
| Massive sphalerite-pyrite ore | Cu-stringer mineralization | | | |
| Massive sphalerite-pyrrhotite ore | | | | |
| Massive sphalerite-chalcopyrite ore | | | | |
| Cu stringer mineralization | | | | |

# Chapter 3. Mineralogy and Mineral Chemistry

Pyrite, pyrrhotite, sphalerite and chalcopyrite are the principal ore minerals in all of the Lenses of Mine D with minor galena and magnetite and trace cassiterite, Ag-tetrahedrite, native Ag, Ag-sulfantimonides, arsenopyrite, cobaltite and Bi-Pb-Ag selenides. Textural relationships are illustrated in Figures 3.1 to 3.11 and are described below. Electron microprobe analyses of selected sulfides were carried out on 22 carbon coated polished sections and the results are listed in Table 3.3 and Table 3.4.

## *3.1 Pyrite*

Pyrite occurs in many forms in the deep orebodies in all stages of mineralization. It is most common in the upper parts of the massive sulfide lenses in association with massive sphalerite as disseminated euhedral to anhedral, millimetre-scale grains and aggregates (Figure 3.4E). It occurs as apparent primary intergrowths with sphalerite in generally sub rounded and disseminated grains in massive sphalerite ores. Pyrite also occurs locally as skeletal growths in massive sphalerite similar to that documented in the upper part of the deposit (Hannington et al, 1999). Recrystallized pyrite is present as coarse euhedral porphyroblastic crystals overprinting mainly sphalerite but also chalcopyrite and pyrrhotite. At the base of the massive sulfides and in the stringer zone pyrite typically occurs as euhedral, fine-to medium-grained (0.01 to 0.1 mm) aggregates (Figure 3.4F).

For the most part, pyrite contains few trace elements, but notable concentrations of Co, As, Se are found in samples at the stratigraphic base of the West Lens. The maximum

concentrations of Co, As, and Se were 0.36 wt %, 0.24 wt % and 0.27 wt %, respectively (Appendix II).

The pyrite-pyrrhotite-magnetite ratio changes through the massive sulfide pile corresponding to stratigraphic depth. Near the stratigraphic top of the pile in heterolithic fragmental ores, sphalerite clast rich ores, and massive pyrite-sphalerite, tend to have a high Py:Po:Mt ratio (such as 66:7:27 respectively). In the middle of the lenses, massive sphalerite and massive pyrrhotite-sphalerite ore, the Py:Po:Mt ratio is different (such as 60:29:11 respectively) due to a lack of magnetite in the middle of the sulfide lenses. Near the bottom of the massive sulfide lenses, in sphalerite-chalcopyrite ores, the Py:Po:Mt ratio is 31:51:18, (Figure 3.12, data from Kidd Operations Hotmuck Project). These ratios do not account for the presence of siderite or chlorite.

### *3.2 Pyrrhotite*

Pyrrhotite occurs as disseminated grains and as crystals intergrown with chalcopyrite, sphalerite, pyrite and arsenopyrite (Figure 3.5A). It most commonly occurs at the base of the massive sulfide lenses and in the chalcopyrite stringer ores with massive chalcopyrite. It can also be found as disseminated grains at the stratigraphic top of the massive sulfides and to a lesser extent in the fragmental ore (Figure 3.5C), as “pyrrhotite disease” in sphalerite. It is found locally as skeletal intergrowths, similar to pyrite, in the upper part of the massive sulfides.

The pyrrhotite at depth in the mine is dominantly non-magnetic, typical of hexagonal pyrrhotite. Only one of 52 analyzed samples had Fe contents less than 46.9 mol % Fe

(Appendix III). This contrasts with the dominantly monoclinic pyrrhotite in the North and Central orebodies in the upper part of the mine (Figure 3.14).

Pyrrhotite, like pyrite, contains few trace elements, but notable concentrations of Co (up to 0.10 wt %) and As (up to 0.14 wt %) are found in samples from the Cu-rich stringer zone and massive Py-Sph ores respectively. Inclusions of other sulfides likely account for some analyses with anomalous Cu, Zn, Pb, Sb, Ag and Au (Appendix III).

### *3.3 Chalcopyrite*

Chalcopyrite occurs as fine-to coarse-grained (0.01 to 2 mm) anhedral masses intergrown with pyrrhotite and, to a lesser extent, with sphalerite and pyrite, mainly in veins and stringers. These are typical of the Cu-rich stringer zone together with silicified rhyolite (Cherty Breccia), which accounts for a significant amount of the chalcopyrite in Mine D. At the base of the massive sulfide lenses chalcopyrite is more disseminated within sphalerite but can be massive when juxtaposed against major structures where it has been remobilized. At the top of the massive sulfides chalcopyrite occurs as discrete masses generally replacing pyrite along grain boundaries or in fractures. Chalcopyrite may contain inclusions of tourmaline, albite and chlorite within stringers.

Chalcopyrite contains notable concentrations of Se (up to 0.16 wt %), In (up to 0.10 wt %), Co (up to 0.09 wt %), Bi (up to 0.23 wt %), and Ag (up to 0.24 wt %) (Appendix V).

### *3.4 Sphalerite*

Sphalerite ranges from fine-grained (<10 μm) to coarsely crystalline (up to 5 mm) and occurs as anhedral masses intergrown with anhedral to euhedral pyrite, pyrrhotite, chalcopyrite and magnetite. At the stratigraphic top of the lenses, massive sphalerite is commonly intergrown with galena and tetrahedrite which occur at grain boundaries. At the base of the massive sulfides in the sphalerite-chalcopyrite ore, it is common to find abundant chalcopyrite disease (Figure 3.1D). Pyrrhotite is also commonly found as blebs in massive sphalerite (Figure 3.1C). Sphalerite also occurs as coarse crystals (up to 8 mm) in chlorite-rich veins in the stringer portion of the mineralized zones.

Most of the sphalerite has a fairly narrow range of iron contents from 9 mol % to 12.5 mol % FeS (Figure 3.13). However, there are samples, typically near the stratigraphic top of the massive sulfide lenses in the heterolithic fragmental ores and sphalerite clast-rich ores that have iron contents as low as 6.4 mol % FeS. There does not appear to be any correlation with any other trace constituents in the sphalerite. The FeS contents of sphalerite increase with stratigraphic depth in the sphalerite-chalcopyrite ores and in association with pyrrhotite. Near the base of the massive sulfide lenses, where sphalerite occurs as intergrowths in locally massive magnetite-sphalerite (Figure 3.6A), the FeS content is generally greater than 12 mol % and commonly between 13 and 15 mol % FeS (Appendix IV). Other trace metals detected in sphalerite are likely due to inclusions of chalcopyrite or galena.

### *3.5 Galena*

Galena generally occurs at the stratigraphic top of the massive sulfide lenses in the heterolithic fragmental ore, sphalerite clast-rich ore and massive sphalerite ore as intergrowths and disseminated crystals. It forms inclusions in sphalerite, magnetite, Ag rich-tetrahedrite and pyrite and commonly occurs along crystal boundaries or in veinlets (Figure 3.3A) and locally in fractures with chalcopyrite in the Cu-rich stringer zone.

Galena typically contains up to 0.73 wt % Ag and 4.5 wt % Se and accounts for 3.2 % of the total Ag in the deposit (Appendix VI and Table 3.7).

### *3.6 Sn-bearing minerals*

Cassiterite and stannite occur almost exclusively in massive sphalerite ores with rare occurrences in the chalcopyrite stringer zone. Stannite generally forms 20-50 µm subrounded intergrowths and rims around cassiterite and sphalerite in massive sphalerite ores or at the grain boundaries of chalcopyrite in the Cu-rich stringer zones (Figure 3.8E). Cassiterite is generally disseminated in massive sphalerite as rounded to subrounded grains up to 50 µm (Figure 3.8A). Some of the coarser cassiterite crystals contain small anhedral pyrite or quartz inclusions. Cassiterite is also found in gangue near the top of the Main orebody and in the stringer zones. Cassiterite in the massive sulfides account for approximately 90% of the bulk Sn in Mine D whereas stannite in the Cu-rich stringer zone represents approximately 10% (Table 3.7).

### *3.7 Magnetite*

Magnetite occurs throughout most of the massive sulfide ores as anhedral masses or aggregates and porphyroblasts ranging from 1 to 6 mm in diameter (Figure 3.6C; up to cm size). This form is most prevalent in massive pyrite-sphalerite ore near the top of the sulfide lenses, where the magnetite is intergrown with massive pyrite and locally with pyrrhotite, Fe-poor sphalerite, and siderite. Similar fine-grained magnetite occurs rarely in massive sphalerite ore in the upper mine, whereas in the deep mine magnetite is also abundant intergrown with Fe-rich sphalerite (greater than 10 mole % Fe), pyrite and galena (Figure 3.6A). Magnetite concentrations up to 30 vol % have been seen in 1.5 m samples both at the base of the Main orebody in the sphalerite-chalcopyrite-rich ores and at the top of the lens in mainly massive pyrite-sphalerite. Magnetite is also seen in the Cu-rich stringer zone, commonly associated with quartz-siderite veins, and locally as cm-wide magnetite stringers with intergrowths of chalcopyrite, sphalerite and pyrrhotite (Figure 3.6F).

### *3.8 Co-Fe-As-bearing minerals*

Arsenopyrite and cobaltite are the principal Co-Fe-As-bearing minerals in the lower mine. They generally occur at the stratigraphic base of the massive sulfides and in the Cu-rich stringer zone.

Arsenopyrite occurs as disseminated euhedral crystals (up to 50 microns) commonly within or proximal to sphalerite and generally in association with pyrrhotite and cobaltite (Figure 3.7D). It also occurs to a lesser extent in chalcopyrite stringers, where it is more

cobalt rich. It may also form discrete aggregates in gangue. Arsenopyrite typically contains up to 1.68 wt % Co (Appendix VII).

Cobaltite occurs as subrounded grains (up to 50 microns) generally within sphalerite, pyrrhotite and chalcopyrite (Figure 3.11A). The amount of contained arsenic ranges around 37 wt % (Appendix VII). Zn, Pb, Fe, Ag, Se, Bi, and Ni, however, likely are present as sulfide inclusions.

Due to the presence of Co in pyrite, pyrrhotite, sphalerite and chalcopyrite (see above) a complete mineral balance is difficult. However, at least 20-30% of the total As at the base of the West and Main lenses is present as cobaltite; the balance is in py, po and arsenopyrite (Table 3.7, samples KCD209782 to KCD209785; see Appendix I and VII).

### *3.9 Bornite*

There is little bornite in the deep mine. Three samples at the base of the West Lens in sphalerite-chalcopyrite ores and in the Cu-rich stringer zone contained bornite along the crystal boundaries of chalcopyrite and exhibited common orange-beige lamellae. No tennantite was observed.

### *3.10 Ag-minerals*

Native silver accounts for approximately 47 % of the Ag in Mine D, Ag-rich tetrahedrite accounts for 18 % and Ag-rich chalcopyrite accounts for 30 % (Table 3.7, Appendix I and VII). No argentite, which was common in the upper part of the mine, was

observed in Mine D. Most of the silver-bearing minerals generally occur at the centre and bottom of the massive sulfides lenses. Ag-tetrahedrite is, however, also found at the stratigraphic top of the massive sulfide lens where it is associated with galena.

Native silver generally occurs in the core of the massive sulfides, either intergrown with sphalerite, chalcopyrite, pyrrhotite or magnetite as irregular masses up to 0.1 mm (Figure 3.9B). Silver can also occur with native bismuth or bismuth selenides as a discrete intergrowth or as a solid solution (Figure 3.9A).

Ag-rich tetrahedrite commonly occurs as anhedral grains up to 0.1 mm in diameter intergrown with galena, sphalerite, pyrrhotite, pyrite and rarely chalcopyrite near the stratigraphic top of the massive sulfide zones (Figure 3.10C). Tetrahedrite may also contain inclusions of pyrrhotite and galena. It commonly has zones of oxidation where it is intergrown with native silver.

Silver-antimonide (possibly allargentum) was seen in one sample in sphalerite-chalcopyrite ore from the base of the West Lens intergrown with native Ag, native Bi and Ag-Bi selenides (not analyzed) (Figure 3.9A). This is also the location of a gold-rich zone (Figure 4.1).

### *3.11 Bi-minerals*

The main bismuth minerals are native bismuth, Bi-Ag-Pb-Cu-Se sulfides and Laitakarite. They generally occur at the base of the massive sulfide lenses in sphalerite-chalcopyrite-rich ores and in the Cu-rich stringer zone. The Bi minerals occur as inclusions

in or near chalcopyrite and pyrrhotite or as discrete irregular growths in the gangue intimately associated with galena, cobaltite and arsenopyrite. One microprobe analysis of native bismuth yielded a gold concentration of 0.14 wt % (Appendix VII).

### *3.12 Ore-related Gangue Minerals*

Quartz is the most common gangue mineral at Kidd Creek associated with intense silicification of the fragmental host rocks and cherty breccia, as gangue in massive sulfides and in the stringer zone of the deposit. It also occurs in late fractures, joints and veins as coarse quartz crystals. There are areas of intense quartz flooding near major structures where quartz veins span a four by four metre section in underground exposures.

Siderite is locally the most abundant gangue mineral in the ore zones with bulk ore containing 10 wt % Fe-carbonate and locally as high as 27.5 wt % in the main massive sulfide body (Table 3.7, Figure 3.12, Appendix IX). However, siderite is almost completely restricted to the massive sulfide lenses and is rarely seen in the Cu-rich stringer zone. It is generally found with massive pyrite-sphalerite ores intergrown with sphalerite and pyrite and locally magnetite (Figure 3.18A). It can also form as late fracture-filling stringers, overprinting the sulfides. The $FeCO_3$ equivalents for the main massive sulfide ore types range from 16 wt % in massive pyrite-sphalerite to 15 wt % in massive pyrite-chalcopyrite, 11 wt % in massive sphalerite-chalcopyrite, and 9 wt % (Appendix I and Table 3.7) in massive sphalerite based on drill core samples (see below). This is significantly higher than the values from the upper mine where the $FeCO_3$ equivalents for the NOB & COB were from

3.5 wt % in massive pyrite and massive sphalerite ores to 5 wt % in sphalerite-chalcopyrite ores to 4 wt % in massive chalcopyrite ores (Hannington et al., 1999).

Electron microprobe analyses of the Fe carbonates indicate that most of the siderite contains between 0.5 and 3.3 wt % MnO and between 2 and 8 wt % MgO. Ankerite and dolomite are also locally part of the ore zones, generally as masses replacing chalcopyrite and pyrrhotite. The ankerite contains between 0.87 to 4.5 wt % MnO and 7 to 17 wt % MgO (Appendix IX, X and Figure 3.22). Calcite is present throughout the ore zones in late quartz-carbonate veins and joints.

Dark green to black chlorite typically occurs with Cu-rich stringers or with sphalerite-chalcopyrite ore at the base of the massive sulfide lenses and accounts for 10s of wt % of the total Fe in the deposit. It also occupies brecciated, locally barren veins between the Cu-rich stringers and the massive sulfides (Figure 3.16C) and in strong faults deep in the mine, such as the major Offset Fault series or the South-dipping faults, commonly in the South Lens. As in the upper mine, the chlorite has a wide range of compositions corresponding to the different stages of mineralization and location in the stratigraphy (Hannington et al, 1999), however, the overall concentrations of Fe are much higher (up to 45 wt %) than that of the upper mine. Fe-rich chlorite is typically found at the base of the Main and West lenses, and Mg-rich chlorite is typically found as a large halo around the Fe-rich chlorite zones (Figure 3.21).

Sericite occurs throughout the deposit but is most abundant in the fragmentals and in the footwall stratigraphically below the massive silicified rhyolite. This is similar to the upper part of the mine, where sericite is most abundant in the immediate hangingwall of the

deposit and less so in the immediate footwall (Figure 3.15; Koopman et al, 1999). Phlogopite (Figure 3.16E), which was seen mainly in samples in the Cu-rich stringers and the South Lens, contains between 3.7 and 4.2 wt % F (Table 3.6). This is similar to the F-rich phlogopite associated with bornite ore in the upper part of the mine.

Tourmaline generally forms columns or broken crystals which are intergrown with sericite, chlorite or quartz and chalcopyrite (Figure 3.17A). As in the upper mine, Fe-Mg contents in tourmaline tend to mimic those of chlorite, with Fe-rich tourmaline occurring mainly at the base of the massive sulfides.

Albite occurs as porphyroblasts up to 1 cm in size, but typically 1-5 mm, in the chalcopyrite stringer zone (Figure 3.19) but also in massive sulfide at the base of the lenses. Albite has been observed locally occupying up to 40 vol % of the core as coarse crystals within chalcopyrite. However, it is generally absent in the altered wall rock.

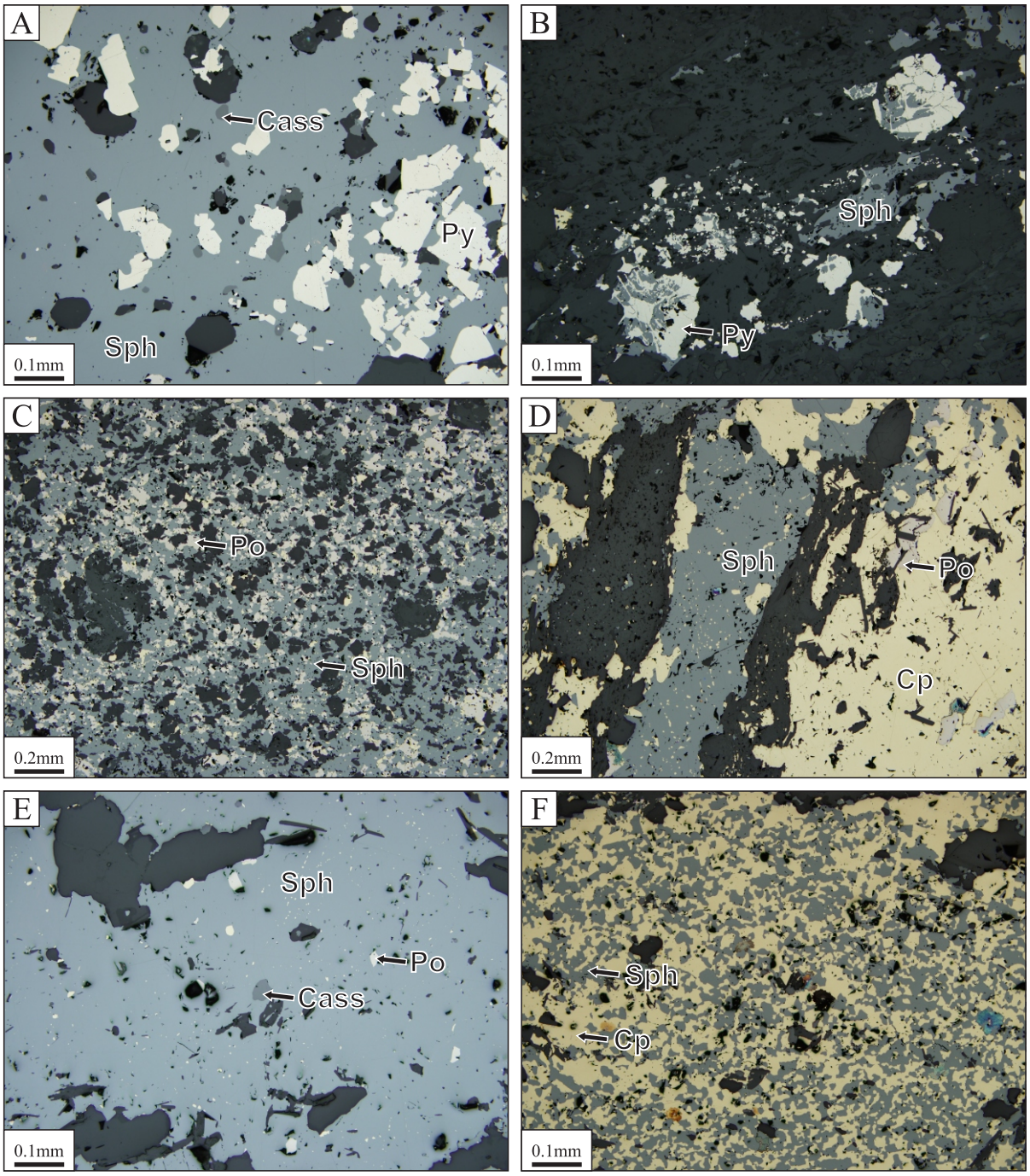


Figure 3.1 Representative reflected light photomicrographs of sphalerite-rich ore in Mine D. A) Massive sphalerite intergrown with subhedral pyrite and minor cassiterite; KCD209769. B) Sphalerite stringers replacing pyrite; KCD209848. C) Pyrrhotite intergrown with stringer sphalerite; KCD209835. D) Remnant sphalerite stringer exhibiting chalcopyrite disease and partly replaced by chalcopyrite stringers; KCD209867. E) Cassiterite and pyrite intergrown with massive sphalerite; KCD209807. F) Chalcopyrite replacing massive sphalerite; KCD209875.

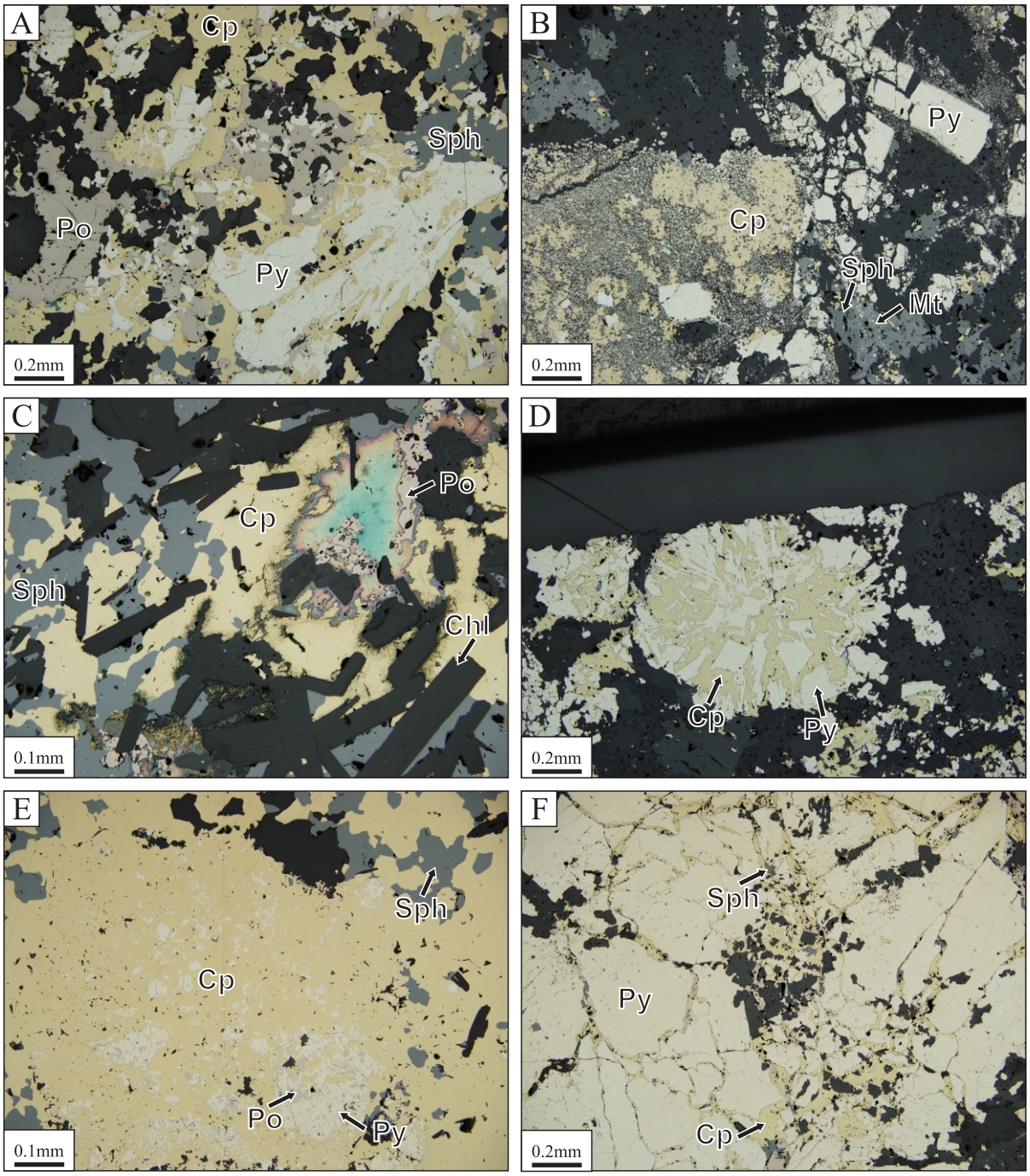


Figure 3.2 Representative reflected light photomicrographs of chalcopyrite-rich ore in Mine D. A) Chalcopyrite and pyrrhotite replacing pyrite and sphalerite; KCD209852. B) Fine grained intergrowths of chalcopyrite and pyrite with interstitial arsenopyrite. Pyrite in gangue ranges from subhedral to anhedral. Sphalerite stringers containing magnetite; KCD209783. C) Intergrown chalcopyrite, pyrrhotite, sphalerite and chlorite. Tarnish is likely due Ag-minerals; KCD209812. D) Chalcopyrite and trace galena replacing remnant nodular pyrite; KCD209811. E) Massive chalcopyrite replacing sphalerite and pyrite and pyrrhotite; KCD209843. F) Chalcopyrite and minor pyrrhotite replacing interstitial sphalerite and massive pyrite around crystal boundaries; KCD209877.

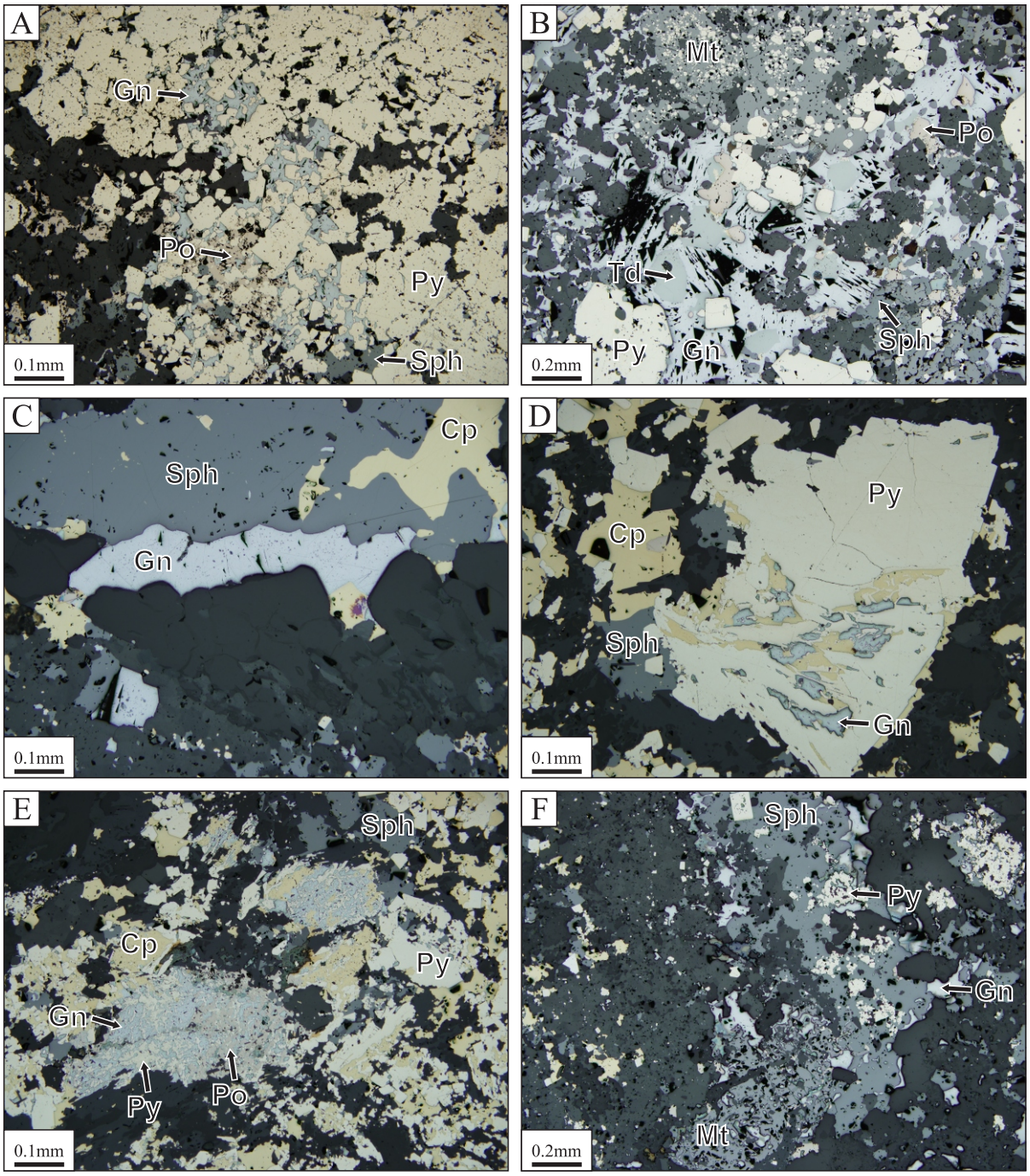


Figure 3.3 Representative reflected light photomicrographs of galena-rich ore in Mine D. A) Galena and pyrrhotite interstitial to pyrite crystals; KCD209769. B) Semi-massive galena intergrown with tetrahedrite, pyrrhotite, pyrite and magnetite; KCD209781. C) Galena and chalcopyrite intergrown with remnant sphalerite; KCD209811. D) Galena and chalcopyrite replacing remnant pyrite; KCD209811. E) Intergrown pyrite, pyrrhotite and galena with pyrite; KCD209811. F) Intergrown magnetite and galena overprinting sphalerite; KCD209811.

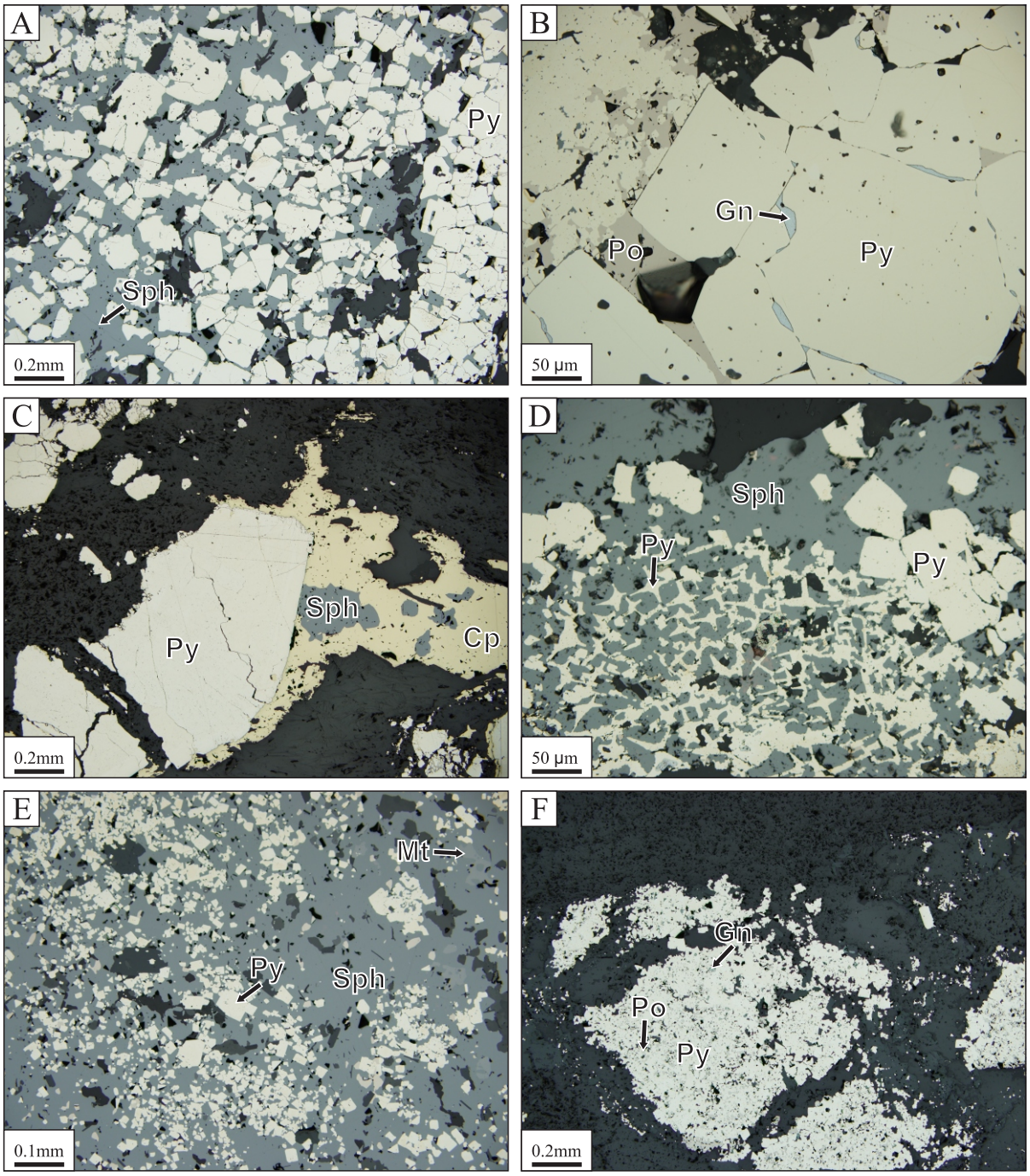


Figure 3.4 Representative reflected light photomicrographs of pyrite-rich ore in Mine D. A) Coarse euhedral pyrite overprinting sphalerite; KCD209779. B) Coarse euhdral pyrite with interstitial pyrrhotite and galena; KCD209780. C) Subhedral pyrite replacing a Cp stringer; KCD209843. D) Pyrite replacing sphalerite at crystal boundaries forming skeletal pyrite; KCD209770. E) Fine grained euhdral pyrite overprinting sphalerite with minor magnetite; KCD209771. F) Very fine grained pyrite stringer in stockwork zone: KCD209776.

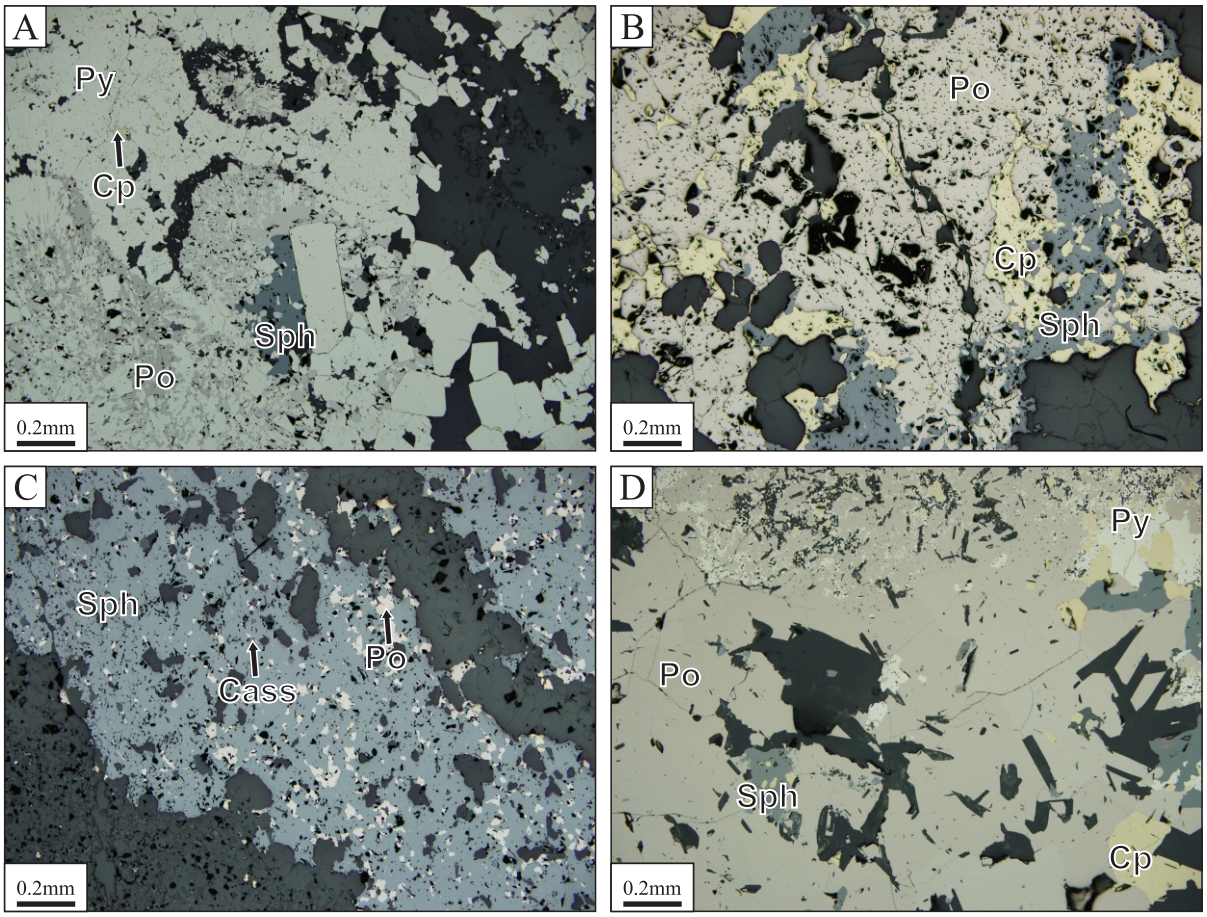


Figure 3.5 Representative reflected light photomicrographs of pyrrhotite-rich ore in Mine D. A) Pyrrhotite partially replacing relict pyrite nodule; KCD209780. B) Massive pyrrhotite and chalcopyrite replacing remnant sphalerite stringer; KCD209816. C) Pyrrhotite beginning to replace sphalerite; KCD209787. D) Massive pyrrhotite replacing sphalerite and chalcopyrite with chlorite laths in the gangue; KCD209811.

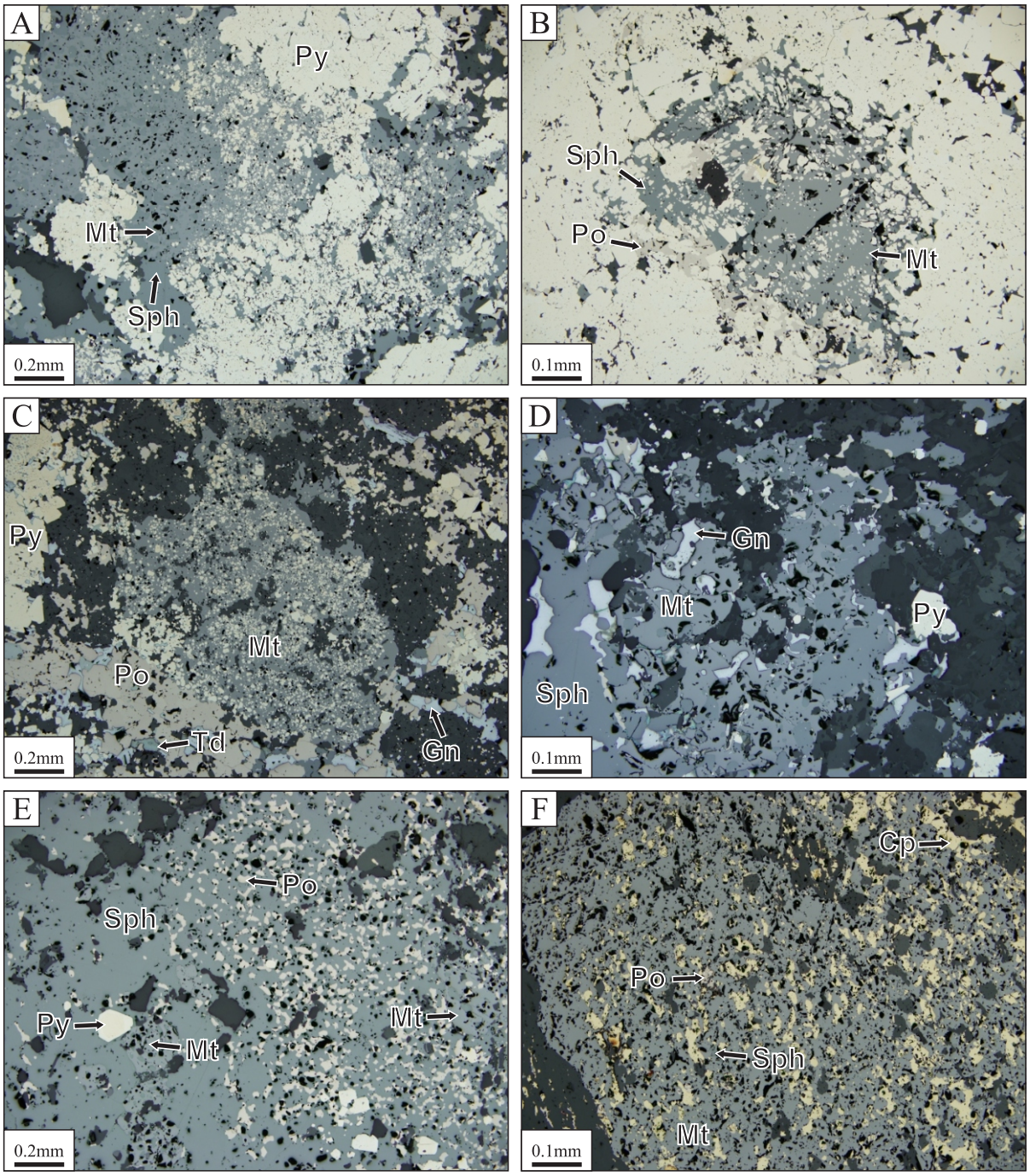


Figure 3.6 Representative reflected light photomicrographs of magnetite-rich ore in Mine D. A) Intergrown magnetite with sphalerite being replaced by late pyrite; KCD209770. B) Intergrown magnetite and sphalerite in late euhedral pyrite; KCD209780. C) Magnetite bleb in gangue surrounded by pyrite and pyrrhotite; KCD209781. D) Magnetite and galena intergrown with sphalerite; KCD209811. E) Magnetite replacing massive sphalerite near pyrrhotite; KCD209814. F) Magnetite stringer with inclusions of chalcopyrite, pyrrhotite and sphalerite; KCD209877..

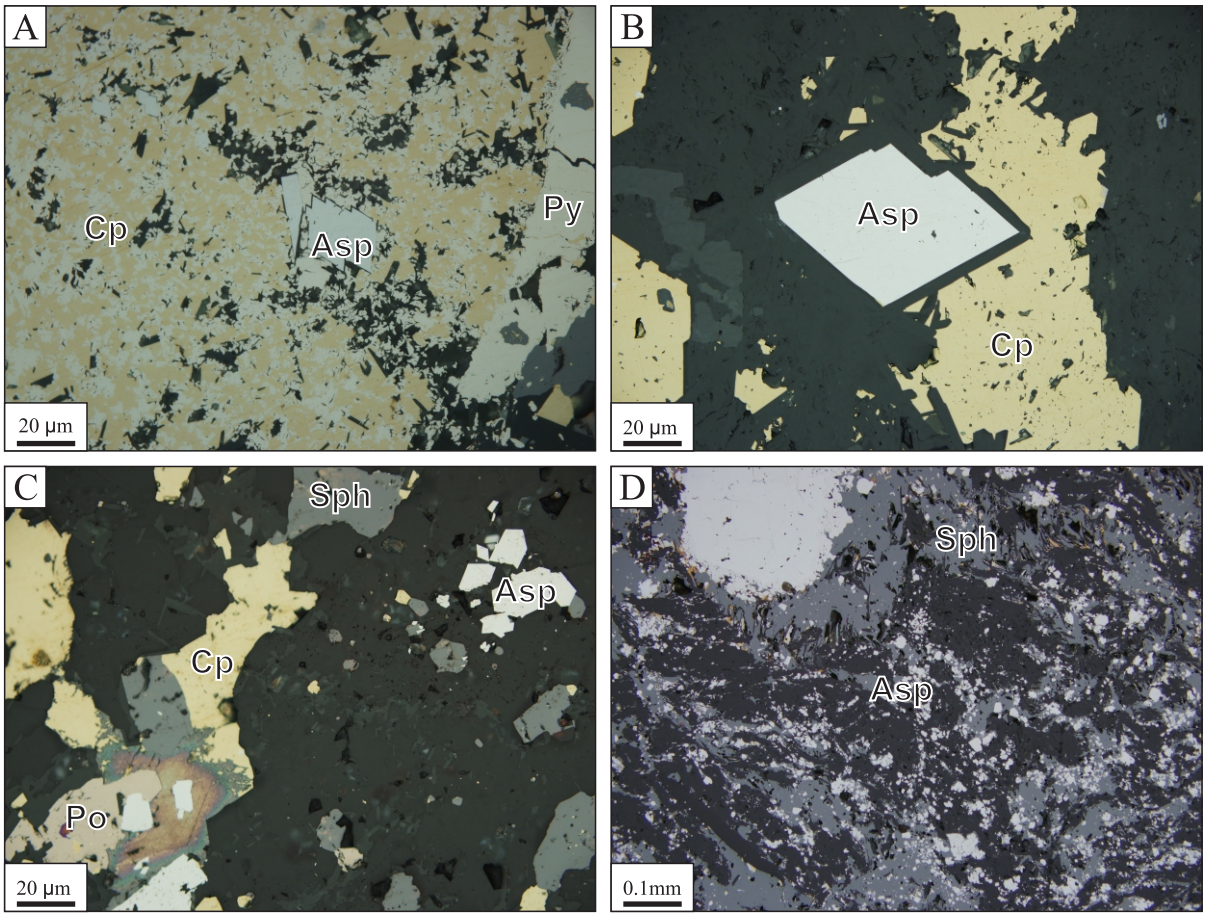


Figure 3.7 Representative reflected light photomicrographs of arsenopyrite-bearing ore in Mine D. A) Euhedral arsenopyrite intergrown with quenched chalcopyrite and pyrite; KCD209783. B) Euhedral arsenopyrite with a chlorite rim overprinting chalcopyrite ; KCD209784. C) Euhedral arsenopyrite intergrown with sphalerite in gangue; KCD209787. D) Representative of the highest As zone. Abundant euhedral arsenopyrite with sphalerite and gangue; KCG108802_10.

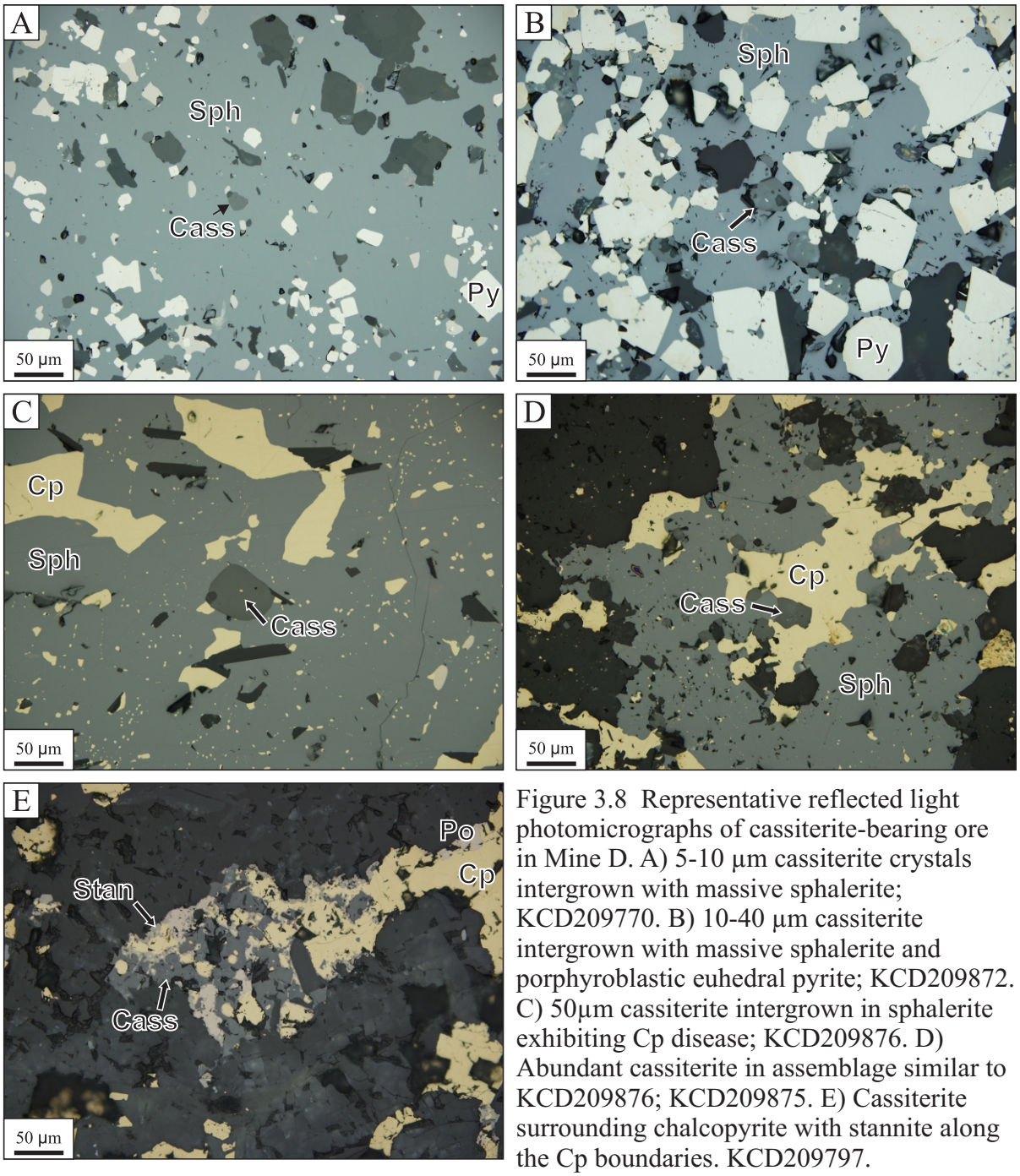


Figure 3.8 Representative reflected light photomicrographs of cassiterite-bearing ore in Mine D. A) 5-10 µm cassiterite crystals intergrown with massive sphalerite; KCD209770. B) 10-40 µm cassiterite intergrown with massive sphalerite and porphyroblastic euhedral pyrite; KCD209872. C) 50µm cassiterite intergrown in sphalerite exhibiting Cp disease; KCD209876. D) Abundant cassiterite in assemblage similar to KCD209876; KCD209875. E) Cassiterite surrounding chalcopyrite with stannite along the Cp boundaries. KCD209797.

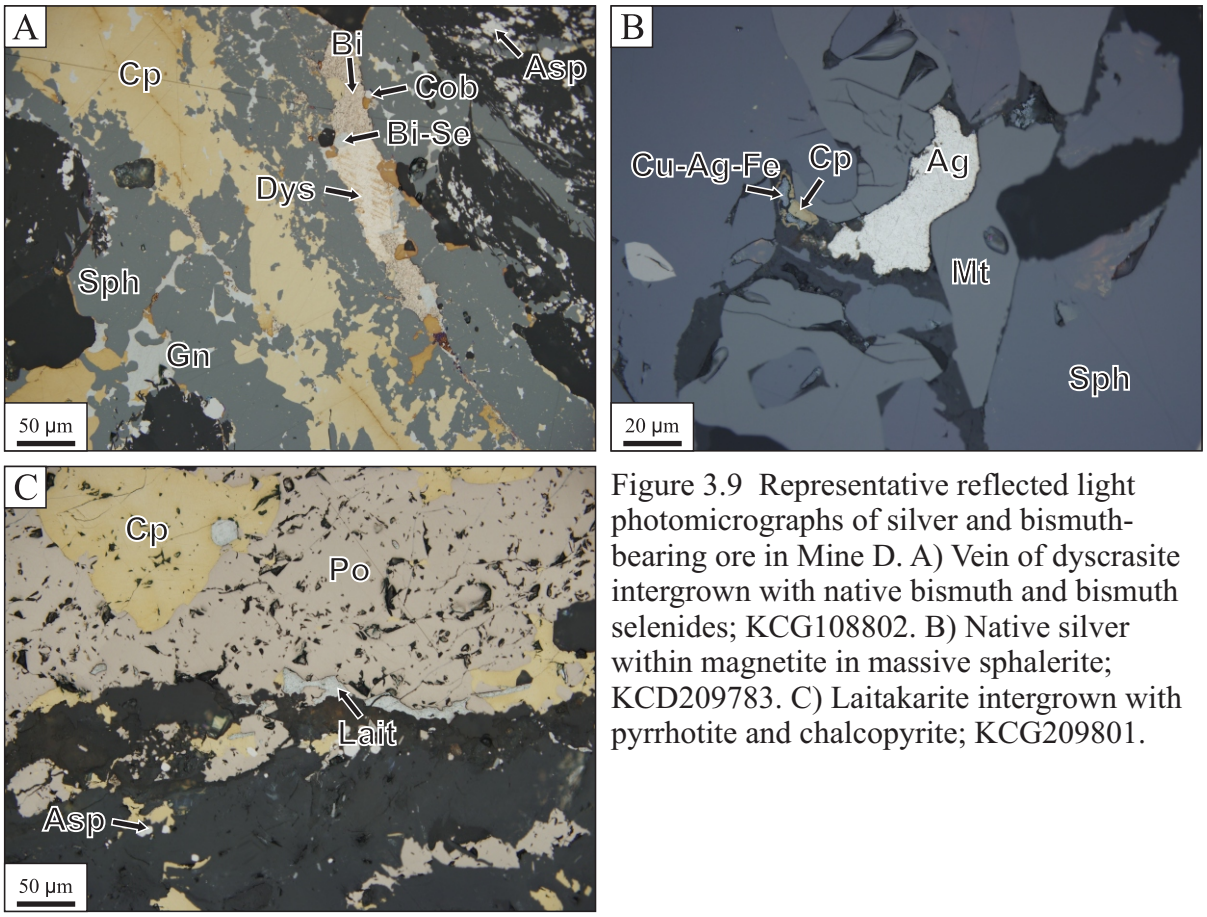


Figure 3.9 Representative reflected light photomicrographs of silver and bismuth-bearing ore in Mine D. A) Vein of dyscrasite intergrown with native bismuth and bismuth selenides; KCG108802. B) Native silver within magnetite in massive sphalerite; KCD209783. C) Laitakarite intergrown with pyrrhotite and chalcopyrite; KCG209801.

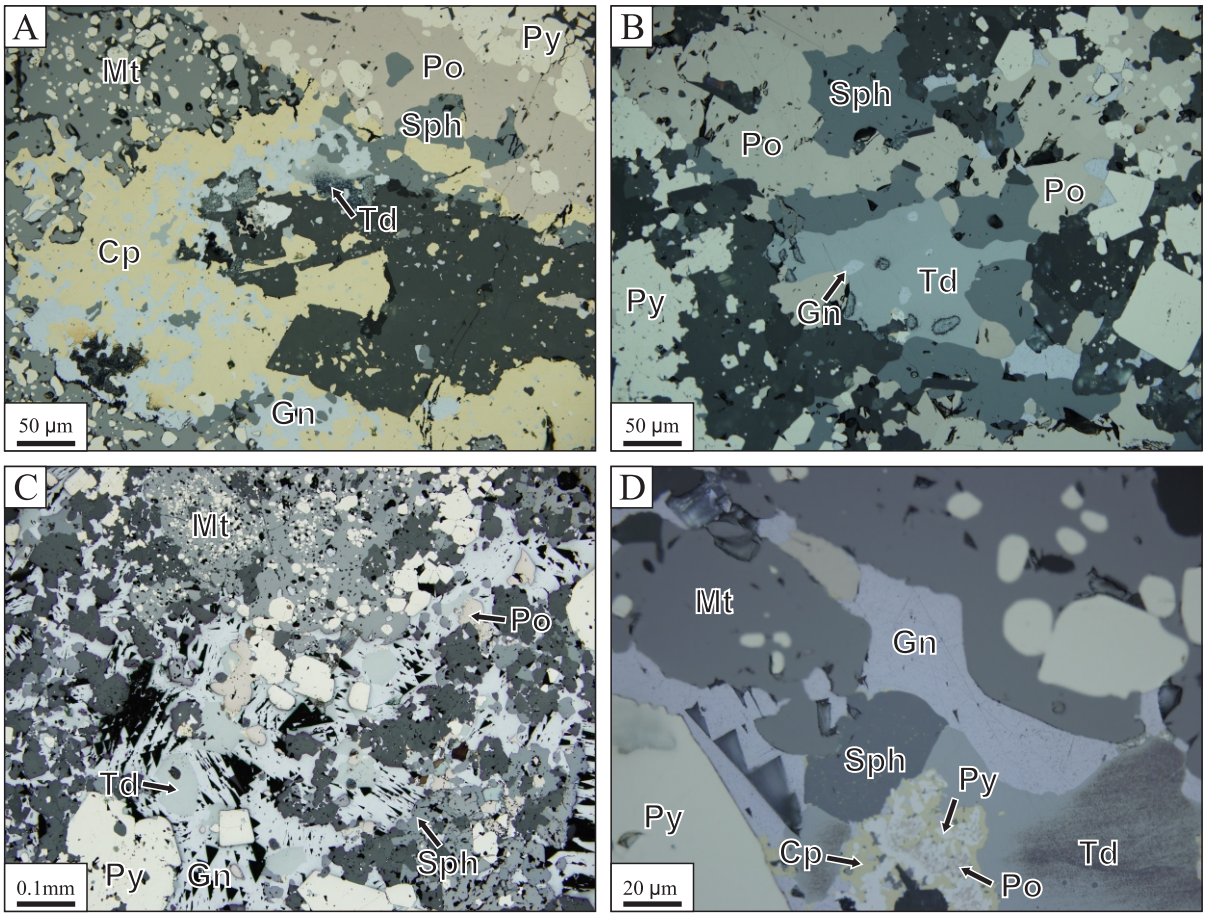


Figure 3.10 Representative reflected light photomicrographs of tetrahedrite-bearing ore in the Kidd Creek Deposit. A) Tetrahedrite intergrown with galena in chalcopyrite; KCD209780. B) Tetrahedrite intergrown with sphalerite and pyrrhotite with inclusions of galena; KCD209781. C) Tetrahedrite intergrown in semi-massive galena; KCD209781. D) Tetrahedrite intergrown within galena with Cp, Po, Py rich inclusions; KCD209781.

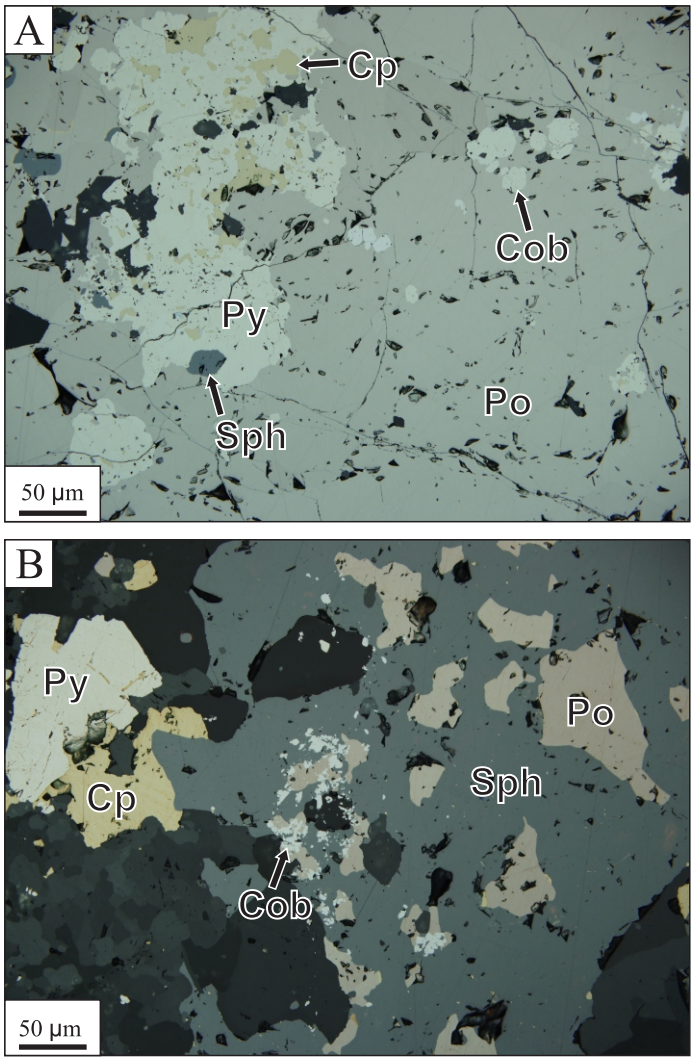


Figure 3.11 Representative reflected light photomicrographs of cobaltite-bearing ore in Mine D. A) Sub-rounded cobaltite intergrown with massive pyrrhotite; KCD209773. B) Sub-rounded cobaltite proximal to pyrrhotite intergrown in sphalerite; KCD209783.

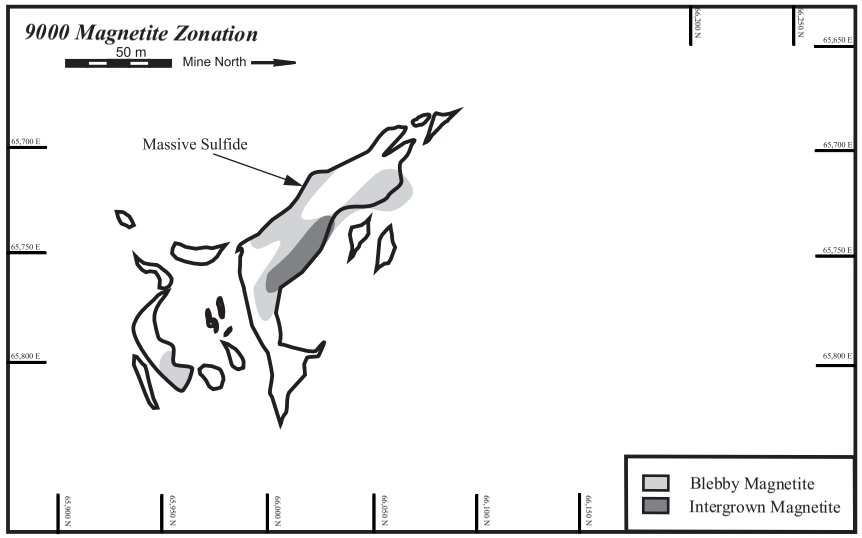


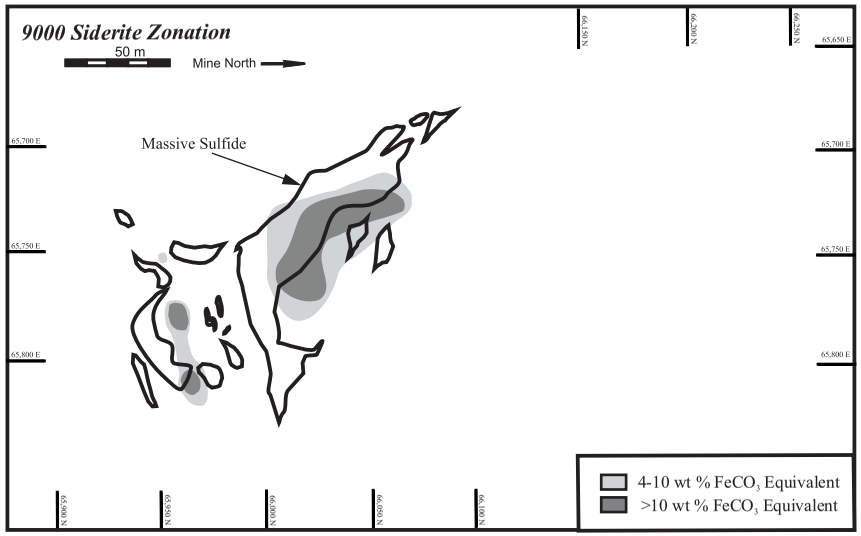


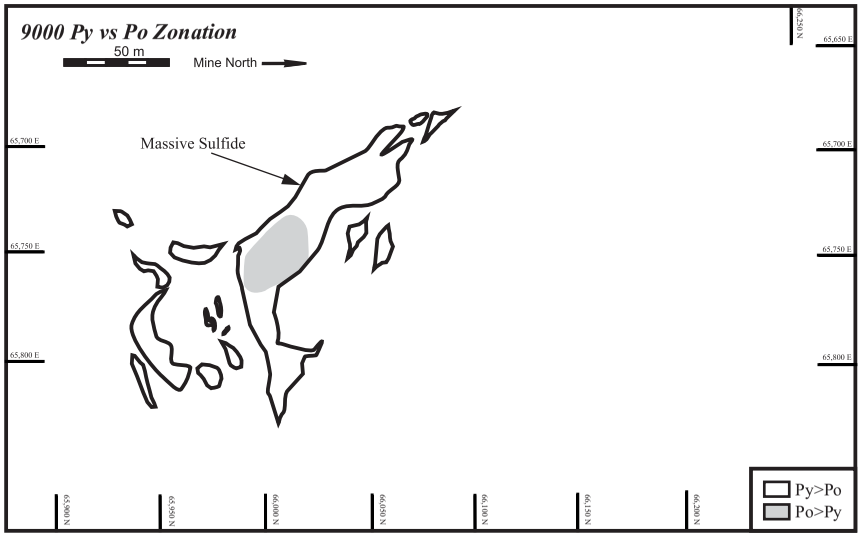


Figure 3.12 Distribution of magnetite, siderite, pyrite and pyrrhotite on the 9000 foot level of Kidd Creek based on underground mapping and drillhole logging (outline is greater than 50% sulfides).

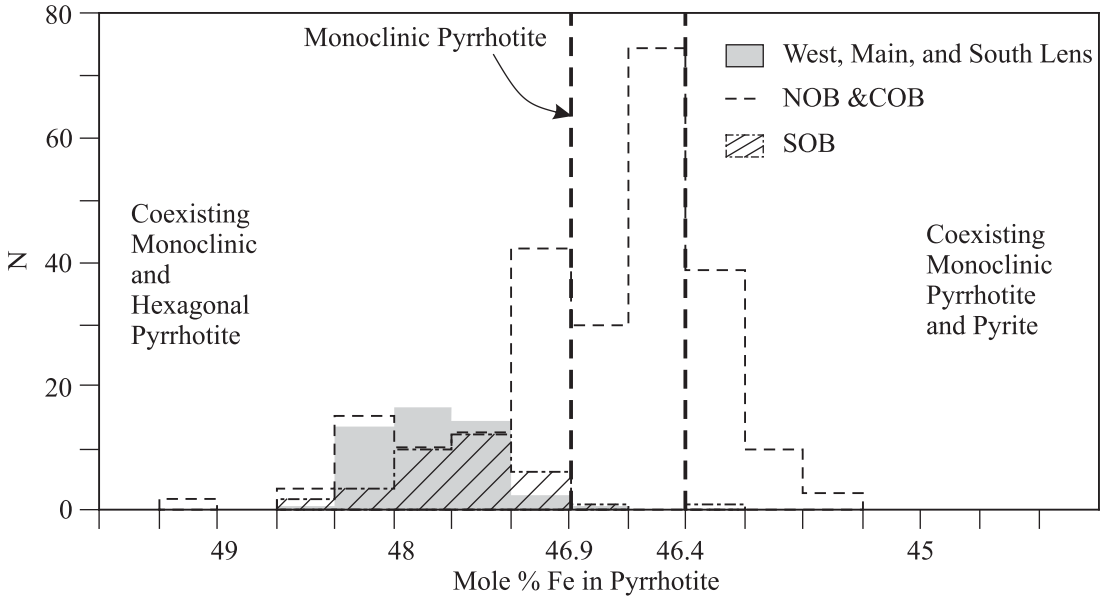


Figure 3.13 Compositions of pyrrhotite in ores from Mine D. Data from NOB, COB and SOB are based on data from 48 samples (287 analyses). West, Main and South Lens based on 19 samples (52 analyses). Dashed lines indicate compositional ranges for monoclinic and hexagonal pyrrhotite (modified from Hannington et al., 1999 and Scott and Kissin, 1973).

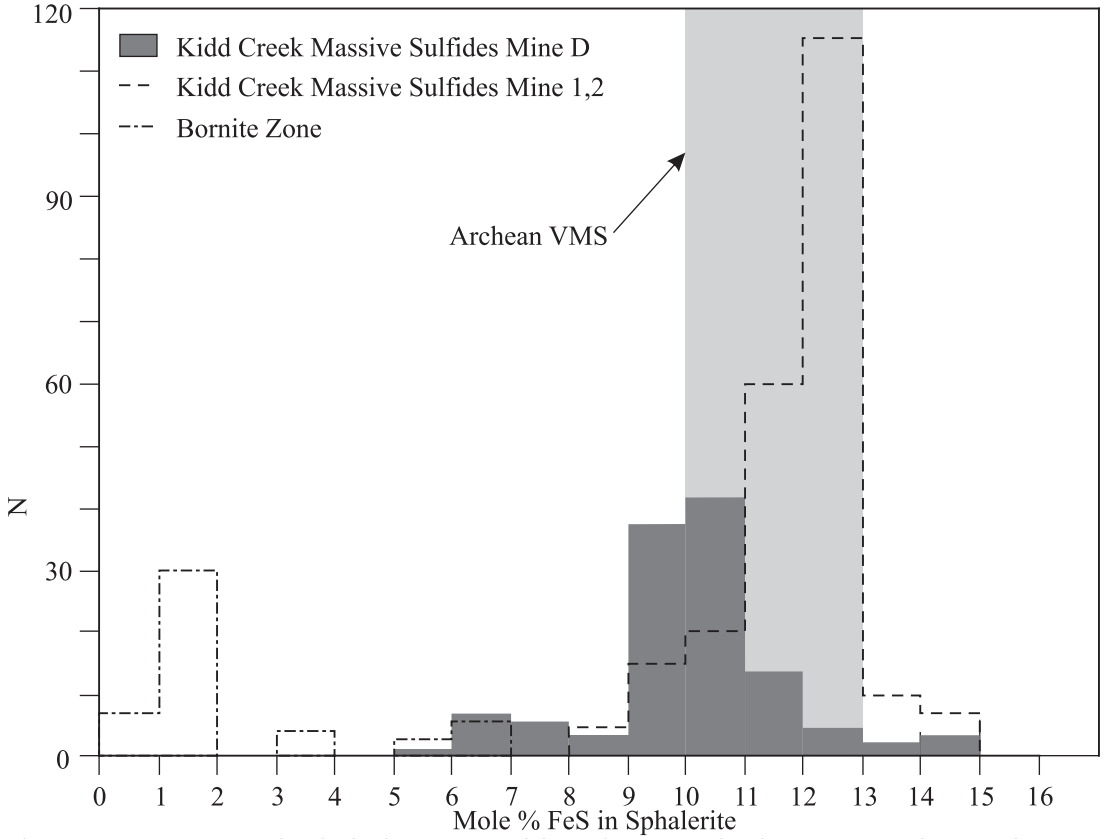


Figure 3.14 Range of sphalerite compositions in ores of Mine D. Data from Mine 1, 2 and Bornite Zone are based on 68 samples (500 analyses). Mine D is based on 18 samples (96 analyses). The range of sphalerite compositions for typical Archean deposits is from Hannington et al. (1999)

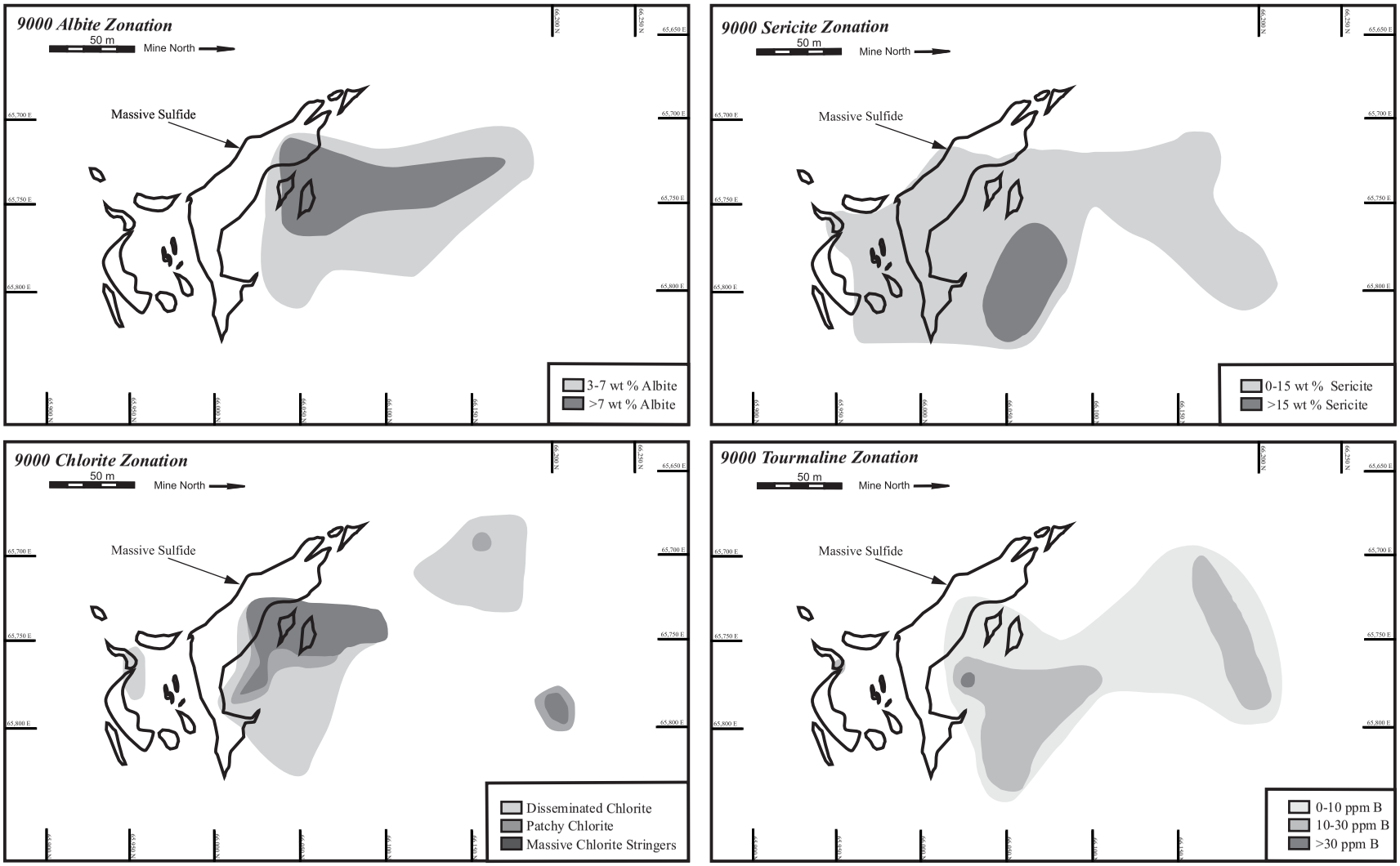


Figure 3.15 Distribution of the main alteration zones on the 9000 foot level of Kidd Creek. All profiles exhibit typical metal zonation profiles for VMS deposits except for sericite, which is most abundant in the footwall. The massive sulfide boundary is based on visual estimates, both underground mapping and drill hole logging, of greater than 50% sulfides. Mineral abundances are a combination of visual estimates from drill core and approximate abundance calculations with data from Appendix I.

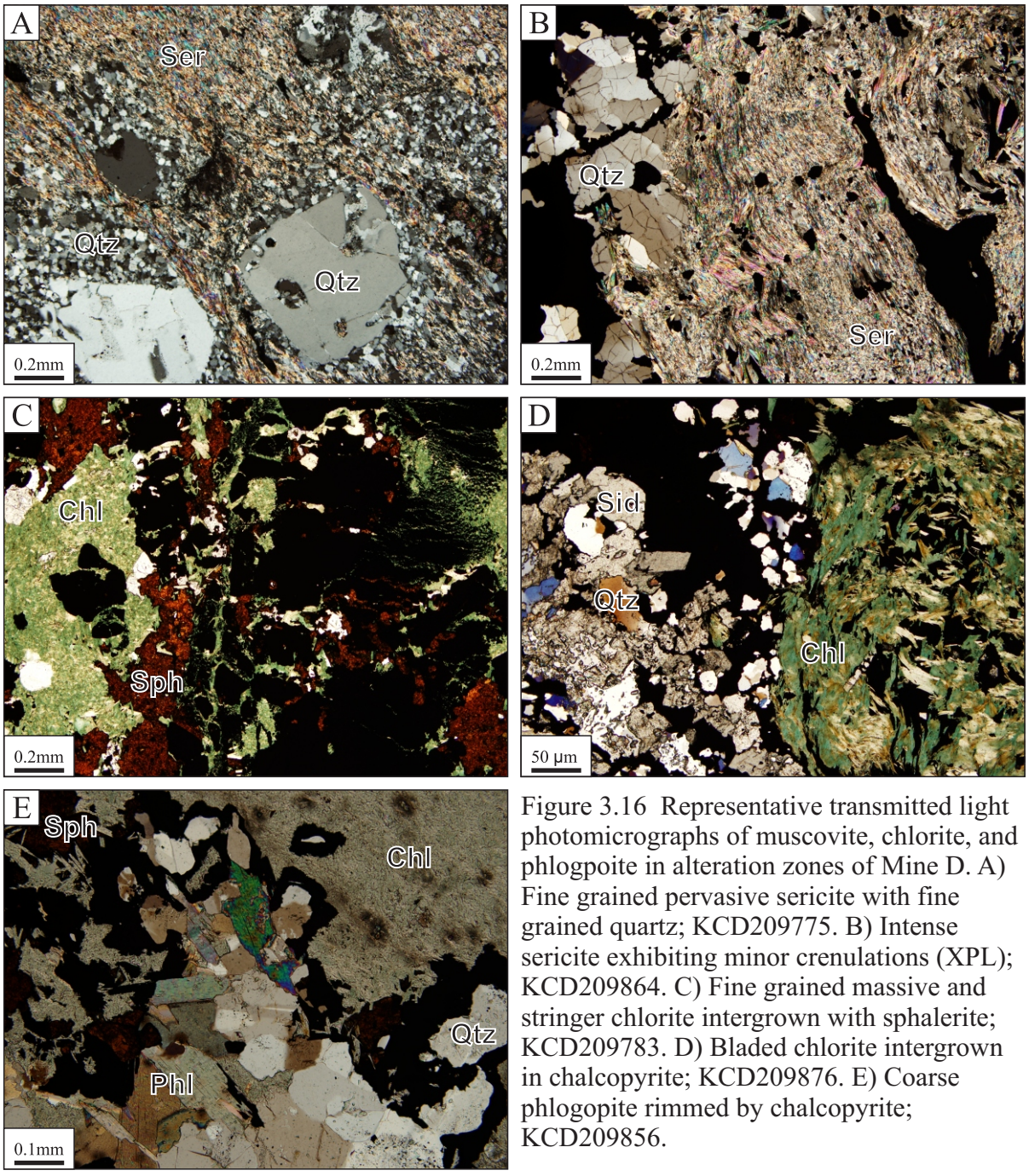


Figure 3.16 Representative transmitted light photomicrographs of muscovite, chlorite, and phlogpoite in alteration zones of Mine D. A) Fine grained pervasive sericite with fine grained quartz; KCD209775. B) Intense sericite exhibiting minor crenulations (XPL); KCD209864. C) Fine grained massive and stringer chlorite intergrown with sphalerite; KCD209783. D) Bladed chlorite intergrown in chalcopyrite; KCD209876. E) Coarse phlogopite rimmed by chalcopyrite; KCD209856.

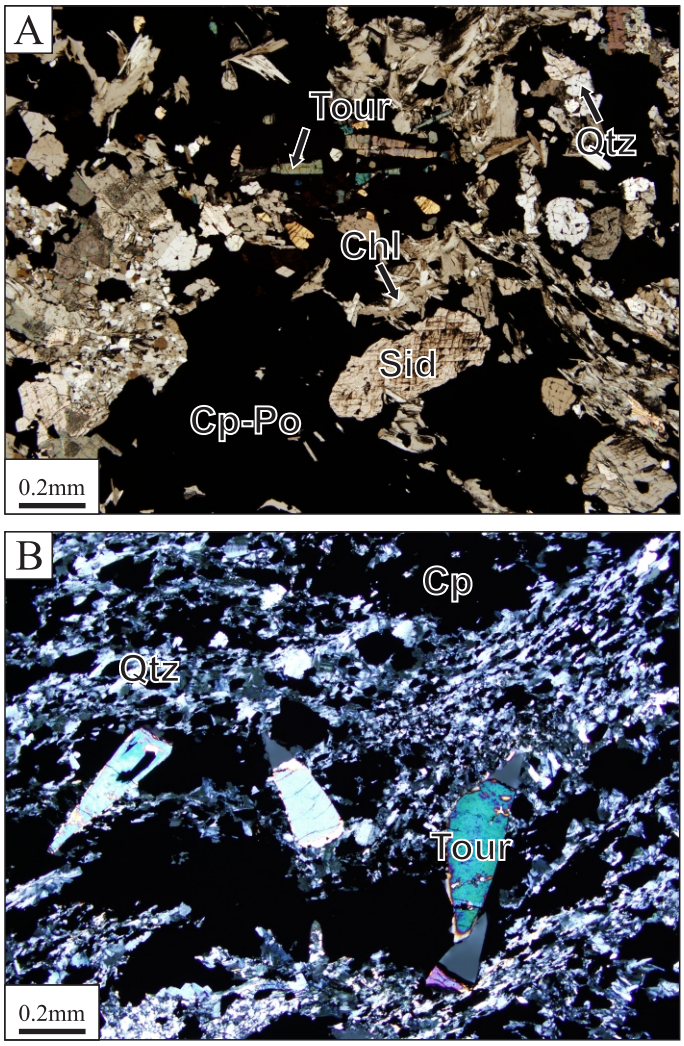


Figure 3.17 Representative transmitted light photomicrographs of tourmaline in altered rhyolite of Mine D. A) 0.2 mm long tourmaline crystals intergrown with pyrrhotite and chalcopyrite; KCD209858. B) 0.2 mm long tourmaline crystals intergrown with chalcopyrite; KCD209790.

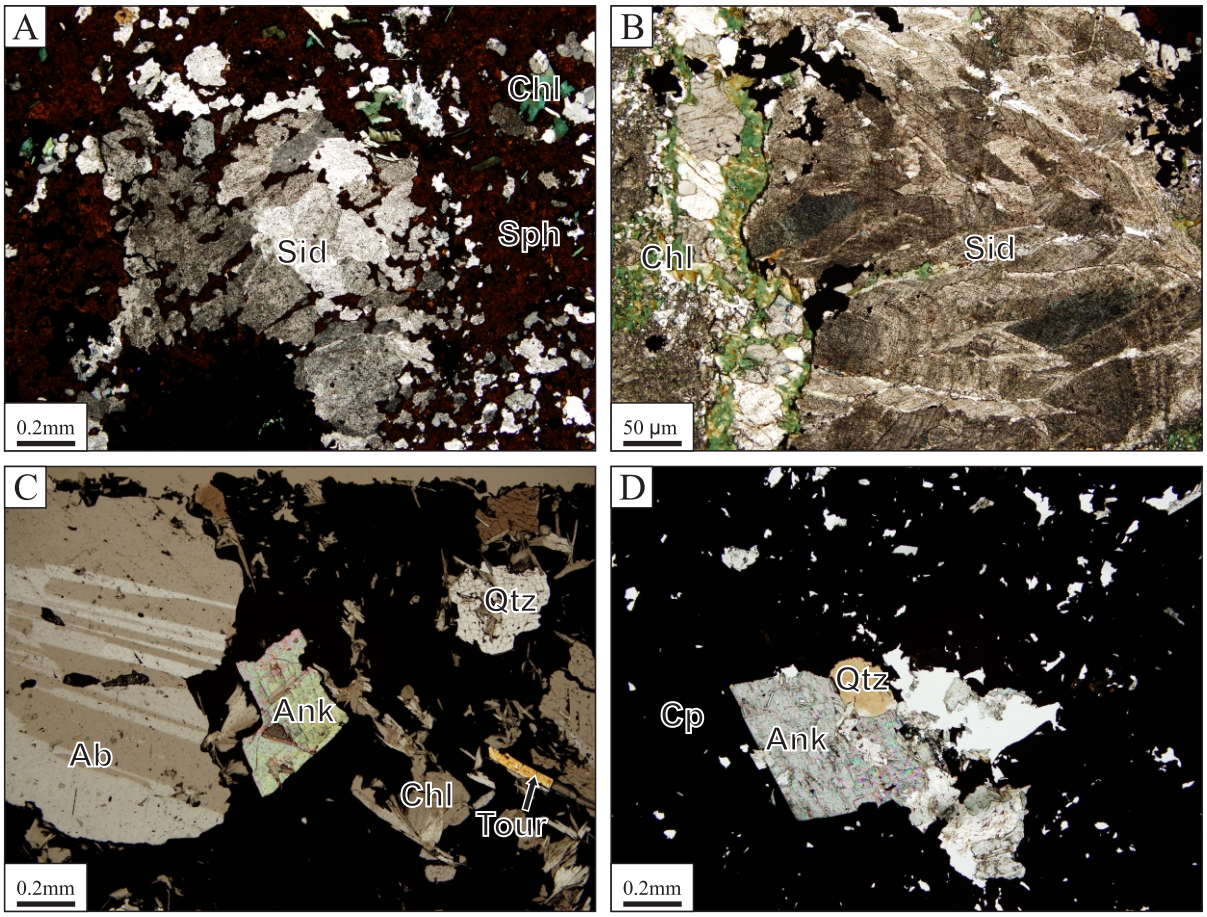


Figure 3.18 Representative transmitted light photomicrographs of carbonates in altered rhyolite of Mine D. A) Coarse siderite intergrown with massive sphalerite; KCD209770. B) Massive siderite stringer; KCD209877. C) Ankerite with replaced albite, tourmaline and chlorite; KCD209858. D) Ankerite intergrown in chalcopyrite-pyrrhotite; KCD209801.

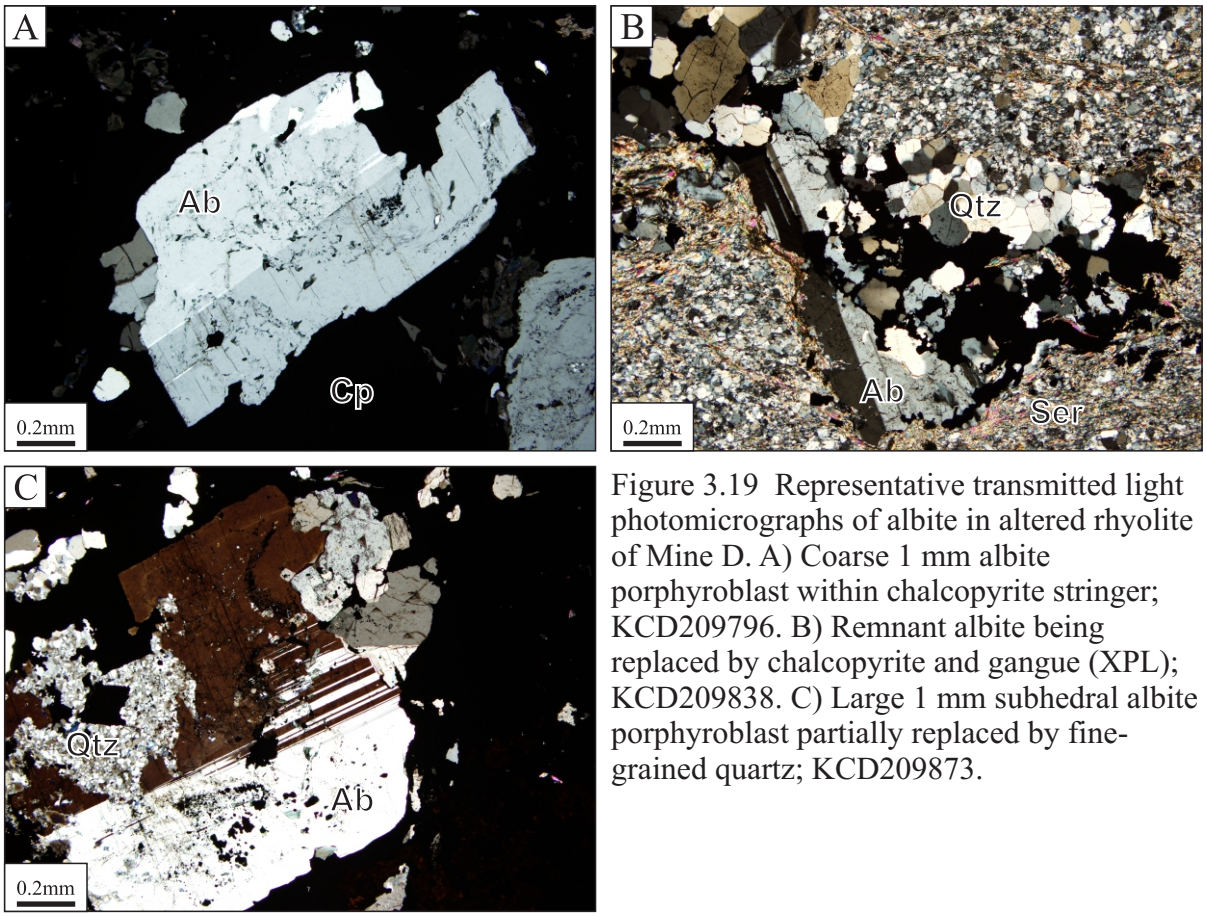


Figure 3.19 Representative transmitted light photomicrographs of albite in altered rhyolite of Mine D. A) Coarse 1 mm albite porphyroblast within chalcopyrite stringer; KCD209796. B) Remnant albite being replaced by chalcopyrite and gangue (XPL); KCD209838. C) Large 1 mm subhedral albite porphyroblast partially replaced by fine-grained quartz; KCD209873.

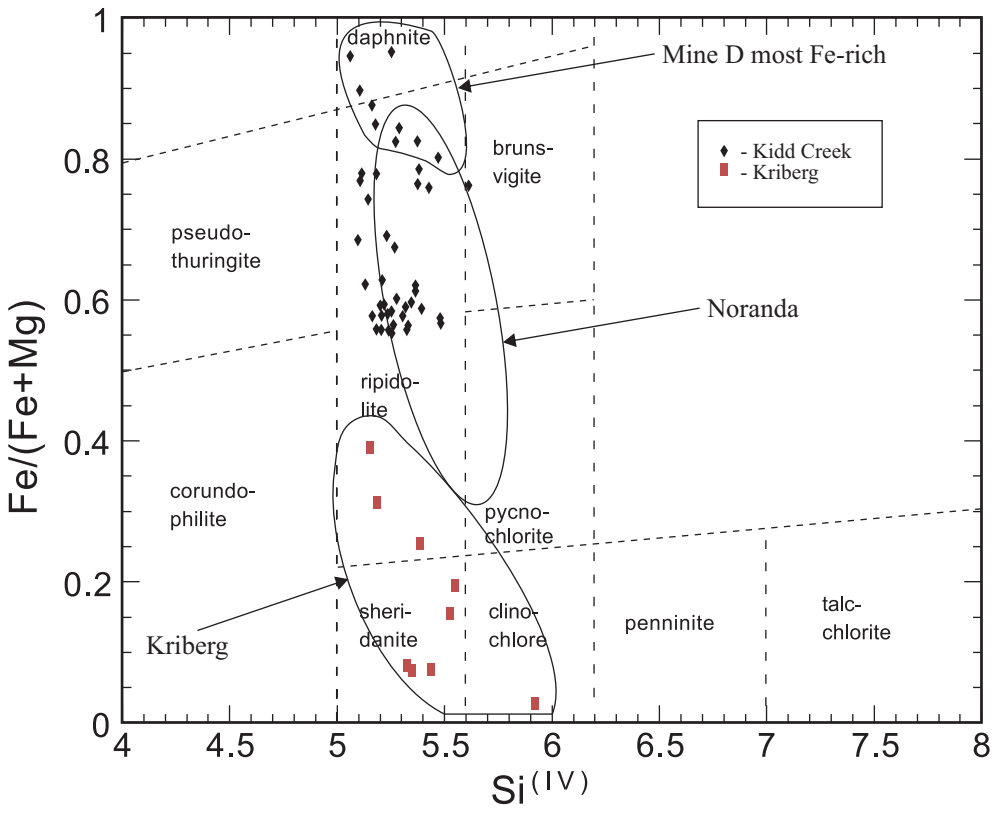


Figure 3.20 Composition of Kidd Creek chlorite in the West, Main and South lenses and Cu-rich stringer zone of Mine D. All ores contain Fe-rich chlorite; however chlorite from the base of the massive sulfides are more Fe-rich. Chlorite from Kidd Creek is generally similar in composition to chlorite from the Noranda camp but much more Fe-rich than the chlorite from other VMS districts, such as the Kristineberge massive sulfide deposit in Skellefte, Sweden. The classification scheme is that of Hey (1954). Data for Noranda and for Kristineberge massive sulfide deposit, Sweden from Hannington et al. (2003). Mine D data based on 28 oxygens.

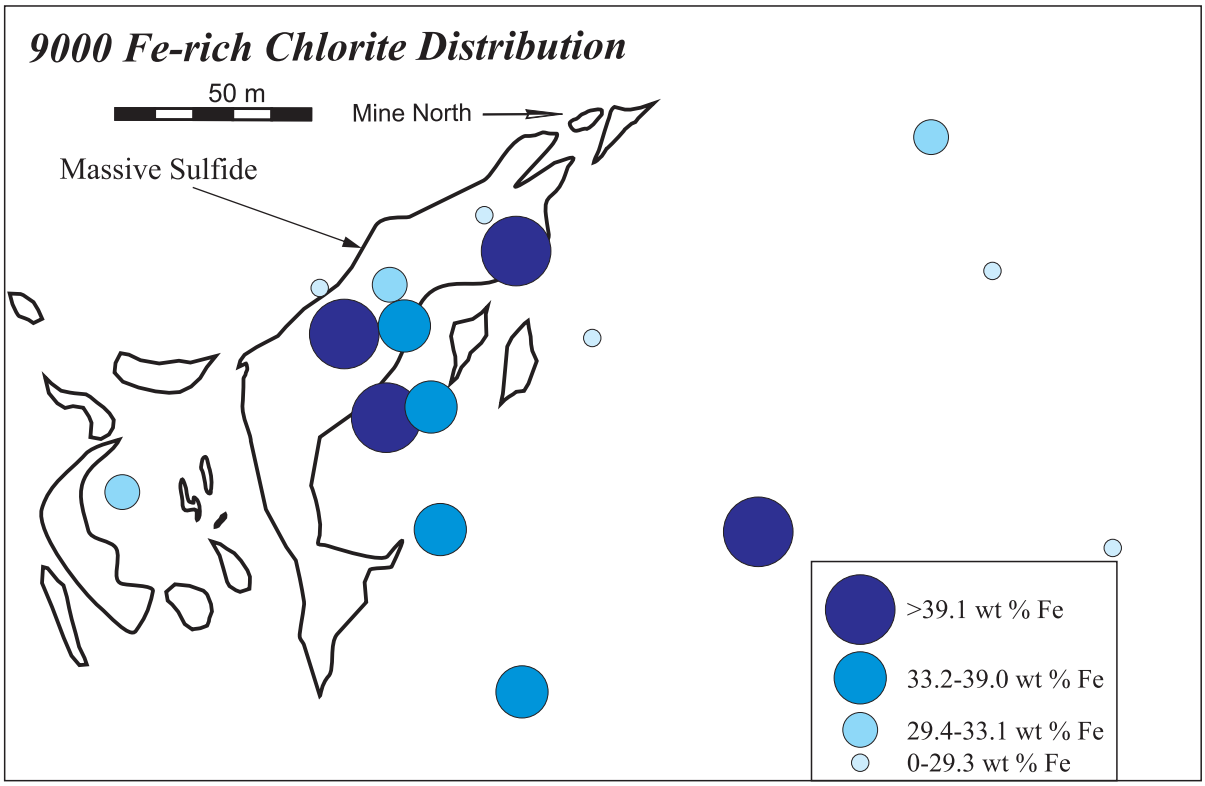


Figure 3.21 Bubble plots showing the distribution of the wt % of Fe (grouped by average per sample) in chlorite in 15 samples projected onto the 9000 level of the Main, West and South lenses and the Cu-rich stringer zone. Samples are grouped by quartiles. Data is from Appendix XIII.

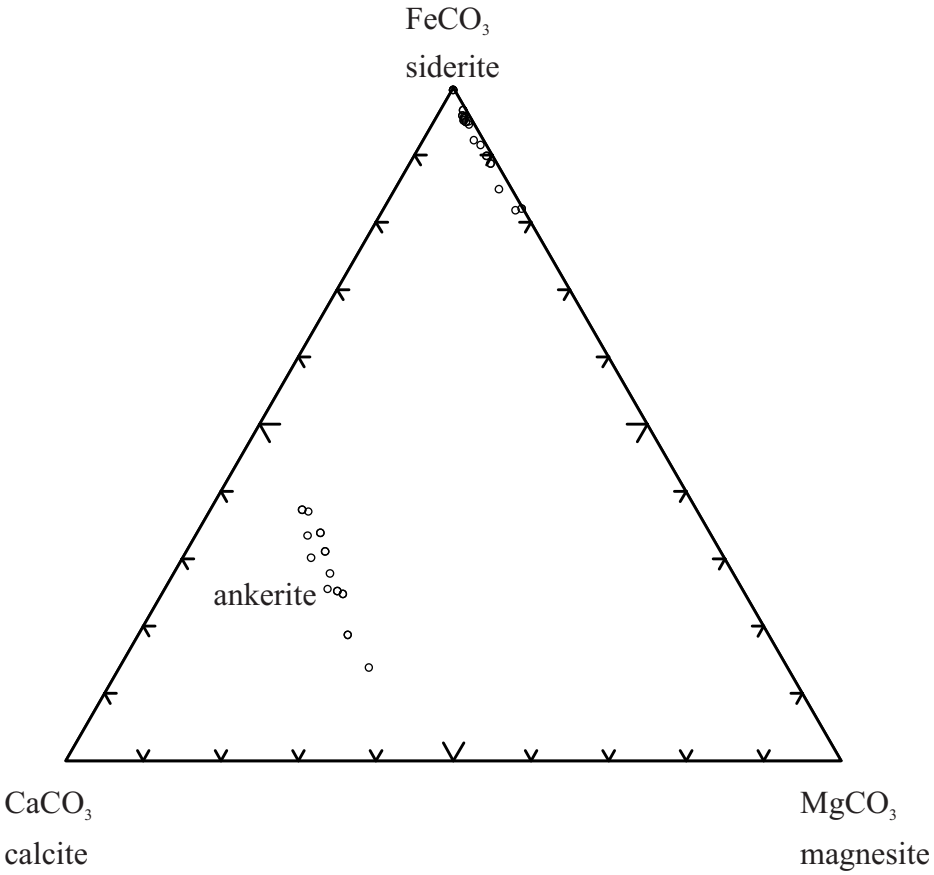


Figure 3.22 Carbonate compositions in 12 samples from mine D (42 analyses). Ankerite was variable in Fe and Mg contents, but had consistent Ca. Siderite contained variable concentrations of Mg.

Table 3.1 Mineralogy of Principal Ore Types in the West and Main Lenses of Mine D

| Heterolithic fragmental ores | Sphalerite clast-bearing ores | Sphalerite + pyrite stringers | Massive sphalerite[1] | Massive sphalerite-chalcopyrite | Chalcopyrite stringer mineralization |
|---|---|---|---|---|---|
| Fe-poor sphalerite<br>pyrite (± Ag)<br>chalcopyrite (± Ag)<br>galena<br>cassiterite<br>arsenopyrite<br>± cobaltite | Fe-poor sphalerite<br>pyrite (± Ag)<br>pyrrhotite<br>chalcopyrite<br>Ag-tetrahedrite<br>galena<br>cassiterite<br>arsenopyrite<br>± cobaltite<br>± blebby magnetite[2] | Sphalerite<br>pyrite<br>chalcopyrite<br>cassiterite<br>± pyrrhotite<br>± blebby magnetite[2] | Fe-rich sphalerite<br>pyrite (± Ag)<br>pyrrhotite<br>chalcopyrite<br>galena (± Se, Bi)<br>Ag-tetrahedrite<br>cassiterite<br>arsenopyrite<br>cobaltite,<br>argentite<br>native silver<br>± magnetite[2]<br>± gudmundite<br>± allargentum[2] | Pyrite<br>pyrrhotite<br>chalcopyrite<br>Fe-rich sphalerite<br>magnetite[2]<br>galena<br>cobaltite<br>stannite<br>± arsenopyrite<br>± cassiterite<br>± allargentum[2]<br>± Bi-Se-Ag-As sulfide<br>± laitakarite[2] | Pyrite<br>chalcopyrite<br>pyrrhotite<br>Fe-rich sphalerite<br>cobaltite<br>galena<br>stannite<br>± Bi-Se-Ag sulfides<br>± native Bi<br>± native Ag<br>± magnetite[2]<br>± cassiterite |
| Associated gangue minerals: | | | | | |
| Sericite<br>Mg-chlorite | Sericite<br>Mg-chlorite<br>siderite[2] | Sericite,<br>Mg-Fe chlorite<br>siderite[2] | Sericite,<br>Mg-Fe chlorite<br>siderite (± Mg, Mn)<br>ankerite (± Mn, Mg)[2]<br>albite<br>± Fe-tourmaline | Sericite<br>Mg-Fe chlorite<br>siderite (± Mg, Mn)<br>ankerite (± Mn, Mg)[2]<br>Fe-Mg tourmaline<br>albite<br>ferroan dolomite[2] | Fe-Mg chlorite<br>sericite<br>ferroan dolomite (± Mn, Mg)[2]<br>ankerite (± Mn, Mg)[2]<br>siderite (± Mg)[2]<br>albite<br>Fe-Mg tourmaline<br>± phlogopite[2]<br>± rutile[2] |

Minerals are listed in approximate order of abundance (± denotes minerals present in only a few samples)

[1]Includes massive pyrite-sphalerite, massive sphalerite, and massive pyrrhotite-sphalerite ores

[2]Minerals not seen in similar ore types from the upper mine (Hannington et al., 1999)

Table 3.2 Mineralogy of Principal Ore Types in the South Lens of Mine D

| Sphalerite + pyrite stringers | Massive sphalerite[1] | Massive sphalerite-chalcopyrite |
|---|---|---|
| Sphalerite<br>pyrite<br>chalcopyrite<br>cassiterite<br>± pyrrhotite<br>± blebby magnetite | Fe-rich sphalerite<br>pyrite (± Ag)<br>pyrrhotite<br>chalcopyrite<br>galena (± Se, Bi)<br>cassiterite<br>± magnetite<br>± arsenopyrite[2]<br>± cobaltite<br>± Ag tetrahedrite<br>± gudmundite | Pyrite (± Ag)<br>pyrrhotite<br>chalcopyrite<br>Fe-rich sphalerite<br>galena[2]<br>± magnetite<br>± cobaltite[2]<br>± arsenopyrite[2]<br>± cassiterite[2]<br>± stannite |
| Associated gangue minerals: | | |
| Sericite<br>Mg-chlorite<br>siderite<br>± phlogopite | Sericite<br>Mg-chlorite<br>siderite<br>± tourmaline[2]<br>± albite | Sericite<br>Mg-chlorite<br>siderite<br>± tourmaline<br>± albite |

Minerals are listed in approximate order of abundance (± denotes minerals present in only a few samples)

[1]Includes massive pyrite-sphalerite, massive sphalerite, and massive pyrrhotite-sphalerite ores

[2]Minerals not seen in similar ore types from the upper mine except sphalerite + pyrite stringers (Hannington et al., 1999)

Table: 3.3 Electron Microprobe Analyses (wt %) of Major Ore Minerals in the West, Main and South Lenses, Mine D

| Mineral | n | Cu | Fe | Zn | Pb | S | Ag | (max) | Sb | (max) | As | (max) | Bi | (max) | Co | (max) | Ni | (max) | Se | (max) |
|---|---|---|---|---|---|---|---|---|---|---|---|---|---|---|---|---|---|---|---|---|
| Pyrite | (26) | 0.01 | 46.9 | 0.08 | <0.10 | 53.0 | <0.02 | 0.07 | <0.02 | 0.04 | <0.04 | 0.24 | <0.08 | 0.09 | 0.04 | 0.36 | <0.01 | 0.02 | <0.05 | 0.27 |
| Pyrrhotite | (52) | 0.03 | 61.0 | 0.15 | <0.10 | 38.7 | <0.02 | 0.11 | <0.02 | 0.04 | <0.02 | 0.14 | <0.08 | - | <0.02 | 0.10 | <0.01 | 0.03 | <0.05 | 0.14 |
| Chalcopyrite | (39) | 34.0 | 30.6 | 0.11 | <0.10 | 34.8 | 0.04 | 0.24 | <0.03 | 0.08 | <0.05 | 0.08 | <0.08 | 0.23 | <0.02 | 0.09 | <0.01 | 0.03 | <0.05 | 0.16 |
| Galena | (11) | 0.08 | 0.30 | 0.13 | 85.7 | 13.2 | 0.15 | 0.73 | <0.03 | 0.12 | <0.10 | - | <0.08 | - | <0.02 | 0.02 | <0.01 | 0.03 | 0.50 | 4.53 |
| Sphalerite | (96) | 0.05 | 7.06 | 59.8 | <0.10 | 33.3 | 0.01 | 0.17 | <0.03 | 0.08 | 0.01 | 0.18 | <0.07 | 0.16 | 0.02 | 0.42 | <0.02 | 0.03 | <0.05 | 0.22 |

Average for all sulfide ores excluding the Greywacke Orebody.
max = maxiumum concentration measured; n = number of analyses
Sphalerite has an average of 0.27 wt % Cd

Table: 3.4 Electron Microprobe Analyses (wt %) of Selected Trace Minerals in the West, Main and South Lenses, Mine D

| Mineral | n | Cu | Fe | Zn | S | Ag | Sb | As | Pb | Bi | Co | Ni | Se | Cd | In | Sn |
|---|---|---|---|---|---|---|---|---|---|---|---|---|---|---|---|---|
| Ag-bearing minerals: | | | | | | | | | | | | | | | | |
| Ag tetrahedrite | (3) | 19.5 | 5.6 | 0.77 | 22 | 26.2 | 27 | <0.10 | <0.10 | <0.07 | <0.02 | <0.02 | <0.06 | - | <0.03 | - |
| Native Ag | (3) | 0.06 | 0.40 | 0.07 | 0.77 | 96.2 | 1.8 | 0.15 | <0.10 | 0.08 | <0.02 | <0.02 | <0.06 | - | <0.03 | - |
| Allargentum | (1) | 0.09 | 0.04 | 0.06 | 0.13 | 83.2 | 15.6 | 0.10 | <0.10 | 0.73 | <0.02 | <0.02 | <0.06 | - | <0.03 | - |
| Co- and As- bearing minerals: | | | | | | | | | | | | | | | | |
| Arsenopyrite | (4) | 0.03 | 35.5 | 0.06 | 21.1 | <0.02 | 0.53 | 41.9 | <0.10 | <0.07 | 0.56 | 0.03 | <0.05 | - | <0.03 | <0.03 |
| Cobaltite | (1) | 0.01 | 10.6 | 0.05 | 23.0 | <0.02 | 0.02 | 37.3 | <0.10 | <0.07 | 29.1 | <0.02 | <0.05 | - | <0.03 | <0.03 |
| Bi-bearing minerals: | | | | | | | | | | | | | | | | |
| Native Bi | (2) | <0.02 | 0.03 | 0.06 | 0.09 | <0.04 | 0.09 | <0.07 | <0.10 | 98.4 | 0.02 | <0.02 | <0.06 | - | <0.05 | - |
| Bi-Ag alloy[1] | (1) | 0.05 | 1.8 | 0.15 | 0.37 | 47.6 | 0.27 | <0.07 | <0.10 | 55.4 | <0.02 | 0.02 | <0.06 | - | <0.05 | - |
| Laitakarite | (1) | <0.02 | 0.51 | <0.04 | 0.37 | <0.04 | <0.03 | <0.07 | 2.3 | 78.0 | 0.02 | <0.02 | 21.4 | - | <0.05 | - |

Average for all sulfide ores excluding the Greywacke Orebody.

n = number of analyses

[1]Bohdanowiczite ($AgBiSe_2$) or matildite ($AgBiS_2$)

Table 3.5 Electron Microprobe Analyses (wt %) of Major Carbonate Gangue Minerals in the West, Main and South Lenses, Mine D

| Mineral | n | FeO | CaO | $CO_2$ | MnO | MgO |
|---|---|---|---|---|---|---|
| Mine D: | | | | | | |
| Siderite | (24) | 54.9 | 0.47 | 38.9 | 1.48 | 3.65 |
| Ankerite | (18) | 15.3 | 28.1 | 44.0 | 1.58 | 10.6 |
| Mine 1,2: | | | | | | |
| Siderite[1] | (1) | 54.3 | 0.37 | - | 0.83 | 4.37 |
| Ankerite[1] | (1) | 15.0 | 28.0 | - | 0.23 | 12.0 |

Average for all sulfide ores excluding the Greywacke Orebody.

n = number of analyses

[1]Data from Schandl et al., 1999

Table 3.6 Electron Microprobe Analyses (wt %) of Major Silicate Gangue Minerals in the West, Main and South Lenses, Mine D

| Mineral | n | $SiO_2$ | $TiO_2$ | $Al_2O_3$ | FeO | MnO | MgO | CaO | $Na_2O$ | $K_2O$ | F | Cl |
|---|---|---|---|---|---|---|---|---|---|---|---|---|
| Mine D: | | | | | | | | | | | | |
| Sericite | (5) | 47.9 | 0.23 | 33.6 | 1.77 | <0.03 | 1.16 | <0.02 | 0.48 | 10.5 | 0.43 | 0.01 |
| Chlorite | (48) | 24.4 | 0.04 | 21.8 | 32.4 | 0.14 | 9.39 | <0.02 | 0.01 | 0.03 | 0.11 | <0.01 |
| Phlogopite | (2) | 40.3 | 0.30 | 12.5 | 17.4 | 0.04 | 15.7 | <0.02 | 0.20 | 9.47 | 4.03 | <0.01 |
| Tourmaline | (5) | 34.6 | 0.17 | 30.7 | 13.0 | 0.02 | 6.56 | 0.16 | 1.47 | 0.00 | 0.22 | 0.00 |
| Albite | (5) | 69.2 | <0.02 | 19.6 | 0.03 | <0.03 | <0.01 | 0.12 | 11.5 | 0.03 | <0.04 | <0.01 |
| Mine 1, 2: | | | | | | | | | | | | |
| Sericite - HW[1] | (5) | 52.0 | 0.20 | 34.0 | 0.73 | 0.01 | 2.31 | 0.01 | 0.31 | 6.87 | 1.10 | 0.01 |
| Sericite - FW[1] | (12) | 48.0 | 0.08 | 32.0 | 0.99 | 0.03 | 1.30 | 0.02 | 0.86 | 9.50 | 1.20 | 0.01 |
| Chlorite - HW[1] | (12) | 25.0 | 0.08 | 21.9 | 20.0 | 0.13 | 17.7 | 0.04 | 0.03 | 0.02 | 0.62 | 0.01 |
| Chlorite - FW[1] | (10) | 26.0 | 0.07 | 22.0 | 30.0 | 0.15 | 11.0 | 0.03 | 0.03 | 0.09 | 0.23 | 0.02 |
| Tourmaline[2] | (1) | 35.0 | 0.41 | 31.0 | 17.0 | 0.05 | 1.77 | 0.16 | 2.02 | - | - | - |
| Albite[3] | (1) | 68.0 | - | 19.0 | - | - | - | - | 12.0 | - | - | - |

Average for all sulfide ores excluding the Greywacke Orebody.

n = number of analyses

[1]Data from Koopman et al., 1999

[2]Data from Slack et al., 1999

[3]Data from Schandl et al., 1999

Table 3.7 Table of approximate mineral balances for selected elements from Mine D

| | Ag | Sb | As | Sn | MgO | Fe | S |
|---|---|---|---|---|---|---|---|
| Pyrite | - | - | - | - | - | 22.6[11] | 44.2[12] |
| Pyrrhotite | - | - | - | - | - | 6.23[11] | 12.1[12] |
| Sphalerite | - | - | - | - | - | 3.70[9] | 24.9[13] |
| Chalcopyrite | 30[1] | - | - | - | - | 23.8[9] | 18.4[13] |
| Galena | 3.2[1] | - | - | - | - | - | 0.02[13] |
| Tetrahedrite | 18[1] | 90[2] | - | - | - | - | - |
| Native Ag | 47[3] | 10[2] | - | - | - | - | - |
| Ag-Antimonide | 1.8[2] | - | - | - | - | - | - |
| Arsenopyrite | - | - | 70[6] | - | - | 0.03[9] | 0.04[13] |
| Cobaltite | - | - | 30[5] | - | - | 0.04[9] | 0.00[13] |
| Magnetite | - | - | - | - | - | 7.04[10] | - |
| Cassiterite | - | - | - | 90[4] | - | - | - |
| Stannite | - | - | - | 10[4] | - | - | - |
| Siderite | - | - | - | - | 9.9[7] | 13.5[9] | - |
| Ankerite | - | - | - | - | 25.4[7] | 3.58[9] | - |
| Chlorite | - | - | - | - | 64.7[8] | 19.4[9] | - |

[1]Assuming 100% of Sb is in tetrahedrite , the mineral balance for Ag was calculated using the average Ag wt % in mineral microprobe analyses and average bulk concentration of Ag from geochemistry

[2]Assuming that the amount of Ag in Ag-antimonides is 10% of that in tetrahedrite

[3]Calculated from the left over bulk Ag concentration assuming native silver is 100% Ag

[4]Plotted Sn vs Cu/Zn and extrapolated Sn for 100% Zn then determined % from the difference between the extrapolated value and the average Sn content in the Cu-rich stringer zone (assumed to be 100% stannite) and massive sulfides (assumed to be 100% cassiterite)

[5]Assuming 100% of Co is in cobaltite, the mineral balance for As was calculated using the average Co wt % in mineral microprobe analyses and average bulk concentration of Co from geochemistry

[6]Calculated from the reamining bulk As after the cobaltite component was removed, assuming that the remaining As is 100% in arsenopyrite

[7]Assuming 50% of $CO_2$ resides in siderite and 50% in ankerite, $CO_2$ was used with the microprobe analysis of each to calculate siderite equivalent and ankerite equivalent

[8]Assuming all MgO is contained only in siderite, ankerite and chlorite, MgO content from siderite and ankerite equivalents and removed it from the total bulk MgO content giving the MgO of chlorite

[9]Assuming Fe only occurs in pyrite, pyrrhotite, sphalerite, chalcopyrite, arsenopyrite, cobaltite, magnetite, siderite, ankerite, and Chlorite, equivalents of each mineral and the average wt % of Fe from microprobe were used to calculate the amount of Fe in each mineral which were then removed from the average bulk Fe

[10]Approximate average value of $Fe^{3+}$ was used to give its percentage of the total bulk Fe. The $Fe^{3+}$ analysis were from the hotmuck project and are biased towards only high Fe samples.

[11]All remaining Fe and S after all other components are removed were used to calculate the ratio between pyrite and pyrrhotite. Calculate remaining Fe/ remaining S (Eqn A). Calculate ratio of Fe to S in both Py and Po (Eqn B and C respectively). (Eqn A-Eqn B)/(Eqn C-Eqn B) = Eqn D (Po). 1-Eqn D = Eqn E (Py). Eqn E*remaining Fe = amount of Fe in Pyrite. Eqn D*remaining Fe = amount of Fe in pyrrhotite

[12]All remaining Fe and S after all other components are removed were used to calculate the ratio between pyrite and pyrrhotite. Calculate remaining Fe/ remaining S (Eqn A). Calculate ratio of Fe to S in both Py and Po (Eqn B and C respectively). (Eqn A-Eqn B)/(Eqn C-Eqn B) = Eqn D (Po). 1-Eqn D = Eqn E (Py). Eqn E*remaining S = amount of S in Pyrite. Eqn D*remaining S = amount of S in pyrrhotite

[13]Assuming S only occurs in pyrite, pyrrhotite, sphalerite, chalcopyrite, arsenopyrite, and cobaltite, equivalents of each mineral and the average wt % of Fe from microprobe were used to calculate the amount of S in each mineral which were then removed from the average bulk S

Mineral formulas: pyrite ($FeS_2$), pyrrhotite ($Fe_{(1-x)}S$), sphalerite (ZnS), chalcopyrite ($CuFeS_2$), galena (PbS), tetrahedrite ($Cu_6[Cu_4(Fe,Zn)_2]Sb_4S_{13}$), native Ag (Ag), Ag-antimonide (Ag-Sb), arsenopyrite (FeAsS), cobaltite (CoAsS), magnetite ($Fe_3O_4$), cassiterite ($SnO_2$), stannite ($Cu_2(Fe,Zn)SnS_4$), siderite ($FeCO_3$), ankerite ($Ca(Fe,Mg)(CO_3)_2$), and chlorite ($((Fe,Mg)_5Al(AlSi_3O_{10})(OH)_8$)

Note: CdS was also calculated using average bulk concentrations and average wt % of Cd in sphalerite microprobe analysis

# Chapter 4. Metal Zoning and Trace Element Geochemistry

Tables 4.1 and 4.2 list average chemical analyses of the principal ore types. Table 4.3 is a matrix of Pearson correlation coeffecients for elements determined in all 71 core samples. The full data set is given in Appendix I. Drill hole assays from 1.5 m delineation sampling were used to construct metal zonation profiles across the West, Main, and South lenses, and the Cu-rich stringer zone. Cu, Zn, Ag, and Pb concentrations, as well as a number trace elements, in 10 drill holes are plotted on drill-hole logs in Figures 4.3 to 4.21, and interelement plots of the major ore elements and trace metals are shown in Figures 4.26 and 4.27. The distribution of selected trace elements is also illustrated on level plans in Figures 4.22 and 4.25.

Copper, Zinc, and Lead metal contents in the West and Main lenses exhibit a consistent stratigraphic zonation typical of VMS deposits. The base of each lens is Cu-rich and grades towards a Zn-rich top. The Cu-rich zone contains 5 to10 wt % Cu, with up to 19.8 wt % Cu in the stockwork, which grades outwards to a zone of sphalerite staining along the margins of the deposit. The bulk of the massive sulfides above the Cu-rich zone are Zn-rich and contain 5 to 20 wt % Zn. The most Zn-rich ores are located at the southeast end of the Main orebody and contain up to 27 wt % Zn. Zn-rich ores contain 0.5-2 wt % Pb, with >2 wt % Pb locally at the top of the massive sulfide lens (Table 4.1). Between 7000 and 8000 levels, zones of high Pb grades appear to have been structurally repeated, which is consistent with the West and Main lenses having been separated by faulting (Figure 4.2).

Metal contents in the South Lens exhibit a complicated zonation due to faulting, and in the largest massive sulfide body zonation is the opposite of that in other lenses (Figure

4.1), with Cu at the "top", 4 to 15 wt % Zn throughout the main body, and a local zone of 0.5 to 1.6 wt % Pb at the bottom (Table 4.2). This is strong evidence that the South Lens is somehow rotated out of position or that Cu-rich ore was faulted into the hanging wall.

*Silver*

The massive sulfides of the West and Main lenses are Ag-rich throughout, containing 50 to 200 ppm Ag. However, the highest concentrations of Ag are at the base of the massive sulfides, immediately above massive silicified rhyolite, where native Ag and Ag-selenides are abundant (typically 200 to 900 ppm Ag, up to 1790 ppm Ag). These minerals are most abundant in the Cu-rich ores. Ag-rich tetrahedrite is associated with the high-grade Pb-rich ores at the stratigraphic top of the lens (typically 200 to 400 ppm Ag, up to 1250 ppm). This explains the strong correlation between Ag, Sb and Pb (Table 4.1) as previously observed in the North orebody in the upper mine, although the average concentrations of Ag and Sb are lower in Mine D (Table 4.4). The Cu-rich stringer zone contains less than 50 ppm Ag (up to 200 ppm Ag, locally), similar to the concentrations of Ag in Cu-stringer ore from the upper mine.

Silver concentrations are lower in the South Lens than in the West and Main lenses, occurring mainly in Ag-rich tetrahedrite. The highest grades are in the main body of the South Lens at 9000 level, which contains 50 to 270 ppm Ag (up to 320 ppm Ag, locally: Table 4.2). This is similar to the South orebody in the upper mine, where only the bornite zone contained high Ag (Hannington et al., 1999).

*Tin*

Tin is correlated with Zn, Cd, Pb, In, Hg, Sb, and Au, which all occur with massive sphalerite and massive sphalerite-chalcopyrite ores (Table 4.4). In samples from the base of the West and Main lenses, sphalerite-chalcopyrite ores contain 115 to 2330 ppm Sn as both cassiterite and stannite. Immediately above this zone, the massive pyrite-sphalerite and sphalerite ores contain 1000 to 5050 ppm Sn. At the top of the West and Main lenses, fragmental and sphalerite stringer ores contain 82 to1960 ppm Sn, but the corresponding Zn grades are variable. The Cu-rich stringer zone contains 48 to 1940 ppm Sn (Table 4.1). The large amount of Sn in the stringer zone is attributed to the presence of stannite. In general, the association of Sn with Zn, Cd, Pb, In, Hg and Sb is weaker than was found in the Zn-rich ores of the North orebody. The ratio of Sn in cassiterite to stannite is 9:1 respectively (Table 3.7).

Similar concentrations of Sn are found in the South Lens within the massive sulfides (225 to 5100 ppm Sn), but Sn is enriched at the bottom of the lens with Pb, as noted above (Table 4.2).

*Cadmium*

Cadmium is strongly correlated with Zn (Table 4.3 and Appendix IV) because it substitutes for Zn in sphalerite. In samples from the base of the West and Main lenses, sphalerite-chalcopyrite ores contain 219 to 1440 ppm Cd. Immediately above this zone, the massive pyrite-sphalerite and sphalerite ores contain 50 to 896 ppm Cd. At the top of the West and Main lenses, fragmental and sphalerite stringer ores contain 4 to 975 ppm Cd. The

zonation of Cd through the West-Main Lens is directly related to the quantity of sphalerite. The Cu-rich stringer zone contains >1 to 233 ppm Cd (Table 4.1). Similar concentrations of Cd are found in the South Lens (Table 4.2). All of the concentrations of Cd are lower than in ores from the upper mine. If all of the Cd in the ore was contained in sphalerite, the average CdS content of the sphalerite would be 0.3 wt %, whereas in the upper mine, sphalerite contains an average of 0.5 wt % CdS (Appendix IV and Table 3.7).

*Antimony*

The Pb-rich ores at the stratigraphic top of the West and Main lenses contain up to 100 ppm Sb in tetrahedrite. Two samples with large amounts of tetrahedrite contained 224 and 1100 ppm Sb. Antimony also occurs locally at the base of the West and Main lenses in Ag-Sb sulfosalts such as allargentum, but the bulk concentration of this ore is less than a few 10s of ppm Sb (Table 4.1). Antimony is also strongly correlated with Ag and Sn in these samples (Table 4.4). Pb-rich ores at the "bottom" of the South Lens contain 51 to 88 ppm Sb (Table 4.2). These concentrations are similar to those from the North orebody.

*Mercury*

Mercury occurs throughout the massive sulfides of the West and Main lenses at concentrations of 100 to 1000 ppb Hg predominantly in sphalerite. The highest concentrations are found at the top of the massive sulfide lens (up to 1900 ppb Hg). Two

samples of sphalerite-chalcopyrite stringers located within the highly silicified rhyolite beneath the Main orebody contained greater than 650 ppb Hg (Table 4.1).

The highest concentrations of Hg were found in samples from the South Lens in massive sphalerite which contained 608 to 3780 ppb Hg (Table 4.2). These concentrations were consistent across the lens, with the highest values in sphalerite-chalcopyrite ores at the "bottom" of the lens, where they are correlated with Sn, Cd and Zn (Table 4.4). Samples containing up to 1500 ppb Hg were also found in Cu-rich stringers in the rhyolite lapillistone to the north of the deposit (Table 4.1). The concentrations of Hg in the West and Main lenses are much lower than the North orebody of the upper mine; however, the concentrations in the South Lens are similar to the South Lens of the upper mine, including the bornite zone.

*Arsenic and Cobalt*

Arsenic and cobalt occur throughout the massive sulfides of the West and Main lenses. At the base of the massive sulfide lens, As concentrations are ~500 to 1310 ppm and Co concentrations are up to 521 ppm, mainly in arsenopyrite and cobaltite within massive sphalerite-chalcopyrite ores. Immediately above this zone the massive sphalerite ores contain ~150 to 499 ppm As and 368 ppm Co. In contrast, the South Lens only contains 18 to 377 ppm As and 5 to 258 ppm Co (Table 4.1 and 4.2). As and Co are correlated with Zn and Sn in Zn-rich ores and with Ni and to a lesser extent Au in Cu-rich ores (cf. Hannington et al., 1999) (Table 4.4). Samples from the Cu-rich stringer zone contain up to 542 ppm As and 506 ppm Co, reflecting the abundance of arsenopyrite, cobaltite and Co-enrichment in chalcopyrite, as observed in the upper mine (Table 4.1).

*Selenium and Indium*

Selenium and In are both strongly correlated with Cu, Au and Co (Table 4.4). The pyrite-sphalerite ores at the top and in the core of the massive sulfides typically contain ~100 to 200 ppm Se. Sphalerite-chalcopyrite ores at the base of the West and Main lenses contain up to 1040 ppm Se and 249 ppm In. The Cu-rich stringer zone contains up to 204 ppm Se and 187 ppm In (Table 4.1), similar to the upper mine. The selenium is contained in most sulfides but mainly in chalcopyrite and galena. Indium occurs mainly in roquesite ($CuInS_2$), both associated with the Zn-rich and Cu-rich component of the ores.

The South Lens contains up to119 ppm Se and up to 104 ppm In, and their distribution reflects the reverse zonation discussed above (Table 4.2). The concentrations of Se and In in the South Lens are much lower than that of the South orebody in the upper mine, mostly reflecting lack of massive and stringer chalcopyrite ores in the South Lens.

*Bismuth*

Bismuth is weakly correlated with Se, In, and Cu (Table 4.4) in both the massive sulfides and the Cu-rich stringer zone. The West and Main lenses contain 10 to 133 ppm as native Bi and Bi selenides, such as laitakarite ($Bi_4Se_2S$), mainly at the base of the massive sulfides in sphalerite-chalcopyrite ore. The Cu-rich stringer zone contains up to 175 ppm Bi and is uniformly enriched in Bi. These concentrations are slightly higher than those from similar ore types in the upper mine (Table 4.1).

The South Lens contains less than 15 ppm Bi (9 samples), which is extremely low when compared to the South orebody in the upper mine (Table 4.2).

*Thallium*

Tl is enriched in the heterolithic fragmental ores of the West and Main lenses, at the stratigraphic top of the massive sulfides, and is weakly correlated with the main alteration minerals (Table 4.4). Up to 48 ppm Tl is contained in muscovite-rich and chlorite-rich samples, suggesting that the Tl is contained in the phyllosilicates rather than in the sulfides (Table 4.1 and 4.2).

*Tungsten*

Tungsten is locally enriched at the top of the West and Main lenses in pyrite-sphalerite ores which contain up to 42 ppm W (Table 4.1). It is correlated with Fe, As, Tl, and the HREEs (Table 4.4) and is enriched in the phyllosilicate alteration. The concentrations of W in the West and Main lenses are similar to the upper mine; however, the South Lens of Mine D has lower W than the South orebody of the upper mine. Most of the W in the upper part of the mine was interpreted to be present in carbonates or scheelite, although a Cu-Sn-W sulfide (Kiddcreekite) was found in the bornite zone (Hannington et al., 1999).

*Gold*

The main massive sulfides in the upper mine contained a maxiumum of 140 ppb gold, although elevated gold (up to 1 ppm), was found in the bornite zone (Hannington et al, 1999). For the most part, the same is true for the lower mine. The massive sulfides contain less than 50 ppb gold (Table 4.1); however, there are small localized zones of higher grade gold in the sphalerite-chalcopyrite-rich ores below 9000 Level at the base of the West Lens (Figure 4.1). Grades of up to 23 ppm gold have been reported in mine assays, and 4-inch samples that were taken as part of this study included numerous samples with over 1 ppm Au. The highest gold grades showed the strongest correlation with Se, Sn, Cd, Zn, and As and appear consistently in chlorite-rich samples (Table 4.4).

One particularly gold-rich sample was collected immediately below the massive sulfides in sphalerite-chalcopyrite stringers in the massive silicified rhyolite of the Main orebody. It consisted of chalcopyrite and coarse sphalerite in a chlorite matrix in contact with intensely altered rhyolite. The sample contained 8 wt % Zn, 0.5 wt % Cu, 896 ppb Au, 17 ppm Ag, 349 ppm Sn, 1.26 wt % As, 342 ppm Bi, 83 ppm Te, 4320 ppm Co, 2300 ppm Ni, 209 ppm Se, and 1263 ppm ΣREE (Appendix I), The unusual composition suggests that gold enrichment is related to late-stage hydrothermal and/or metamorphic remobilization.

A second gold-rich sample located 10 m stratigraphically above the first gold-rich sample in massive sphalerite-chalcopyrite ore consisted of coarse pyrite, fine- to medium-grained sphalerite and chlorite stringers. The sample contained 23 wt % Zn, 4.7 wt% Cu, 736 ppb Au, 1310 ppm As, 1370 ppm Ag, 1620 ppm Sn, 54 ppm Bi, <3 ppm Te, 521 ppm Co, 30 ppm Ni, 1040 ppm Se, and 40 ppm ΣREE (Appendix I). Microprobe analyses of

chalcopyrite in the sample yielded 0.17 wt % Au (Appendix V) and analyses of pyrrhotite contained 0.12 wt % Au (Appendix III). The high concentrations of trace metals, and especially the high ΣREE, suggest that the chloritic matrix of the sample may represent a late shear-controlled overprint. Microprobe analysis of pyrrhotite in a third gold-rich sample located proximal to the first contained 0.10 wt % Au (Appendix III); chalcopyrite contained 0.17 wt % Au (Appendix V), native bismuth 0.14 wt % Au (Appendix VII), Ag-antimonide 0.14 wt % Au, and Ag-Cu-Sb-Bi-selenide 0.22 wt % Au (Appendix VIII). The bulk Au concentration of the sample was 23 ppm Au.

*Major Oxides*

The phyllosilicate component of the ore is correlated with Rb, Ba, $Al_2O_3$ Th, U, Hf, Y and the REEs, and accounts for the high $K_2O$, which reaches up 3.4 wt % in the Cu-rich stringers and up to 0.7 wt % in the massive sulfides (Appendix I and Table 4.3) which occur in white micas. MgO, which is contained in the chlorite component of the ore, is correlated with W, V, Sc, Hf, Y, Ga, Mo, Ge, As and $P_2O_5$ (Table 4.4) both in the massive sulfides and in the Cu-rich stringer zone.

The albite component accounts for the high $Na_2O$, which reaches up to 2.3 wt % in the Cu-rich stringers and up to 0.5 wt % in the massive sulfides (Appendix I). Cu is poorly correlated with $Na_2O$ at low Cu grades (Table 4.3), but when Cu reaches >1 wt %, there is a strong positive correlation (Figure 4.29).

$TiO_2$, which is present mainly in rutile, occurs throughout the massive sulfides and the Cu-rich stringer zone at concentrations up to 0.5 wt % in association with alteration minerals such as chlorite where it has replaced biotite (Appendix I).

The carbonate component of the ore accounts for the high CaO, which is correlated with $CO_2$, Sr, and Eu (Table 4.3 and Table 4.4), and occurs throughout the massive sulfides and Cu-rich stringer zone with up to 4.1 wt % CaO (Appendix I). $CO_2$ is also correlated with Mn, Fe, and S (Table 4.4) and occurs up to 11 wt % in the West and Main Lenses, up to 7 wt % in the South Lens and up to 19 wt % in the Cu-rich stringer zone, accounting for the correlation with Cu and In. The carbonate content of the ore is notable greater than in ores from the upper mine.

*Rare Earth Elements*

Rare earth elements are locally enriched throughout the West, Main, South Lenses and the Cu-rich stringer zone in mainly heterolithic, sphalerite and chalcopyrite stringer ores and are strongly correlated with Y, Hf, Nb, Th, U, Ba, Cs, Rb, Sr, Li, $SiO_2$, $Al_2O_3$, $K_2O$, $Na_2O$, and CaO (Table 4.3). The LREEs have a stronger correlation with Ba and $Al_2O_3$, whereas the HREEs have a stronger correlation with $SiO_2$, Y, Rb, Li, and Cs. In the upper mine, LREEs were association with Zn-rich ores and HREEs with Cu-rich ores, but this is not as clear in Mine D. In general the REEs are enriched in the phyllosilicate alteration assemblages, and most likely present in hydrothermal monazite and xenotime.

$P_2O_5$ is correlated with Cu, In, Ba, REEs, Y and Ga (Table 4.4) and occurs with Cu-rich ores with up to 0.19 wt % $P_2O_5$ (Appendix I). $P_2O_5$ occurs in association with xenotime in the Cu-rich ores which make up the REE-bearing phosphates component of the ore.

*Boron*

The Cu-rich stringer zone and its margins contain up to 1110 ppm B, hosted by tourmaline throughout the West, Main and South Lenses. It is poorly correlated with the REE's and Ba (Table 4.4). The overall concentration of boron in Mine D is lower than that of the upper mine but it shows the most consistent correlations with other elements in phyllosilicate alteration with Hg and LREE.

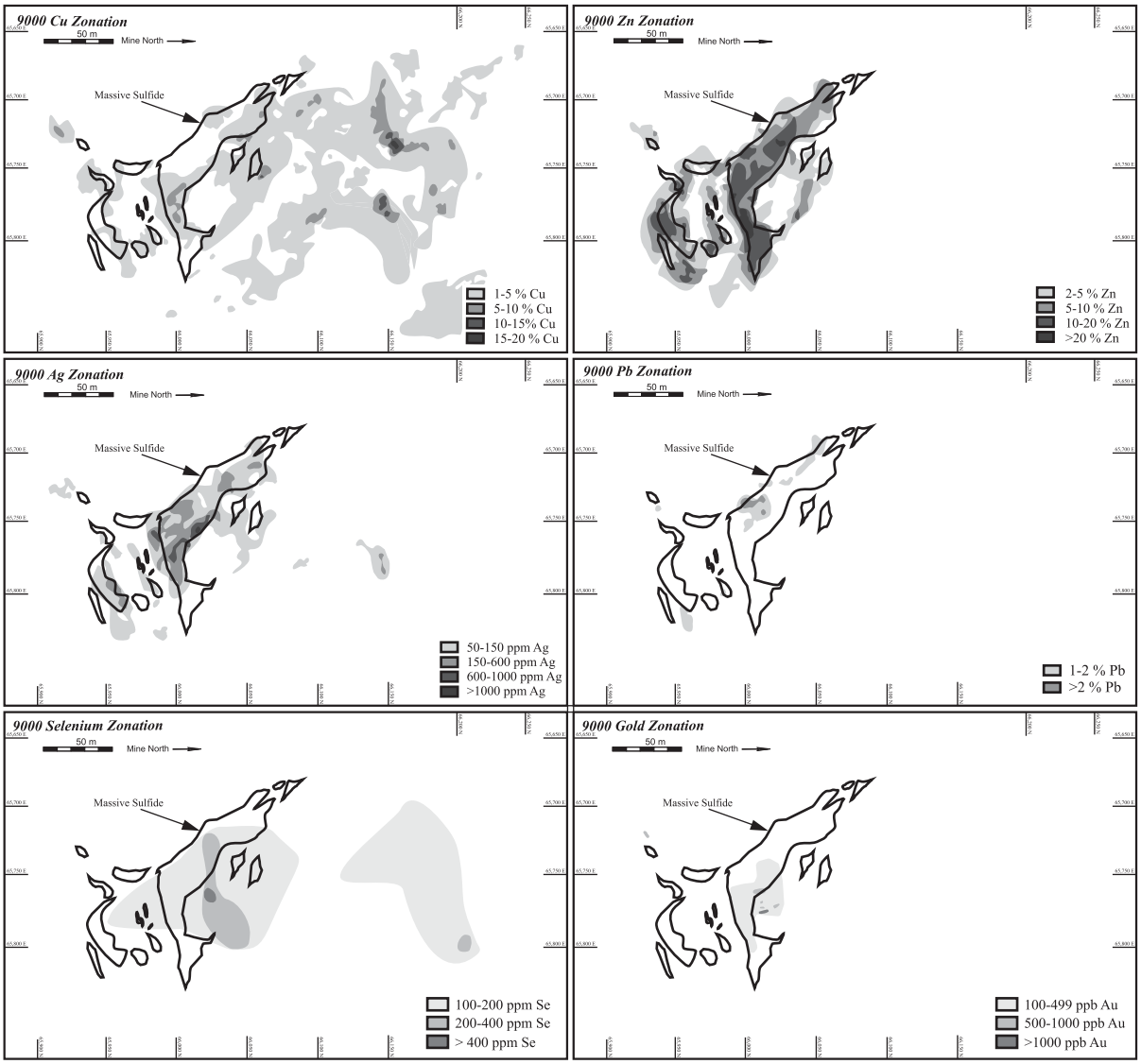


Figure 4.1 Zonation of the main ore metals, selenium and gold on the 9000 foot level of Mine D. All main ore metal exhibit typical metal zonation for a VMS deposit. Selenium zonation shows highest concentrations at the base of the sulfide lens and in the Cu-rich stringer zone. The South Lens at depth has low concentrations of selenium compared to the South orebody in the upper mine. The massive Sulfide boundary is based on visual estimates, both underground mapping and drillhole logging, of greater than 50% sulfides.

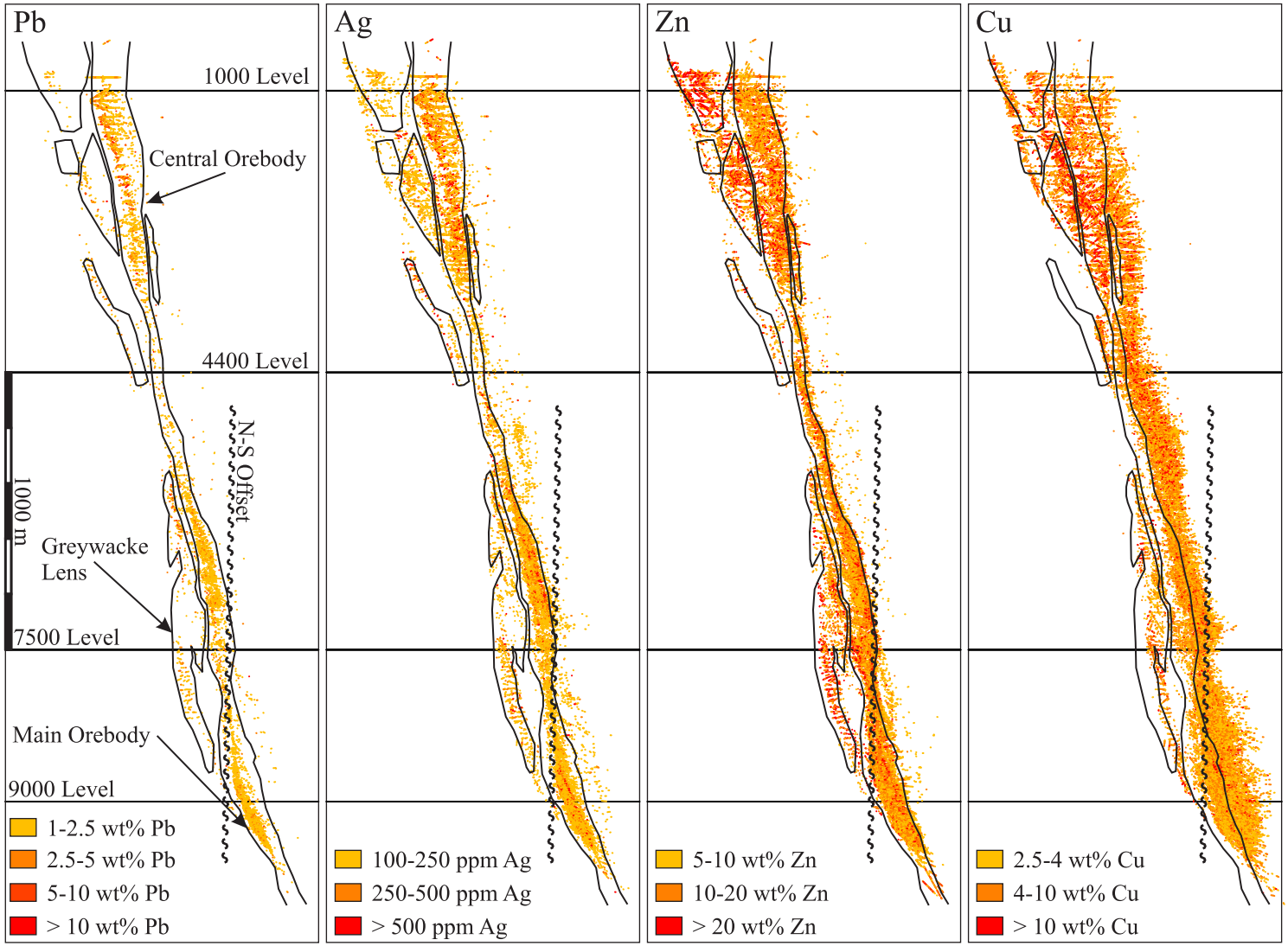


Figure 4.2 Long section of Mine 1, 2, 3, and D looking approximately West, showing Pb, Ag, Zn, and Cu grades from DDH intercepts. The N-S Offset can be seen displacing all mineralization between 7500 and 9000 Levels.

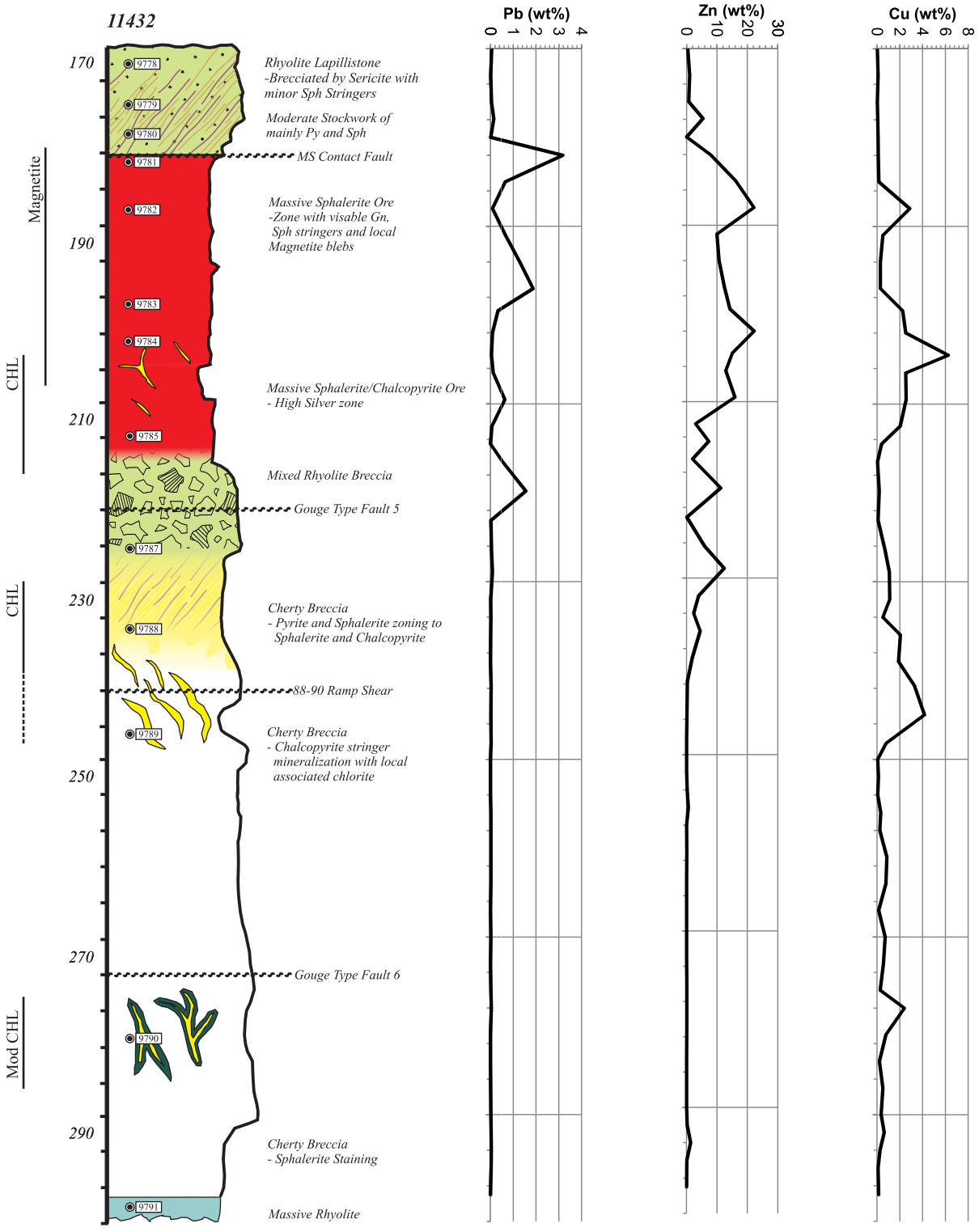


Figure 4.3 Drill-hole lithological profile and concentrations of Pb, Zn and Cu in core from hole 11432 through the Main orebody.

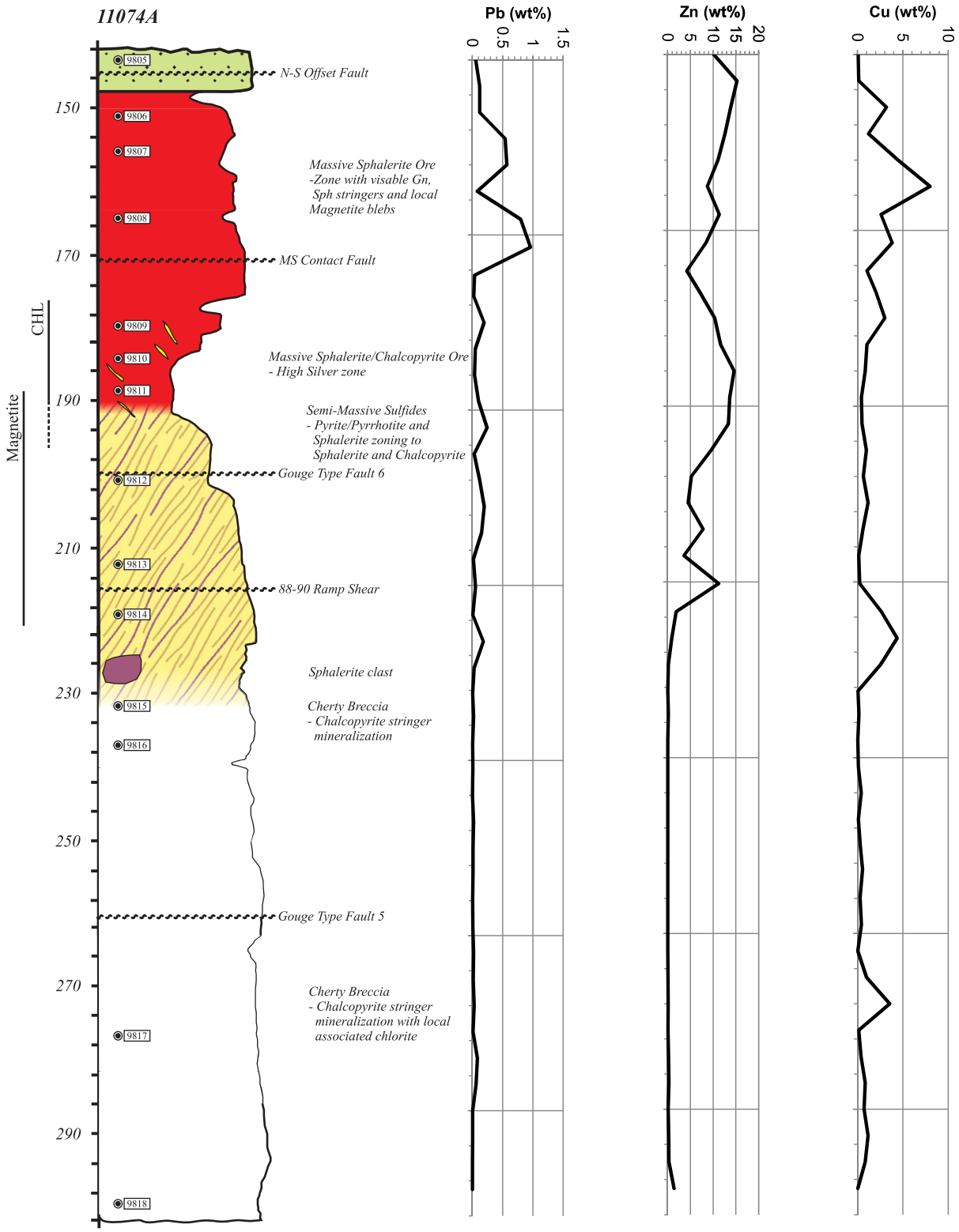


Figure 4.4 Drill-hole lithological profile and concentrations of Pb, Zn, and Cu in core from hole 11074A through the Main orebody.

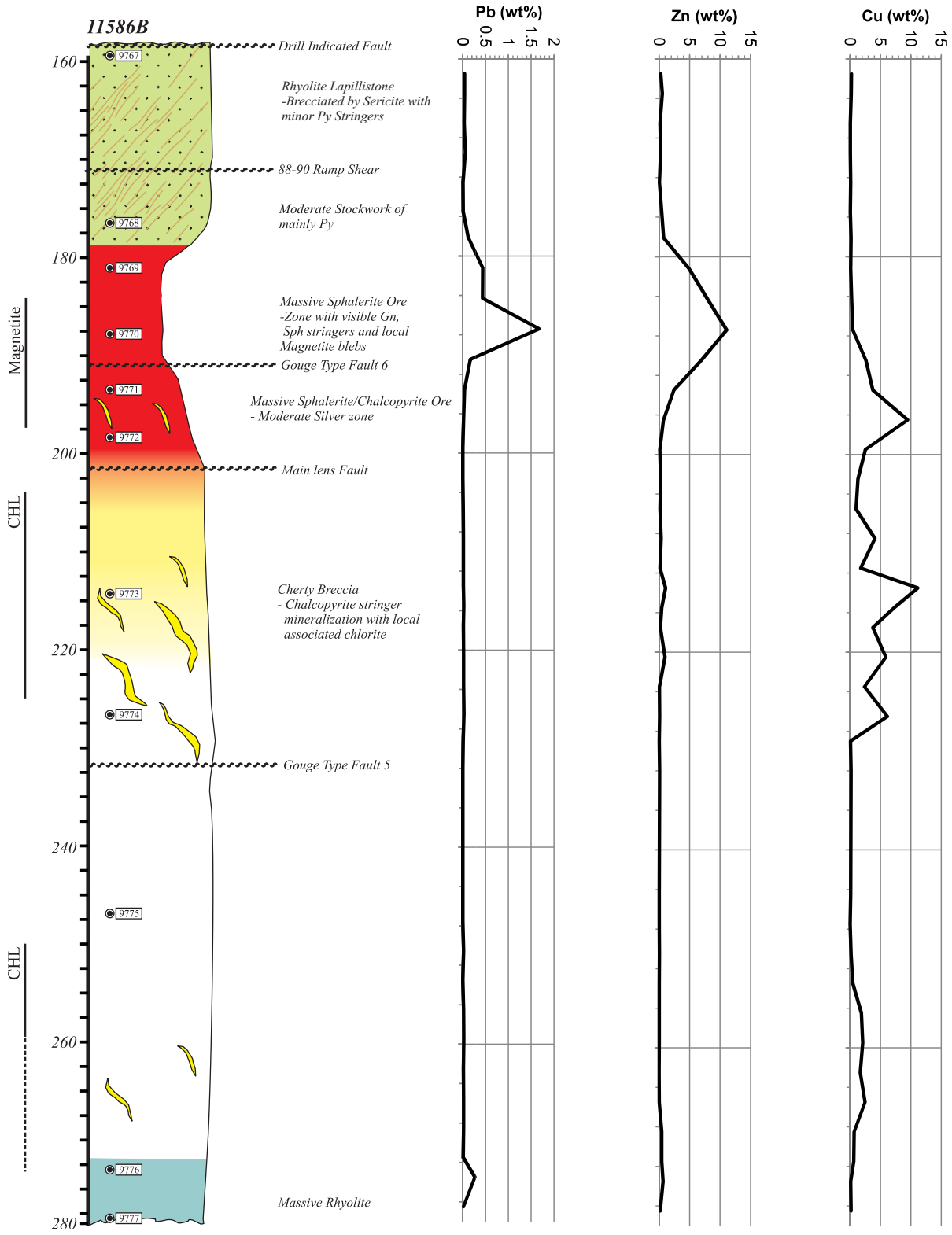


Figure 4.5 Drill-hole lithological profile and concentrations of Pb, Zn, and Cu in core from hole 11586B through the Main orebody.

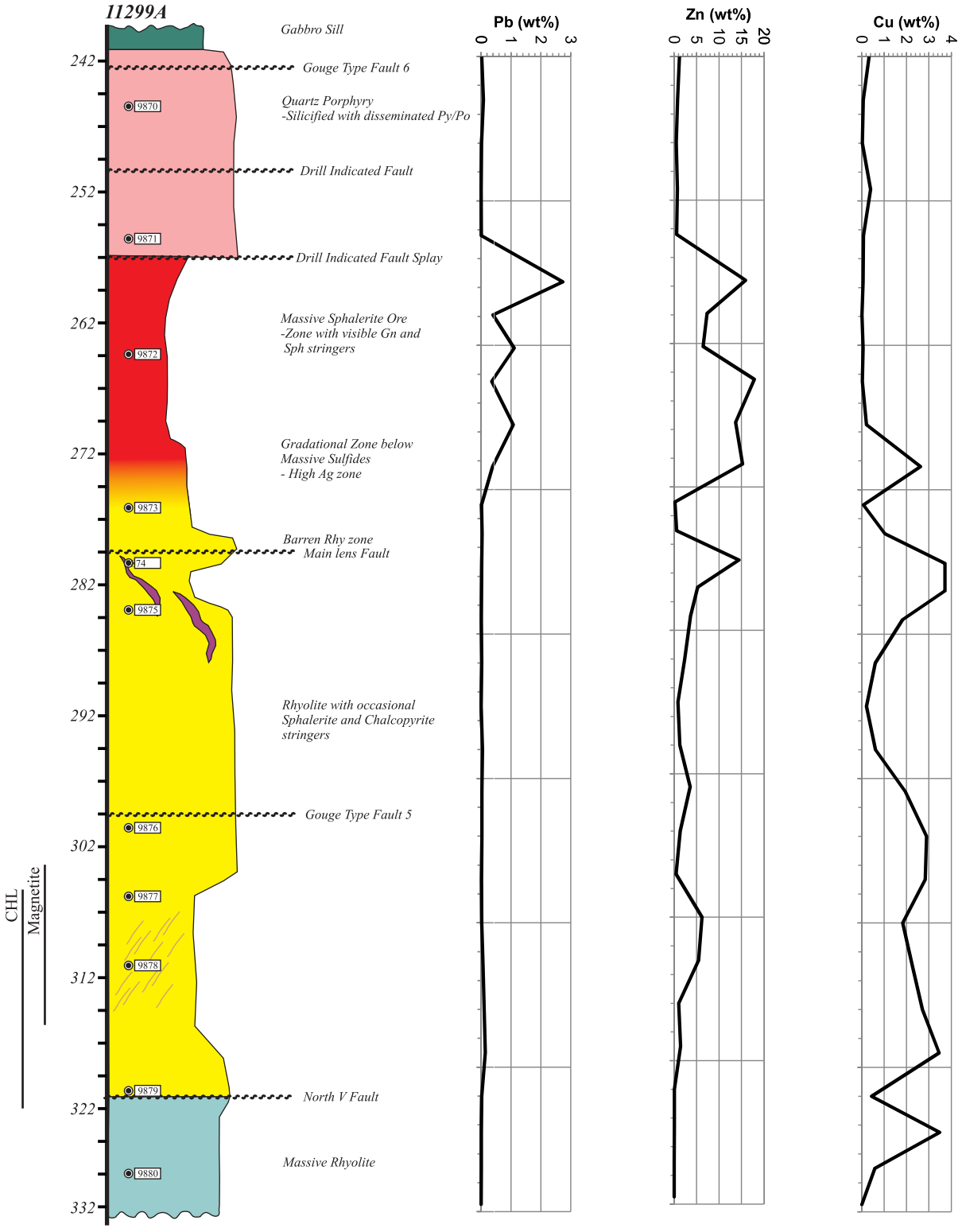


Figure 4.6 Drill-hole lithological profile and concentrations of Pb, Zn, and Cu in core from hole 11299A through the Main orebody.

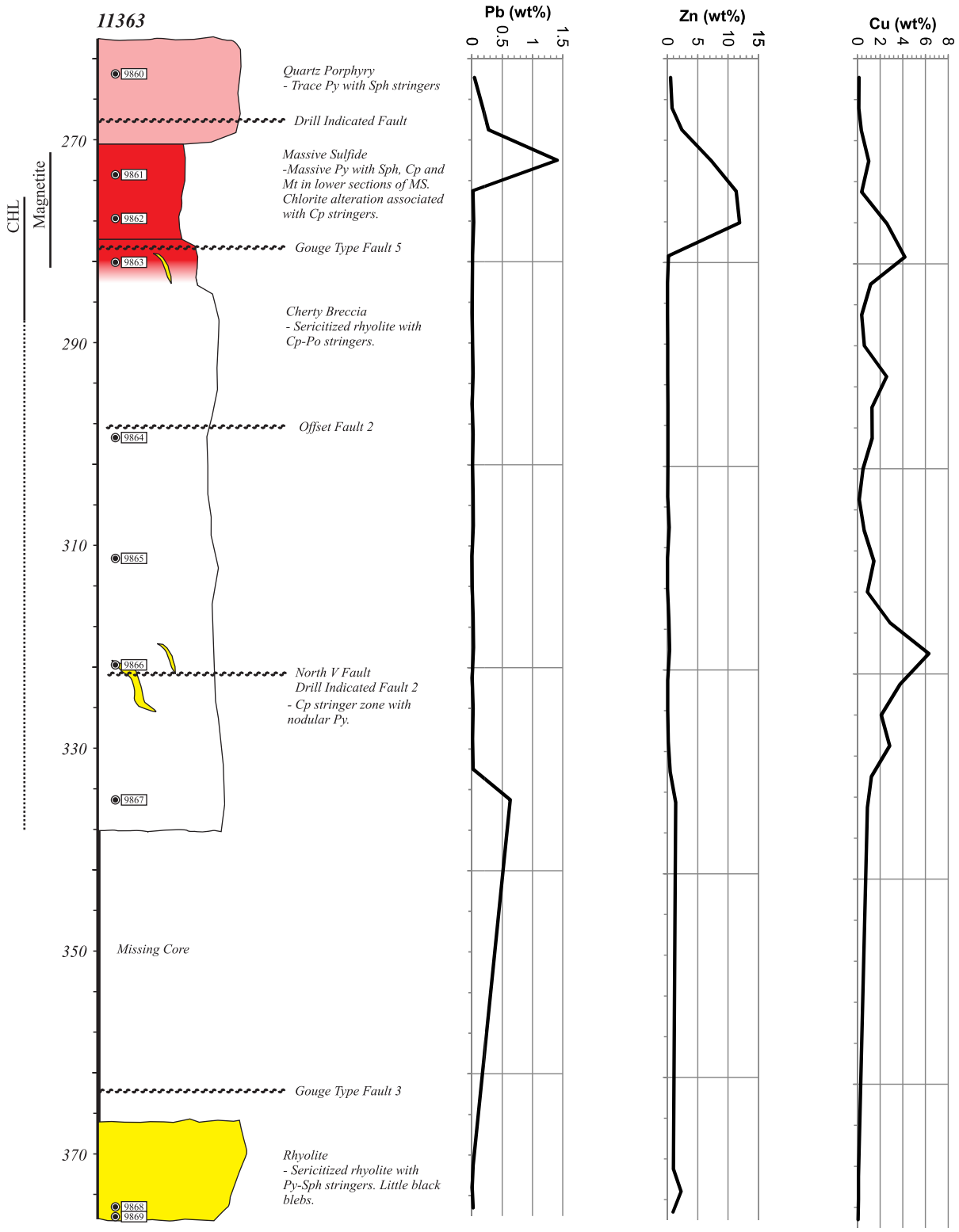


Figure 4.7 Drill-hole lithological profile and concentrations of Pb, Zn, and Cu in core from hole 11363 through the Main orebody.

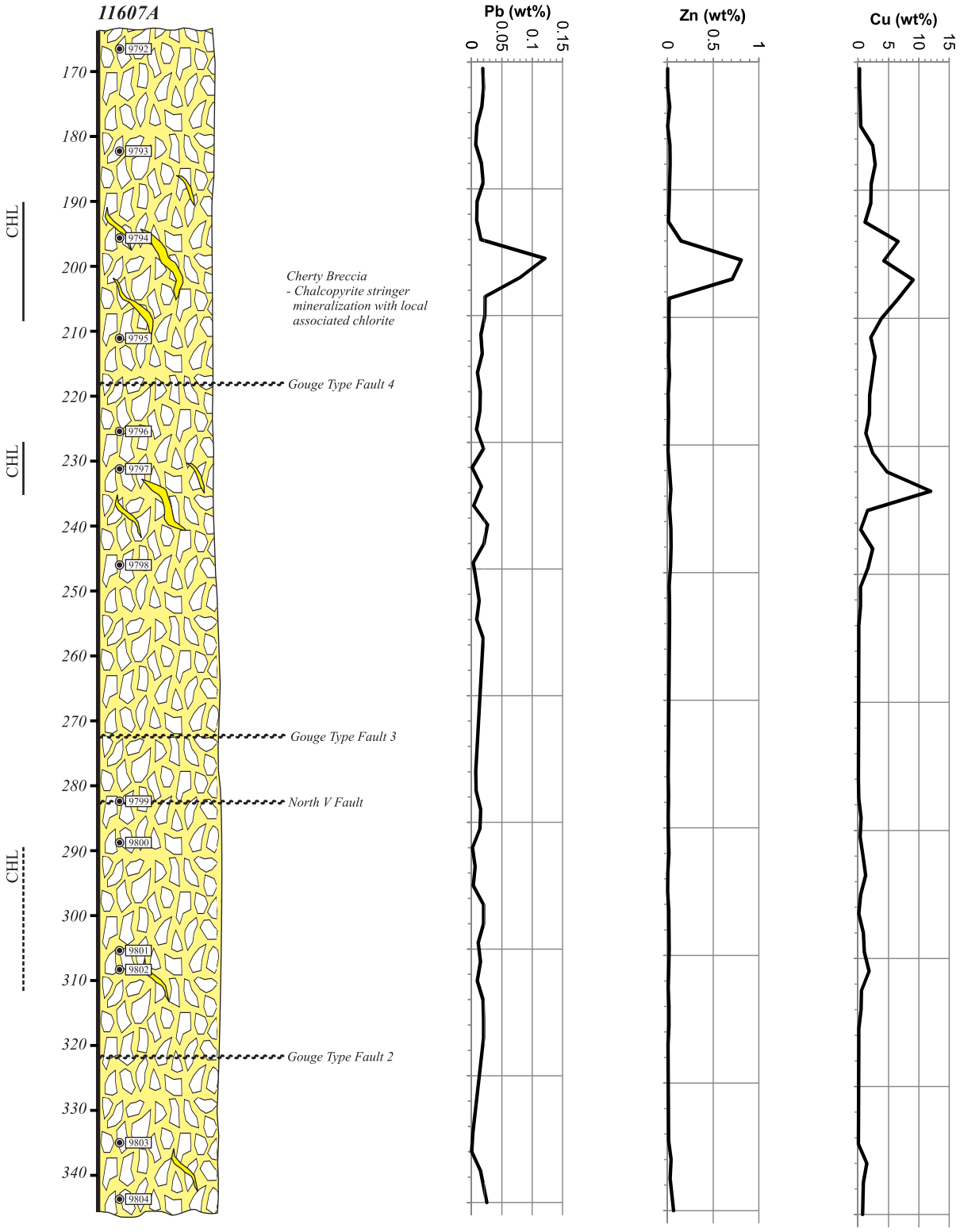


Figure 4.8 Drill-hole lithological profile and concentrations of Pb, Zn, and Cu in core from hole 11607A through the Cu-rich Stringer Zone.

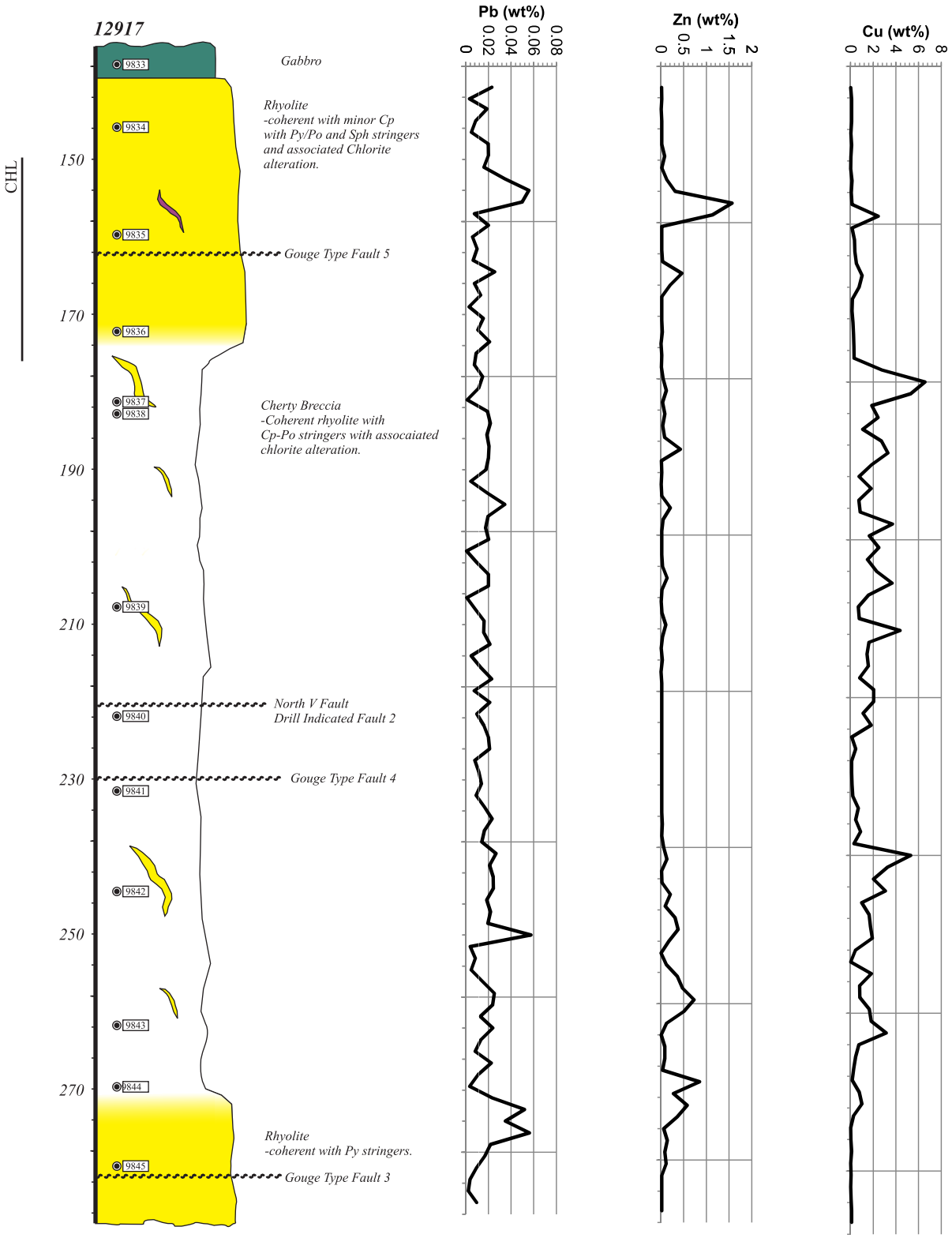


Figure 4.9 Drill-hole lithological profile and concentrations of Pb, Zn, and Cu in core from hole 12917 through the Cu-rich Stringer Zone.

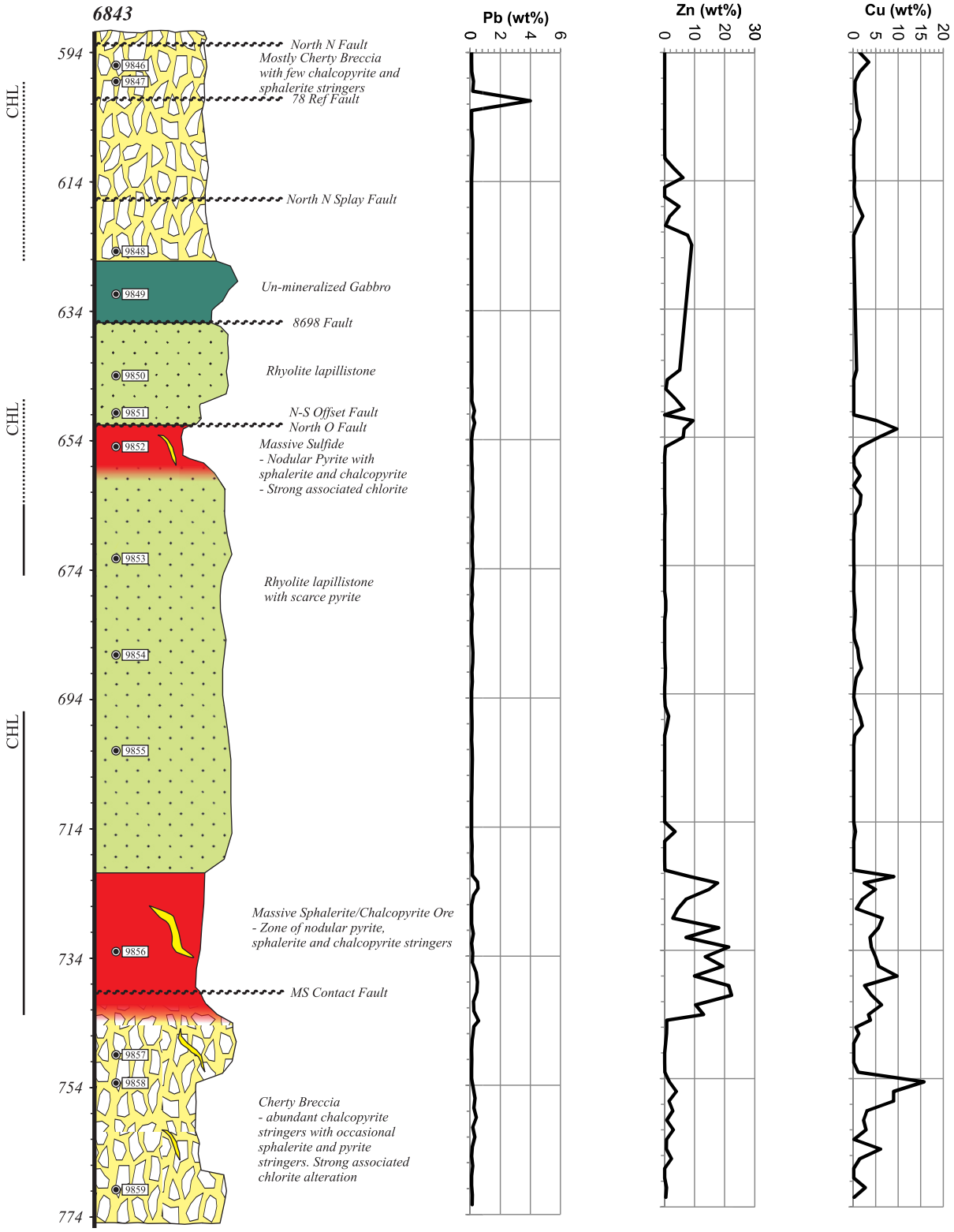


Figure 4.10 Drill-hole lithological profile and concentrations of Pb, Zn, and Cu in core from hole 6843 through the Main orebody. It is a very steep hole and was therefore not used for mineral distributions on 9500 level.

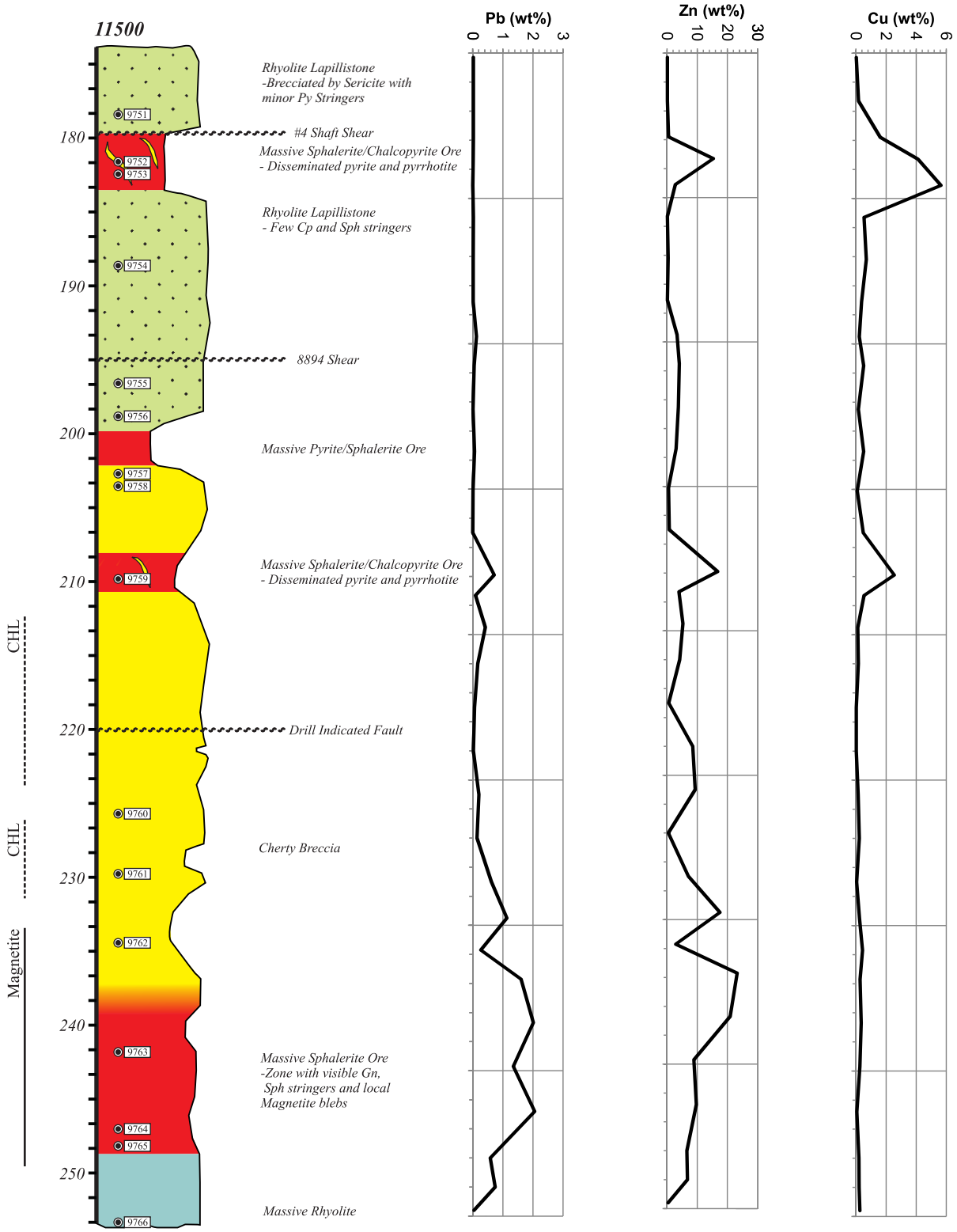


Figure 4.11 Drill-hole lithological profile and concentrations of Pb, Zn, and Cu in core from hole 11500 through the South Lens.

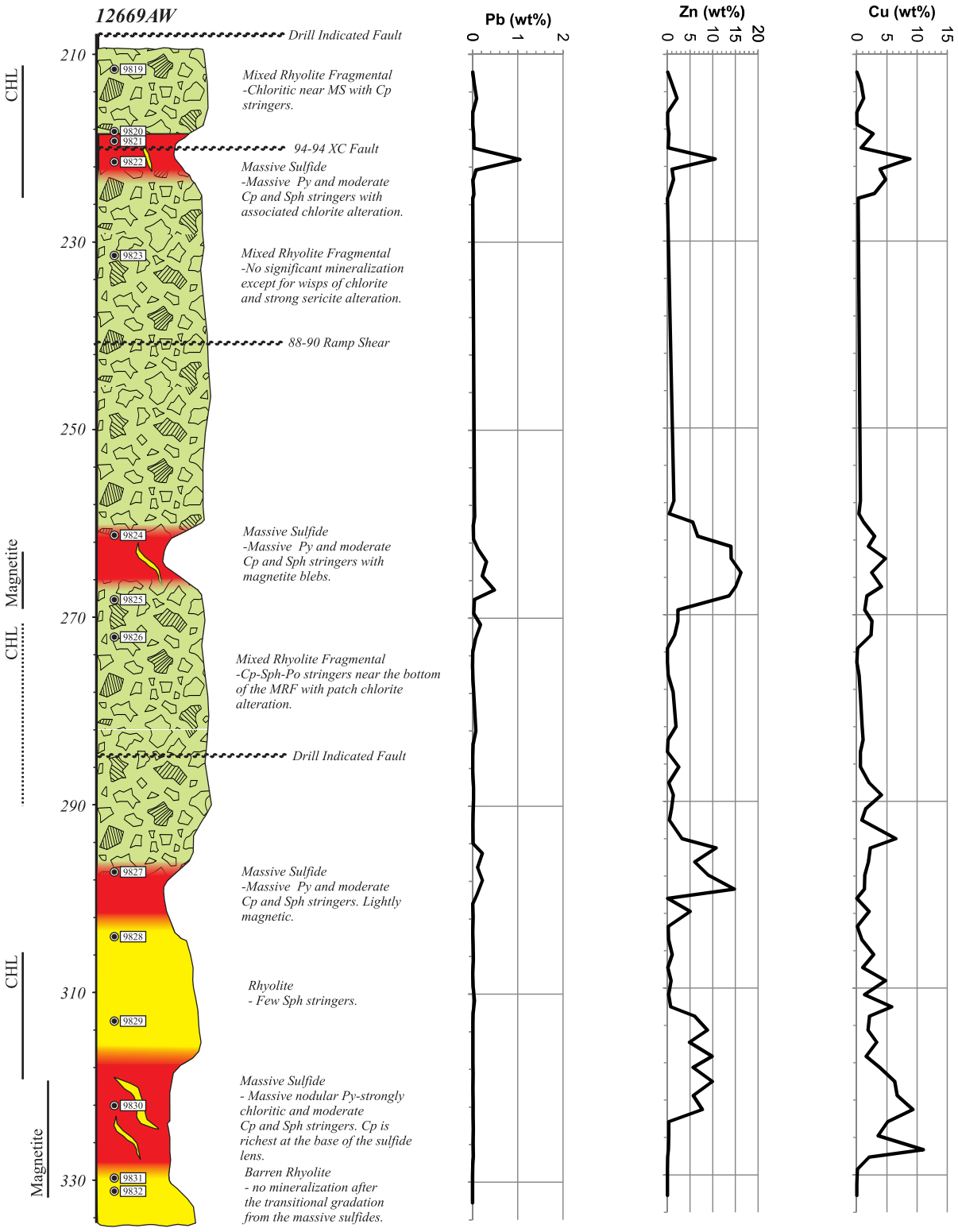


Figure 4.12 Drill-hole lithological profile and concentrations of Pb, Zn, and Cu in core from hole 12669AW through the South Lens. ICP was not run on the samples from this hole.

*11432*

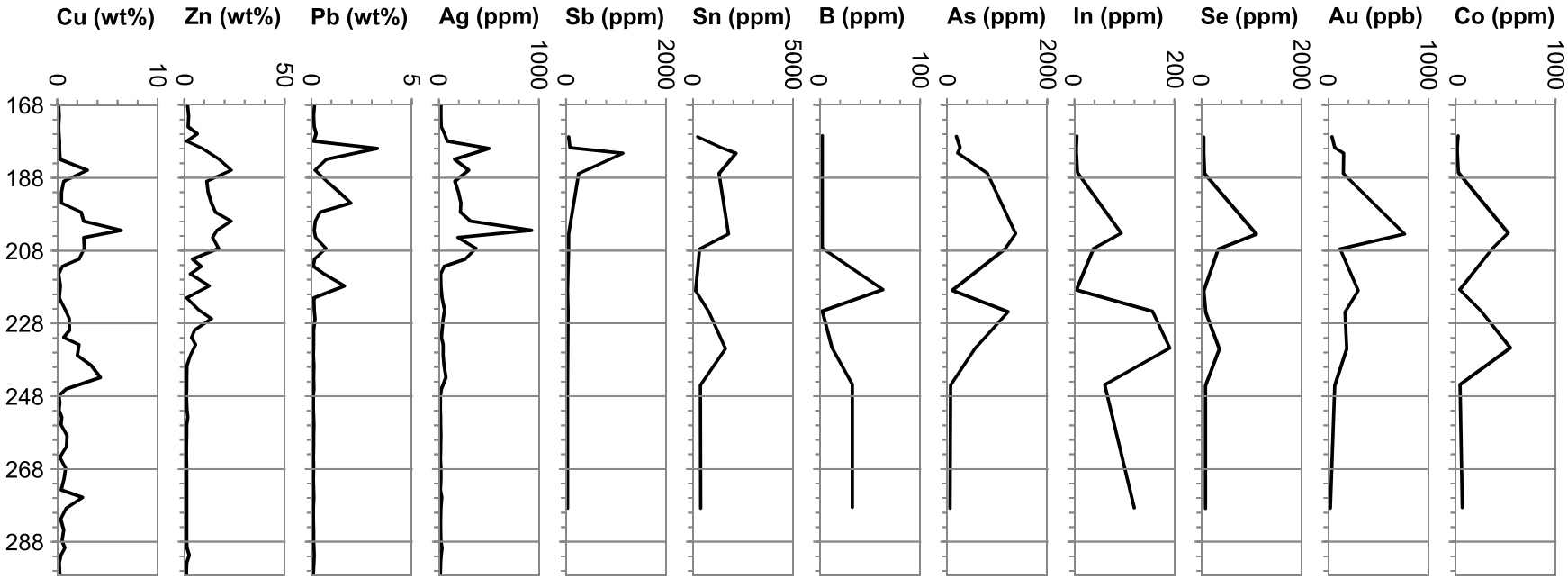


Figure 4.13 Major and trace element concentrations in core from hole 11432 through the Main orebody. Cu, Zn, Pb and Ag are from Mine Assays and the trace elements are from Appendix I.

*11074A*

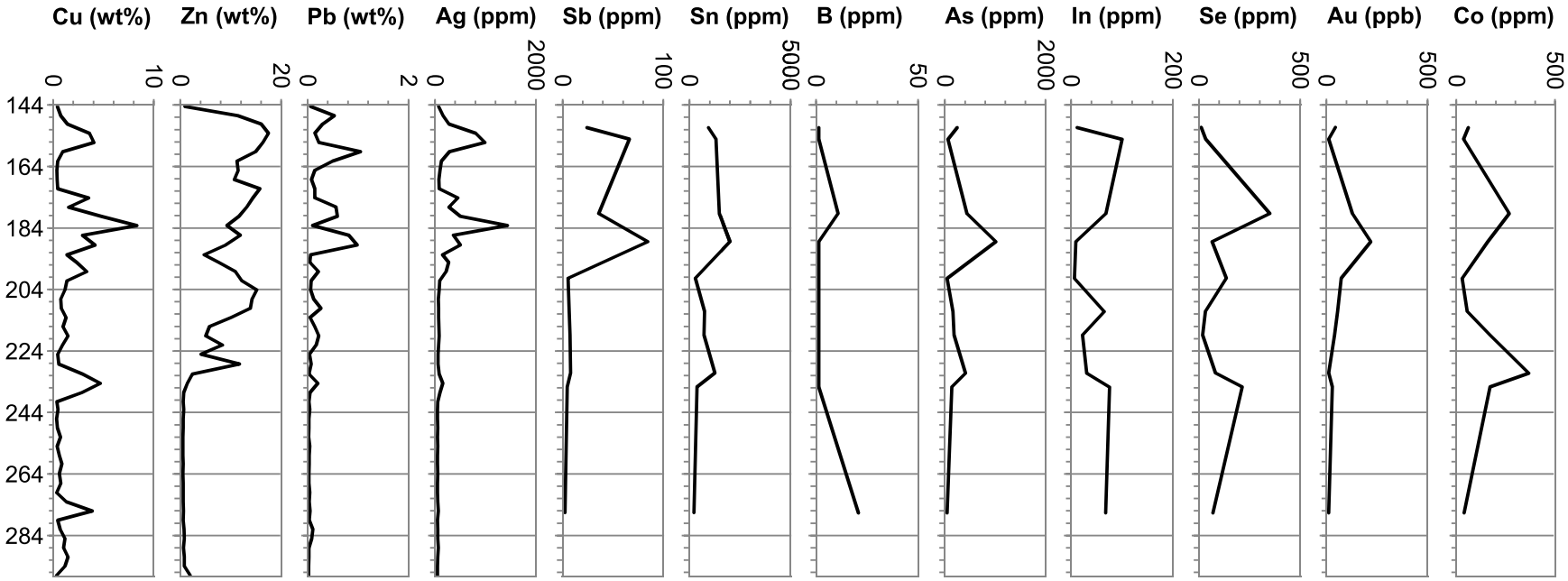


Figure 4.14 Major and trace element concentrations in core from hole 11074A through the Main orebody. Cu, Zn, Pb and Ag are from Mine Assays and the trace elements are from Appendix I.

*11586B*

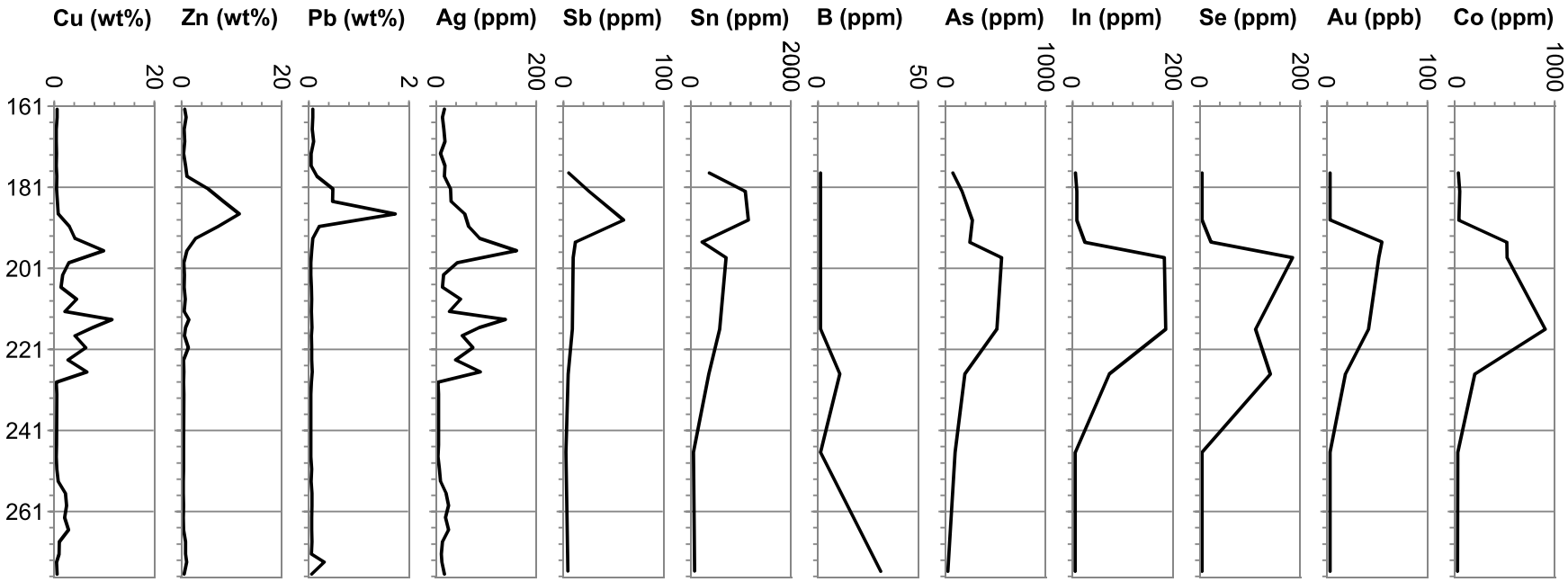


Figure 4.15 Major and trace element concentrations in core from hole 11586B through the Main orebody. Cu, Zn, Pb and Ag are from Mine Assays and the trace elements are from Appendix I.

*11299A*

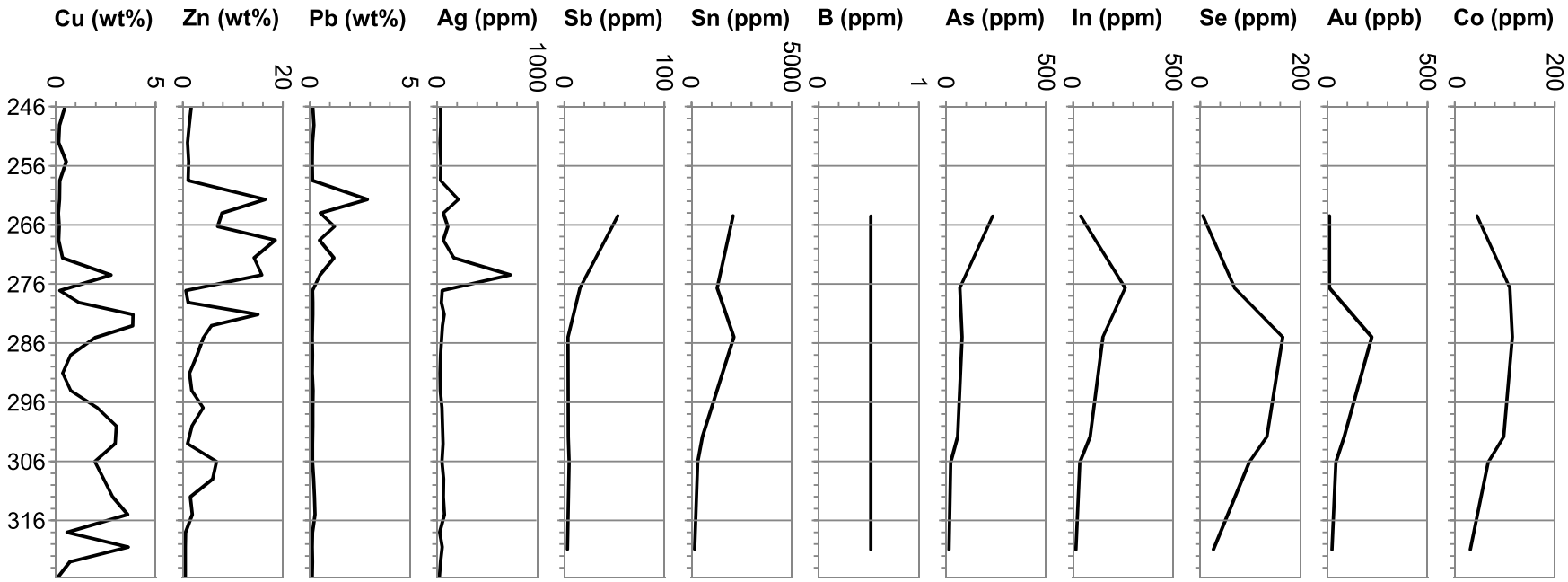


Figure 4.16 Major and trace element concentrations in core from hole 11299A through the Main orebody. Cu, Zn, Pb and Ag are from Mine Assays and the trace elements are from Appendix I.

*11363*

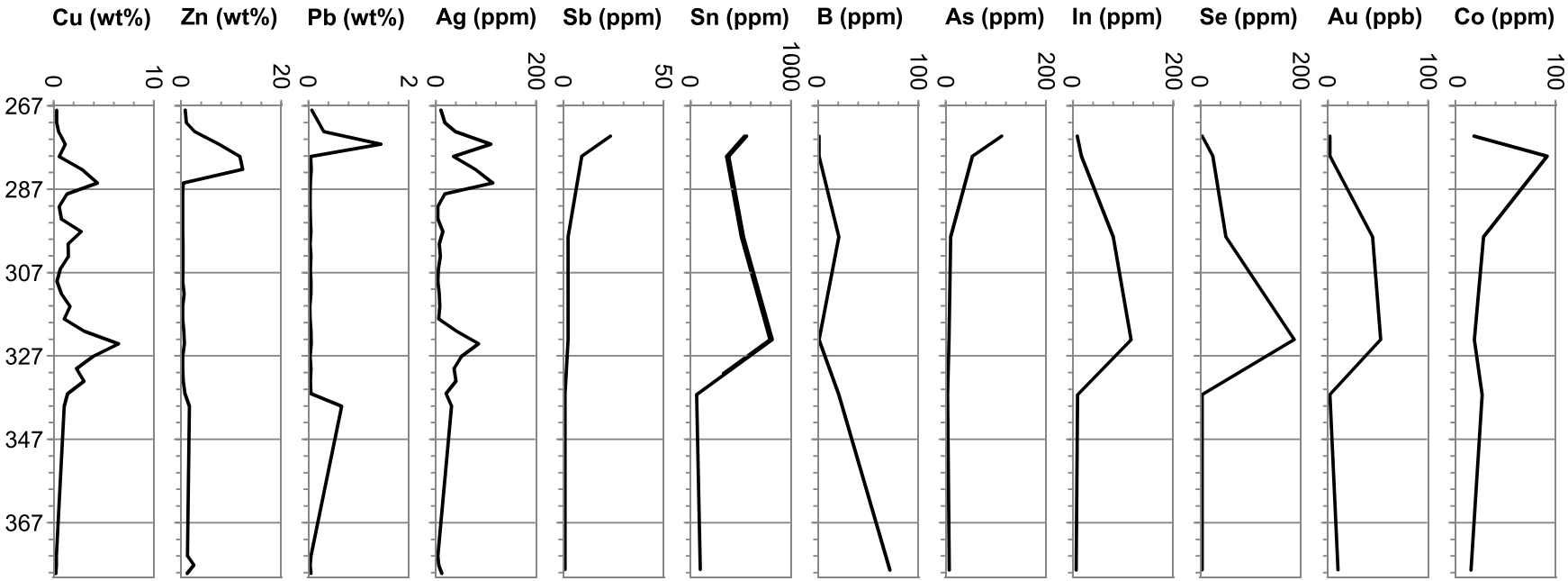


Figure 4.17 Major and trace element concentrations in core from hole 11363 through the Main orebody. Cu, Zn, Pb and Ag are from Mine Assays and the trace elements are from Appendix I.

*11607A*

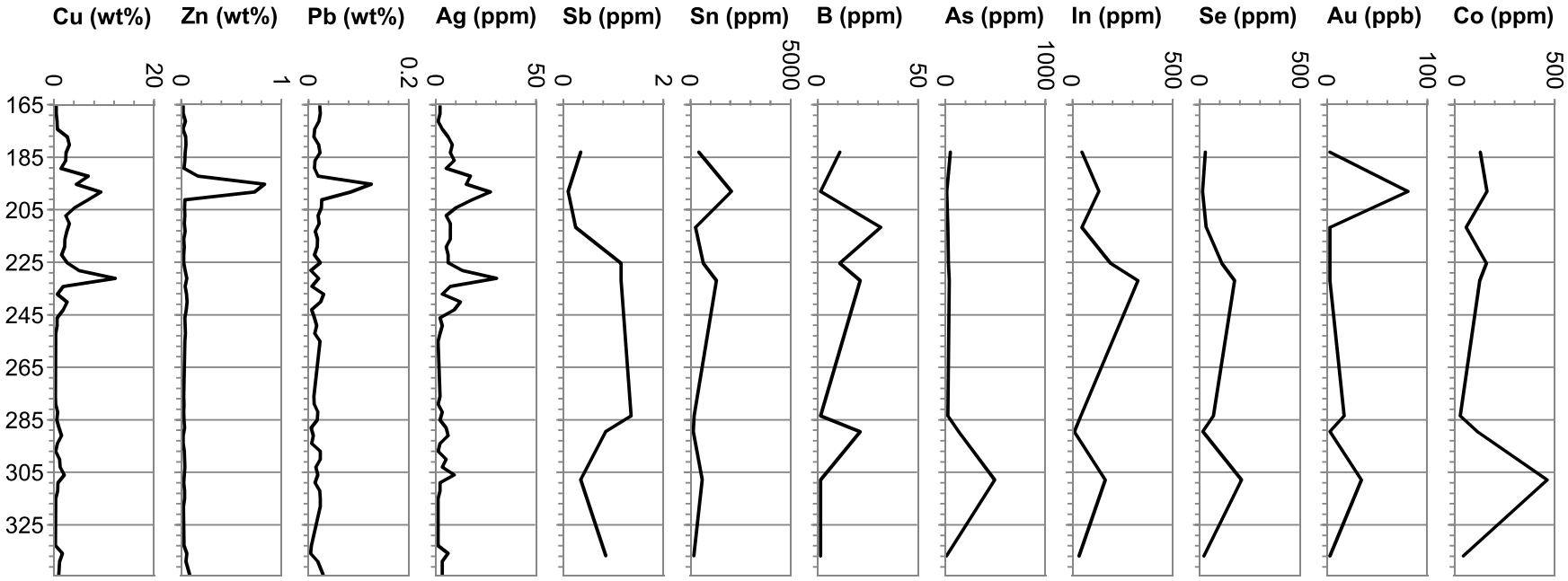


Figure 4.18 Major and trace element concentrations in core from hole 11607A through the Cu-rich stringer zone. Cu, Zn, Pb and Ag are from Mine Assays and the trace elements are from Appendix I.

*12917*

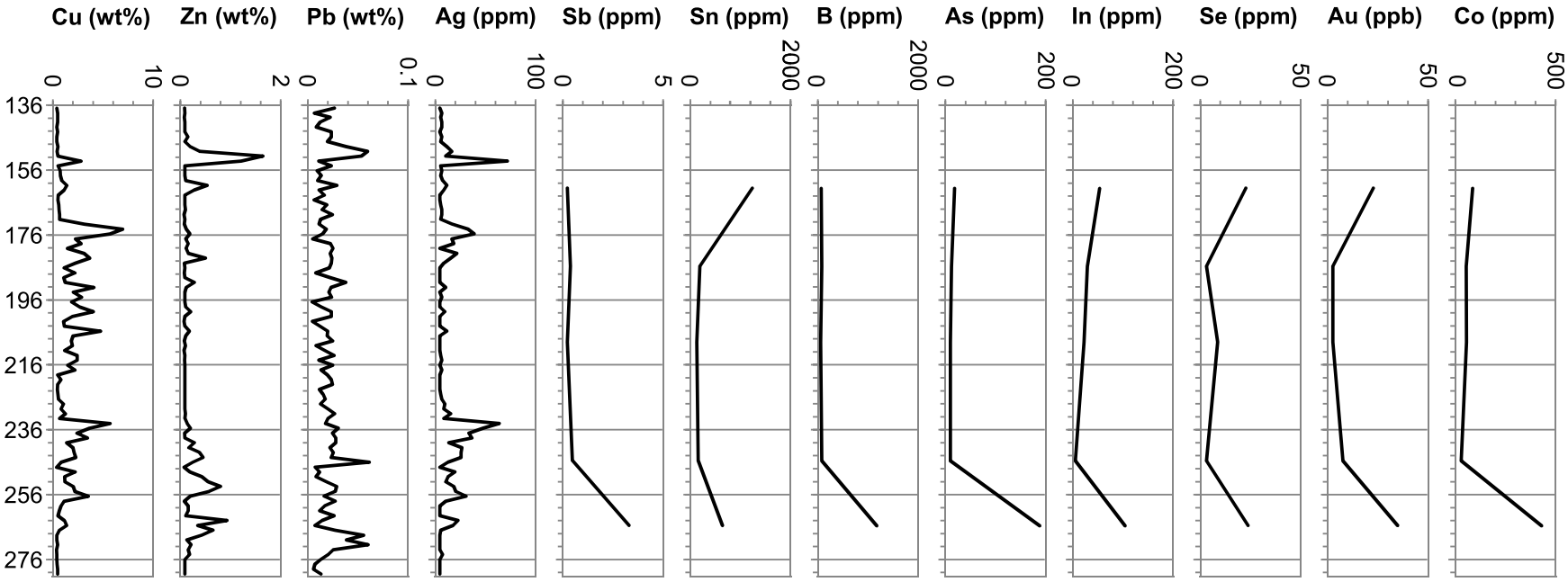


Figure 4.19 Major and trace element concentrations in core from hole 12917 through the Cu-rich stringer zone. Cu, Zn, Pb and Ag are from Mine Assays and the trace elements are from Appendix I.

*6843*

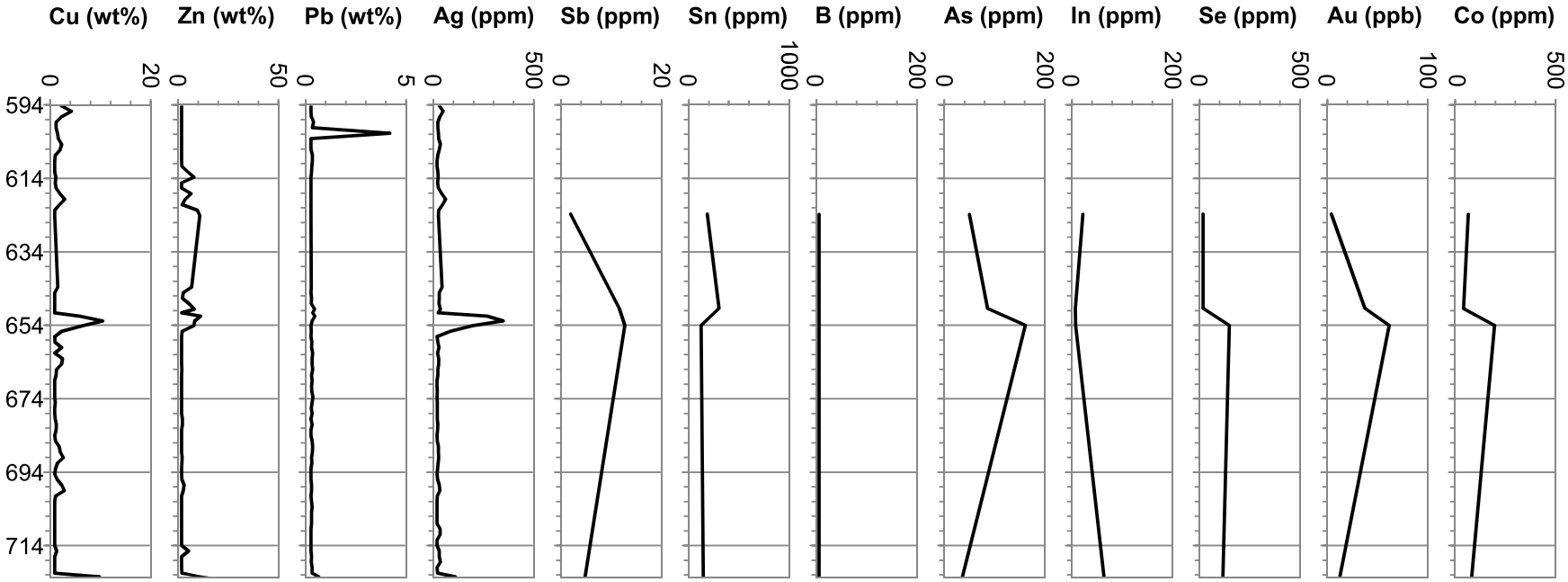


Figure 4.20 Major and trace element concentrations in core from hole 6843 through the Main orebody. Cu, Zn, Pb and Ag are from Mine Assays and the trace elements are from Appendix I.

*11500*

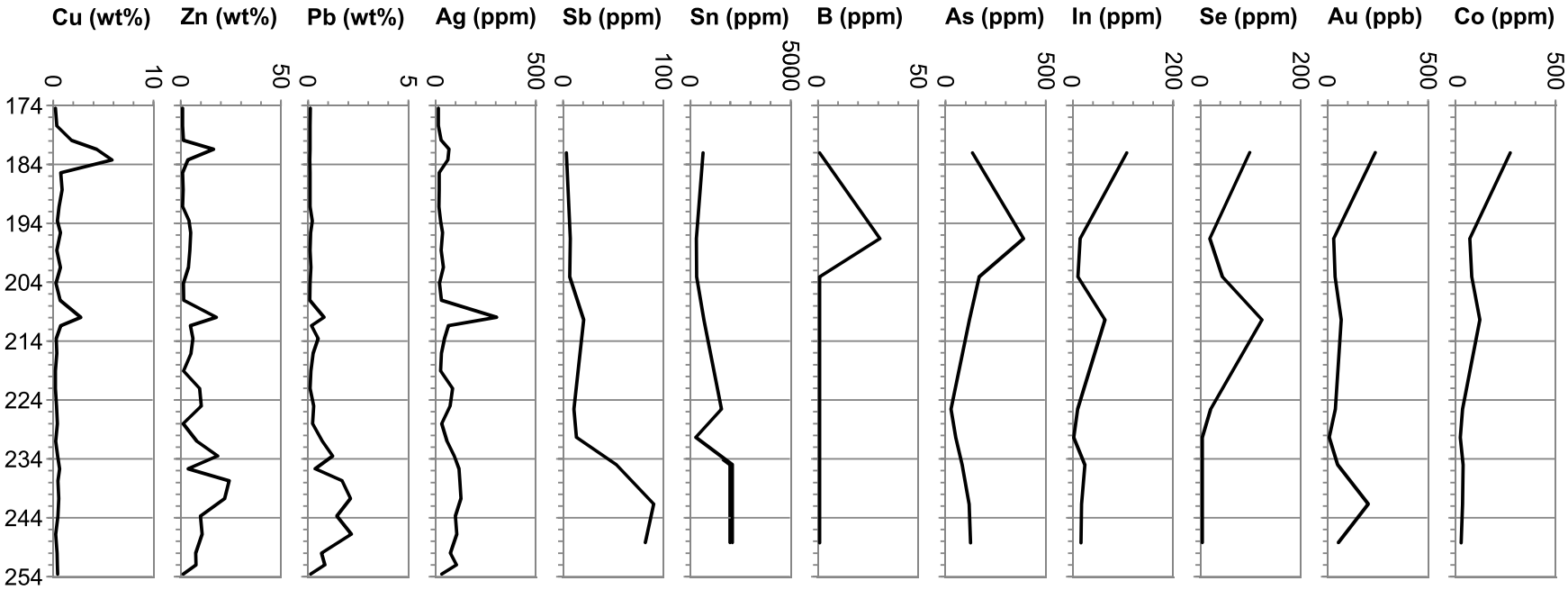


Figure 4.21 Major and trace element concentrations in core from hole 11500 through the South Lens. Cu, Zn, Pb and Ag are from Mine Assays and the trace elements are from Appendix I.

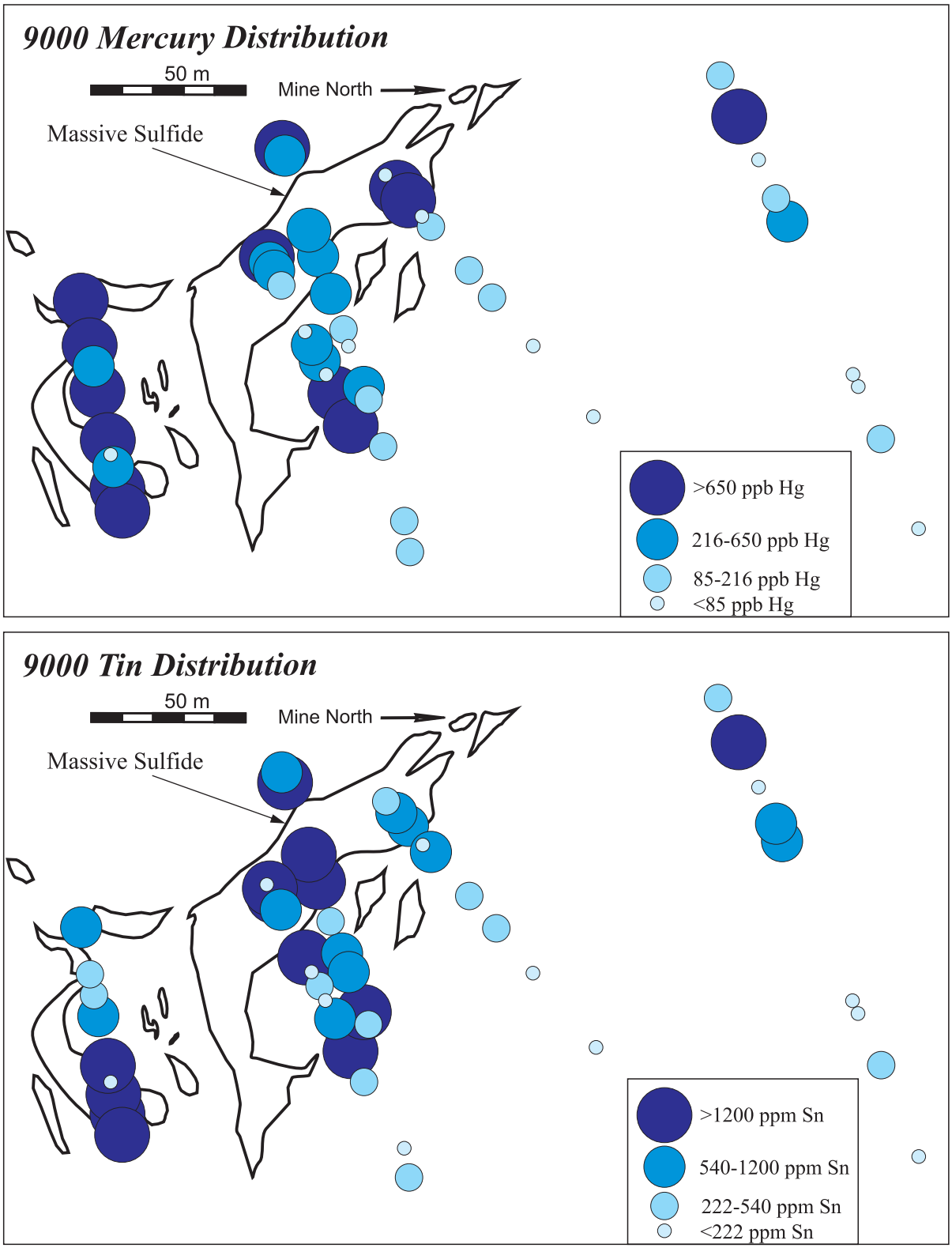


Figure 4.22 Bubble plots showing the distribution of mercury and tin in samples projected onto the 9000 level of the Main, West and South lenses and the Cu-rich stringer zone. Samples are grouped by quartiles. Data is from Appendix I.

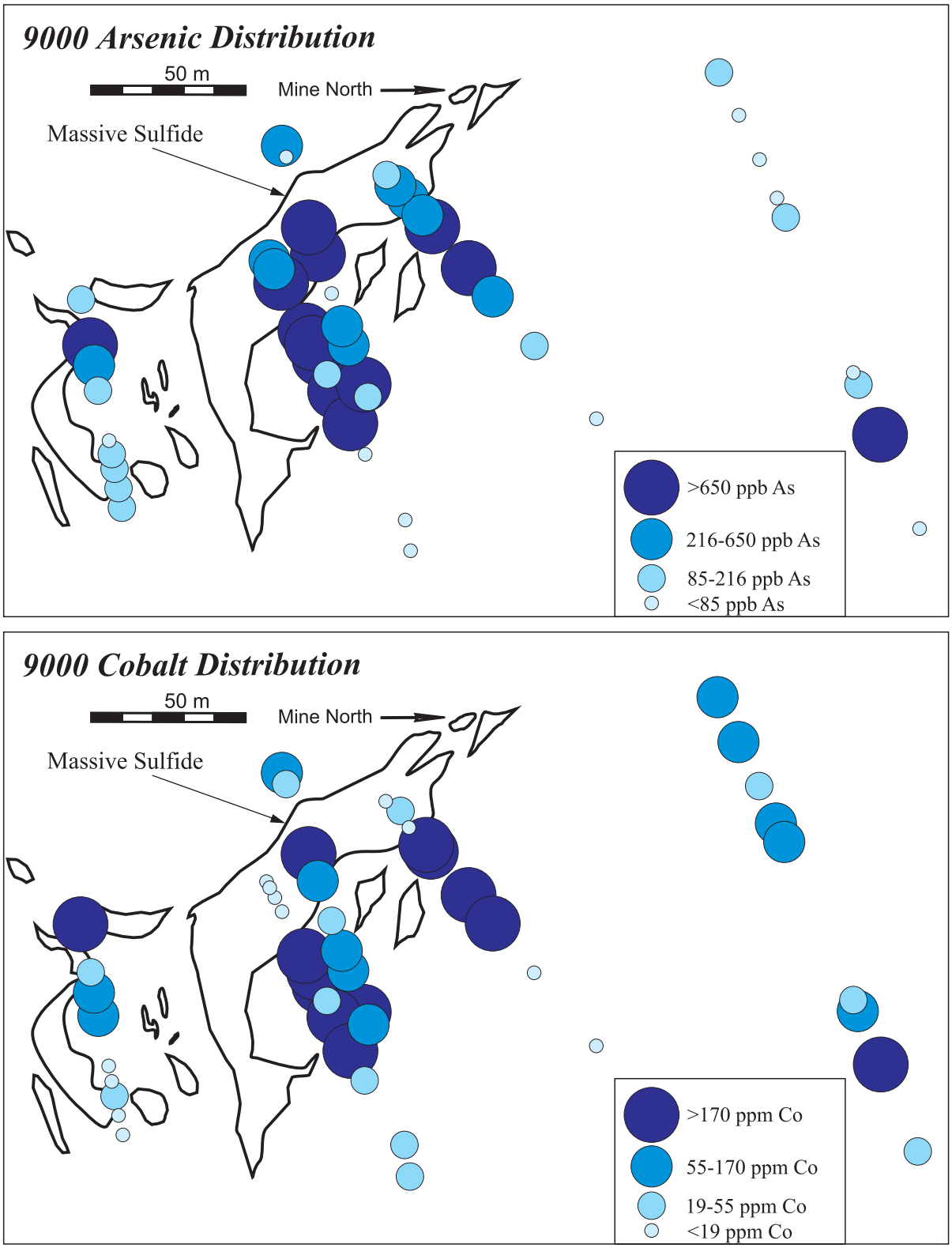


Figure 4.23 Bubble plots showing the distribution of arsenic and cobalt in samples projected onto the 9000 level of the Main, West and South lenses and the Cu-rich stringer zone. Samples are grouped by quartiles. Data is from Appendix I.

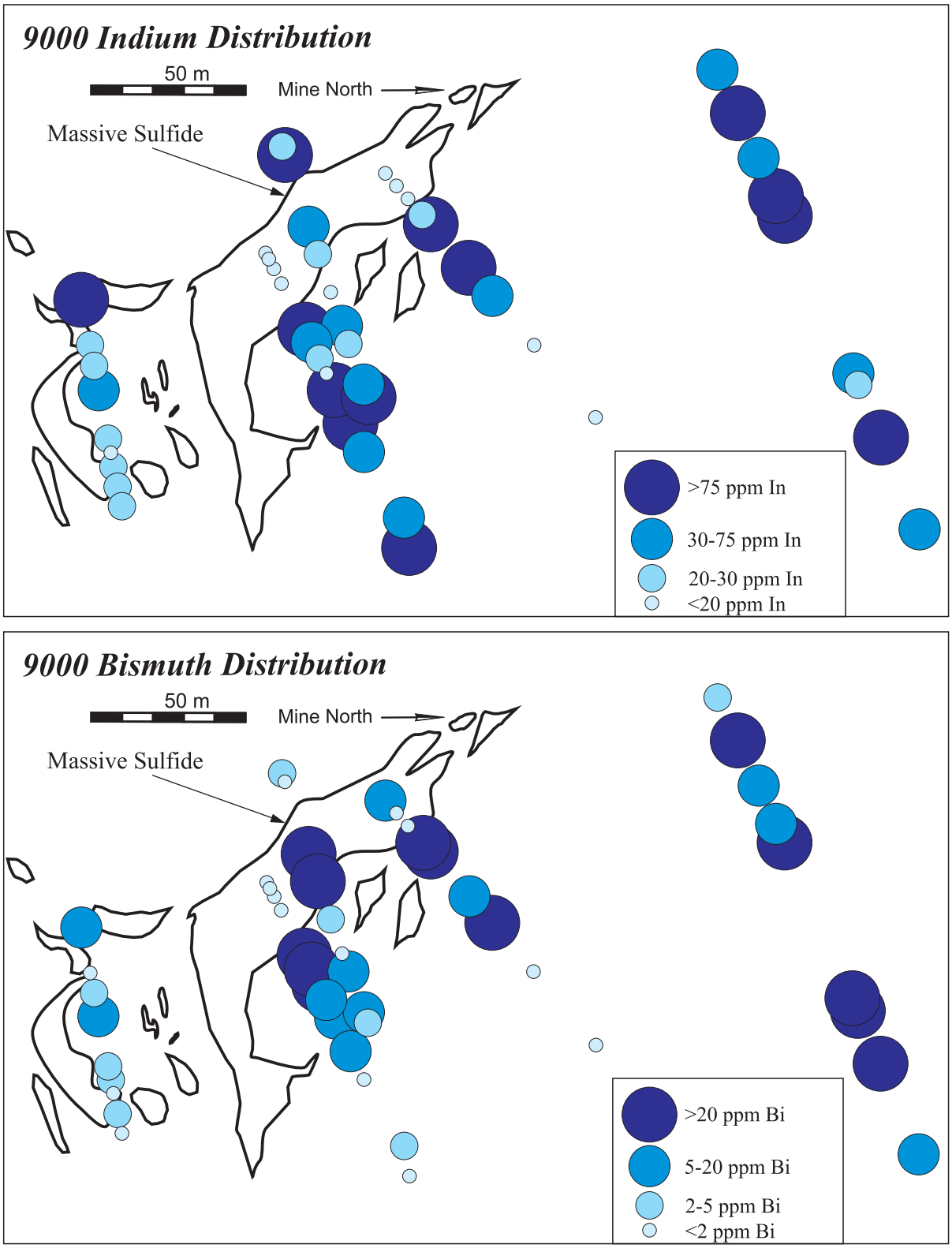


Figure 4.24 Bubble plots showing the distribution of indium and bismuth in samples projected onto the 9000 level of the Main, West and South lenses and the Cu-rich stringer zone. Samples are grouped by quartiles. Data is from Appendix I.

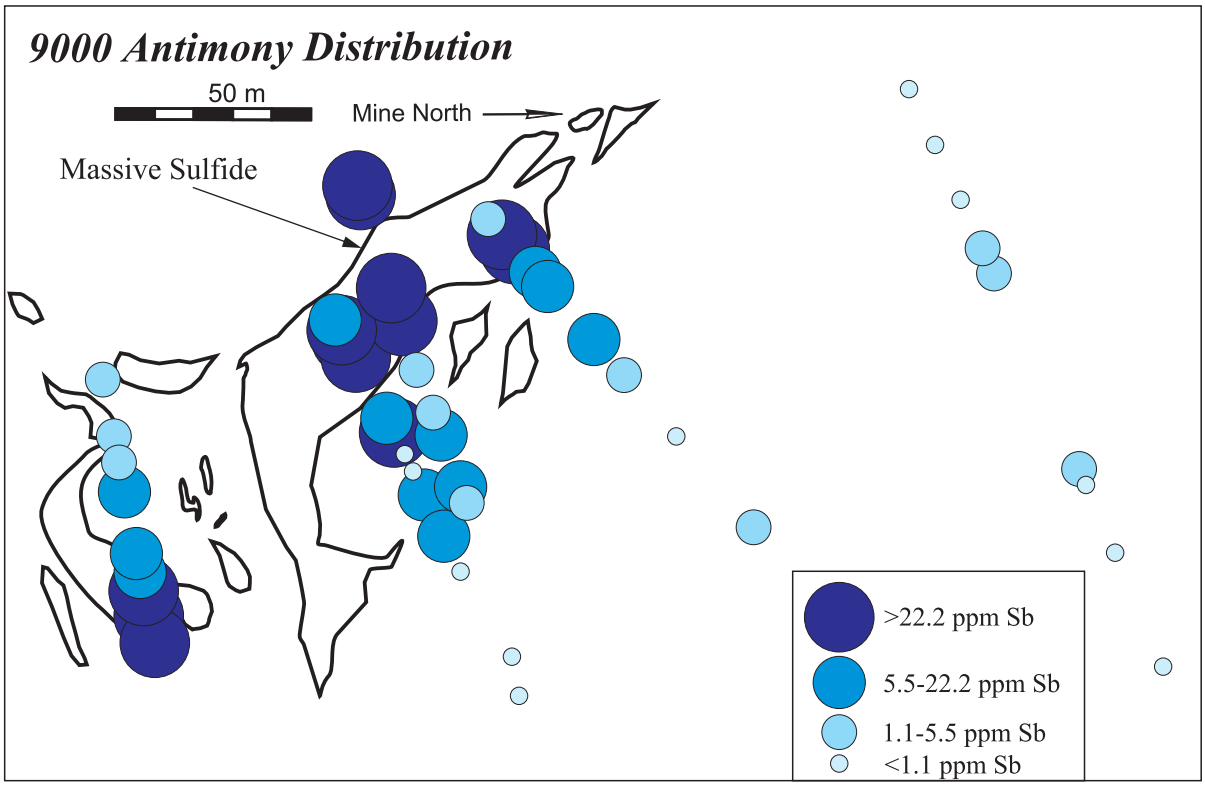


Figure 4.25 Bubble plots showing the distribution of antimony in samples projected onto the 9000 level of the Main, West and South lenses and the Cu-rich stringer zone. Samples are grouped by quartiles. Data is from Appendix I.

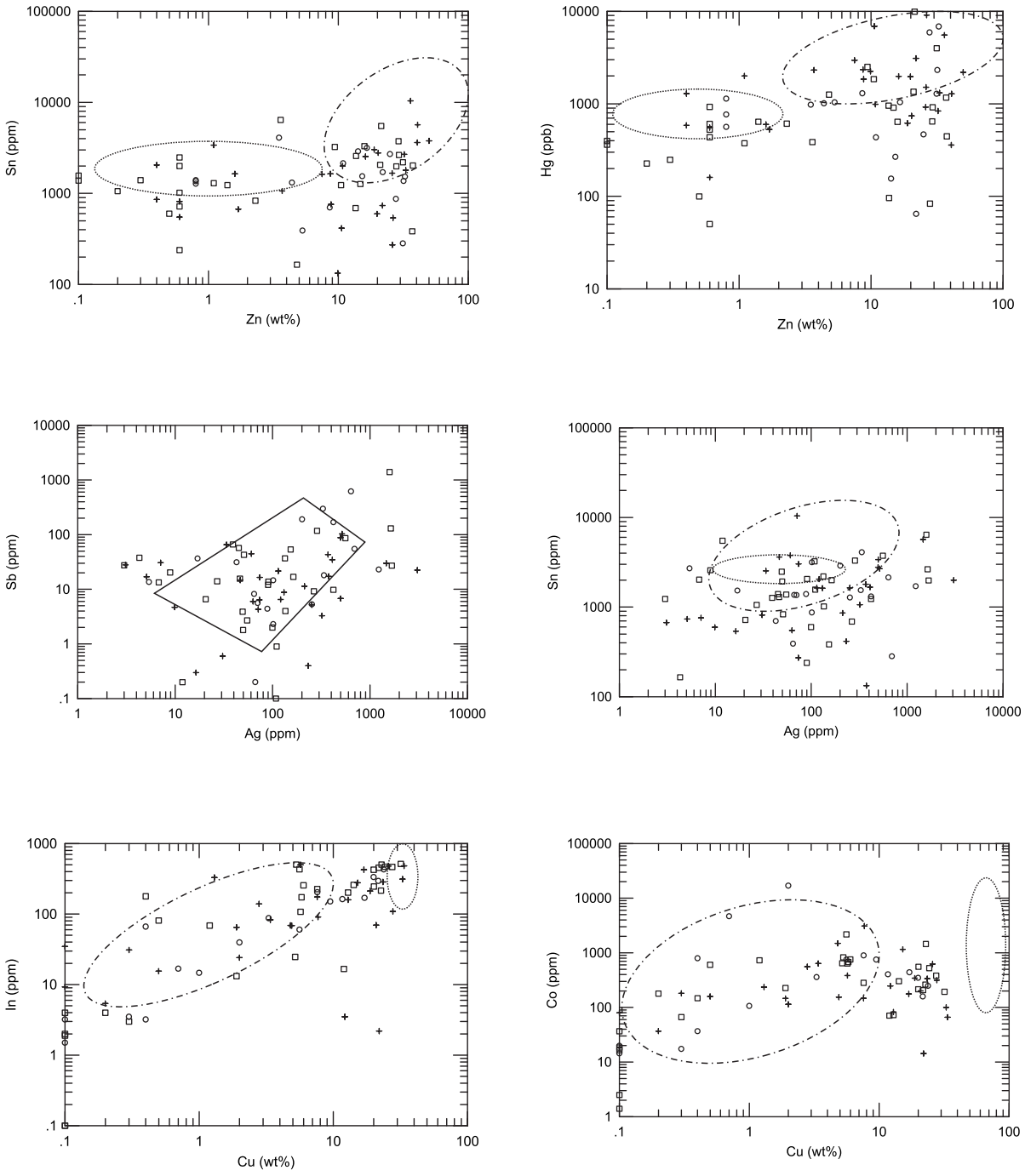


Figure 4.26 Interelement plots of selected ore metals and trace elements from the Zn-rich and Cu-rich zones of Mine D. Squares = > 4 wt% Zn, Crosses => 2 wt% Cu, and Circles = both (*n*-75). Clear correlations are seen between Zn and Sn, Hg, Cd, Sb, and Ag and between Cu and Co, In, Bi, and Se. All values have been normalized to 100% sulfides by dividing all elements by the sum of Fe, S, Cu, Zn, and Pb. Dashed ellipse represents approximate field of Zn-rich assemblages from the upper mine. Dotted ellipse represents approximate field of Cu-rich assemblages from the upper mine. Solid polygon represents approximate field of both Zn-rich and Cu-rich assemblages from the upper mine.(Hannington et al, 1999).

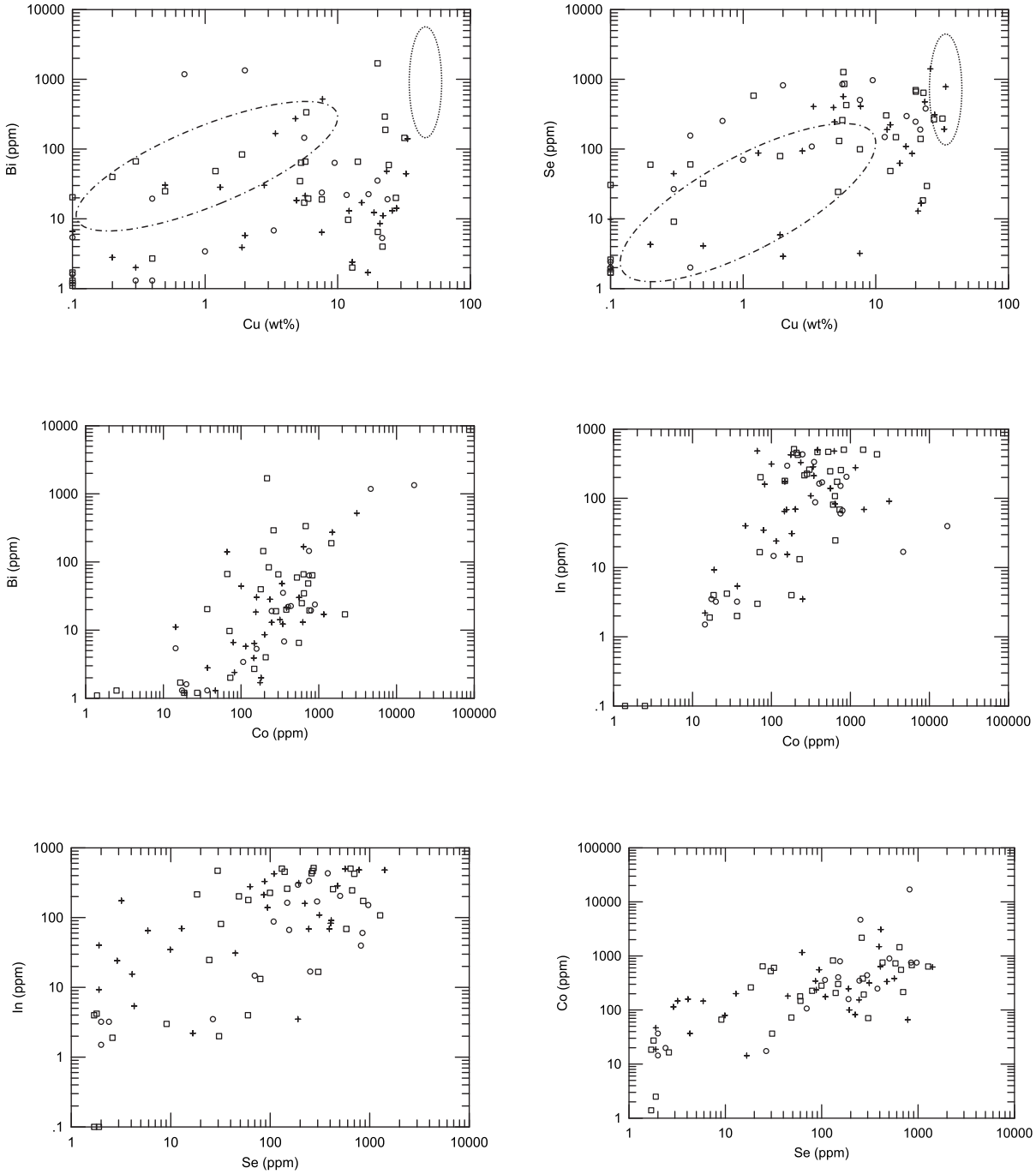


Figure 4.27 Interelement plots of selected ore metals and trace elements from the Zn-rich and Cu-rich zones of Mine D. Squares = > 4 wt% Zn, Crosses => 2 wt% Cu, and Circles = both (*n*-75). Clear correlations are seen between Zn and Sn, Hg, Cd, Sb, and Ag and between Cu and Co, In, Bi, and Se. All values have been normalized to 100% sulfides by dividing all elements by the sum of Fe, S, Cu, Zn, and Pb. Dashed ellipse represents approximate field of Zn-rich assemblages from the upper mine. Dotted ellipse represents approximate field of Cu-rich assemblages from the upper mine. Solid polygon represents approximate field of both Zn-rich and Cu-rich assemblages from the upper mine.(Hannington et al, 1999).

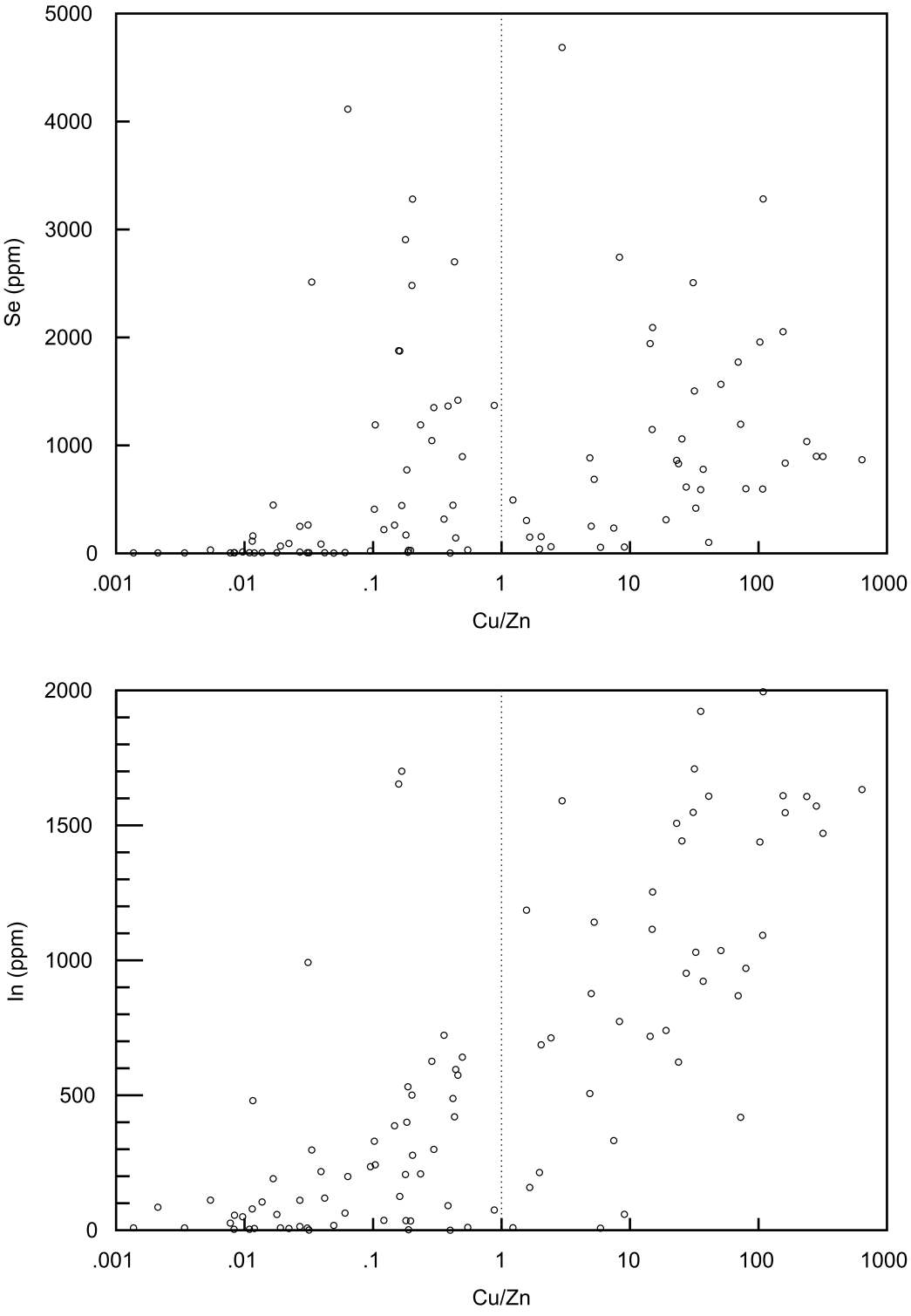


Figure 4.28 Plots of concentrations of In and Se versus Cu/Zn ratio in ores from the West, Main, and South lenses and the Cu-rich stringer zone of Mine D (n=75) normalized to 100 percent sulfide for all elements. It exhibits a strong coenrichment with Cu and is highest in the most Cu-rich ores. Se, unlike in the upper mine (hannington et al, 1999) has a fairly uniform enrichment throughout the Cu/Zn spectrum. This may be due to overprinting.

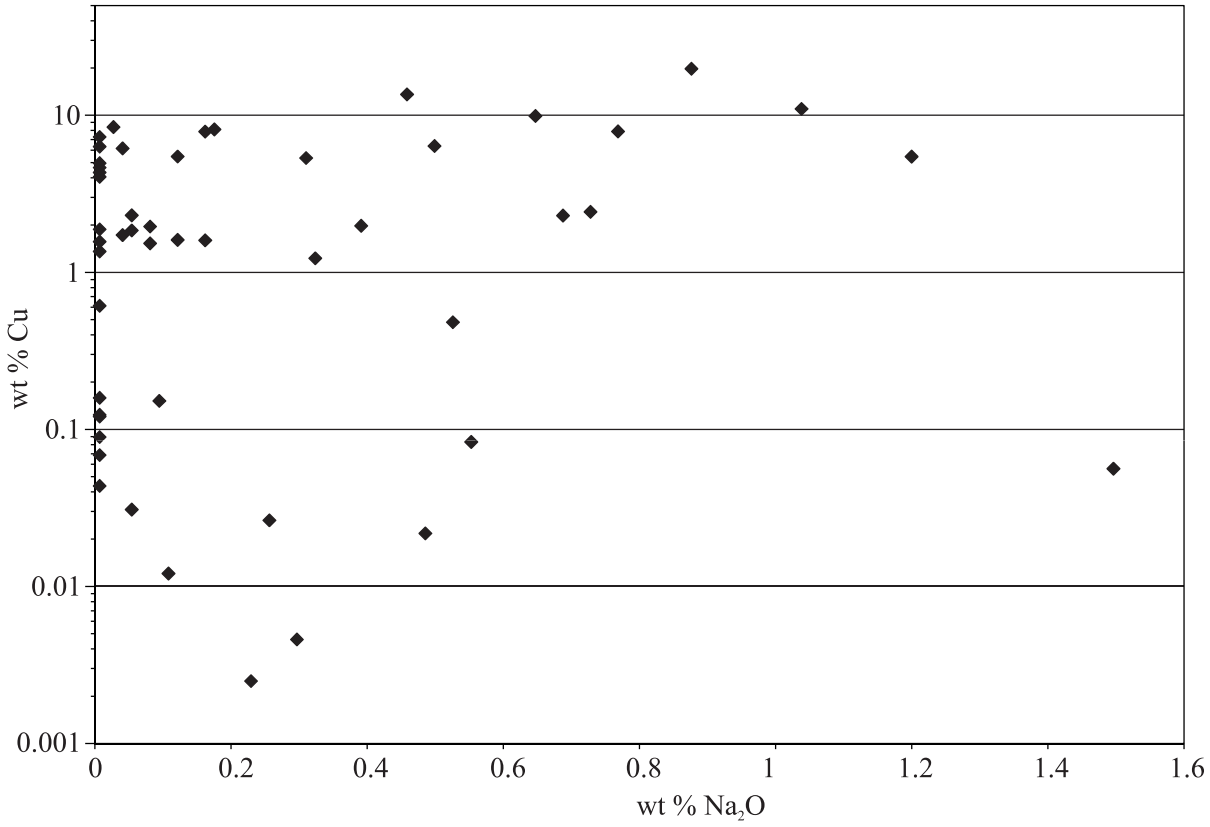


Figure 4.29 Plot of Na enrichment versus Cu in the most Cu-rich samples of Mine D. This is coincident with data from the upper mine (n=50).

Table 4.1 Chemical Compositions of Representative Ore Samples from the Main orebody

| | | HW Frag | Py Stringer | Sph Stringer | Massive Py | Massive Sph | Massive Sph-Cp | Sph-Cp Stringer | Massive Cp | Cp Stringer |
|---|---|---|---|---|---|---|---|---|---|---|
| | *n* | 6 | 2 | 5 | 2 | 3 | 9 | 4 | 1 | 17 |
| Fe | (wt %) | 22.3 | 23.4 | 11.1 | 31.7 | 35.0 | 21.3 | 10.0 | 22.7 | 11.1 |
| Cu | (wt %) | 0.13 | 0.06 | 0.41 | 3.18 | 0.05 | 5.12 | 3.35 | 19.8 | 5.05 |
| Zn | (wt %) | 5.45 | 0.21 | 5.84 | 0.44 | 8.16 | 12.4 | 8.42 | 0.03 | 0.69 |
| S | (wt %) | 23.3 | 24.1 | 9.81 | 24.1 | 37.2 | 20.2 | 10.1 | 19.6 | 6.52 |
| $SiO_2$ | (wt %) | 34.0 | 39.2 | 61.2 | 30.6 | 5.87 | 23.0 | 53.4 | 20.0 | 60.3 |
| $TiO_2$ | (wt %) | 4.47 | 5.56 | 5.10 | 1.68 | 0.51 | 4.26 | 4.69 | 8.39 | 6.94 |
| $Al2O_3$ | (wt %) | 0.25 | 1.54 | 0.71 | 0.06 | 0.06 | 0.18 | 0.50 | 0.06 | 1.24 |
| $K_2O$ | (wt %) | 0.39 | 0.12 | 0.25 | 0.35 | 0.04 | 0.27 | 0.25 | 0.88 | 0.24 |
| $Na_2O$ | (wt %) | 1.43 | 0.19 | 0.44 | 0.15 | 0.83 | 0.63 | 1.70 | 0.13 | 0.19 |
| CaO | (wt %) | 1.61 | 0.30 | 0.92 | 0.41 | 0.50 | 2.59 | 2.52 | 3.47 | 1.37 |
| MgO | (wt %) | 0.10 | 0.05 | 0.06 | <0.01 | <0.01 | 0.09 | 0.04 | 0.07 | 0.07 |
| $CO_2$ | (wt %) | 1.77 | 0.93 | 0.40 | 4.33 | 4.65 | 4.09 | 2.52 | 0.13 | 1.40 |
| Mn | (wt %) | 0.10 | 0.11 | 0.04 | 0.17 | 0.13 | 0.28 | 0.11 | 0.02 | 0.10 |
| B | (ppm) | <10.0 | 17.5 | 21.0 | <10.0 | <10.0 | <10.0 | 30.0 | 20.0 | 76.8 |
| ∑REE | (ppm) | 100 | 85.4 | 93.3 | 29.2 | 26.8 | 59.0 | 51.7 | 97 | 96.1 |
| Pb | (ppm) | 0.09 | 0.15 | 0.04 | 0.03 | 2.77 | 0.23 | 0.13 | 0.01 | 0.06 |
| Ag | (ppm) | 10.5 | 21.8 | <5.00 | 44.5 | 429 | 524 | 79.0 | 31.0 | 38.3 |
| Sn | (ppm) | 573 | 655 | 595 | 360 | 2397 | 955 | 1390 | 1200 | 396 |
| Cd | (ppm) | 307 | <2.00 | 407 | 23.0 | 300 | 592 | 492 | 5.00 | 33.0 |
| Sb | (ppm) | 18.0 | 27.0 | 4.30 | 7.90 | 394 | 26.4 | 13.3 | 1.10 | 1.11 |
| W | (ppm) | 9.30 | 12.5 | 5.19 | 5.23 | 13.6 | 4.67 | 3.41 | 3.00 | 3.94 |
| Ga | (ppm) | 19.4 | 11.2 | 24.1 | 8.70 | 9.37 | 38.4 | 34.3 | 28.3 | 19.2 |
| Tl | (ppm) | 10.4 | 24.5 | 0.46 | 0.95 | 7.13 | 1.62 | 3.31 | <0.10 | 0.74 |
| In | (ppm) | 12.0 | <0.20 | 28.6 | 98.6 | 2.37 | 82.4 | 126 | 320 | 69.7 |
| Bi | (ppm) | 2.67 | <2.00 | 2.80 | 17.0 | <2.00 | 18.6 | 40.5 | 90.0 | 28.7 |
| As | (ppm) | 101 | 106 | 73.2 | 360 | 184 | 460 | 454 | 30.2 | 52.1 |
| Co | (ppm) | 33.1 | 1.55 | 61.7 | 698 | 13.7 | 218 | 203 | 120 | 103 |
| Se | (ppm) | 4.92 | <3.00 | 11.0 | 63.0 | <3.00 | 237 | 243 | 170 | 67.7 |
| Ni | (ppm) | <10.0 | <10.0 | <10.0 | <10.0 | <10.0 | 26.7 | 16.3 | <10.0 | <10.0 |
| V | (ppm) | 16.3 | 24.0 | 9.30 | 24.0 | 24.3 | 18.7 | 13.5 | 11.0 | 5.88 |
| Hg | (ppb) | 799 | 128 | 864 | 96.5 | 884 | 632 | 928 | <5.00 | 310 |
| Au | (ppb) | 3.67 | 23.0 | 27.4 | 45.5 | 44.7 | 147 | 139 | <2.00 | 23.6 |

Table 4.2 Average Chemical Compositions of Representative Ore Samples from the South Lens, Mine D

| | | Py Stringer | Sph Stringer | Massive Sph | Massive Sph-Cp |
|---|---|---|---|---|---|
| | *n* | 1 | 2 | 4 | 2 |
| Fe | (wt %) | 15.8 | 9.65 | 24.7 | 16.6 |
| Cu | (wt %) | 0.09 | 0.39 | 0.32 | 5.38 |
| Zn | (wt %) | 0.46 | 7.75 | 13.6 | 17.9 |
| S | (wt %) | 5.21 | 5.56 | 24.4 | 18.4 |
| $SiO_2$ | (wt %) | 52.4 | 55.9 | 19.8 | 24.2 |
| $TiO_2$ | (wt %) | 0.12 | 0.13 | 0.03 | 0.05 |
| $Al2O_3$ | (wt %) | 7.54 | 6.09 | 1.17 | 2.63 |
| $K_2O$ | (wt %) | 0.72 | 0.45 | 0.11 | 0.06 |
| $Na_2O$ | (wt %) | 0.34 | 0.07 | 0.12 | 0.26 |
| CaO | (wt %) | 0.15 | 0.41 | 0.75 | 1.43 |
| MgO | (wt %) | 2.79 | 3.05 | 1.31 | 2.08 |
| $CO_2$ | (wt %) | 3.13 | 1.54 | 4.48 | 4.40 |
| Mn | (wt %) | 0.11 | 0.11 | 0.152 | 0.37 |
| B | (ppm) | <10.0 | 15.3 | <10.0 | <10.0 |
| ∑REE | (ppm) | 112 | 119 | 36.7 | 55.8 |
| Pb | (ppm) | 0.12 | 0.10 | 1.08 | 0.29 |
| Ag | (ppm) | 22.0 | 38.3 | 84.0 | 193 |
| Sn | (ppm) | 193 | 843 | 2900 | 573 |
| Cd | (ppm) | 14.0 | 262 | 549 | 692 |
| Sb | (ppm) | 11.4 | 7.20 | 55.9 | 10.1 |
| W | (ppm) | 1.30 | 5.78 | 3.35 | 1.90 |
| Ga | (ppm) | 17.4 | 26.1 | 22.4 | 35.0 |
| Tl | (ppm) | 1.60 | 0.60 | 1.14 | <0.10 |
| In | (ppm) | <0.20 | 10.5 | 15.1 | 82.8 |
| Bi | (ppm) | 5.00 | 2.50 | <2.00 | 11.0 |
| As | (ppm) | 41.0 | 197 | 113 | 117 |
| Co | (ppm) | 4.90 | 35.0 | 26.8 | 181 |
| Se | (ppm) | <3.00 | 17.0 | 11.4 | 107 |
| Ni | (ppm) | <10.0 | <10.0 | <10.0 | <10.0 |
| V | (ppm) | 6.00 | 9.8 | <5.00 | 5.25 |
| Hg | (ppb) | 30.0 | 856 | 1416 | 3365 |
| Au | (ppb) | <2.00 | 27.0 | 77.5 | 143 |

Table 4.3 Correlation matrix for selected Trace Elements in Massive Sulfides from the West, Main and South Lenses and the Cu-rich Stringer zone, Mine D

| | *Fe* | *Zn* | *Cu* | *Pb* | *Mn* | *$SiO_2$* | *$Al_2O_3$* | *$K_2O$* | *$Na_2O$* | *MgO* | *$P_2O_5$* | *$TiO_2$* | *CaO* | *S* | *$CO_2$* | *Au* |
|---|---|---|---|---|---|---|---|---|---|---|---|---|---|---|---|---|
| *Zn* | 0.19 | | | | | | | | | | | | | | | |
| *Cu* | 0.00 | -0.13 | | | | | | | | | | | | | | |
| *Pb* | 0.41 | 0.06 | -0.13 | | | | | | | | | | | | | |
| *Mn* | 0.46 | 0.18 | -0.03 | 0.14 | | | | | | | | | | | | |
| *$SiO_2$* | -0.92 | -0.46 | -0.10 | -0.37 | -0.46 | | | | | | | | | | | |
| *$Al_2O_3$* | -0.67 | -0.41 | 0.12 | -0.28 | -0.32 | 0.57 | | | | | | | | | | |
| *$K_2O$* | -0.62 | -0.37 | -0.14 | -0.17 | -0.31 | 0.61 | 0.63 | | | | | | | | | |
| *$Na_2O$* | -0.22 | -0.19 | 0.32 | -0.15 | -0.20 | 0.16 | 0.45 | 0.06 | | | | | | | | |
| *MgO* | 0.06 | 0.19 | -0.08 | -0.02 | 0.17 | -0.16 | -0.12 | -0.23 | 0.20 | | | | | | | |
| *$P_2O_5$* | -0.04 | 0.03 | 0.24 | -0.09 | 0.22 | -0.12 | 0.43 | -0.32 | 0.28 | 0.25 | | | | | | |
| *$TiO_2$* | 0.05 | -0.01 | 0.90 | -0.14 | 0.06 | -0.20 | 0.17 | -0.23 | 0.25 | -0.02 | 0.44 | | | | | |
| *CaO* | -0.17 | -0.15 | 0.12 | -0.09 | -0.08 | 0.07 | 0.61 | 0.05 | 0.36 | 0.19 | 0.67 | 0.33 | | | | |
| *S* | 0.86 | 0.39 | -0.04 | 0.28 | 0.12 | -0.86 | -0.71 | -0.49 | -0.24 | 0.10 | -0.28 | -0.03 | -0.30 | | | |
| *$CO_2$* | 0.51 | 0.19 | -0.12 | 0.35 | 0.91 | -0.51 | -0.39 | -0.33 | -0.22 | 0.27 | 0.18 | -0.05 | -0.12 | 0.17 | | |
| *Au* | 0.15 | 0.57 | 0.03 | 0.14 | 0.13 | -0.31 | -0.32 | -0.19 | -0.24 | -0.03 | -0.04 | 0.05 | -0.12 | 0.23 | 0.23 | |
| *Ag* | 0.23 | 0.34 | 0.19 | 0.41 | 0.16 | -0.32 | -0.32 | -0.15 | 0.00 | 0.04 | -0.15 | 0.15 | -0.17 | 0.25 | 0.22 | 0.47 |
| *Sb* | 0.36 | 0.01 | -0.14 | 0.97 | 0.12 | -0.32 | -0.26 | -0.14 | -0.13 | -0.04 | -0.10 | -0.16 | -0.13 | 0.24 | 0.32 | 0.12 |
| *As* | 0.23 | 0.61 | -0.12 | 0.09 | 0.24 | -0.37 | -0.39 | -0.32 | -0.28 | 0.04 | -0.02 | 0.04 | -0.28 | 0.28 | 0.30 | 0.70 |
| *Tl* | 0.51 | -0.02 | -0.25 | 0.00 | 0.00 | -0.41 | -0.33 | -0.13 | -0.16 | 0.09 | -0.23 | -0.23 | -0.16 | 0.63 | -0.06 | -0.09 |
| *Hg* | 0.11 | 0.38 | -0.03 | -0.01 | 0.01 | -0.19 | -0.14 | -0.09 | -0.04 | 0.21 | -0.08 | -0.01 | -0.01 | 0.27 | -0.08 | -0.01 |
| *Sn* | 0.42 | 0.35 | 0.04 | 0.76 | 0.06 | -0.46 | -0.45 | -0.28 | -0.15 | 0.10 | -0.19 | 0.00 | -0.17 | 0.43 | 0.24 | 0.40 |
| *Cd* | 0.09 | 0.95 | -0.13 | -0.02 | 0.08 | -0.34 | -0.41 | -0.31 | -0.21 | 0.17 | -0.07 | -0.06 | -0.18 | 0.34 | 0.10 | 0.61 |
| *In* | -0.06 | 0.05 | 0.76 | -0.17 | -0.16 | -0.02 | -0.02 | -0.22 | 0.30 | -0.02 | 0.10 | 0.67 | -0.13 | -0.03 | -0.20 | 0.12 |
| *Bi* | -0.01 | 0.07 | 0.39 | 0.04 | 0.03 | -0.09 | -0.06 | -0.18 | -0.05 | 0.17 | 0.12 | 0.41 | 0.13 | -0.02 | 0.06 | 0.22 |
| *Co* | 0.19 | 0.24 | 0.17 | -0.11 | 0.09 | -0.19 | -0.31 | -0.27 | -0.06 | -0.02 | -0.07 | 0.17 | -0.22 | 0.17 | 0.13 | 0.42 |
| *Ni* | 0.14 | 0.34 | 0.02 | 0.04 | 0.32 | -0.30 | 0.10 | -0.25 | -0.20 | 0.12 | 0.57 | 0.34 | 0.54 | -0.01 | 0.31 | 0.38 |
| *Se* | 0.03 | 0.48 | 0.26 | -0.09 | 0.15 | -0.23 | -0.22 | -0.23 | -0.09 | 0.14 | 0.16 | 0.24 | -0.12 | 0.11 | 0.20 | 0.83 |
| *B* | -0.09 | -0.08 | 0.08 | -0.05 | -0.09 | 0.06 | 0.20 | 0.30 | 0.05 | -0.06 | -0.09 | 0.04 | 0.03 | -0.04 | -0.10 | -0.04 |
| *Ta* | 0.06 | -0.13 | 0.57 | -0.04 | -0.09 | -0.13 | 0.15 | -0.08 | 0.26 | -0.08 | 0.17 | 0.52 | 0.02 | 0.03 | -0.09 | -0.08 |
| *Ge* | 0.23 | 0.24 | 0.05 | 0.13 | 0.08 | -0.35 | -0.10 | -0.40 | 0.23 | 0.53 | 0.32 | 0.17 | 0.29 | 0.22 | 0.17 | -0.01 |
| *Mo* | 0.18 | -0.12 | -0.07 | -0.06 | -0.06 | -0.14 | -0.06 | -0.03 | -0.11 | -0.02 | -0.06 | 0.05 | -0.07 | 0.23 | -0.09 | -0.10 |
| *Ba* | -0.54 | -0.31 | 0.01 | -0.16 | -0.28 | 0.53 | 0.51 | 0.81 | 0.06 | -0.25 | -0.29 | -0.09 | 0.03 | -0.43 | -0.30 | -0.14 |
| *Ga* | -0.23 | 0.51 | 0.08 | -0.20 | 0.07 | -0.04 | 0.25 | -0.08 | 0.06 | 0.12 | 0.51 | 0.22 | 0.23 | -0.20 | 0.06 | 0.53 |
| *Rb* | -0.64 | -0.37 | -0.11 | -0.18 | -0.32 | 0.62 | 0.66 | 0.99 | 0.10 | -0.21 | -0.27 | -0.22 | 0.07 | -0.51 | -0.34 | -0.20 |
| *Sr* | -0.20 | -0.08 | 0.04 | -0.17 | -0.06 | 0.12 | 0.34 | 0.10 | 0.59 | 0.60 | 0.31 | 0.03 | 0.34 | -0.17 | -0.04 | -0.19 |
| *Li* | -0.47 | -0.23 | 0.30 | -0.21 | -0.26 | 0.35 | 0.67 | 0.18 | 0.32 | 0.09 | 0.64 | 0.31 | 0.44 | -0.51 | -0.29 | -0.12 |
| *Cs* | -0.55 | -0.22 | 0.04 | -0.19 | -0.24 | 0.45 | 0.74 | 0.69 | 0.30 | -0.07 | 0.25 | -0.03 | 0.28 | -0.51 | -0.26 | -0.17 |
| *ΣREE* | -0.45 | -0.25 | 0.00 | -0.24 | -0.37 | 0.39 | 0.63 | 0.53 | 0.23 | -0.14 | 0.08 | 0.10 | 0.35 | -0.36 | -0.41 | -0.25 |
| *La* | -0.25 | -0.14 | -0.02 | -0.18 | -0.32 | 0.20 | 0.46 | 0.31 | 0.15 | -0.12 | 0.12 | 0.10 | 0.28 | -0.17 | -0.33 | -0.22 |
| *Pr* | -0.23 | -0.11 | -0.25 | -0.10 | -0.24 | 0.20 | 0.34 | 0.33 | 0.23 | -0.01 | -0.03 | -0.17 | 0.23 | -0.14 | -0.22 | -0.08 |
| *Nd* | -0.32 | -0.19 | 0.07 | -0.20 | -0.33 | 0.26 | 0.50 | 0.38 | 0.12 | -0.17 | 0.11 | 0.17 | 0.26 | -0.24 | -0.35 | -0.23 |
| *Sm* | -0.46 | -0.26 | 0.06 | -0.24 | -0.35 | 0.39 | 0.64 | 0.53 | 0.17 | -0.18 | 0.13 | 0.14 | 0.34 | -0.39 | -0.38 | -0.21 |
| *Eu* | -0.13 | -0.15 | -0.20 | -0.14 | -0.18 | 0.09 | 0.44 | 0.18 | 0.31 | 0.19 | 0.27 | 0.00 | 0.59 | -0.12 | -0.19 | -0.20 |
| *Gd* | -0.55 | -0.28 | -0.01 | -0.25 | -0.34 | 0.48 | 0.68 | 0.63 | 0.20 | -0.15 | 0.07 | 0.07 | 0.37 | -0.47 | -0.39 | -0.21 |
| *Tb* | -0.60 | -0.29 | -0.02 | -0.24 | -0.32 | 0.54 | 0.65 | 0.64 | 0.20 | -0.14 | 0.02 | 0.04 | 0.34 | -0.51 | -0.38 | -0.23 |
| *Dy* | -0.58 | -0.26 | 0.00 | -0.24 | -0.30 | 0.53 | 0.60 | 0.62 | 0.22 | -0.12 | -0.02 | 0.05 | 0.30 | -0.49 | -0.37 | -0.24 |
| *Ho* | -0.56 | -0.27 | 0.06 | -0.24 | -0.28 | 0.51 | 0.57 | 0.59 | 0.25 | -0.09 | -0.02 | 0.09 | 0.28 | -0.48 | -0.36 | -0.24 |
| *Er* | -0.52 | -0.27 | 0.13 | -0.23 | -0.25 | 0.48 | 0.55 | 0.56 | 0.27 | -0.06 | -0.02 | 0.14 | 0.25 | -0.45 | -0.35 | -0.25 |
| *Tm* | -0.51 | -0.29 | 0.16 | -0.22 | -0.25 | 0.47 | 0.55 | 0.56 | 0.27 | -0.06 | -0.02 | 0.15 | 0.24 | -0.45 | -0.35 | -0.25 |
| *Yb* | -0.51 | -0.30 | 0.17 | -0.23 | -0.24 | 0.47 | 0.56 | 0.56 | 0.28 | -0.06 | -0.01 | 0.16 | 0.24 | -0.46 | -0.34 | -0.25 |
| *Lu* | -0.52 | -0.37 | 0.17 | -0.23 | -0.24 | 0.50 | 0.59 | 0.59 | 0.29 | -0.09 | -0.02 | 0.14 | 0.23 | -0.48 | -0.33 | -0.27 |
| *Y* | -0.43 | -0.15 | 0.08 | -0.21 | -0.20 | 0.38 | 0.42 | 0.45 | 0.25 | -0.03 | -0.05 | 0.11 | 0.22 | -0.35 | -0.30 | -0.21 |
| *Hf* | -0.71 | -0.45 | 0.05 | -0.26 | -0.41 | 0.66 | 0.93 | 0.73 | 0.33 | -0.17 | 0.25 | 0.02 | 0.43 | -0.70 | -0.44 | -0.29 |
| *Sc* | -0.14 | 0.01 | 0.13 | -0.05 | 0.14 | -0.01 | 0.51 | 0.00 | 0.28 | 0.27 | 0.68 | 0.39 | 0.91 | -0.30 | 0.08 | 0.00 |
| *Nb* | -0.45 | -0.35 | 0.40 | -0.22 | -0.34 | 0.34 | 0.78 | 0.44 | 0.45 | -0.20 | 0.36 | 0.36 | 0.37 | -0.45 | -0.39 | -0.26 |
| *Th* | -0.69 | -0.45 | 0.06 | -0.30 | -0.47 | 0.64 | 0.92 | 0.70 | 0.31 | -0.23 | 0.25 | 0.05 | 0.43 | -0.66 | -0.51 | -0.35 |
| *U* | -0.49 | -0.36 | 0.01 | -0.26 | -0.09 | 0.49 | 0.65 | 0.57 | 0.16 | -0.21 | 0.15 | -0.02 | 0.29 | -0.56 | -0.17 | -0.19 |
| *W* | 0.45 | -0.05 | -0.29 | 0.62 | 0.05 | -0.37 | -0.19 | -0.22 | -0.02 | 0.03 | 0.02 | -0.31 | 0.04 | 0.37 | 0.16 | -0.10 |
| *V* | 0.34 | 0.20 | -0.15 | 0.21 | 0.16 | -0.42 | -0.03 | -0.32 | 0.01 | 0.24 | 0.37 | 0.11 | 0.50 | 0.24 | 0.23 | 0.25 |

Table 4.3 Continued

| | *Ag* | *Sb* | *As* | *Tl* | *Hg* | *Sn* | *Cd* | *In* | *Bi* | *Co* | *Ni* | *Se* | *B* | *Ta* | *Ge* | *Mo* | *Ba* |
|---|---|---|---|---|---|---|---|---|---|---|---|---|---|---|---|---|---|
| *Zn* | | | | | | | | | | | | | | | | | |
| *Cu* | | | | | | | | | | | | | | | | | |
| *Pb* | | | | | | | | | | | | | | | | | |
| *Mn* | | | | | | | | | | | | | | | | | |
| *$SiO_2$* | | | | | | | | | | | | | | | | | |
| *$Al_2O_3$* | | | | | | | | | | | | | | | | | |
| *$K_2O$* | | | | | | | | | | | | | | | | | |
| *$Na_2O$* | | | | | | | | | | | | | | | | | |
| *MgO* | | | | | | | | | | | | | | | | | |
| *$P_2O_5$* | | | | | | | | | | | | | | | | | |
| *$TiO_2$* | | | | | | | | | | | | | | | | | |
| *CaO* | | | | | | | | | | | | | | | | | |
| *S* | | | | | | | | | | | | | | | | | |
| *$CO_2$* | | | | | | | | | | | | | | | | | |
| *Au* | | | | | | | | | | | | | | | | | |
| *Ag* | | | | | | | | | | | | | | | | | |
| *Sb* | 0.46 | | | | | | | | | | | | | | | | |
| *As* | 0.24 | 0.03 | | | | | | | | | | | | | | | |
| *Tl* | -0.02 | 0.01 | -0.05 | | | | | | | | | | | | | | |
| *Hg* | -0.08 | -0.05 | 0.02 | 0.07 | | | | | | | | | | | | | |
| *Sn* | 0.49 | 0.72 | 0.22 | 0.14 | 0.23 | | | | | | | | | | | | |
| *Cd* | 0.34 | -0.03 | 0.53 | -0.02 | 0.38 | 0.35 | | | | | | | | | | | |
| *In* | 0.24 | -0.14 | 0.13 | -0.20 | 0.01 | 0.18 | 0.08 | | | | | | | | | | |
| *Bi* | 0.01 | -0.06 | 0.18 | -0.15 | -0.04 | 0.18 | 0.08 | 0.27 | | | | | | | | | |
| *Co* | 0.10 | -0.10 | 0.59 | -0.22 | -0.05 | 0.05 | 0.24 | 0.44 | 0.19 | | | | | | | | |
| *Ni* | 0.08 | -0.04 | 0.48 | -0.14 | 0.01 | 0.09 | 0.24 | -0.07 | 0.22 | 0.15 | | | | | | | |
| *Se* | 0.39 | -0.07 | 0.58 | -0.17 | -0.11 | 0.14 | 0.51 | 0.32 | 0.25 | 0.50 | 0.29 | | | | | | |
| *B* | -0.06 | -0.04 | -0.02 | -0.07 | 0.14 | -0.05 | -0.07 | 0.08 | -0.06 | 0.20 | -0.08 | -0.05 | | | | | |
| *Ta* | -0.05 | -0.04 | -0.09 | -0.07 | -0.09 | 0.06 | -0.12 | 0.50 | 0.25 | -0.02 | -0.06 | 0.06 | 0.00 | | | | |
| *Ge* | 0.04 | 0.13 | 0.09 | 0.13 | -0.10 | 0.20 | 0.21 | 0.09 | 0.17 | -0.01 | 0.29 | 0.07 | -0.10 | 0.28 | | | |
| *Mo* | -0.08 | -0.04 | -0.07 | 0.31 | -0.05 | -0.09 | -0.12 | -0.10 | -0.08 | -0.13 | -0.09 | -0.08 | -0.01 | -0.04 | -0.01 | | |
| *Ba* | -0.12 | -0.13 | -0.31 | -0.14 | 0.02 | -0.18 | -0.24 | -0.07 | -0.11 | -0.21 | -0.22 | -0.17 | 0.30 | 0.01 | -0.39 | -0.02 | |
| *Ga* | 0.14 | -0.18 | 0.42 | -0.28 | -0.06 | -0.10 | 0.45 | 0.13 | 0.06 | 0.23 | 0.43 | 0.66 | 0.00 | 0.05 | 0.10 | -0.08 | -0.05 |
| *Rb* | -0.15 | -0.15 | -0.34 | -0.14 | -0.08 | -0.30 | -0.31 | -0.19 | -0.18 | -0.27 | -0.25 | -0.21 | 0.32 | -0.08 | -0.40 | -0.04 | 0.82 |
| *Sr* | -0.01 | -0.16 | -0.24 | -0.07 | 0.12 | -0.17 | -0.12 | 0.04 | -0.16 | -0.15 | -0.09 | -0.02 | 0.08 | -0.04 | 0.05 | -0.01 | 0.09 |
| *Li* | -0.20 | -0.19 | -0.25 | -0.24 | -0.11 | -0.17 | -0.21 | 0.29 | 0.17 | -0.15 | 0.18 | 0.09 | 0.01 | 0.25 | 0.08 | -0.08 | 0.13 |
| *Cs* | -0.17 | -0.16 | -0.35 | -0.18 | -0.14 | -0.30 | -0.22 | -0.08 | -0.16 | -0.26 | -0.11 | -0.05 | 0.21 | -0.01 | -0.26 | -0.03 | 0.51 |
| *ΣREE* | -0.16 | -0.22 | -0.32 | -0.13 | -0.20 | -0.35 | -0.18 | -0.02 | -0.16 | -0.23 | -0.05 | -0.21 | 0.40 | 0.17 | 0.04 | 0.23 | 0.40 |
| *La* | -0.23 | -0.17 | -0.26 | -0.06 | -0.12 | -0.28 | -0.10 | -0.04 | -0.17 | -0.15 | -0.04 | -0.18 | 0.45 | 0.16 | 0.10 | 0.35 | 0.26 |
| *Pr* | -0.14 | -0.11 | -0.01 | -0.02 | -0.22 | -0.25 | -0.10 | -0.17 | -0.17 | -0.07 | -0.04 | -0.10 | 0.13 | 0.05 | 0.19 | 0.05 | -0.08 |
| *Nd* | -0.23 | -0.18 | -0.30 | -0.10 | -0.13 | -0.28 | -0.14 | 0.01 | -0.11 | -0.16 | -0.04 | -0.16 | 0.44 | 0.22 | 0.04 | 0.30 | 0.40 |
| *Sm* | -0.22 | -0.22 | -0.32 | -0.17 | -0.20 | -0.35 | -0.20 | -0.04 | -0.11 | -0.24 | -0.01 | -0.15 | 0.38 | 0.19 | -0.01 | 0.24 | 0.48 |
| *Eu* | -0.16 | -0.14 | -0.24 | 0.08 | -0.11 | -0.27 | -0.14 | -0.28 | -0.21 | -0.29 | 0.17 | -0.20 | 0.15 | -0.07 | 0.37 | 0.40 | 0.07 |
| *Gd* | -0.17 | -0.23 | -0.32 | -0.20 | -0.25 | -0.37 | -0.20 | -0.07 | -0.12 | -0.27 | -0.01 | -0.18 | 0.30 | 0.13 | -0.01 | 0.16 | 0.47 |
| *Tb* | -0.09 | -0.22 | -0.34 | -0.22 | -0.27 | -0.35 | -0.19 | -0.05 | -0.10 | -0.30 | -0.03 | -0.22 | 0.23 | 0.08 | -0.06 | 0.03 | 0.48 |
| *Dy* | 0.02 | -0.21 | -0.35 | -0.20 | -0.22 | -0.31 | -0.17 | 0.00 | -0.12 | -0.29 | -0.06 | -0.24 | 0.19 | 0.04 | -0.12 | -0.01 | 0.51 |
| *Ho* | 0.10 | -0.20 | -0.35 | -0.20 | -0.20 | -0.28 | -0.18 | 0.08 | -0.11 | -0.28 | -0.07 | -0.24 | 0.18 | 0.06 | -0.12 | -0.05 | 0.50 |
| *Er* | 0.19 | -0.20 | -0.35 | -0.18 | -0.15 | -0.26 | -0.20 | 0.16 | -0.10 | -0.26 | -0.08 | -0.22 | 0.18 | 0.07 | -0.14 | -0.05 | 0.50 |
| *Tm* | 0.22 | -0.19 | -0.35 | -0.17 | -0.14 | -0.24 | -0.22 | 0.18 | -0.09 | -0.26 | -0.08 | -0.23 | 0.19 | 0.07 | -0.16 | -0.06 | 0.50 |
| *Yb* | 0.23 | -0.20 | -0.36 | -0.18 | -0.12 | -0.25 | -0.24 | 0.19 | -0.10 | -0.25 | -0.08 | -0.22 | 0.19 | 0.06 | -0.19 | -0.06 | 0.52 |
| *Lu* | 0.21 | -0.19 | -0.37 | -0.19 | -0.16 | -0.29 | -0.31 | 0.18 | -0.12 | -0.25 | -0.11 | -0.24 | 0.20 | 0.08 | -0.20 | -0.08 | 0.54 |
| *Y* | 0.20 | -0.18 | -0.31 | -0.13 | -0.12 | -0.20 | -0.07 | 0.13 | -0.12 | -0.25 | -0.07 | -0.21 | 0.15 | 0.02 | -0.09 | -0.02 | 0.41 |
| *Hf* | -0.27 | -0.22 | -0.44 | -0.31 | -0.17 | -0.42 | -0.41 | -0.06 | -0.14 | -0.35 | -0.06 | -0.20 | 0.24 | 0.15 | -0.21 | -0.07 | 0.63 |
| *Sc* | -0.14 | -0.11 | -0.06 | -0.21 | 0.02 | -0.10 | -0.08 | -0.11 | 0.29 | -0.11 | 0.66 | 0.00 | -0.01 | -0.03 | 0.32 | -0.08 | -0.02 |
| *Nb* | -0.22 | -0.19 | -0.39 | -0.24 | -0.12 | -0.27 | -0.32 | 0.26 | 0.03 | -0.27 | -0.06 | -0.12 | 0.14 | 0.67 | -0.02 | -0.05 | 0.44 |
| *Th* | -0.34 | -0.26 | -0.50 | -0.27 | -0.18 | -0.47 | -0.39 | -0.06 | -0.13 | -0.37 | -0.09 | -0.27 | 0.23 | 0.15 | -0.21 | 0.05 | 0.60 |
| *U* | -0.21 | -0.22 | -0.49 | -0.13 | -0.04 | -0.21 | -0.29 | -0.01 | -0.14 | -0.38 | -0.05 | -0.20 | 0.14 | 0.05 | -0.29 | 0.18 | 0.61 |
| *W* | 0.11 | 0.62 | -0.13 | 0.38 | -0.11 | 0.46 | -0.08 | -0.34 | -0.06 | -0.28 | -0.08 | -0.24 | -0.16 | -0.08 | 0.26 | 0.03 | -0.28 |
| *V* | 0.06 | 0.18 | 0.37 | 0.13 | -0.08 | 0.14 | 0.11 | -0.13 | 0.11 | 0.18 | 0.59 | 0.12 | -0.12 | -0.03 | 0.52 | -0.16 | -0.45 |

Table 4.3 continued

| | Ga | Rb | Sr | Li | Cs | ΣREE | La | Pr | Nd | Sm | Eu | Gd | Tb | Dy | Ho | Er | Tm |
|---|---|---|---|---|---|---|---|---|---|---|---|---|---|---|---|---|---|
| Zn | | | | | | | | | | | | | | | | | |
| Cu | | | | | | | | | | | | | | | | | |
| Pb | | | | | | | | | | | | | | | | | |
| Mn | | | | | | | | | | | | | | | | | |
| $SiO_2$ | | | | | | | | | | | | | | | | | |
| $Al_2O_3$ | | | | | | | | | | | | | | | | | |
| $K_2O$ | | | | | | | | | | | | | | | | | |
| $Na_2O$ | | | | | | | | | | | | | | | | | |
| MgO | | | | | | | | | | | | | | | | | |
| $P_2O_5$ | | | | | | | | | | | | | | | | | |
| $TiO_2$ | | | | | | | | | | | | | | | | | |
| CaO | | | | | | | | | | | | | | | | | |
| S | | | | | | | | | | | | | | | | | |
| $CO_2$ | | | | | | | | | | | | | | | | | |
| Au | | | | | | | | | | | | | | | | | |
| Ag | | | | | | | | | | | | | | | | | |
| Sb | | | | | | | | | | | | | | | | | |
| As | | | | | | | | | | | | | | | | | |
| Tl | | | | | | | | | | | | | | | | | |
| Hg | | | | | | | | | | | | | | | | | |
| Sn | | | | | | | | | | | | | | | | | |
| Cd | | | | | | | | | | | | | | | | | |
| In | | | | | | | | | | | | | | | | | |
| Bi | | | | | | | | | | | | | | | | | |
| Co | | | | | | | | | | | | | | | | | |
| Ni | | | | | | | | | | | | | | | | | |
| Se | | | | | | | | | | | | | | | | | |
| B | | | | | | | | | | | | | | | | | |
| Ta | | | | | | | | | | | | | | | | | |
| Ge | | | | | | | | | | | | | | | | | |
| Mo | | | | | | | | | | | | | | | | | |
| Ba | | | | | | | | | | | | | | | | | |
| Ga | | | | | | | | | | | | | | | | | |
| Rb | -0.06 | | | | | | | | | | | | | | | | |
| Sr | 0.19 | 0.15 | | | | | | | | | | | | | | | |
| Li | 0.31 | 0.26 | 0.27 | | | | | | | | | | | | | | |
| Cs | 0.26 | 0.74 | 0.34 | 0.59 | | | | | | | | | | | | | |
| ΣREE | 0.09 | 0.52 | 0.17 | 0.27 | 0.49 | | | | | | | | | | | | |
| La | 0.14 | 0.30 | 0.13 | 0.17 | 0.35 | 0.91 | | | | | | | | | | | |
| Pr | 0.02 | 0.30 | 0.08 | 0.07 | 0.27 | 0.54 | 0.39 | | | | | | | | | | |
| Nd | 0.14 | 0.36 | 0.09 | 0.21 | 0.38 | 0.91 | 0.96 | 0.26 | | | | | | | | | |
| Sm | 0.15 | 0.52 | 0.11 | 0.31 | 0.51 | 0.96 | 0.91 | 0.38 | 0.95 | | | | | | | | |
| Eu | 0.08 | 0.18 | 0.27 | 0.15 | 0.26 | 0.70 | 0.67 | 0.58 | 0.58 | 0.62 | | | | | | | |
| Gd | 0.08 | 0.62 | 0.12 | 0.33 | 0.55 | 0.96 | 0.80 | 0.52 | 0.82 | 0.94 | 0.64 | | | | | | |
| Tb | -0.01 | 0.64 | 0.13 | 0.33 | 0.53 | 0.86 | 0.62 | 0.45 | 0.66 | 0.81 | 0.53 | 0.95 | | | | | |
| Dy | -0.04 | 0.63 | 0.18 | 0.31 | 0.51 | 0.77 | 0.49 | 0.34 | 0.54 | 0.69 | 0.44 | 0.86 | 0.97 | | | | |
| Ho | -0.05 | 0.60 | 0.21 | 0.32 | 0.47 | 0.71 | 0.42 | 0.28 | 0.47 | 0.62 | 0.39 | 0.79 | 0.92 | 0.99 | | | |
| Er | -0.05 | 0.58 | 0.25 | 0.33 | 0.45 | 0.64 | 0.34 | 0.20 | 0.40 | 0.54 | 0.32 | 0.70 | 0.85 | 0.94 | 0.98 | | |
| Tm | -0.06 | 0.58 | 0.26 | 0.34 | 0.43 | 0.59 | 0.28 | 0.18 | 0.35 | 0.49 | 0.28 | 0.65 | 0.79 | 0.90 | 0.95 | 0.99 | |
| Yb | -0.04 | 0.59 | 0.28 | 0.35 | 0.45 | 0.57 | 0.26 | 0.16 | 0.33 | 0.47 | 0.27 | 0.62 | 0.76 | 0.87 | 0.93 | 0.98 | 1.00 |
| Lu | -0.05 | 0.61 | 0.28 | 0.36 | 0.45 | 0.58 | 0.27 | 0.17 | 0.35 | 0.49 | 0.26 | 0.64 | 0.77 | 0.87 | 0.92 | 0.97 | 0.99 |
| Y | -0.06 | 0.47 | 0.23 | 0.23 | 0.37 | 0.61 | 0.34 | 0.19 | 0.38 | 0.49 | 0.36 | 0.67 | 0.83 | 0.93 | 0.97 | 0.97 | 0.94 |
| Hf | 0.18 | 0.75 | 0.30 | 0.61 | 0.77 | 0.65 | 0.48 | 0.32 | 0.54 | 0.69 | 0.36 | 0.72 | 0.68 | 0.62 | 0.60 | 0.58 | 0.58 |
| Sc | 0.36 | 0.02 | 0.26 | 0.38 | 0.22 | 0.20 | 0.14 | 0.16 | 0.12 | 0.21 | 0.48 | 0.25 | 0.23 | 0.20 | 0.18 | 0.16 | 0.15 |
| Nb | 0.20 | 0.47 | 0.21 | 0.64 | 0.61 | 0.54 | 0.42 | 0.19 | 0.49 | 0.57 | 0.23 | 0.55 | 0.51 | 0.47 | 0.47 | 0.47 | 0.47 |
| Th | 0.14 | 0.73 | 0.25 | 0.60 | 0.75 | 0.74 | 0.59 | 0.32 | 0.64 | 0.76 | 0.43 | 0.78 | 0.74 | 0.68 | 0.65 | 0.60 | 0.59 |
| U | 0.04 | 0.60 | 0.20 | 0.53 | 0.57 | 0.44 | 0.32 | 0.08 | 0.38 | 0.46 | 0.25 | 0.48 | 0.48 | 0.49 | 0.48 | 0.50 | 0.51 |
| W | -0.29 | -0.22 | -0.06 | -0.06 | -0.10 | -0.18 | -0.11 | -0.02 | -0.19 | -0.20 | 0.11 | -0.17 | -0.16 | -0.17 | -0.18 | -0.21 | -0.21 |
| V | 0.22 | -0.33 | -0.01 | 0.00 | -0.25 | -0.12 | -0.14 | 0.33 | -0.24 | -0.19 | 0.25 | -0.10 | -0.11 | -0.14 | -0.15 | -0.19 | -0.20 |

Table 4.3 continued

| | *Yb* | *Lu* | *Y* | *Hf* | *Sc* | *Nb* | *Th* | *U* | *W* |
|---|---|---|---|---|---|---|---|---|---|
| *Zn* | | | | | | | | | |
| *Cu* | | | | | | | | | |
| *Pb* | | | | | | | | | |
| *Mn* | | | | | | | | | |
| *$SiO_2$* | | | | | | | | | |
| *$Al_2O_3$* | | | | | | | | | |
| *$K_2O$* | | | | | | | | | |
| *$Na_2O$* | | | | | | | | | |
| *MgO* | | | | | | | | | |
| *$P_2O_5$* | | | | | | | | | |
| *$TiO_2$* | | | | | | | | | |
| *CaO* | | | | | | | | | |
| *S* | | | | | | | | | |
| *$CO_2$* | | | | | | | | | |
| *Au* | | | | | | | | | |
| *Ag* | | | | | | | | | |
| *Sb* | | | | | | | | | |
| *As* | | | | | | | | | |
| *Tl* | | | | | | | | | |
| *Hg* | | | | | | | | | |
| *Sn* | | | | | | | | | |
| *Cd* | | | | | | | | | |
| *In* | | | | | | | | | |
| *Bi* | | | | | | | | | |
| *Co* | | | | | | | | | |
| *Ni* | | | | | | | | | |
| *Se* | | | | | | | | | |
| *B* | | | | | | | | | |
| *Ta* | | | | | | | | | |
| *Ge* | | | | | | | | | |
| *Mo* | | | | | | | | | |
| *Ba* | | | | | | | | | |
| *Ga* | | | | | | | | | |
| *Rb* | | | | | | | | | |
| *Sr* | | | | | | | | | |
| *Li* | | | | | | | | | |
| *Cs* | | | | | | | | | |
| *ΣREE* | | | | | | | | | |
| *La* | | | | | | | | | |
| *Pr* | | | | | | | | | |
| *Nd* | | | | | | | | | |
| *Sm* | | | | | | | | | |
| *Eu* | | | | | | | | | |
| *Gd* | | | | | | | | | |
| *Tb* | | | | | | | | | |
| *Dy* | | | | | | | | | |
| *Ho* | | | | | | | | | |
| *Er* | | | | | | | | | |
| *Tm* | | | | | | | | | |
| *Yb* | | | | | | | | | |
| *Lu* | 0.99 | | | | | | | | |
| *Y* | 0.92 | 0.89 | | | | | | | |
| *Hf* | 0.60 | 0.64 | 0.43 | | | | | | |
| *Sc* | 0.15 | 0.13 | 0.15 | 0.28 | | | | | |
| *Nb* | 0.48 | 0.50 | 0.36 | 0.77 | 0.24 | | | | |
| *Th* | 0.59 | 0.62 | 0.50 | 0.94 | 0.27 | 0.79 | | | |
| *U* | 0.53 | 0.52 | 0.41 | 0.68 | 0.19 | 0.55 | 0.69 | | |
| *W* | -0.23 | -0.24 | -0.16 | -0.18 | -0.03 | -0.15 | -0.18 | -0.21 | |
| *V* | -0.21 | -0.21 | -0.16 | -0.21 | 0.56 | -0.18 | -0.25 | -0.36 | 0.23 |

Correlations are based on 50 samples; from RAW data
Coefficients greater than 0.14 are significant at the 95% confidence level

Table 4.4 Correlation matrix for selected Trace Elements in Massive Sulfides from the West, Main and South Lenses and the Cu-rich Stringer zone, Mine D normalized to 100%

| | *Fe* | *Zn* | *Cu* | *Pb* | *Mn* | *$Na_2O$* | *MgO* | *$P_2O_5$* | *CaO* | *S* | *$CO_2$* | *Au* | *Ag* | *Sb* | *As* | *Tl* | *Hg* |
|---|---|---|---|---|---|---|---|---|---|---|---|---|---|---|---|---|---|
| *Zn* | -0.59 | | | | | | | | | | | | | | | | |
| *Cu* | -0.16 | -0.42 | | | | | | | | | | | | | | | |
| *Pb* | 0.01 | -0.03 | -0.21 | | | | | | | | | | | | | | |
| *Mn* | 0.47 | 0.02 | -0.23 | 0.03 | | | | | | | | | | | | | |
| *Na2O* | 0.46 | -0.23 | 0.02 | -0.12 | 0.03 | | | | | | | | | | | | |
| *MgO* | 0.66 | -0.19 | -0.02 | -0.11 | 0.20 | 0.63 | | | | | | | | | | | |
| *P2O5* | 0.07 | -0.35 | 0.73 | -0.22 | -0.13 | 0.35 | 0.25 | | | | | | | | | | |
| *CaO* | 0.12 | 0.07 | -0.15 | -0.03 | 0.18 | 0.33 | 0.19 | -0.03 | | | | | | | | | |
| *S* | -0.55 | 0.11 | -0.33 | 0.12 | -0.44 | -0.39 | -0.68 | -0.46 | -0.09 | | | | | | | | |
| *CO2* | 0.36 | 0.03 | -0.23 | 0.17 | 0.92 | -0.06 | 0.03 | -0.18 | 0.37 | -0.32 | | | | | | | |
| *Au* | -0.33 | 0.44 | -0.03 | 0.06 | 0.01 | -0.25 | -0.10 | -0.07 | -0.05 | -0.04 | 0.05 | | | | | | |
| *Ag* | -0.24 | 0.13 | 0.07 | 0.31 | 0.02 | -0.09 | -0.16 | -0.05 | -0.03 | 0.07 | 0.04 | 0.20 | | | | | |
| *Sb* | 0.02 | -0.04 | -0.20 | 0.96 | 0.02 | -0.12 | -0.11 | -0.21 | -0.06 | 0.11 | 0.14 | 0.04 | 0.37 | | | | |
| *As* | 0.09 | 0.29 | -0.27 | 0.00 | 0.14 | 0.16 | 0.39 | -0.03 | -0.01 | -0.18 | 0.04 | 0.41 | 0.00 | -0.02 | | | |
| *Tl* | 0.15 | -0.18 | -0.21 | -0.09 | -0.09 | 0.37 | 0.16 | 0.10 | 0.13 | 0.24 | -0.14 | -0.11 | -0.07 | -0.06 | -0.03 | | |
| *Hg* | -0.30 | 0.39 | -0.06 | -0.12 | -0.12 | 0.08 | -0.15 | -0.10 | 0.11 | 0.03 | -0.13 | 0.10 | -0.14 | -0.11 | -0.08 | -0.06 | |
| *Sn* | -0.32 | 0.31 | -0.02 | 0.41 | -0.16 | -0.15 | -0.19 | -0.08 | 0.12 | 0.07 | -0.03 | 0.52 | 0.20 | 0.39 | -0.01 | 0.11 | 0.28 |
| *Cd* | -0.57 | 0.93 | -0.38 | -0.08 | -0.06 | -0.22 | -0.20 | -0.33 | 0.11 | 0.12 | -0.03 | 0.45 | 0.11 | -0.06 | 0.20 | -0.12 | 0.51 |
| *In* | -0.24 | -0.09 | 0.65 | -0.23 | -0.26 | -0.11 | -0.05 | 0.52 | -0.08 | -0.24 | -0.25 | 0.23 | 0.07 | -0.19 | 0.09 | -0.19 | 0.01 |
| *Bi* | 0.09 | -0.12 | 0.19 | -0.02 | -0.06 | -0.06 | 0.15 | 0.19 | 0.00 | -0.20 | -0.06 | 0.09 | -0.06 | -0.05 | 0.00 | -0.11 | -0.12 |
| *Co* | -0.07 | 0.02 | 0.09 | -0.15 | -0.08 | -0.12 | -0.09 | 0.08 | -0.08 | 0.00 | -0.06 | 0.25 | -0.07 | -0.13 | 0.44 | -0.27 | -0.08 |
| *Ni* | 0.06 | 0.24 | -0.13 | 0.00 | 0.25 | -0.05 | 0.20 | 0.13 | 0.14 | -0.24 | 0.22 | 0.31 | -0.02 | -0.05 | 0.38 | -0.11 | -0.04 |
| *Se* | -0.24 | 0.13 | 0.34 | -0.12 | 0.07 | -0.19 | 0.04 | 0.15 | 0.13 | -0.18 | 0.13 | 0.62 | 0.16 | -0.11 | 0.21 | -0.26 | -0.11 |
| *B* | -0.06 | -0.08 | 0.10 | -0.07 | -0.10 | 0.11 | -0.07 | 0.13 | -0.05 | 0.08 | -0.11 | -0.07 | -0.08 | -0.05 | -0.04 | 0.00 | 0.17 |
| *Ge* | 0.40 | -0.14 | -0.12 | -0.03 | 0.10 | 0.64 | 0.43 | 0.24 | 0.64 | -0.27 | 0.15 | -0.19 | -0.08 | -0.04 | 0.09 | 0.31 | -0.22 |
| *Mo* | 0.42 | -0.30 | 0.11 | -0.11 | 0.01 | 0.37 | 0.57 | 0.25 | -0.06 | -0.35 | -0.12 | -0.14 | -0.11 | -0.09 | 0.15 | 0.25 | -0.14 |
| *Ba* | 0.02 | -0.22 | 0.42 | -0.12 | -0.16 | 0.37 | 0.03 | 0.66 | -0.13 | -0.20 | -0.18 | -0.06 | -0.08 | -0.10 | -0.18 | 0.31 | 0.18 |
| *Ga* | 0.49 | -0.16 | 0.06 | -0.16 | 0.04 | 0.75 | 0.76 | 0.48 | 0.06 | -0.56 | -0.11 | -0.05 | -0.14 | -0.14 | 0.32 | 0.35 | -0.03 |
| *ΣREE* | 0.46 | -0.28 | 0.08 | -0.12 | -0.02 | 0.74 | 0.57 | 0.56 | 0.02 | -0.39 | -0.15 | -0.18 | -0.13 | -0.10 | 0.16 | 0.45 | -0.09 |
| *Y* | 0.52 | -0.24 | 0.04 | -0.12 | 0.03 | 0.78 | 0.77 | 0.40 | 0.02 | -0.48 | -0.15 | -0.14 | -0.08 | -0.10 | 0.29 | 0.40 | -0.04 |
| *Hf* | 0.53 | -0.29 | 0.08 | -0.13 | -0.01 | 0.77 | 0.69 | 0.47 | 0.01 | -0.48 | -0.16 | -0.16 | -0.14 | -0.10 | 0.21 | 0.40 | -0.03 |
| *Sc* | 0.60 | -0.24 | -0.01 | -0.10 | 0.13 | 0.87 | 0.79 | 0.39 | 0.27 | -0.54 | -0.01 | -0.15 | -0.15 | -0.12 | 0.25 | 0.37 | -0.04 |
| *W* | 0.62 | -0.24 | -0.12 | -0.01 | 0.09 | 0.72 | 0.87 | 0.16 | 0.06 | -0.47 | -0.09 | -0.13 | -0.09 | 0.00 | 0.38 | 0.34 | -0.15 |
| *V* | 0.62 | -0.16 | -0.24 | -0.04 | 0.15 | 0.73 | 0.84 | 0.09 | 0.20 | -0.42 | -0.01 | -0.09 | -0.09 | -0.04 | 0.48 | 0.32 | -0.15 |

Table 4.4 Continued

| | *Sn* | *Cd* | *In* | *Bi* | *Co* | *Ni* | *Se* | *B* | *Ge* | *Mo* | *Ba* | *Ga* | *ΣREE* | *Y* | *Hf* | *Sc* | W |
|---|---|---|---|---|---|---|---|---|---|---|---|---|---|---|---|---|---|
| *Zn* | | | | | | | | | | | | | | | | | |
| *Cu* | | | | | | | | | | | | | | | | | |
| *Pb* | | | | | | | | | | | | | | | | | |
| *Mn* | | | | | | | | | | | | | | | | | |
| *Na2O* | | | | | | | | | | | | | | | | | |
| *MgO* | | | | | | | | | | | | | | | | | |
| *P2O5* | | | | | | | | | | | | | | | | | |
| *CaO* | | | | | | | | | | | | | | | | | |
| *S* | | | | | | | | | | | | | | | | | |
| *CO2* | | | | | | | | | | | | | | | | | |
| *Au* | | | | | | | | | | | | | | | | | |
| *Ag* | | | | | | | | | | | | | | | | | |
| *Sb* | | | | | | | | | | | | | | | | | |
| *As* | | | | | | | | | | | | | | | | | |
| *Tl* | | | | | | | | | | | | | | | | | |
| *Hg* | | | | | | | | | | | | | | | | | |
| *Sn* | | | | | | | | | | | | | | | | | |
| *Cd* | 0.44 | | | | | | | | | | | | | | | | |
| *In* | 0.30 | -0.01 | | | | | | | | | | | | | | | |
| *Bi* | 0.01 | -0.10 | 0.25 | | | | | | | | | | | | | | |
| *Co* | 0.02 | 0.02 | 0.45 | 0.02 | | | | | | | | | | | | | |
| *Ni* | 0.02 | 0.14 | -0.09 | 0.01 | 0.08 | | | | | | | | | | | | |
| *Se* | 0.15 | 0.12 | 0.44 | 0.29 | 0.34 | 0.14 | | | | | | | | | | | |
| *B* | -0.04 | -0.06 | 0.08 | -0.06 | 0.25 | -0.11 | -0.09 | | | | | | | | | | |
| *Ge* | -0.03 | -0.12 | -0.12 | 0.03 | -0.13 | 0.24 | -0.13 | -0.02 | | | | | | | | | |
| *Mo* | -0.17 | -0.27 | -0.06 | -0.04 | -0.12 | -0.11 | -0.08 | 0.01 | 0.19 | | | | | | | | |
| *Ba* | -0.03 | -0.17 | 0.10 | 0.02 | -0.04 | -0.13 | -0.10 | 0.18 | 0.08 | 0.29 | | | | | | | |
| *Ga* | -0.13 | -0.15 | -0.03 | 0.03 | -0.05 | 0.02 | -0.02 | 0.10 | 0.37 | 0.59 | 0.49 | | | | | | |
| *ΣREE* | -0.13 | -0.24 | -0.04 | -0.01 | -0.09 | -0.06 | -0.19 | 0.21 | 0.44 | 0.53 | 0.59 | 0.91 | | | | | |
| *Y* | -0.13 | -0.19 | -0.10 | 0.04 | -0.13 | -0.05 | -0.16 | 0.10 | 0.40 | 0.62 | 0.47 | 0.92 | 0.89 | | | | |
| *Hf* | -0.15 | -0.25 | -0.07 | 0.03 | -0.12 | -0.06 | -0.15 | 0.15 | 0.38 | 0.62 | 0.54 | 0.96 | 0.96 | 0.94 | | | |
| *Sc* | -0.16 | -0.23 | -0.19 | 0.04 | -0.16 | 0.20 | -0.15 | 0.07 | 0.61 | 0.51 | 0.37 | 0.89 | 0.83 | 0.89 | 0.89 | | |
| *W* | -0.13 | -0.22 | -0.17 | 0.17 | -0.15 | -0.02 | -0.10 | -0.02 | 0.41 | 0.59 | 0.15 | 0.83 | 0.72 | 0.90 | 0.83 | 0.85 | |
| *V* | -0.14 | -0.16 | -0.22 | 0.01 | -0.09 | 0.16 | -0.13 | -0.01 | 0.51 | 0.51 | -0.01 | 0.78 | 0.68 | 0.83 | 0.78 | 0.88 | 0.929 |

Correlations are based on 50 samples; data are normalized to 100% sulfides
Coefficients greater than 0.14 are significant at the 95% confidence level

# Chapter 5. Discussion

The current model of the Kidd Creek deposit is that it formed during a period of felsic volcanism and sedimentation within a linear synvolcanic graben-like structure that acted as the main upflow zone for hydrothermal fluids (Bleeker, 1999 and Hannington et al., 1999). The bulk of the massive sulfide is in pyrite-sphalerite-rich lenses that are interpreted to have formed during relatively low-temperature hydrothermal activity (<300°C: Hannington et al., 1999). The Cu-rich ores appear to have formed during pulses of higher temperature upflow associated with felsic volcanism. The North orebody in the upper part of the mine formed close to the seafloor after the eruption of the lower massive rhyolite. A major hydrothermal vent complex is thought to have been present at the thickest part of the deposit which was exposed in the open pit at surface (Figure 1.13). Most of the orebody, however, was deposited below the paleo-seafloor in permeable epiclastic deposits and felsic fragmental units. The presence of graphitic argillite on top of the North and Central orebodies was interpreted to represent a hiatus in volcanism prior to additional felsic volcanism and the deposition of the South orebody, which was as a stacked lens offset from the main lenses (Hannington et al., 1999).

The form of the deposit and metal grades are remarkably uniform down-plunge from surface to below 10,200 ft (3109 m); however, there are some subtle differences. There is significantly less epiclastic material and graphitic argillite above the massive sulfides at depth in the mine. Instead argillites occur within the hanging-wall basalt and mafic volcanics, significantly higher in the sequence. Minor argillite is present stratigraphically below the South Lens (Figure 1.5); however, isolated bodies of massive sulfide to the south of the West and Main lenses are interpreted to be structural offsets from the main ore zones

owing to the presence of many of the major faults in the lower mine, some of which appear to have vertical offsets of up to ~100s of metres based on a combination of modelled displacements in the Northwest Lens, Main orebody and the gabbro window. An early interpretation was that the South Lens was a downplunge continuation of the SOB in the upper part of the mine, but the southern massive sulfides lack a Cu-rich stockwork zone and the metal zonation is inconsistent with that of the other lenses, suggesting that it is a fragment of the Main orebody. It cannot be ruled out that sinistral South-dipping faults may also be responsible for the absence of a Cu-rich stringer zone below the South Lens.

The West and Main lenses exhibit strong metal zonation, similar to that of the ore lenses in the upper part of the mine. Low-temperature pyrite-rich mineralization with associated Pb-Sn-Ag minerals and carbonate-sericite alteration represents the bulk of the massive sulfides. Higher temperature pyrrhotite-chalcopyrite-rich mineralization with associated Co-Bi-As-Ni-Se minerals and tourmaline-chlorite-silica alteration underlies the main massive sulfides. An important difference is the presence of local semi-massive magnetite in the keel of the main massive sulfide lens (Figure 3.12). The overall abundance of pyrrhotite increases with depth in the mine based on mapping throughout the mine.

### *5.1 Upflow Zones*

The main upflow zone at Kidd Creek was located near the open pit at the top of the mine. This is where the deposit was the thickest and where the highest-temperature mineralization was recognized (e.g., the bornite zone) (Hannington et al., 1999). The main upflow zone appears to have been a continuous feature from the surface to the bottom of the

mine. However, it is difficult to follow at depth in the mine due to the significant brittle deformation. There are many major faults in Mine D, such as the Offset Faults that have combined displacements of up to 100s of subvertical metres. Much of the Cu-rich ore at depth is located in close proximity to large, originally subvertical offset faults such as the Offset Fault and the Offset Fault 2, and some of the Cu-rich ore has been preferentially mobilized into these faults zones (Figure 4.1). Some features of the deep mine indicate the proximity to another significant upflow zone.

For example, as the Offset Fault migrates through the massive sulfides with depth, strong Cu-rich mineralization is always bound to its northern flank (see Figures 1.5 to 1.10) and due to its original vertical nature it may represent another upflow zone at depth. This could be an analogue to the East-West Shear from the upper mine possibly representing the upflow zone for the bornite zone (Hannington et al., 1999). One of the deepest drill-holes at the mine to the Southeast contains up to 4800 ppm Co, 361 ppm Ni, 1000 ppm Bi (at detection limit), 6900 ppm As, and 1000 ppm Se (at detection limit) in the last 10 metres of the hole (Appendix I). This zone is within 25 metres of the Offset Fault and grade increases towards it.

### *5.2 Mineralogical Zonation*

Galena formed near the top of the main massive sulfide lenses, commonly intergrown with tetrahedrite; in contrast to the upper mine no tennantite was observed (Hannington et al., 1999). Arsenopyrite is common in the centre of the massive sphalerite lenses, together with cassiterite. Pyrite and sphalerite stringers formed at the distal margins of the massive

sulfides, and adjacent to the main upflow zone. A large halo of sericitization occurs around the main pyrite-sphalerite lenses. Due to the large amount of carbonate in the sulfides, $CO_2$ was likely an important constituent in the ore-forming fluids. Kidd Creek is one of few tin rich VMS deposits. The closest analogue is likely NevesCorvo in the Iberian Pyrite Belt of Portugal (Relvas et al., 2006).

Pyrrhotite-chalcopyrite-rich mineralization with Fe-rich chlorite, tourmaline and albite appears to have overprinted the main massive pyrite-sphalerite lenses, and a Cu-rich stringer zone now occupies the main upflow zone. The Cu-rich mineralization penetrated into the base of the massive sulfides but apparently did not reach the top of the massive sulfide lenses. The Cu-rich vein mineralization is concentrated along major faults, such as the offset faults (Figure 4.2), which would have been subvertical in their original orientation and located at the keel of the massive sulfides.

The massive sphalerite at the base of the sulfide mound exhibits abundant "chalcopyrite disease" (Eldridge et al., 1988) at the micro- and macro scale. High temperatures that are inferred from the Cu-rich nature of the mineralization would also explain the enrichment of Co, Ni, Bi, As, Ag, In, and Se (Hannington et al., 1999). The presence of significant concentrations of magnetite at the keel of the massive sulfides and in the Cu-stringer zone may also be a part of this higher-temperature mineralization (Figure 5.2). Magnetite has always been recognized at Kidd Creek in the Cu-rich keel, in the Cu stringer zone and as discrete magnetite porphyroblasts up to 2 mm in the sphalerite-rich massive sulfides (Hannington et al., 1999). However it has never been observed in the quantities documented here (>30 wt %) in some samples.

Albite porphyroblasts, up to 1cm in size, are also a significant constituent of the Cu-stringer zone of the deposit. They are commonly found at the base of the massive sulfides, as well, but are smaller in size and quantity. The large size of the porphyroblasts likely reflects a higher temperature of metamorphic recrystallization, although the bulk Na content of the ores is similar to that observed in the upper part of the mine. The presence of such high concentrations of sodium in the Cu-rich ores, in contrast to the very low Na in the alteration zones of most massive sulfide deposits (Franklin et al., 1981), must reflect a fluid sodic precursor (Hannington et al., 1999). Hannington et al. (1999) suggested that the high Na may have been a product of a supercritical brine phase.

Gold grades in the upper mine were well below average for typical Archean Cu-Zn deposits in the Abitibi (Mercier et al., 2011). Hannington et al. (1999) suggested that the ore-forming fluids were undersaturated with gold throughout the venting history and that either the hydothermal fluids were unsuitable for gold transport or the metal source zone was already depleted of gold. The elevated levels of gold in the upper mine were located above the North orebody and in the bornite zone. Gold grades in the lower mine are only elevated locally in sphalerite-chalcopyrite and Cu-rich stringer ores around 9000 level at the stratigraphic base of the massive sulfides and into the sphalerite-stained massive silicified rhyolite. This rhyolite may have influenced the direction of the hydrothermal upflow (Figure 1.9). No native gold was identified.

### *5.3 Conditions of Mineralization*

The conditions of mineralization in the different ore lenses also appear to have been remarkably consistent downplunge. The orebody was interpreted to have formed at low $fO_2$-$fS_2$ conditions due to the abundance of pyrite, pyrrhotite, arsenopyrite, high Fe-sphalerite, and siderite (Hannington et al., 1999). The presence of significant concentrations of intergrown magnetite in predominantly sphalerite-chalcopyrite ores, however, suggests a change in the conditions in the deepest portions of the known ore body. There is abundant siderite mineralization, which was documented in the upper mine to be a primary feature and is associated with magnetite stringers and veins. This would imply that the $H_2S/CO_2$ ratio of the fluids decreased allowing for the co-precipitation of magnetite, siderite, and Fe-sulfide.

There is abundant evidence for metamorphism being a factor in the dominant Fe mineralogy. In the upper mine it was noted that pyrrhotite was changing from monoclinic to hexagonal with depth and therefore higher metamorphic temperatures and pressures (248°C: Scott and Kissin, 1973). Most of the pyrrhotite in Mine D is hexagonal (Figure 3.13). At the inferred temperature of peak metamorphism at depth in Mine D (below 450°C, Galley et al., 2000), pyrrhotite can break down with the loss of sulfur and forms magnetite and pyrite (Craig and Vokes, 1993). However, this process would leave inclusions of pyrrhotite within the magnetite which is not seen in either variety of magnetite in the deep mine. Other evidence of the effects of metamorphism include the remobilization of galena within fractures of late pyrite, the size of the albite porphyroblasts, native Ag being expelled from solid solution in sulfide minerals at the base of the West and Main lenses, and the remobilization of Au along with Bi minerals in the gold rich zone, again at the base of the West and Main lenses. Metamorphism will generally homogenize Fe contents of sphalerite

throughout a deposit; however, the Fe contents of sphalerite at depth show a strong gradation between Fe-poor sphalerite at the top of the sulfide lens to Fe-rich sphalerite at the base. There are also abundant sphalerite inclusions in the magnetite, which would argue against porphyroblastic growth during annealing of the massive sulfide.

The large mass of magnetite at the base of the sulfide mound and into the Cu-rich stringer is most reasonably interpreted in terms of a decrease in total available sulfur and/or a rise in hydrothermal temperatures (Figure 5.1 and Figure 5.2). This is comparable to the formation of massive magnetite at the Gossan Hill deposit in Australia where massive magnetite formed from high-temperature, low-$fO_2$ reducing, and sulfur-poor fluids. This fluid composition prevented the precipitation of hematite and sulfide. Co-depositional ankerite-siderite and Fe-rich chlorite in massive magnetite at Gossan Hill also suggests these fluids were Fe and $CO_2$ rich (Sharpe and Gemmell, 2002).

### *5.4 Hotmuck and Magnetite*

The presence of magnetite has a significant impact on mining at Kidd Creek. When development blasts are taken, if there are large amounts of pyrite it can result in a "secondary sulfide ignition" which is the combustion of $SO_2$ gas caused by many fine-grained sulfide dust particles in the air. These events can normally be predicted and preventative measures taken, such as smaller blasts and less water used to wash the muck pile.

When large stopes are blasted and if there is a large amount of pyrrhotite in the ore, "hotmuck" can result from the rapid oxidation of pyrrhotite (especially when the blasted ore is wet), causing it to heat up and release $SO_2$ gas. Because the reaction is exothermic, it can

accelerate rapidly causing huge issues for the mine, both for production (the ore starts to solidify) and for safety as these gases are very dangerous. Smaller blasts help this condition as there is not as much ore to remove, so there is less sitting time and therefore less time to heat up and start a chain reaction.

The mine needs to know when these situations will arise. For this, an algorithm exists which calculates a mass balance for all the routinely assayed elements. The Fe and S are first allocated to chalcopyrite, sphalerite, and galena in proportion to the Cu, Zn and Pb assays, the remaining Fe (total) and S are then allocated to pyrite and pyrrhotite. As pyrrhotite has a higher Fe-S ratio, if there is abundant Fe left over, the algorithm will favour pyrrhotite and vice versa. However magnetite was never significant in the upper mine and the equation that is used to calculate the hotmuck does not include the extra Fe as an oxide or incorporate siderite. As a result, a high Fe:S ratio is assumed to represent larger amounts of pyrrhotite than are present in the ore. This is evident in some stopes where large blasts were taken, and the ore did not heat up nearly as much as expected. Lower pyrrhotite content means that larger, less expensive blasts can be taken without fear of hotmuck issues. To resolve this, a suite of high magnetite sample pulps were analyzed for ferric iron determination as there are no other significant minerals at the mine that contain ferric iron.

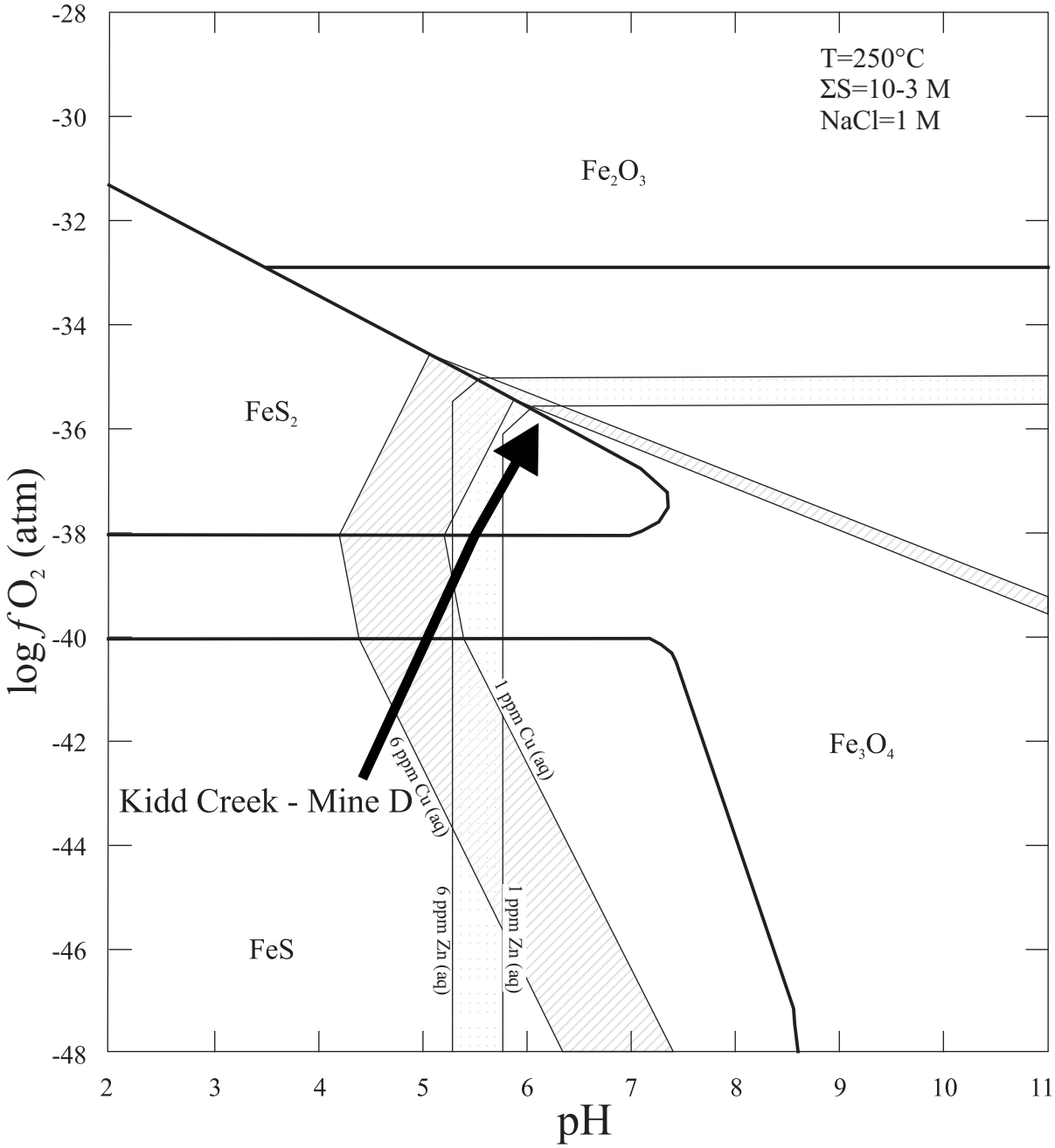


Figure 5.1 pH versus $fO_2$ diagram modified from Large (1977) showing the stability fields of pyrite, pyrrhotite, magnetite, and hematite in the Fe-S-O system and possible conditions of formation of ore from Mine D from a 1 M NaCl solution at 250°C with ΣS = 10-3 M. The diagonally shaded area represents chalcopyrite deposition between the 6-ppm and 1-ppm contours of soluble copper. The stippled area represents sphalerite deposition between the 6-ppm and 1-ppm contours of soluble zinc. The arrow shows that magnetite may form in both Cu-rich and Zn-rich ores at low ΣS concentrations.

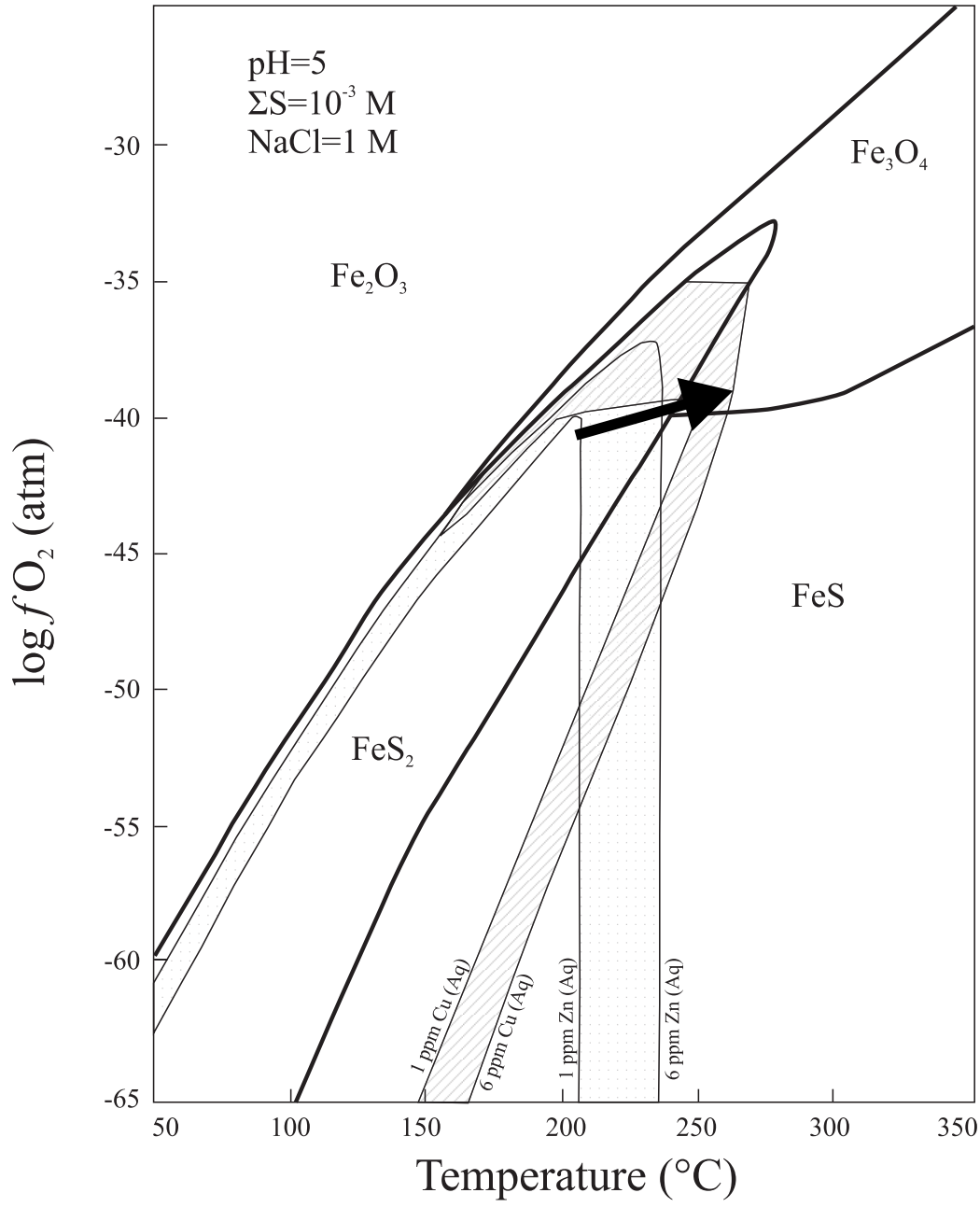


Figure 5.2 Temperature versus $fO_2$ diagram modified from Large (1977) showing the stability fields of pyrite, pyrrhotite, magnetite, and hematite in the Fe-S-O system and possible conditions of formation of ore from Mine D from a 1 M NaCl solution at pH = 5 with ΣS = 10-3 M. The diagonally shaded area represents chalcopyrite deposition between the 6-ppm and 1-ppm contours of soluble copper. The stippled area represents sphalerite deposition between the 6-ppm and 1-ppm contours of soluble zinc. The arrow shows that magnetite may form in both Cu-rich and Zn-rich ores at higher temperatures.

# Chapter 6. Conclusions

The deep ore lenses of Kidd Creek are remarkably uniform downplunge and are similar to those in the upper mine in both form and metal grades, suggesting that the main upflow zone was continuous from surface to the bottom of the mine below 10,200 feet (3109 metres). Even after restoring the offsets on the steeply dipping faults, such as the Offset fault series and South dipping faults (and considering possible stretching), this upflow zone would have had a strike length of at least 2 km on the paleo-seafloor. This is a minimum estimate, given that the orebody extends to an unknown depth and has been partly eroded at surface. After restoring the offsets, the Main orebody can be traced up to the Central orebody in the upper mine. However, the South Lens in the deep mine is not an extension of the South orebody in the upper mine; it is a fragment of the Main orebody.

The deep mine is characterized by the following: 1) A much broader Cu-stringer zone than in the upper mine, likely due to structural offsets such as the Offset fault series. These faults may be related to the East-West shear in the upper part of the mine and therefore are candidates for the high-temperature upflow zone in the deep part of the mine. 2) An abundance of magnetite that was likely stabilized by a decrease in $H_2S$ or an increase in temperature. A decrease in the $H_2S/CO_2$ ratio would also account for the co-deposition of abundant siderite. 3) Abundant large albite porphyroblasts in the Cu-rich ore are interpreted to reflect primary Na-metasomatism, similar to that observed in the Cu-stringer of the upper part of the mine. The larger size of the porphyroblasts may reflect a higher metamorphic grade and recrystallization of albite. 4) A lack of significant argillite as host for ore, which

suggests a different depositional environment compared to the upper part of the mine, possibly at the margins of the graben.

In conclusion, the structure, mineralogy and geochemistry of the deep orebodies indicate that they are, in fact, a downplunge extension of the orebodies in the upper mine and were part of the same massive hydrothermal system. There is no indication of that they hydrothermal system diminishes with depth beyond 10,200 feet (3109 metres). The deepest drill holes have intersected massive sulfides with “bornite” like signatures (high Se, As, Co, Bi and Ni), suggesting that high-temperature upflow extended even farther than presently known.

## References

Ayer, J.A., Thurston, P.C., Bateman, R., Dubé, B., Gibson, H.L., Hamilton, M.A., Hathway, B., Hocker, S.M., Houlé, M.G., Hudak, G., Ispolatov, V.O., Lafrance, B., Lesher, C.M., MacDonald, P.J., Péloquin, A.S., Piercey, S.J., Reed, L.E. and Thompson, P.H., 2005. Overview of results from the Greenstone Architecture Project: Discover Abitibi Initiative; Ontario Geological Survey, Open File Report 6154, 146p.

Barrie, C.T., and Davis. D.W., 1990. Timing of magmatism and deformation in the Kamiskotia-Kidd Creek area, Western Abitibi subprovince, Canada: *Precambrian Research*, v. 46, p. 217-240.

Berger, B.R., Bleeker, W., van Breemen, O., Chapman, J.B., Peter, J.M., Layton-Matthews, D. and Gemmell, J.B. 2011. Results from the Targeted Geoscience Initiative III Kidd–Munro Project; Ontario Geological Survey, Open File Report 6258, 142p.

Bleeker, W., 1999. Structure, Stratigraphy, and Primary Setting of the Kidd Creek Volcanogenic Massive Sulfide Deposit: A Semiquantitative Reconstruction. *Economic Geology Monograph 10*, p. 71-122.

Bleeker, W. and van Breemen, O. 2011. New geochronological, stratigraphic, and structural observations on the Kidd-Munro assemblage and the terrane architecture of the south- central Abitibi greenstone belt, Superior craton, Canada; in Results from the Targeted Geoscience Initiative III Kidd-Munro Project, Ontario Geological Survey, Open File Report 6258, p. 142.

Craig, J.R. and Vokes, F.M., 1993. The metamorphism of pyrite and pyritic ores: an overview. *Mineralogical Magazine*, 57, p. 3-18.

Eldridge, C.S., Bourcier, W.L., Ohmoto, H., and Barnes, H.L., 1988. Hydrothermal Inoculation and Incubation of the Chalcopyrite Disease in Sphalerite. *Economic Geology*, 83: p. 978-989.

Franklin, J.M., Lydon, J.W., and Sangster, D.F., 1981. Volcanic-accociated massive sulfide deposits: *Economic Geology 75$^{th}$ Anniversary Volume*, p. 485-627.

Galley, A.G., Jonasson, I.R., Watkinson, D.H., 2000. Magnetite-rich calc-silicate alteration in relation to synvolcanic intrusion at the Ansil volcanogenic massive sulfide deposit, Rouyn-Noranda, Quebec, Canada. *Mineralium Deposita*, 35: p. 619-637.

Hannington, M., 2010. The Giant Kidd Creek Volcanogenic Massive Sulfide Deposit, Timmins, Ontario: *Field Guide for Society of Economic Geologists*, Biennial Meeting, Keystone, Colorado, Post-meeting Excursion, October 7, 2010.

Hannington, M.D., Bleeker, W., and Kjarsgaard, I., 1999. Sulfide Mineralogy, Geochemistry and Ore Genesis of the Kidd Creek Deposit: Part I. North, Central, and South orebodies. *Economic Geology Monograph 10*, p. 163-224.

Hannington, M.D., Bleeker, W., and Kjarsgaard, I., 1999. Sulfide Mineralogy, Geochemistry and Ore Genesis of the Kidd Creek Deposit: Part II. The bornite zone. *Economic Geology Monograph 10*, p. 225-266.

Hannington, M.D., Kjarsgaard, I.M., Galley, A.G., Taylor, B., 2003. Mineral-chemical studies of metamorphosed hydrothermal alteration in the Kristineberg volcanogenic massive sulfide district, Sweden. *Mineralium Deposita*, 38: p. 423-442.

Hannington, M.D., Santaguida, F., Kjarsgaard. I.M., Cathles, L.M., 2003. Regional-scale hydrothermal alteration in the Central Blake River Group, western Abitibi subprovince, Canada: implications for VMS prospectivity. *Mineralium Deposita*, 38: p. 393-422.

Hey, M.H., 1954. A new review of the chlorite. *Mineralogical Magazine*, 30: p. 277-292.

Jackson, S.L., and Fyon, J.A., 1991, The Western Abitibi Subprovince in Ontario, in Thurston, P.C., Williams, H.R., Sutcliffe, R.H., and stott, G.M., Geology of Ontario: Ontario Geological Survey, Special Voume 4, Part I., p. 405-482.

Koopman, E.R., Hannington, M.D., Santaguida, F., Cameron, B.I., 1999. Petrology and Geochemistry of Proximal Hydrothermal Alteration in the Mine Rhyolite at Kidd Creek. *Economic Geology Monograph 10*, p. 267-296.

Large, R.R., 1992. Australian Volcanic-Hosted Massive Sulfide Deposits: Features, Styles, and Genetic Models. *Economic Geology*, 87: p. 471-510.

Ludden, J.N., Hubert, C., and Gariepy, C., 1986, The tectonic evolution of the Abitibi greenstone belt of Canada: Geol. Mag., 123: p. 123-166.

Mercier-Langevin, P., 2011, The gold content of volcanogenic massive sulfide deposits. *Mineralium Deposita*, 46: p. 509-539.

Pyke, D.R., Naldrett, A.J., and Eckstrand, O.R., 1973, Archean ultramafic flows in Munro Township: Geol. Soc. Am. Bull., 84: p. 955-978.

Relvas, J.M.R.S., Barriga, J.A.S., Ferreira, A., Noiva, P.C., Pacheco, N., Barriga, G., 2006. Hydrothermal Alteration and Mineralization in the Neves- Corvo Volcanic-Hosted Massive Sulfide Deposit, Portugal. I. Geology, Mineralogy, and Geochemistry. *Economic Geology*, 101: p. 753-790.

Schandl, E.S., Bleeker, W., 1999. Hydrothermal and Metamorphic Fluids of the Kidd Creek Volcanogenic Massive Sulfide Deposit: Preliminary Evidence from Fluid Inclusions. *Economic Geology Monograph 10,* p. 379-388.

Schandl, E.S., Gorton, M.P., Bleeker, W., 1999. A Systematic Study of Rare Earth and Trace Element Geochemistry of Host Rocks to the Kidd Creek Volcanogenic Massive Sulfide Deposit. *Economic Geology Monograph 10,* p. 309-334.

Scott, S.D., Kissin, S.A., 1973. Sphalerite Composition in the Zn-Fe-S System Below 300°C. Economic Geology, 68: p. 475-479.

Sharpe, R., Gemmell, B.J., 2002. The Archean Cu-Zn Magnetite-Rich Gossan Hill Volcanic-Hosted Massive Sulfide Deposit, Western Australia: Genesis of a Multistage Hydrothermal System. *Economic Geology*, 97: p. 517-539.

Slack, J.F., Ramsden, A.R., Griffin, W.L., Win, T.T., French, D.H., Ryan, C.G., 1999. Trace Elements in Tourmaline from the Kidd Creek Massive Sulfide Deposit and Vicinity, Timmins, Ontario: A Proton Microprobe Study. *Economic Geology Monograph 10,* p. 415-430.

## List of Appendices

# Appendix I Chemical Compositions of Representative Ore Samples from Mine D

| Lens | Ore Type | Sample # | Fe INAA (wt%) | Zn MS (wt%) | Cu MS (wt%) | Pb MS (wt%) | Mn MS (wt%) | $SiO_2$ OES (wt%) | $Al_2O_3$ OES (wt%) | $K_2O$ OES (wt%) | $Na_2O$ INAA (wt%) | CaO OES (wt%) | MgO OES (wt%) |
|---|---|---|---|---|---|---|---|---|---|---|---|---|---|
| West | Heterolithic Py | KCD209768 | 11.5 | 0.10 | 0.16 | 0.06 | 0.12 | 57.5 | 8.58 | <0.1 | 1.50 | 2.81 | 3.15 |
| West | | KCD209861 | 36.5 | 1.39 | 0.07 | 0.04 | 0.13 | 9.48 | 1.81 | <0.1 | <0.01 | 0.67 | 0.53 |
| West | Heterolithic Py-Sph | KCD209779 | 25.8 | 2.83 | 0.03 | 0.03 | 0.08 | 29.3 | 2.97 | 1.0 | 0.14 | 1.02 | 0.56 |
| West | | KCD209862 | 18.9 | 10.8 | 0.12 | 0.07 | 0.02 | 38.5 | 5.75 | 0.2 | <0.01 | 0.08 | 1.81 |
| West | Massive Py-Sph | KCD209769 | 33.5 | 8.86 | 0.01 | 0.27 | 0.08 | 7.34 | 0.76 | <0.1 | 0.11 | 2.21 | 0.56 |
| West | | KCD209770 | 31.5 | 12.8 | 0.04 | 1.31 | 0.03 | 7.72 | 0.38 | <0.1 | <0.01 | 0.08 | 0.22 |
| West | | KCD209781 | 40.1 | 2.82 | 0.09 | 6.73 | 0.28 | 2.55 | 0.40 | <0.1 | <0.01 | 0.20 | 0.71 |
| West | | KCD209782 | 32.5 | 11.5 | 0.22 | 1.13 | 0.16 | 2.27 | 0.53 | <0.1 | <0.01 | <0.01 | 0.22 |
| West | Massive Py-Cp | KCD209771 | 40.6 | 0.45 | 4.06 | 0.05 | 0.31 | 7.44 | 0.47 | <0.1 | <0.01 | 0.15 | 0.41 |
| West | Massive Sph-Cp | KCD209783 | 22.4 | 22.9 | 4.65 | 0.03 | 0.16 | 7.12 | 0.11 | <0.1 | <0.01 | 0.08 | 0.61 |
| West | | KCD209784 | 18.8 | 18.4 | 0.61 | 0.24 | 0.76 | 16.6 | 5.03 | <0.1 | <0.01 | 1.13 | 3.86 |
| West | | KCD209807 | 11.8 | 14.5 | 6.38 | 0.01 | 0.02 | 46.0 | 1.61 | 0.2 | 0.50 | 0.35 | 0.30 |
| West | | KCD209811 | 30.7 | 11.2 | 1.36 | 1.68 | 0.34 | 9.43 | 1.68 | <0.1 | <0.01 | 0.59 | 1.38 |
| West | Cp Stringer | KCD209864 | 8.55 | 0.10 | 8.14 | <0.01 | 0.01 | 57.3 | 8.79 | 2.4 | 0.18 | 0.20 | 0.51 |
| West | | KCD209866 | 7.93 | 0.25 | 7.88 | 0.03 | 0.03 | 64.8 | 6.65 | 1.9 | 0.16 | 0.59 | 0.45 |
| West | | KCD209867 | 4.17 | 1.23 | 2.43 | <0.01 | <0.01 | 70.2 | 11.1 | 3.0 | 0.73 | <0.01 | 0.23 |
| West | Sph Stringer | KCD209780 | 43.6 | 0.30 | 0.12 | 0.28 | 0.21 | 2.80 | 0.47 | <0.1 | <0.01 | 0.21 | 0.27 |
| West | | KCD209868 | 6.43 | 4.02 | 0.02 | <0.01 | 0.18 | 68.5 | 8.81 | 1.8 | 0.49 | 0.16 | 0.48 |
| West | | KCD209806 | 13.8 | 17.2 | 1.04 | 0.22 | 0.07 | 37.6 | 2.32 | 0.5 | 0.12 | 0.46 | 0.15 |
| West | Sph-Cp Stringer | KCD209809 | 11.6 | 11.5 | 2.31 | 0.42 | 0.23 | 42.4 | 3.36 | 0.6 | 0.14 | 4.13 | 2.34 |
| West/Main | Lapillistone Rhy | KCD209786 | 0.48 | 0.03 | <0.01 | <0.01 | <0.01 | 78.5 | 11.0 | 3.1 | 0.39 | <0.01 | 0.27 |
| West/Main | Heterolithic Py-Sph | KCD209848 | 12.8 | 5.05 | 0.48 | 0.01 | 0.12 | 51.8 | 6.82 | <0.1 | 0.53 | 2.49 | 3.08 |
| West/Main | | KCD209872 | 28.0 | 12.5 | 0.03 | 0.33 | 0.20 | 17.5 | 0.89 | <0.1 | 0.26 | 1.48 | 0.51 |
| West/Main | Massive Sph-Cp | KCD209852 | 27.2 | 6.86 | 8.42 | <0.01 | 0.61 | 22.0 | 0.32 | <0.1 | 0.03 | 0.49 | 1.01 |
| West/Main | | KCD209856 | 15.2 | 11.0 | 5.46 | 0.15 | 0.07 | 30.8 | 12.1 | 0.2 | 1.20 | 0.16 | 6.07 |
| West/Main | | KCD209873 | 21.2 | 6.34 | 9.91 | 0.04 | 0.26 | 32.7 | 3.48 | 0.7 | 0.65 | 1.34 | 0.58 |
| West/Main | Cp Stringer | KCD209876 | 14.0 | 0.42 | 6.33 | 0.02 | 0.10 | 58.4 | 5.92 | 0.2 | <0.01 | 0.22 | 2.50 |
| West/Main | | KCD209877 | 32.6 | 0.23 | 1.88 | <0.01 | 1.20 | 26.7 | 1.85 | <0.1 | <0.01 | 0.41 | 2.85 |
| West/Main | | KCD209879 | 3.22 | 0.03 | 1.96 | <0.01 | 0.01 | 77.2 | 8.11 | 2.4 | 0.08 | <0.01 | 0.51 |
| West/Main | Sph Stringer | KCD209851 | 18.3 | 3.09 | 0.08 | 0.10 | 0.08 | 48.6 | 7.52 | 0.5 | 0.55 | 0.25 | 2.17 |
| West/Main | Sph-Cp Stringer | KCD209785 | 11.8 | 8.12 | 0.52 | 0.01 | 0.36 | 43.9 | 8.69 | 0.2 | 0.14 | 0.07 | 5.57 |
| West/Main | | KCD209787 | 10.0 | 9.39 | 1.57 | 0.02 | 0.13 | 58.2 | 4.23 | <0.1 | <0.01 | 0.10 | 1.82 |
| West/Main | | KCD209858 | 10.7 | 2.67 | 7.90 | 0.09 | 0.13 | 50.7 | 5.61 | <0.1 | 0.77 | 2.39 | 4.99 |
| West/Main | | KCD209875 | 7.86 | 10.1 | 1.60 | 0.01 | 0.03 | 62.5 | 5.56 | 1.2 | 0.16 | 0.20 | 0.93 |
| Main | Massive Sph | KCD209815 | 18.4 | 11.6 | 0.19 | 0.03 | 0.01 | 37.2 | 1.53 | <0.1 | 0.07 | <0.01 | 0.08 |
| Main | Massive Sph-Cp | KCD209788 | 22.9 | 15.1 | 4.33 | 0.01 | 0.08 | 23.3 | 1.02 | <0.1 | <0.01 | 0.80 | 0.65 |
| Main | | KCD209812 | 21.6 | 5.65 | 4.96 | 0.02 | 0.23 | 19.0 | 13.0 | <0.1 | <0.01 | 0.85 | 8.89 |
| Main | SphStringer | KCD209813 | 9.10 | 13.7 | 0.16 | 0.01 | 0.02 | 56.7 | 1.81 | <0.1 | <0.01 | <0.01 | 0.61 |
| Main | | KCD209814 | 13.5 | 3.86 | 0.15 | 0.09 | 0.01 | 66.7 | 2.17 | 0.2 | 0.09 | 0.16 | 0.38 |
| South | Massive Py-Sph | KCD209757 | 30.7 | 3.10 | 0.56 | 0.11 | 0.16 | 16.7 | 1.25 | 0.2 | 0.11 | 0.90 | 2.92 |
| South | | KCD209762 | 21.4 | 20.0 | 0.27 | 0.92 | 0.20 | 22.0 | 1.80 | <0.1 | 0.11 | 0.77 | 1.19 |
| South | Massive Sph | KCD209763 | 20.9 | 20.0 | 0.36 | 1.67 | 0.17 | 17.1 | 0.89 | <0.1 | 0.18 | 0.36 | 0.53 |
| South | | KCD209764 | 25.8 | 11.1 | 0.09 | 1.67 | 0.19 | 23.5 | 0.74 | <0.1 | 0.09 | 0.98 | 0.58 |
| South | Massive Sph-Cp | KCD209752 | 17.4 | 17.8 | 7.46 | <0.01 | 0.15 | 29.5 | 1.51 | <0.1 | 0.04 | 0.74 | 0.98 |
| South | | KCD209759 | 15.8 | 18.0 | 3.30 | 0.57 | 0.60 | 18.9 | 3.74 | <0.1 | 0.47 | 2.13 | 3.18 |
| South | Py Stringer | KCD209761 | 15.8 | 0.46 | 0.09 | 0.12 | 0.11 | 52.4 | 7.54 | 0.7 | 0.34 | 0.15 | 2.79 |
| South | Sph Stringer | KCD209755 | 5.50 | 4.80 | 0.49 | 0.04 | 0.02 | 69.5 | 4.89 | 0.8 | 0.04 | 0.27 | 2.29 |
| South | | KCD209760 | 13.8 | 10.7 | 0.29 | 0.16 | 0.19 | 42.4 | 7.30 | <0.1 | 0.09 | 0.55 | 3.81 |
| Cu Str | Lapillistone Rhy | KCD209775 | 2.38 | 0.01 | <0.01 | <0.01 | 0.02 | 75.7 | 11.6 | 2.5 | 0.30 | <0.01 | 1.89 |
| Cu Str | Massive Py-Cp | KCD209773 | 22.7 | 0.44 | 2.30 | 0.02 | 0.02 | 53.7 | 2.89 | <0.1 | 0.69 | 0.15 | 0.41 |
| Cu Str | Massive Cp | KCD209797 | 22.7 | 0.03 | 19.8 | 0.01 | 0.02 | 20.0 | 8.39 | <0.1 | 0.88 | 0.13 | 3.47 |
| Cu Str | Cp Stringer | KCD209772 | 18.2 | 0.64 | 9.59 | 0.01 | 0.12 | 34.0 | 5.95 | 0.6 | 1.97 | 0.25 | 0.61 |
| Cu Str | | KCD209774 | 9.68 | 0.10 | 6.74 | <0.01 | 0.09 | 56.0 | 6.80 | 0.7 | 2.26 | 0.67 | 0.68 |
| Cu Str | | KCD209789 | 8.80 | 0.15 | 4.11 | <0.01 | 0.01 | 64.4 | 4.14 | 0.2 | 0.55 | 0.13 | 0.99 |
| Cu Str | | KCD209790 | 13.5 | 0.15 | 5.47 | <0.01 | 0.02 | 57.8 | 6.97 | 0.2 | 0.12 | 0.46 | 2.27 |
| Cu Str | | KCD209793 | 9.16 | 0.03 | 3.34 | <0.01 | 0.03 | 63.3 | 7.22 | 1.0 | 0.08 | 0.36 | 1.96 |
| Cu Str | | KCD209794 | 21.7 | 5.60 | 13.6 | 0.83 | 0.14 | 28.0 | 5.54 | <0.1 | 0.46 | 0.69 | 2.09 |
| Cu Str | | KCD209795 | 6.31 | 0.01 | 2.85 | <0.01 | 0.03 | 70.8 | 5.01 | 0.5 | 0.51 | 0.22 | 1.29 |
| Cu Str | | KCD209796 | 17.1 | 0.04 | 11.0 | <0.01 | 0.03 | 43.4 | 7.50 | <0.1 | 1.04 | 0.21 | 2.57 |
| Cu Str | | KCD209799 | 5.42 | 0.02 | 1.85 | <0.01 | 0.01 | 73.6 | 5.69 | 0.6 | 0.14 | <0.01 | 1.76 |
| Cu Str | | KCD209800 | 12.7 | 0.02 | 0.92 | <0.01 | 0.03 | 53.1 | 13.3 | 0.6 | 0.09 | 0.07 | 5.62 |
| Cu Str | | KCD209801 | 14.5 | 0.05 | 7.29 | <0.01 | 0.01 | 53.9 | 5.12 | <0.1 | <0.01 | 0.07 | 2.32 |
| Cu Str | | KCD209803 | 8.25 | 0.08 | 1.73 | <0.01 | 0.02 | 70.4 | 7.03 | 0.6 | 0.04 | 0.08 | 2.65 |
| Cu Str | | KCD209816 | 13.5 | 0.43 | 6.16 | 0.02 | 0.01 | 65.9 | 1.21 | <0.1 | 0.04 | <0.01 | 0.18 |
| Cu Str | | KCD209817 | 7.93 | 0.12 | 3.77 | 0.02 | 0.02 | 62.3 | 7.73 | 1.3 | 0.36 | 0.62 | 1.29 |
| Cu Str | | KCD209838 | 2.33 | 0.03 | 1.23 | <0.01 | <0.01 | 75.1 | 11.6 | 3.4 | 0.32 | 0.07 | 0.30 |
| Cu Str | | KCD209839 | 4.87 | 0.05 | 1.53 | <0.01 | 0.02 | 78.3 | 6.80 | 1.2 | 0.08 | <0.01 | 1.34 |
| Cu Str | | KCD209842 | 4.00 | 0.34 | 1.98 | 0.01 | 0.01 | 74.9 | 8.62 | 2.3 | 0.39 | <0.01 | 0.38 |
| Cu Str | | KCD209843 | 12.9 | 2.63 | 5.35 | <0.01 | 0.01 | 49.0 | 9.53 | 2.5 | 0.31 | 0.11 | 0.41 |
| Cu Str | Py Stringer | KCD209776 | 3.14 | 0.11 | <0.01 | 0.01 | 0.01 | 75.5 | 10.6 | 3.0 | 0.23 | 0.17 | 0.33 |
| Cu Str | Sph Stringer | KCD209835 | 8.35 | 4.51 | 1.61 | <0.01 | 0.03 | 65.5 | 5.18 | 1.0 | 0.12 | 1.80 | 0.95 |

| Lens | Ore Type | Sample # | $P_2O_5$ OES (wt%) | $TiO_2$ OES (wt%) | S OES (wt%) | $CO_2$ COUL (wt%) | $FeCO_3$ eq[1] (wt%) | Au INAA (ppb) | Ag INAA (ppm) | As INAA (ppm) | Hg FIMS (ppb) | Sb INAA (ppm) | Tl MS (ppm) |
|---|---|---|---|---|---|---|---|---|---|---|---|---|---|
| West | Heterolithic Py | KCD209768 | 0.027 | 0.32 | 4.80 | 2.72 | 7.16 | <2 | 27 | 57 | 72 | 2.8 | 4.1 |
| West | | KCD209861 | 0.127 | 0.02 | 42.3 | 0.52 | 1.37 | <2 | <5 | 108 | 425 | 22.6 | 23.7 |
| West | Heterolithic Py-Sph | KCD209779 | 0.006 | 0.03 | 30.0 | 1.45 | 3.82 | 17 | <5 | 132 | 738 | 22.1 | 17.2 |
| West | | KCD209862 | 0.018 | 0.10 | 19.4 | 0.09 | 0.24 | <2 | <5 | 49.5 | 1530 | 8.4 | 5.3 |
| West | Massive Py-Sph | KCD209769 | 0.006 | <0.01 | 41.6 | 3.31 | 8.72 | <2 | <5 | 149 | 1560 | 23.2 | 9.6 |
| West | | KCD209770 | 0.014 | <0.01 | 41.0 | 0.95 | 2.50 | <2 | 34 | 251 | 788 | 57.4 | 10.7 |
| West | | KCD209781 | 0.006 | <0.01 | 28.9 | 9.68 | 25.49 | 132 | 1250 | 151 | 304 | 1100 | 1.1 |
| West | | KCD209782 | 0.014 | <0.01 | 29.9 | 5.29 | 13.93 | 130 | 248 | 746 | 201 | 224 | 0.8 |
| West | Massive Py-Cp | KCD209771 | 0.048 | <0.01 | 32.6 | 8.39 | 22.09 | 52 | 70 | 226 | 39 | 9.4 | 1.5 |
| West | Massive Sph-Cp | KCD209783 | 0.104 | <0.01 | 31.7 | 4.26 | 11.22 | 736 | 1370 | 1310 | 68 | 22.1 | 0.3 |
| West | | KCD209784 | 0.076 | 0.02 | 11.5 | 11.0 | 28.96 | 98 | 76 | 1100 | 579 | 26.6 | <0.1 |
| West | | KCD209807 | 0.066 | <0.01 | 16.8 | 0.57 | 1.50 | <2 | 810 | 26 | 454 | 64.6 | 3.5 |
| West | | KCD209811 | 0.039 | 0.02 | 25.5 | 8.78 | 23.12 | 208 | 202 | 980 | 450 | 82.8 | 0.5 |
| West | Cp Stringer | KCD209864 | 0.078 | 0.07 | 8.01 | 0.16 | 0.42 | 43 | 30 | 6.4 | 145 | 1.6 | 3.6 |
| West | | KCD209866 | 0.069 | 0.10 | 7.30 | 0.72 | 1.90 | 51 | 117 | 3 | 468 | 1.6 | 0.8 |
| West | | KCD209867 | 0.025 | 0.08 | 3.79 | 0.11 | 0.29 | <2 | 27 | <0.5 | 803 | <0.1 | 1 |
| West | Sph Stringer | KCD209780 | 0.006 | <0.01 | 46.6 | 1.66 | 4.37 | 45 | 41 | 204 | 226 | 51.9 | 48.2 |
| West | | KCD209868 | 0.006 | 0.07 | 4.75 | 0.07 | 0.18 | 9 | <5 | 3.9 | 1390 | <0.1 | 0.4 |
| West | | KCD209806 | 0.021 | 0.02 | 19.7 | 0.23 | 0.61 | 34 | 193 | 209 | 682 | 22.5 | 7.4 |
| West | Sph-Cp Stringer | KCD209809 | 0.032 | 0.10 | 13.7 | 6.26 | 16.48 | 117 | 221 | 401 | 255 | 34.2 | 5.3 |
| West/Main | Lapillistone Rhy | KCD209786 | 0.039 | 0.30 | 0.08 | <0.01 | - | 277 | <5 | 47 | 6 | 1 | 8 |
| West/Main | Heterolithic Py-Sph | KCD209848 | 0.021 | 0.15 | 7.00 | 3.79 | 9.98 | <2 | <5 | 42.3 | 499 | 1.2 | <0.1 |
| West/Main | | KCD209872 | 0.006 | 0.02 | 36.2 | 2.05 | 5.40 | <2 | 26 | 219 | 1530 | 50.7 | 12.2 |
| West/Main | Massive Sph-Cp | KCD209852 | 0.080 | <0.01 | 26.5 | 5.31 | 13.98 | 58 | 260 | 153 | 1550 | 11.9 | 0.3 |
| West/Main | | KCD209856 | 0.173 | 0.17 | 10.5 | 0.10 | 0.26 | <2 | 31 | 6.9 | 639 | 2.7 | 0.7 |
| West/Main | | KCD209873 | 0.108 | 0.02 | 21.0 | 2.16 | 5.69 | <2 | 1790 | 55.6 | 578 | 13.1 | 7.6 |
| West/Main | Cp Stringer | KCD209876 | 0.173 | 0.10 | 6.12 | 0.75 | 1.97 | 74 | 68 | 44.5 | 161 | 1.4 | 1.3 |
| West/Main | | KCD209877 | 0.025 | 0.02 | 3.39 | 19.1 | 50.29 | 32 | 24 | 10.4 | 61 | 2.3 | 0.2 |
| West/Main | | KCD209879 | 0.023 | 0.07 | 1.84 | 0.10 | 0.26 | 13 | 15 | 2.1 | 91 | 0.8 | 1 |
| West/Main | Sph Stringer | KCD209851 | 0.021 | 0.17 | 13.6 | 0.34 | 0.90 | 34 | <5 | 78.5 | 650 | 10.8 | 0.3 |
| West/Main | Sph-Cp Stringer | KCD209785 | 0.128 | 0.28 | 5.08 | 2.60 | 6.85 | 896 | 17 | 12600 | 591 | <0.1 | 1.2 |
| West/Main | | KCD209787 | 0.073 | 0.02 | 8.82 | 0.07 | 0.18 | 146 | 40 | 1160 | 1190 | 11 | <0.1 |
| West/Main | | KCD209858 | 0.085 | 0.10 | 9.24 | 3.48 | 9.16 | 82 | 35 | 189 | 718 | 6.6 | 0.4 |
| West/Main | | KCD209875 | 0.016 | 0.10 | 8.47 | 0.26 | 0.68 | 210 | 20 | 67.3 | 1550 | 1.2 | 7.5 |
| Main | Massive Sph | KCD209815 | 0.016 | <0.01 | 16.1 | 0.13 | 0.34 | <2 | <5 | 374 | 216 | 6.3 | 0.2 |
| Main | Massive Sph-Cp | KCD209788 | 0.044 | <0.01 | 29.4 | 1.74 | 4.58 | 162 | 65 | 499 | 971 | 9.9 | 0.2 |
| Main | | KCD209812 | 0.133 | 0.52 | 9.20 | 2.96 | 7.79 | 62 | 110 | 8.3 | 396 | 3.8 | 1.4 |
| Main | SphStringer | KCD209813 | 0.034 | 0.02 | 13.6 | 0.10 | 0.26 | 44 | <5 | 127 | 163 | 4.9 | 0.3 |
| Main | | KCD209814 | 0.006 | 0.02 | 10.5 | 0.11 | 0.29 | 29 | <5 | 146 | 27 | 5.7 | 0.2 |
| South | Massive Py-Sph | KCD209757 | 0.016 | 0.03 | 24.2 | 5.65 | 14.88 | 29 | 38 | 157 | 608 | 4.8 | 1.2 |
| South | | KCD209762 | 0.021 | 0.10 | 21.2 | 4.88 | 12.85 | 42 | 77 | 72.6 | 624 | 51 | <0.1 |
| South | Massive Sph | KCD209763 | 0.021 | 0.03 | 26.3 | 3.98 | 10.48 | 193 | 122 | 108 | 2530 | 88 | 0.8 |
| South | | KCD209764 | 0.014 | <0.01 | 26.0 | 3.39 | 8.93 | 46 | 99 | 114 | 1900 | 79.6 | 2.5 |
| South | Massive Sph-Cp | KCD209752 | 0.064 | <0.01 | 21.3 | 1.74 | 4.58 | 227 | 65 | 124 | 3780 | 1.5 | <0.1 |
| South | | KCD209759 | 0.039 | 0.08 | 15.4 | 7.05 | 18.56 | 59 | 320 | 109 | 2950 | 18.7 | <0.1 |
| South | Py Stringer | KCD209761 | 0.018 | 0.12 | 5.21 | 3.13 | 8.24 | <2 | 22 | 41 | 30 | 11.4 | 1.6 |
| South | Sph Stringer | KCD209755 | 0.027 | 0.08 | 3.91 | 0.56 | 1.47 | 23 | <5 | 377 | 1010 | 5.4 | 0.7 |
| South | | KCD209760 | 0.025 | 0.18 | 7.21 | 2.52 | 6.64 | 31 | 74 | 17.8 | 702 | 9 | 0.5 |
| Cu Str | Lapillistone Rhy | KCD209775 | 0.006 | 0.08 | 0.11 | 0.02 | 0.05 | <2 | <5 | 80.5 | <0.5 | <0.1 | 0.8 |
| Cu Str | Massive Py-Cp | KCD209773 | 0.027 | 0.02 | 15.6 | 0.27 | 0.71 | 39 | 19 | 494 | 154 | 6.4 | 0.4 |
| Cu Str | Massive Cp | KCD209797 | 0.195 | 0.07 | 19.6 | 0.13 | 0.34 | <2 | 31 | 30.2 | 226 | 1.1 | <0.1 |
| Cu Str | Cp Stringer | KCD209772 | 0.076 | 0.10 | 15.7 | 0.74 | 1.95 | 49 | 147 | 542 | 105 | 7.4 | 5.1 |
| Cu Str | | KCD209774 | 0.150 | 0.10 | 7.68 | 0.39 | 1.03 | 16 | 83 | 175 | 168 | 2.3 | 0.4 |
| Cu Str | | KCD209789 | 0.034 | 0.03 | 5.86 | 0.25 | 0.66 | 45 | 48 | 16.7 | 215 | 1 | 0.2 |
| Cu Str | | KCD209790 | 0.127 | 0.10 | 5.93 | 0.66 | 1.74 | <2 | 34 | 3.1 | 152 | 1 | <0.1 |
| Cu Str | | KCD209793 | 0.034 | 0.08 | 4.20 | 0.10 | 0.26 | <2 | <5 | 39.4 | 95 | 0.3 | 0.5 |
| Cu Str | | KCD209794 | 0.165 | 0.28 | 18.1 | 0.71 | 1.87 | 78 | 65 | 5 | 1500 | <0.1 | 0.2 |
| Cu Str | | KCD209795 | 0.025 | 0.03 | 2.80 | 0.09 | 0.24 | <2 | 9 | 15.9 | 51 | 0.2 | 0.4 |
| Cu Str | | KCD209796 | 0.105 | 0.10 | 11.9 | 0.61 | 1.61 | <2 | 22 | 19.8 | 159 | 1.1 | <0.1 |
| Cu Str | | KCD209799 | 0.027 | 0.10 | 1.98 | 0.03 | 0.08 | 15 | <5 | 15.1 | 21 | 1.3 | <0.1 |
| Cu Str | | KCD209800 | 0.027 | 0.08 | 0.83 | <0.01 | - | <2 | <5 | 124 | 14 | 0.8 | 0.2 |
| Cu Str | | KCD209801 | 0.080 | 0.03 | 9.94 | 0.04 | 0.11 | 32 | 35 | 480 | 115 | 0.3 | <0.1 |
| Cu Str | | KCD209803 | 0.023 | 0.07 | 2.09 | 0.03 | 0.08 | <2 | <5 | 1.5 | 64 | 0.8 | <0.1 |
| Cu Str | | KCD209816 | 0.066 | <0.01 | 10.5 | 0.15 | 0.39 | 18 | 129 | 104 | 196 | 3 | <0.1 |
| Cu Str | | KCD209817 | 0.025 | 0.07 | 3.99 | 0.47 | 1.24 | <2 | 14 | 10.3 | 89 | 0.7 | 0.4 |
| Cu Str | | KCD209838 | 0.041 | 0.10 | 1.48 | 0.04 | 0.11 | <2 | <5 | 4.8 | 47 | 0.2 | 2.1 |
| Cu Str | | KCD209839 | 0.025 | 0.10 | 1.67 | 0.40 | 1.05 | <2 | <5 | 2.5 | 45 | <0.1 | 0.5 |
| Cu Str | | KCD209842 | 0.025 | 0.07 | 2.68 | 0.26 | 0.68 | 6 | 29 | 2.8 | 209 | 0.3 | 0.6 |
| Cu Str | | KCD209843 | 0.173 | 0.08 | 14.2 | 0.03 | 0.08 | 33 | 46 | 180 | 1040 | 3.1 | 0.9 |
| Cu Str | Py Stringer | KCD209776 | 0.006 | 0.08 | 1.64 | 0.19 | 0.50 | <2 | <5 | 8.1 | 30 | 2.1 | 0.8 |
| Cu Str | Sph Stringer | KCD209835 | 0.021 | 0.10 | 6.62 | 1.42 | 3.74 | 21 | <5 | 10.8 | 2090 | <0.1 | 1.1 |

| Lens | Ore Type | Sample # | Sn MS (ppm) | Cd MS (ppm) | Ga MS (ppm) | Ge MS (ppm) | In MS (ppm) | Bi MS (ppm) | Te MS (ppm) | Co MS (ppm) | Ni MS (ppm) | Se INAA (ppm) | Mo MS (ppm) |
|---|---|---|---|---|---|---|---|---|---|---|---|---|---|
| West | Heterolithic Py | KCD209768 | 330 | 4 | 14.3 | 12.9 | 0.5 | 11 | <6 | 11 | 10 | <3 | <1 |
| West | | KCD209861 | 539 | 66 | 11.8 | 3.8 | 7.5 | <2 | <6 | 15.1 | <5 | <3 | 38 |
| West | Heterolithic Py-Sph | KCD209779 | 96.8 | 125 | 8.5 | 5.3 | 1.1 | <2 | <6 | 9.7 | <5 | <3 | <1 |
| West | | KCD209862 | 363 | 665 | 36.9 | 4 | 15.3 | <2 | <6 | 89.4 | <5 | 22 | 2 |
| West | Massive Py-Sph | KCD209769 | 1040 | 281 | 9.4 | 3.7 | 3.5 | <2 | <6 | 23 | <5 | <3 | <1 |
| West | | KCD209770 | 1100 | 561 | 14.7 | 3.7 | 3.5 | <2 | <6 | 16 | <5 | <3 | <1 |
| West | | KCD209781 | 5050 | 57 | 4 | 4.8 | <0.2 | <2 | <6 | 2 | <5 | <3 | <1 |
| West | | KCD209782 | 1160 | 316 | 16.8 | 4.2 | 2.6 | <2 | <6 | 13.1 | <5 | 20 | <1 |
| West | Massive Py-Cp | KCD209771 | 186 | 25 | 4.1 | 1.4 | 19.2 | 27 | <6 | 502 | <5 | 19 | <1 |
| West | Massive Sph-Cp | KCD209783 | 1620 | 1440 | 82.5 | 1.7 | 88.1 | 54 | <6 | 521 | 30 | 1040 | <1 |
| West | | KCD209784 | 190 | 653 | 75.8 | 5.3 | 34.2 | 24 | <6 | 362 | 40 | 289 | 3 |
| West | | KCD209807 | 1310 | 809 | 16.2 | 6.4 | 100 | <2 | <6 | 36 | <5 | 24 | <1 |
| West | | KCD209811 | 2330 | 417 | 13.6 | 3.5 | 9.3 | 59 | <6 | 160 | 50 | 56 | <1 |
| West | Cp Stringer | KCD209864 | 510 | 8 | 22.5 | <0.7 | 77.7 | 11 | <6 | 24.9 | <5 | 48 | 1 |
| West | | KCD209866 | 794 | 13 | 17.4 | 0.7 | 113 | 33 | <6 | 15.5 | <5 | 183 | 8 |
| West | | KCD209867 | 48.3 | 69 | 21.8 | <0.7 | 8.1 | <2 | <6 | 23.4 | <5 | <3 | <1 |
| West | Sph Stringer | KCD209780 | 1270 | <2 | 3.1 | 3.2 | <0.2 | <2 | <6 | 1.3 | <5 | <3 | <1 |
| West | | KCD209868 | 82 | 224 | 18 | <0.7 | 5.3 | <2 | <6 | 12.1 | <5 | <3 | <1 |
| West | | KCD209806 | 936 | 639 | 14.6 | 9.4 | 12.5 | 3 | <6 | 59.6 | <5 | <3 | 1 |
| West | Sph-Cp Stringer | KCD209809 | 1480 | 723 | 36.9 | 12.2 | 68.6 | 133 | <6 | 268 | 20 | 340 | <1 |
| West/Main | Lapillistone Rhy | KCD209786 | 7.8 | <2 | 10.5 | 2.1 | <0.2 | 7 | 14 | 27.7 | <5 | <3 | 4 |
| West/Main | Heterolithic Py-Sph | KCD209848 | 151 | 175 | 39.5 | 1.8 | 16.5 | <2 | <6 | 37 | <5 | <3 | <1 |
| West/Main | | KCD209872 | 1960 | 806 | 5.2 | 4.1 | 30.9 | <2 | <6 | 36.1 | <5 | <3 | <1 |
| West/Main | Massive Sph-Cp | KCD209852 | 91.8 | 324 | 4.8 | 1.3 | 2.4 | 9 | <6 | 171 | 10 | 131 | 2 |
| West/Main | | KCD209856 | 115 | 399 | 53.5 | 1.8 | 67.3 | <2 | <6 | 34.8 | <5 | 94 | 4 |
| West/Main | | KCD209873 | 1170 | 295 | 17.5 | 1.5 | 249 | <2 | <6 | 103 | <5 | 64 | 1 |
| West/Main | Cp Stringer | KCD209876 | 441 | 20 | 40.1 | 1.1 | 76.7 | 13 | <6 | 90.4 | <5 | 128 | <1 |
| West/Main | | KCD209877 | 210 | 10 | 11.5 | 1.6 | 26.2 | 7 | <6 | 58.9 | 10 | 93 | <1 |
| West/Main | | KCD209879 | 60.6 | <2 | 19.6 | <0.7 | 7.7 | <2 | <6 | 22.3 | <5 | 22 | 3 |
| West/Main | Sph Stringer | KCD209851 | 267 | 130 | 26.4 | 2.7 | 1.9 | <2 | <6 | 13 | 20 | <3 | <1 |
| West/Main | Sph-Cp Stringer | KCD209785 | 349 | 196 | 19.6 | 3.5 | 10.1 | 342 | 83 | 4320 | 2300 | 209 | 8 |
| West/Main | | KCD209787 | 656 | 490 | 24.8 | 2.2 | 150 | 19 | <6 | 246 | 30 | 39 | <1 |
| West/Main | | KCD209858 | 503 | 95 | 44.5 | 0.9 | 147 | 4 | <6 | 191 | <5 | 433 | 1 |
| West/Main | | KCD209875 | 2920 | 661 | 31 | 0.8 | 140 | 6 | <6 | 108 | 10 | 159 | <1 |
| Main | Massive Sph | KCD209815 | 1250 | 467 | 23.9 | 2.4 | 30.7 | 9 | <6 | 368 | <5 | 72 | <1 |
| Main | Massive Sph-Cp | KCD209788 | 1480 | 770 | 28.9 | 6.4 | 184 | 14 | <6 | 543 | <5 | 307 | <1 |
| Main | | KCD209812 | 286 | 219 | 52.7 | 8.1 | 6.9 | 4 | <6 | 29.4 | 90 | 126 | <1 |
| Main | SphStringer | KCD209813 | 741 | 975 | 18.2 | 3.7 | 65.3 | <2 | <6 | 54.1 | <5 | 22 | <1 |
| Main | | KCD209814 | 724 | 183 | 38.4 | 3.1 | 22.8 | 7 | <6 | 170 | <5 | 9 | <1 |
| South | Massive Py-Sph | KCD209757 | 229 | 121 | 8.7 | 1.7 | 8.6 | 2 | <6 | 62.5 | <5 | 41 | <1 |
| South | | KCD209762 | 3640 | 801 | 36.2 | 6.9 | 22.2 | <2 | <6 | 19.1 | <5 | <3 | <1 |
| South | Massive Sph | KCD209763 | 5100 | 896 | 32.9 | 11.6 | 15.3 | 4 | <6 | 16.4 | <5 | <3 | <1 |
| South | | KCD209764 | 2630 | 376 | 11.8 | 7.3 | 14.4 | <2 | <6 | 9.2 | <5 | <3 | <1 |
| South | Massive Sph-Cp | KCD209752 | 556 | 743 | 38.9 | 1 | 104 | 14 | <6 | 258 | <5 | 95 | <1 |
| South | | KCD209759 | 589 | 640 | 31.1 | 1.8 | 61.6 | 8 | <6 | 104 | <5 | 119 | <1 |
| South | Py Stringer | KCD209761 | 193 | 14 | 17.4 | 9 | <0.2 | 5 | <6 | 4.9 | <5 | <3 | <1 |
| South | Sph Stringer | KCD209755 | 225 | 125 | 19.3 | 2 | 12.9 | <2 | <6 | 52.9 | <5 | 16 | <1 |
| South | | KCD209760 | 1460 | 399 | 32.8 | 7.4 | 8 | 4 | <6 | 17 | 10 | 18 | <1 |
| Cu Str | Lapillistone Rhy | KCD209775 | 15 | <2 | 21.3 | 0.8 | <0.2 | <2 | <6 | 4.5 | <5 | <3 | 2 |
| Cu Str | Massive Py-Cp | KCD209773 | 533 | 21 | 13.3 | 1.6 | 178 | 7 | <6 | 894 | <5 | 107 | <1 |
| Cu Str | Massive Cp | KCD209797 | 1200 | 5 | 28.3 | 8.6 | 320 | 90 | <6 | 120 | <5 | 170 | <1 |
| Cu Str | Cp Stringer | KCD209772 | 660 | 45 | 21.3 | 2.6 | 175 | 29 | <6 | 506 | <5 | 180 | <1 |
| Cu Str | | KCD209774 | 318 | 5 | 20.2 | 1 | 66.7 | 30 | <6 | 176 | <5 | 136 | 90 |
| Cu Str | | KCD209789 | 242 | 7 | 13.2 | 1.4 | 55.8 | <2 | <6 | 30 | <5 | 36 | <1 |
| Cu Str | | KCD209790 | 255 | 8 | 17.3 | 5.1 | 114 | <2 | <6 | 52 | <5 | 35 | 5 |
| Cu Str | | KCD209793 | 333 | <2 | 18.7 | 0.9 | 45.9 | 4 | <6 | 122 | 10 | 25 | <1 |
| Cu Str | | KCD209794 | 1940 | 233 | 15 | 1.6 | 129 | 175 | <6 | 157 | 20 | 11 | 2 |
| Cu Str | | KCD209795 | 170 | <2 | 14 | 1.2 | 45 | 7 | <6 | 50.2 | <5 | 29 | <1 |
| Cu Str | | KCD209796 | 553 | 3 | 20.8 | 5.8 | 187 | 8 | <6 | 153 | <5 | 107 | <1 |
| Cu Str | | KCD209799 | 98.2 | 2 | 14.2 | 0.8 | 39.5 | 157 | <6 | 20 | <5 | 65 | <1 |
| Cu Str | | KCD209800 | 50.7 | <2 | 37.6 | 1.3 | 8.6 | 25 | <6 | 109 | 10 | 13 | 9 |
| Cu Str | | KCD209801 | 498 | <2 | 13.4 | 0.8 | 160 | 60 | <6 | 462 | 20 | 204 | <1 |
| Cu Str | | KCD209803 | 87.5 | 10 | 17.5 | 1.1 | 31.5 | 8 | <6 | 36.7 | <5 | 18 | <1 |
| Cu Str | | KCD209816 | 378 | 23 | 14.2 | 1.8 | 75.4 | 2 | <6 | 170 | <5 | 204 | <1 |
| Cu Str | | KCD209817 | 221 | 5 | 17.2 | 1.5 | 68.2 | 3 | <6 | 39.2 | <5 | 60 | <1 |
| Cu Str | | KCD209838 | 126 | 2 | 25.7 | 1.4 | 23.8 | 3 | <6 | 26.6 | <5 | <3 | <1 |
| Cu Str | | KCD209839 | 66.2 | 2 | 16.1 | 1.3 | 17.2 | <2 | <6 | 28 | <5 | 7 | 7 |
| Cu Str | | KCD209842 | 95.8 | 13 | 16.5 | 1.7 | 0.2 | <2 | <6 | 1.3 | <5 | <3 | <1 |
| Cu Str | | KCD209843 | 571 | 143 | 22 | 1.3 | 97.5 | 6 | <6 | 408 | <5 | 22 | 2 |
| Cu Str | Py Stringer | KCD209776 | 40.8 | 2 | 19.3 | 1.1 | <0.2 | <2 | <6 | 1.8 | <5 | <3 | 1 |
| Cu Str | Sph Stringer | KCD209835 | 1160 | 522 | 19.7 | 1 | 47.8 | 4 | <6 | 59.5 | <5 | 21 | <1 |

| Lens | Ore Type | Sample # | Ir INAA (ppm) | Ba MS (ppm) | Rb MS (ppm) | Sr MS (ppm) | Li MS (ppm) | B MS (ppm) | Br INAA (ppm) | Cs MS (ppm) | Be MS (ppm) | ΣREE (ppm) | La MS (ppm) |
|---|---|---|---|---|---|---|---|---|---|---|---|---|---|
| West | Heterolithic Py | KCD209768 | <5 | <3 | 3.9 | 59 | 14 | <5 | <0.5 | 0.3 | <3 | 137 | 22.3 |
| West | | KCD209861 | <5 | <3 | <0.4 | 20 | <3 | <5 | <0.5 | <0.1 | <3 | 165 | 53.5 |
| West | Heterolithic Py-Sph | KCD209779 | <5 | 4 | 24.7 | 15 | 7 | <5 | <0.5 | 0.6 | <3 | 46 | 9.4 |
| West | | KCD209862 | <5 | 60 | 5.9 | 9 | 14 | <5 | <0.5 | 0.3 | <3 | 149 | 45.2 |
| West | Massive Py-Sph | KCD209769 | <5 | <3 | <0.4 | 30 | <3 | <5 | <0.5 | <0.1 | <3 | 17 | 3.8 |
| West | | KCD209770 | <5 | <3 | 0.6 | 7 | <3 | <5 | <0.5 | <0.1 | <3 | 57 | 12.7 |
| West | | KCD209781 | <5 | <3 | <0.4 | <3 | <3 | <5 | <0.5 | <0.1 | <3 | 5 | 1.1 |
| West | | KCD209782 | <5 | <3 | <0.4 | <3 | <3 | <5 | <0.5 | <0.1 | <3 | 3 | 1.2 |
| West | Massive Py-Cp | KCD209771 | <5 | <3 | 0.9 | 7 | <3 | <5 | <0.5 | <0.1 | <3 | 5 | 0.7 |
| West | Massive Sph-Cp | KCD209783 | <5 | <3 | <0.4 | <3 | <3 | <5 | <0.5 | <0.1 | <3 | 40 | 6.1 |
| West | | KCD209784 | <5 | <3 | <0.4 | 11 | 6 | <5 | <0.5 | <0.1 | <3 | 19 | 3.6 |
| West | | KCD209807 | <5 | 15 | 6 | 12 | <3 | <5 | <0.5 | 0.2 | <3 | 30 | 8.5 |
| West | | KCD209811 | <5 | <3 | <0.4 | 8 | <3 | <5 | <0.5 | <0.1 | <3 | 40 | 10.6 |
| West | Cp Stringer | KCD209864 | <5 | 251 | 58.2 | 28 | 16 | 20 | <0.5 | 2.1 | <3 | 74 | 4.6 |
| West | | KCD209866 | <5 | 209 | 48.2 | 24 | 13 | <5 | <0.5 | 1.5 | <3 | 83 | 14.5 |
| West | | KCD209867 | <5 | 328 | 69.3 | 38 | 13 | 20 | <0.5 | 1.9 | <3 | 65 | 10.2 |
| West | Sph Stringer | KCD209780 | <5 | <3 | <0.4 | 4 | <3 | <5 | <0.5 | <0.1 | <3 | 2 | <0.4 |
| West | | KCD209868 | <5 | 175 | 46.7 | 17 | 13 | 70 | <0.5 | 1.0 | <3 | 91 | 11.3 |
| West | | KCD209806 | <5 | 33 | 13.2 | 17 | 7 | <5 | <0.5 | 0.6 | <3 | 71 | 19.7 |
| West | Sph-Cp Stringer | KCD209809 | <5 | 33 | 17.5 | 33 | 34 | 10 | <0.5 | 1.4 | <3 | 57 | 11.6 |
| West/Main | Lapillistone Rhy | KCD209786 | <5 | 145 | 52.8 | 28 | 24 | 60 | <0.5 | 2.0 | <3 | 183 | 40.1 |
| West/Main | Heterolithic Py-Sph | KCD209848 | <5 | 7 | 3.2 | 109 | 7 | <5 | <0.5 | 0.4 | <3 | 74 | 22.8 |
| West/Main | | KCD209872 | <5 | 4 | 0.7 | 27 | <3 | <5 | <0.5 | <0.1 | <3 | 28 | 5.5 |
| West/Main | Massive Sph-Cp | KCD209852 | <5 | 4 | 0.8 | 22 | <3 | <5 | <0.5 | <0.1 | <3 | 12 | <0.4 |
| West/Main | | KCD209856 | <5 | 10 | 16 | 44 | 41 | <5 | <0.5 | 4.1 | <3 | 86 | 26.8 |
| West/Main | | KCD209873 | <5 | 71 | 18 | 54 | 14 | <5 | <0.5 | 0.7 | <3 | 110 | 7 |
| West/Main | Cp Stringer | KCD209876 | <5 | 48 | 6.7 | 6 | 14 | <5 | <0.5 | 1.3 | <3 | 83 | 18 |
| West/Main | | KCD209877 | <5 | 14 | 0.6 | 7 | <3 | <5 | <0.5 | 0.4 | <3 | 18 | 3.3 |
| West/Main | | KCD209879 | <5 | 331 | 60 | 21 | 22 | <5 | <0.5 | 2.1 | <3 | 114 | 13.6 |
| West/Main | Sph Stringer | KCD209851 | <5 | 56 | 10.9 | 42 | 15 | <5 | <0.5 | 0.4 | <3 | 94 | 24.1 |
| West/Main | Sph-Cp Stringer | KCD209785 | <5 | 21 | 8.3 | 7 | 63 | 30 | <0.5 | 1.7 | <3 | 633 | 76.8 |
| West/Main | | KCD209787 | <5 | <3 | <0.4 | 3 | 15 | <5 | <0.5 | <0.1 | <3 | 46 | 6.2 |
| West/Main | | KCD209858 | <5 | <3 | 10.2 | 83 | 43 | 100 | <0.5 | 2.2 | <3 | 67 | 18.2 |
| West/Main | | KCD209875 | <5 | 175 | 31.9 | 26 | 39 | <5 | <0.5 | 1.4 | <3 | 37 | 5.2 |
| Main | Massive Sph | KCD209815 | <5 | 15 | 5.8 | <3 | 5 | <5 | <0.5 | 0.6 | <3 | 32 | 9.1 |
| Main | Massive Sph-Cp | KCD209788 | <5 | <3 | <0.4 | 18 | <3 | 10 | <0.5 | 0.2 | <3 | 38 | 10.8 |
| Main | | KCD209812 | <5 | 9 | 5.6 | 24 | 44 | <5 | <0.5 | 1.6 | <3 | 158 | 35.7 |
| Main | SphStringer | KCD209813 | <5 | 7 | 2.8 | <3 | 5 | <5 | <0.5 | 0.5 | <3 | 191 | 45.6 |
| Main | | KCD209814 | <5 | 13 | 3.5 | 6 | 6 | <5 | <0.5 | 0.3 | <3 | 54 | 16.1 |
| South | Massive Py-Sph | KCD209757 | <5 | 5 | 14.5 | 27 | 51 | <5 | <0.5 | 4.2 | <3 | 26 | 7.6 |
| South | | KCD209762 | <5 | <3 | <0.4 | 16 | <3 | <5 | <0.5 | <0.1 | <3 | 63 | 13.5 |
| South | Massive Sph | KCD209763 | <5 | <3 | <0.4 | 8 | <3 | <5 | <0.5 | <0.1 | <3 | 32 | 7.3 |
| South | | KCD209764 | <5 | <3 | <0.4 | 20 | <3 | <5 | <0.5 | <0.1 | <3 | 24 | 4.3 |
| South | Massive Sph-Cp | KCD209752 | <5 | <3 | <0.4 | 23 | <3 | <5 | <0.5 | <0.1 | <3 | 32 | 10 |
| South | | KCD209759 | <5 | 4 | <0.4 | 59 | 8 | <5 | <0.5 | <0.1 | <3 | 78 | 17.9 |
| South | Py Stringer | KCD209761 | <5 | 71 | 22.2 | 7 | 38 | <5 | <0.5 | <0.1 | <3 | 107 | 23.5 |
| South | Sph Stringer | KCD209755 | <5 | 59 | 25.3 | 12 | 43 | 30 | <0.5 | 1.2 | <3 | 80 | 20.7 |
| South | | KCD209760 | <5 | 11 | 2.8 | 18 | 16 | <5 | <0.5 | <0.1 | <3 | 150 | 35.4 |
| Cu Str | Lapillistone Rhy | KCD209775 | <5 | 14 | 65.1 | 29 | 43 | <5 | <0.5 | 2.7 | <3 | 126 | 11.6 |
| Cu Str | Massive Py-Cp | KCD209773 | <5 | <3 | 3.1 | 19 | 6 | <5 | <0.5 | 0.2 | <3 | 51 | 8 |
| Cu Str | Massive Cp | KCD209797 | <5 | 52 | 0.9 | 15 | 35 | 20 | <0.5 | 0.6 | <3 | 144 | 33.6 |
| Cu Str | Cp Stringer | KCD209772 | <5 | 36 | 8.5 | 33 | 11 | <5 | <0.5 | <0.1 | <3 | 140 | 41.4 |
| Cu Str | | KCD209774 | <5 | 59 | 12.9 | 33 | 11 | 10 | <0.5 | <0.1 | <3 | 93 | 17.9 |
| Cu Str | | KCD209789 | <5 | 15 | 8 | 11 | 14 | 30 | <0.5 | 0.3 | <3 | 52 | 12.2 |
| Cu Str | | KCD209790 | <5 | 12 | 6.2 | 8 | 35 | 30 | <0.5 | 0.2 | <3 | 93 | 27.7 |
| Cu Str | | KCD209793 | <5 | 97 | 25.8 | 11 | 26 | 10 | <0.5 | 0.8 | <3 | 107 | 23.2 |
| Cu Str | | KCD209794 | <5 | <3 | <0.4 | 14 | 14 | <5 | <0.5 | <0.1 | <3 | 43 | 8.5 |
| Cu Str | | KCD209795 | <5 | 33 | 13.2 | 19 | 15 | 30 | <0.5 | 0.4 | <3 | 79 | 10 |
| Cu Str | | KCD209796 | <5 | 3 | 1.4 | 25 | 24 | 10 | <0.5 | 0.2 | <3 | 80 | 14.6 |
| Cu Str | | KCD209799 | <5 | 71 | 14.3 | 6 | 23 | <5 | <0.5 | 0.4 | <3 | 55 | 5.2 |
| Cu Str | | KCD209800 | <5 | 73 | 18.1 | 10 | 86 | 20 | <0.5 | 1.0 | <3 | 175 | 37.2 |
| Cu Str | | KCD209801 | <5 | 12 | 2.9 | <3 | 25 | <5 | <0.5 | <0.1 | <3 | 37 | 7.5 |
| Cu Str | | KCD209803 | <5 | 57 | 14 | 3 | 23 | <5 | <0.5 | 0.5 | <3 | 58 | 7.8 |
| Cu Str | | KCD209816 | <5 | 11 | 2.7 | 3 | 3 | <5 | <0.5 | <0.1 | <3 | 29 | 8.1 |
| Cu Str | | KCD209817 | <5 | 87 | 31.1 | 25 | 23 | 20 | <0.5 | 1.1 | <3 | 99 | 20.2 |
| Cu Str | | KCD209838 | <5 | 263 | 68.6 | 27 | 14 | 30 | <0.5 | 2.4 | <3 | 256 | 66.5 |
| Cu Str | | KCD209839 | <5 | 107 | 25.6 | 12 | 16 | 10 | <0.5 | 0.9 | <3 | 109 | 24 |
| Cu Str | | KCD209842 | <5 | 192 | 49.3 | 16 | 11 | 30 | <0.5 | 1.6 | <3 | 194 | 38.3 |
| Cu Str | | KCD209843 | <5 | 234 | 61.7 | 27 | 12 | 1110 | <0.5 | 1.9 | <3 | 239 | 65.9 |
| Cu Str | Py Stringer | KCD209776 | <5 | 14 | 61.3 | 20 | 14 | 30 | <0.5 | 2.5 | <3 | 170 | 27.2 |
| Cu Str | Sph Stringer | KCD209835 | <5 | 67 | 20.1 | 19 | 11 | 20 | <0.5 | 0.6 | <3 | 45 | 4.5 |

| Lens | Ore Type | Sample # | Nd MS (ppm) | Sm MS (ppm) | Eu MS (ppm) | Tb MS (ppm) | Yb MS (ppm) | Lu INAA (ppm) | Pr MS (ppm) | Gd MS (ppm) | Dy MS (ppm) | Er MS (ppm) | Tm MS (ppm) |
|---|---|---|---|---|---|---|---|---|---|---|---|---|---|
| West | Heterolithic Py | KCD209768 | 16.3 | 6.2 | 2.6 | 1.9 | 7 | 0.74 | 46.7 | 9.3 | 12.4 | 7.8 | 1.1 |
| West | | KCD209861 | 62 | 11.7 | 1.9 | 1 | 2 | 0.12 | 15.8 | 8.8 | 5.1 | 2.4 | 0.3 |
| West | Heterolithic Py-Sph | KCD209779 | 6.5 | 1.6 | 0.4 | 0.3 | 1.5 | 0.14 | 19.9 | 1.9 | 2 | 1.4 | 0.2 |
| West | | KCD209862 | 57.9 | 10.7 | 1 | 0.7 | 3.5 | 0.29 | 14.8 | 6.8 | 3.9 | 2.8 | 0.4 |
| West | Massive Py-Sph | KCD209769 | 2.2 | 0.6 | 0.3 | <0.1 | 0.5 | <0.05 | 6.6 | 0.9 | 0.9 | 0.6 | <0.1 |
| West | | KCD209770 | 9.1 | 2.3 | 0.5 | 0.2 | 0.3 | <0.05 | 29.2 | 1.9 | 0.7 | 0.3 | <0.1 |
| West | | KCD209781 | 0.6 | <0.1 | <0.1 | <0.1 | 0.2 | <0.05 | 1.7 | 0.2 | 0.3 | 0.2 | <0.1 |
| West | | KCD209782 | 0.9 | <0.1 | <0.1 | <0.1 | <0.1 | <0.05 | 0.3 | <0.1 | <0.3 | <0.1 | <0.1 |
| West | Massive Py-Cp | KCD209771 | 0.4 | <0.1 | <0.1 | <0.1 | 0.7 | 0.12 | 1.3 | 0.3 | 0.6 | 0.6 | <0.1 |
| West | Massive Sph-Cp | KCD209783 | 6 | 3.7 | 0.2 | 0.5 | 0.8 | <0.05 | 15.2 | 3.8 | 2.5 | 1 | <0.1 |
| West | | KCD209784 | 2.8 | 1.3 | 0.2 | 0.2 | 0.4 | <0.05 | 7 | 1.6 | 1.1 | 0.5 | <0.1 |
| West | | KCD209807 | 10.8 | 2.2 | 0.2 | 0.2 | 1.1 | <0.05 | 2.8 | 1.5 | 1.2 | 0.9 | 0.2 |
| West | | KCD209811 | 12.3 | 3 | 0.3 | 0.5 | 1.7 | 0.11 | 3 | 2.8 | 2.9 | 1.9 | 0.3 |
| West | Cp Stringer | KCD209864 | 9.9 | 4.4 | 0.3 | 1.7 | 12.3 | 1.22 | 1.9 | 6.2 | 14.4 | 11.7 | 1.8 |
| West | | KCD209866 | 25.6 | 7.5 | 0.5 | 1.2 | 5.7 | 0.59 | 5.5 | 7.1 | 7.8 | 4.9 | 0.7 |
| West | | KCD209867 | 16.1 | 4.8 | 0.4 | 1 | 7.3 | 0.85 | 3.6 | 4.7 | 7.7 | 5.8 | 0.9 |
| West | Sph Stringer | KCD209780 | <0.4 | <0.1 | <0.1 | <0.1 | <0.1 | <0.05 | 0.4 | <0.1 | <0.3 | <0.1 | <0.1 |
| West | | KCD209868 | 21.1 | 6.6 | 0.4 | 1.7 | 10.3 | 0.97 | 4.6 | 7.9 | 12.6 | 9.2 | 1.4 |
| West | | KCD209806 | 25.2 | 4.9 | 0.5 | 0.5 | 2.9 | 0.53 | 6.3 | 3.4 | 3.2 | 2.5 | 0.4 |
| West | Sph-Cp Stringer | KCD209809 | 17.6 | 4.4 | 0.3 | 0.8 | 3.4 | 0.31 | 4.1 | 4.5 | 4.7 | 3.6 | 0.5 |
| West/Main | Lapillistone Rhy | KCD209786 | 53.3 | 13.7 | 1 | 2.4 | 11.3 | 2.22 | 12.4 | 13.4 | 16.7 | 11.5 | 1.7 |
| West/Main | Heterolithic Py-Sph | KCD209848 | 24.4 | 4.8 | 0.4 | 0.5 | 3.6 | 0.39 | 6.3 | 3.2 | 3.5 | 3 | 0.5 |
| West/Main | | KCD209872 | 6.9 | 1.9 | 0.4 | 0.5 | 1.7 | <0.05 | 1.7 | 2.5 | 3.6 | 2 | 0.3 |
| West/Main | Massive Sph-Cp | KCD209852 | 1 | 0.7 | <0.1 | 0.3 | 2 | 0.22 | 0.2 | 1.4 | 2.6 | 2 | 0.3 |
| West/Main | | KCD209856 | 27.7 | 6.6 | 0.7 | 0.7 | 2.9 | 0.27 | 6.8 | 5.1 | 4.6 | 3 | 0.4 |
| West/Main | | KCD209873 | 11 | 3.9 | 0.4 | 2 | 24.5 | 2.55 | 2.5 | 6.4 | 20.4 | 21 | 3.4 |
| West/Main | Cp Stringer | KCD209876 | 32.3 | 6.9 | 0.8 | 0.7 | 3.9 | 0.41 | 6.9 | 5 | 3.7 | 2.9 | 0.5 |
| West/Main | | KCD209877 | 5.6 | 1.9 | <0.1 | 0.3 | 1.1 | 0.12 | 1.2 | 1.7 | 1.5 | 0.9 | <0.1 |
| West/Main | | KCD209879 | 30.9 | 10.3 | 0.4 | 2.1 | 9.8 | 1.16 | 6.5 | 10.6 | 14.8 | 9.5 | 1.4 |
| West/Main | Sph Stringer | KCD209851 | 25.7 | 6.2 | 0.7 | 1.2 | 6.1 | 0.7 | 6.5 | 6.1 | 8 | 5.6 | 0.8 |
| West/Main | Sph-Cp Stringer | KCD209785 | 90 | 43.8 | 2.4 | 17.6 | 64.8 | 8.8 | 20.3 | 83.9 | 118 | 71.8 | 10.2 |
| West/Main | | KCD209787 | 6.1 | 2.5 | 0.2 | 0.5 | 3.2 | 0.33 | 16.4 | 2.9 | 3.4 | 2.6 | 0.4 |
| West/Main | | KCD209858 | 22.6 | 5.7 | 0.4 | 0.6 | 2.7 | 0.22 | 5.4 | 4.2 | 3.5 | 2.3 | 0.3 |
| West/Main | | KCD209875 | 8.3 | 1.9 | <0.1 | 0.5 | 5.1 | 0.41 | 2 | 2.3 | 4.7 | 4.2 | 0.7 |
| Main | Massive Sph | KCD209815 | 10.2 | 1.9 | <0.1 | 0.3 | 1.7 | 0.21 | 2.7 | 1.5 | 1.7 | 1.5 | 0.3 |
| Main | Massive Sph-Cp | KCD209788 | 13.6 | 2.2 | 0.2 | 0.4 | 1.1 | 0.07 | 3.3 | 2.5 | 2.2 | 1.4 | 0.2 |
| Main | | KCD209812 | 48.2 | 12.7 | 1.7 | 2.1 | 8.6 | 0.85 | 11.8 | 11.7 | 12.9 | 8 | 1.2 |
| Main | SphStringer | KCD209813 | 54.2 | 11.7 | 0.7 | 3.3 | 7.6 | 0.69 | 14.5 | 13.6 | 22.5 | 11.2 | 1.3 |
| Main | | KCD209814 | 18.4 | 3.7 | 0.2 | 0.4 | 2.2 | 0.23 | 4.9 | 2.6 | 2.5 | 2 | 0.3 |
| South | Massive Py-Sph | KCD209757 | 7.9 | 1.7 | 0.2 | 0.2 | 1.1 | 0.19 | 1.8 | 1.6 | 1.8 | 1.1 | <0.1 |
| South | | KCD209762 | 17.8 | 3.9 | 0.5 | 0.9 | 4.1 | 0.57 | 3.1 | 4.8 | 6.7 | 4.9 | 0.6 |
| South | Massive Sph | KCD209763 | 6.3 | 1.8 | 0.3 | 0.5 | 2.8 | 0.22 | 1.5 | 2.6 | 4.2 | 3.4 | 0.4 |
| South | | KCD209764 | 4.5 | 1.2 | 0.3 | 0.4 | 2.2 | 0.18 | 1 | 2.4 | 3.7 | 2.7 | 0.3 |
| South | Massive Sph-Cp | KCD209752 | 10.8 | 2.5 | <0.1 | 0.2 | 0.7 | <0.05 | 2.7 | 2 | 1.4 | 0.8 | <0.1 |
| South | | KCD209759 | 22.7 | 6 | 0.6 | 1 | 3.9 | 0.62 | 5.2 | 6.7 | 7 | 4.2 | 0.5 |
| South | Py Stringer | KCD209761 | 30.2 | 7.3 | 0.9 | 1.4 | 6.7 | 1.42 | 7.3 | 7.9 | 10.5 | 7 | 0.9 |
| South | Sph Stringer | KCD209755 | 23.3 | 4.5 | 0.4 | 0.8 | 5.2 | 1.09 | 5.9 | 4.6 | 6.7 | 5.1 | 0.7 |
| South | | KCD209760 | 46.3 | 12 | 0.8 | 2 | 6.8 | 1.26 | 10.7 | 12.1 | 12.3 | 7.3 | 1 |
| Cu Str | Lapillistone Rhy | KCD209775 | 13.3 | 7.1 | 0.7 | 2.6 | 11.4 | 1.24 | 33.6 | 10.9 | 17.4 | 11.1 | 1.7 |
| Cu Str | Massive Py-Cp | KCD209773 | 6.8 | 1.9 | <0.1 | 0.5 | 2.9 | 0.28 | 19.6 | 2.7 | 3.9 | 2.8 | 0.4 |
| Cu Str | Massive Cp | KCD209797 | 51.9 | 11 | 0.2 | 1.4 | 6.2 | 0.7 | 13.9 | 8.7 | 7.5 | 6.1 | 0.9 |
| Cu Str | Cp Stringer | KCD209772 | 47.8 | 9.1 | 0.5 | 1 | 6 | 1.1 | 12.4 | 7.1 | 6.4 | 5.2 | 0.8 |
| Cu Str | | KCD209774 | 30.5 | 6.7 | 0.2 | 1 | 6.5 | 1.34 | 7.1 | 5.9 | 7.6 | 5.7 | 0.9 |
| Cu Str | | KCD209789 | 16.9 | 3.1 | <0.1 | 0.5 | 3.6 | 0.78 | 4.2 | 2.8 | 3.8 | 3.1 | 0.5 |
| Cu Str | | KCD209790 | 20.7 | 7 | 0.7 | 1.2 | 5.1 | 0.6 | 8.6 | 7.5 | 6.5 | 4.9 | 0.8 |
| Cu Str | | KCD209793 | 29.4 | 7.3 | 0.4 | 1.5 | 7.9 | 1.61 | 7.1 | 7.6 | 9.9 | 7.4 | 1.1 |
| Cu Str | | KCD209794 | 12.9 | 3.6 | 0.3 | 0.6 | 2.6 | 0.15 | 3 | 3.5 | 4 | 2.6 | 0.4 |
| Cu Str | | KCD209795 | 17.5 | 5.4 | 0.2 | 1.4 | 9.2 | 1.98 | 3.9 | 6.4 | 10.4 | 8.5 | 1.3 |
| Cu Str | | KCD209796 | 28.2 | 6.8 | 0.2 | 1 | 5 | 0.64 | 6.4 | 5.4 | 5.8 | 4.4 | 0.7 |
| Cu Str | | KCD209799 | 11.1 | 4.1 | <0.1 | 1.3 | 7 | 0.72 | 2.4 | 4.9 | 9.2 | 6.4 | 1 |
| Cu Str | | KCD209800 | 58.6 | 14.1 | 0.5 | 2.1 | 9.1 | 1.9 | 13.4 | 12.4 | 13.1 | 8.5 | 1.3 |
| Cu Str | | KCD209801 | 11.5 | 2.4 | <0.1 | 0.5 | 2.9 | 0.28 | 3 | 2.3 | 3 | 2.4 | 0.4 |
| Cu Str | | KCD209803 | 16.5 | 4.7 | <0.1 | 1 | 5.7 | 0.67 | 3.8 | 4.3 | 6.7 | 4.8 | 0.8 |
| Cu Str | | KCD209816 | 10.4 | 2.1 | <0.1 | 0.2 | 1 | 0.09 | 2.7 | 1.4 | 1.2 | 0.9 | <0.1 |
| Cu Str | | KCD209817 | 30.4 | 7.7 | 0.8 | 1.3 | 6.7 | 1.24 | 7.1 | 7 | 7.8 | 5.6 | 0.9 |
| Cu Str | | KCD209838 | 86.4 | 19.4 | 1.2 | 3 | 8.8 | 1.02 | 21.4 | 17.3 | 17.1 | 9.4 | 1.3 |
| Cu Str | | KCD209839 | 34.6 | 8.3 | 0.3 | 1.4 | 6.4 | 0.65 | 8.5 | 7.4 | 9.1 | 6 | 0.9 |
| Cu Str | | KCD209842 | 62.7 | 17 | 1 | 2.8 | 9.1 | 1.06 | 14.2 | 15.3 | 17.4 | 9.9 | 1.4 |
| Cu Str | | KCD209843 | 81.7 | 16.8 | 1 | 2.2 | 9.8 | 1.08 | 20.7 | 13.4 | 13.2 | 9.1 | 1.4 |
| Cu Str | Py Stringer | KCD209776 | 22.7 | 9.6 | 0.9 | 2.3 | 7.3 | 0.76 | 64.2 | 12.9 | 12.6 | 6.4 | 1 |
| Cu Str | Sph Stringer | KCD209835 | 9.1 | 3.5 | 0.2 | 1 | 5.2 | 0.61 | 1.9 | 4.1 | 7.1 | 5.1 | 0.8 |

| Lens | Ore Type | Sample # | Y MS (ppm) | Hf INAA (ppm) | Sc INAA (ppm) | Ta MS (ppm) | Nb MS (ppm) | Th MS (ppm) | U MS (ppm) | W MS (ppm) | V MS (ppm) | Ho MS (ppm) |
|---|---|---|---|---|---|---|---|---|---|---|---|---|
| West | Heterolithic Py | KCD209768 | 81.5 | 3 | 5.6 | 0.7 | 10.9 | 3.3 | 0.8 | 12.2 | 45 | 2.7 |
| West | | KCD209861 | 29.5 | <1 | 0.3 | 0.3 | 4.8 | 3.1 | 1.6 | 8.1 | <5 | 0.8 |
| West | Heterolithic Py-Sph | KCD209779 | 10.7 | <1 | 0.6 | 0.2 | 3.3 | 1.8 | 0.2 | 3 | 27 | 0.4 |
| West | | KCD209862 | 20.4 | 3 | 0.7 | 1 | 14.1 | 5 | 1.2 | 7.3 | <5 | 0.8 |
| West | Massive Py-Sph | KCD209769 | 5.4 | <1 | 0.4 | <0.1 | <2.4 | 0.3 | <0.1 | 2.6 | 22 | <0.2 |
| West | | KCD209770 | 2.2 | <1 | <0.1 | <0.1 | <2.4 | 0.6 | <0.1 | 9.6 | 23 | <0.2 |
| West | | KCD209781 | 1.5 | <1 | 0.4 | <0.1 | <2.4 | <0.1 | <0.1 | 28.7 | 28 | <0.2 |
| West | | KCD209782 | 1.4 | <1 | <0.1 | <0.1 | <2.4 | <0.1 | <0.1 | 30.5 | <5 | <0.2 |
| West | Massive Py-Cp | KCD209771 | 3.7 | <1 | 0.2 | <0.1 | <2.4 | 0.8 | <0.1 | 10.1 | 25 | <0.2 |
| West | Massive Sph-Cp | KCD209783 | 9.9 | <1 | 0.8 | <0.1 | <2.4 | <0.1 | <0.1 | <0.7 | 29 | 0.4 |
| West | | KCD209784 | 4.9 | <1 | 3.9 | <0.1 | <2.4 | <0.1 | <0.1 | <0.7 | 37 | <0.2 |
| West | | KCD209807 | 5.2 | <1 | <0.1 | <0.1 | 3.3 | 1.1 | 0.2 | 2.9 | <5 | 0.3 |
| West | | KCD209811 | 15 | <1 | 1.7 | <0.1 | <2.4 | 0.9 | 0.2 | 8.2 | 13 | 0.6 |
| West | Cp Stringer | KCD209864 | 104 | 4 | 1.7 | 1.4 | 23.4 | 6.2 | 1.8 | 3.3 | <5 | 3.4 |
| West | | KCD209866 | 35.9 | 4 | 1.1 | 0.5 | 8 | 4.4 | 1.4 | 3.3 | <5 | 1.5 |
| West | | KCD209867 | 42.8 | 5 | 2.2 | 1.8 | 25.7 | 7.6 | 2.1 | 3.6 | <5 | 1.7 |
| West | Sph Stringer | KCD209780 | 0.6 | <1 | <0.1 | <0.1 | <2.4 | <0.1 | <0.1 | 19.9 | 30 | <0.2 |
| West | | KCD209868 | 84.5 | 4 | 1.3 | 1.5 | 23.2 | 6 | 1.6 | 4.1 | <5 | 2.8 |
| West | | KCD209806 | 17.5 | <1 | 0.5 | 0.2 | 4.9 | 1.6 | <0.1 | 8.7 | <5 | 0.7 |
| West | Sph-Cp Stringer | KCD209809 | 26.4 | 2 | 2.5 | 0.4 | 5.2 | 2.1 | 0.5 | 6.8 | 18 | 1.1 |
| West/Main | Lapillistone Rhy | KCD209786 | 94 | 6 | 7.5 | 1.4 | 23.4 | 7 | 1.6 | 11.9 | 30 | 3.7 |
| West/Main | Heterolithic Py-Sph | KCD209848 | 17.6 | 3 | 2 | 0.8 | 11.7 | 4.2 | 1 | 4 | 18 | 0.8 |
| West/Main | | KCD209872 | 25.3 | <1 | 0.4 | <0.1 | 2.9 | 0.8 | 0.3 | 21.2 | <5 | 0.7 |
| West/Main | Massive Sph-Cp | KCD209852 | 21.7 | <1 | 0.2 | <0.1 | <2.4 | <0.1 | 0.2 | 3.2 | <5 | 0.6 |
| West/Main | | KCD209856 | 27.5 | 5 | 2.8 | 1.8 | 32.9 | 6.7 | 1.5 | 11.6 | <5 | 0.9 |
| West/Main | | KCD209873 | 187 | 2 | 0.6 | 0.4 | 9.9 | 1.9 | 1.3 | 1.8 | <5 | 5.4 |
| West/Main | Cp Stringer | KCD209876 | 20.5 | 3 | 1.6 | 1 | 14.6 | 4.7 | 0.6 | 3.9 | <5 | 0.8 |
| West/Main | | KCD209877 | 8.8 | <1 | 1.4 | <0.1 | <2.4 | 0.3 | 2.3 | 3.5 | <5 | 0.3 |
| West/Main | | KCD209879 | 74 | 5 | 1.3 | 1.4 | 22.1 | 6.2 | 1.9 | 4.2 | <5 | 3 |
| West/Main | Sph Stringer | KCD209851 | 44.7 | 4 | 3 | 0.9 | 11.9 | 4.5 | 1 | 8.7 | 20 | 1.8 |
| West/Main | Sph-Cp Stringer | KCD209785 | 630 | 14 | 29.2 | 2.8 | 42.6 | 11.6 | 3.7 | 23.2 | 34 | 24.5 |
| West/Main | | KCD209787 | 18.4 | 2 | 0.9 | 0.2 | 6.4 | 1.6 | 0.2 | <0.7 | 31 | 0.8 |
| West/Main | | KCD209858 | 20.1 | 3 | 1.6 | 0.8 | 14.2 | 3.7 | 0.7 | 4.2 | <5 | 0.7 |
| West/Main | | KCD209875 | 34.3 | 3 | 1 | 0.9 | 14.6 | 3.6 | 3.8 | 2.3 | <5 | 1.1 |
| Main | Massive Sph | KCD209815 | 10.3 | <1 | 0.3 | <0.1 | 3.1 | 1.1 | <0.1 | 7.9 | <5 | 0.4 |
| Main | Massive Sph-Cp | KCD209788 | 14.8 | <1 | 0.6 | <0.1 | <2.4 | 0.3 | <0.1 | 6.2 | 20 | 0.5 |
| Main | | KCD209812 | 66.7 | 5 | 8.7 | 1.7 | 25.4 | 7.2 | 1.8 | 7.4 | 59 | 2.7 |
| Main | SphStringer | KCD209813 | 149 | <1 | 0.5 | 0.3 | 5.1 | 4.2 | 0.5 | 5.2 | 10 | 4.4 |
| Main | | KCD209814 | 13.1 | 2 | 0.4 | <0.1 | 4.1 | 1.6 | 0.4 | 7.6 | 8 | 0.6 |
| South | Massive Py-Sph | KCD209757 | 9.7 | <1 | 0.7 | 0.7 | 2.5 | 1.2 | 0.2 | 1.8 | <5 | 0.3 |
| South | | KCD209762 | 59.8 | <1 | 1.1 | 0.8 | 9.1 | 4 | 0.4 | 5.6 | <5 | 1.5 |
| South | Massive Sph | KCD209763 | 44.8 | <1 | 0.8 | <0.1 | 3.1 | 0.4 | <0.1 | 4.6 | <5 | 1 |
| South | | KCD209764 | 34.1 | <1 | 0.7 | <0.1 | <2.4 | 0.2 | <0.1 | 1.4 | <5 | 0.8 |
| South | Massive Sph-Cp | KCD209752 | 7.3 | <1 | 0.9 | <0.1 | <2.4 | 1.3 | 0.2 | 0.9 | <5 | 0.2 |
| South | | KCD209759 | 39.8 | 2 | 2.3 | 1.1 | 4.5 | 1.7 | 0.4 | 2.9 | 8 | 1.4 |
| South | Py Stringer | KCD209761 | 59.7 | 5 | 3 | 1 | 14.5 | 5.5 | 1.3 | 1.3 | 6 | 2.2 |
| South | Sph Stringer | KCD209755 | 38.9 | 4 | 1.5 | 0.7 | 9.9 | 3.6 | 0.8 | 11.2 | <5 | 1.5 |
| South | | KCD209760 | 71 | 4 | 3.9 | 0.8 | 12.9 | 4.9 | 1.1 | <0.7 | 17 | 2.5 |
| Cu Str | Lapillistone Rhy | KCD209775 | 84 | 5 | 1.7 | 1.5 | 21.3 | 7.3 | 1.7 | 10.9 | 23 | 3.7 |
| Cu Str | Massive Py-Cp | KCD209773 | 19.4 | <1 | 0.6 | <0.1 | 3.9 | 1.4 | <0.1 | <0.7 | 23 | 0.9 |
| Cu Str | Massive Cp | KCD209797 | 39.9 | 4 | 1 | 138 | 60.4 | 5.5 | 1.1 | 3 | 11 | 1.8 |
| Cu Str | Cp Stringer | KCD209772 | 33.2 | 5 | 1.1 | 0.8 | 12.4 | 5.6 | 1.1 | 2.6 | <5 | 1.5 |
| Cu Str | | KCD209774 | 38.6 | 6 | 1.3 | 0.9 | 14.1 | 4.7 | 1.2 | 42.1 | <5 | 1.7 |
| Cu Str | | KCD209789 | 23.1 | 3 | 0.7 | 0.5 | 7.6 | 2.7 | 0.3 | 2 | <5 | 0.9 |
| Cu Str | | KCD209790 | 32.2 | 3 | 1.2 | 1 | 13.8 | 4.7 | 1.3 | 10.8 | 16 | 1.5 |
| Cu Str | | KCD209793 | 59.4 | 5 | 1.9 | 0.8 | 15.9 | 4.9 | 0.8 | 1.4 | <5 | 2.3 |
| Cu Str | | KCD209794 | 23.1 | <1 | 7.1 | 0.4 | 5.9 | 1.6 | 0.6 | 3 | 29 | 0.8 |
| Cu Str | | KCD209795 | 70.2 | 4 | 1.2 | 0.6 | 11.3 | 4 | 0.6 | 2.5 | <5 | 2.5 |
| Cu Str | | KCD209796 | 25.4 | 3 | 0.7 | 1 | 12.2 | 4.4 | 1.1 | 3.6 | 14 | 1.3 |
| Cu Str | | KCD209799 | 44.1 | 3 | 0.9 | 0.9 | 12.4 | 4.4 | 1.2 | 10.2 | 6 | 2 |
| Cu Str | | KCD209800 | 61.6 | 9 | 2.4 | 1.8 | 41.9 | 9.6 | 2.6 | 5.8 | <5 | 2.8 |
| Cu Str | | KCD209801 | 15.9 | 2 | 0.6 | 0.6 | 8 | 3.1 | 0.7 | 3.9 | <5 | 0.7 |
| Cu Str | | KCD209803 | 28.1 | 4 | 1.1 | 1.2 | 16 | 5.2 | 1.4 | 1.4 | <5 | 1.5 |
| Cu Str | | KCD209816 | 6.2 | <1 | 0.3 | <0.1 | <2.4 | 0.9 | <0.1 | 3.7 | <5 | 0.3 |
| Cu Str | | KCD209817 | 39.5 | 6 | 1.1 | 1.1 | 17.4 | 6.3 | 1.4 | 3.8 | <5 | 1.8 |
| Cu Str | | KCD209838 | 68 | 6 | 1.4 | 1.6 | 23.2 | 8.4 | 1.7 | 2.6 | <5 | 3.3 |
| Cu Str | | KCD209839 | 40.7 | 4 | 0.7 | 1 | 15.4 | 4.9 | 1.9 | 2 | <5 | 1.9 |
| Cu Str | | KCD209842 | 81.9 | 5 | 1.4 | 1.1 | 16.3 | 5.4 | 1.3 | 3.6 | <5 | 3.5 |
| Cu Str | | KCD209843 | 72.9 | 5 | 1.4 | 1.3 | 19.3 | 6.6 | 1.6 | <0.7 | 5 | 2.8 |
| Cu Str | Py Stringer | KCD209776 | 47.9 | 6 | 1.7 | 1.4 | 20.5 | 7.2 | 1.6 | 5.1 | 18 | 2.3 |
| Cu Str | Sph Stringer | KCD209835 | 36.8 | 3 | 1 | 0.6 | 10.3 | 3.5 | 0.7 | <0.7 | 6 | 1.6 |

MS = ICP-MS and OES = ICP-OES

[1] $FeCO_3$ equivalent that was calculated assuming 100% of $CO_2$ is in $FeCO_3$

## Appendix II Electron Microprobe Analysis (wt %) of Pyrite in Mine D

| Lens | Ore Type | Sample # | Cu | Zn | Pb | Fe | S | Au | Ag | Hg | Sb | As | In | Se | Bi | Ni | Co | Total |
|---|---|---|---|---|---|---|---|---|---|---|---|---|---|---|---|---|---|---|
| South | Massive Py-Sph | KCD209757 | <0.02 | <0.03 | <0.10 | 46.95 | 52.87 | - | 0.03 | - | <0.02 | <0.06 | - | <0.05 | <0.08 | <0.01 | <0.02 | 99.92 |
| South | Massive Py-Sph | KCD209757 | <0.02 | <0.03 | <0.10 | 47.40 | 53.10 | - | 0.05 | - | <0.02 | <0.06 | - | <0.05 | <0.08 | <0.01 | <0.02 | 100.58 |
| South | Massive Py-Sph | KCD209757 | <0.02 | 0.09 | <0.10 | 46.84 | 52.52 | - | <0.02 | - | 0.04 | 0.06 | - | <0.05 | <0.08 | <0.01 | 0.08 | 99.67 |
| South | Massive Sph | KCD209763 | <0.02 | <0.03 | <0.10 | 46.79 | 52.75 | - | <0.02 | - | <0.02 | 0.12 | - | <0.05 | 0.09 | <0.01 | 0.05 | 99.83 |
| South | Massive Sph | KCD209763 | <0.02 | 0.30 | <0.10 | 46.39 | 52.32 | - | 0.07 | - | <0.02 | <0.06 | - | 0.05 | <0.08 | <0.01 | <0.02 | 99.20 |
| South | Massive Sph | KCD209763 | <0.02 | <0.03 | <0.10 | 46.64 | 52.84 | - | <0.02 | - | <0.02 | 0.08 | - | <0.05 | <0.08 | <0.01 | 0.03 | 99.62 |
| West | Heterolithic Py | KCD209768 | <0.02 | <0.03 | <0.10 | 46.94 | 53.22 | - | <0.02 | - | <0.02 | 0.06 | - | <0.05 | <0.08 | 0.02 | 0.03 | 100.31 |
| West | Heterolithic Py | KCD209768 | <0.02 | <0.03 | <0.10 | 46.76 | 52.86 | - | 0.04 | - | <0.02 | <0.06 | - | <0.05 | <0.08 | <0.01 | <0.02 | 99.70 |
| West | Massive Py-Sph | KCD209770 | <0.02 | 0.43 | <0.10 | 47.00 | 52.51 | - | <0.02 | - | <0.02 | 0.07 | - | <0.05 | <0.08 | <0.01 | 0.07 | 100.08 |
| West | Massive Py-Sph | KCD209770 | <0.02 | <0.03 | <0.10 | 47.02 | 52.99 | - | <0.02 | - | <0.02 | <0.06 | - | <0.05 | <0.08 | <0.01 | <0.02 | 100.07 |
| Cu Str | Massive Py-Cp | KCD209773 | <0.02 | 0.03 | <0.10 | 46.72 | 52.98 | - | <0.02 | - | 0.03 | <0.06 | - | 0.14 | <0.08 | <0.01 | 0.10 | 100.06 |
| Cu Str | Massive Py-Cp | KCD209773 | 2.23 | <0.03 | <0.10 | 44.89 | 50.81 | - | 0.08 | - | <0.02 | 0.47 | - | <0.05 | <0.08 | <0.01 | 0.71 | 99.22 |
| Cu Str | Py Stringer | KCD209776 | 0.03 | <0.03 | <0.10 | 47.16 | 53.14 | - | <0.02 | - | 0.03 | 0.08 | - | <0.05 | <0.08 | <0.01 | <0.02 | 100.45 |
| Cu Str | Py Stringer | KCD209776 | <0.02 | 0.05 | <0.10 | 46.51 | 52.99 | - | <0.02 | - | <0.02 | <0.06 | - | <0.05 | <0.08 | <0.01 | <0.02 | 99.57 |
| West | Heterolithic Py | KCD209778 | 0.03 | <0.03 | <0.10 | 46.37 | 52.63 | - | <0.02 | - | <0.02 | <0.06 | - | <0.05 | <0.08 | <0.01 | <0.02 | 99.05 |
| West | Massive Py-Sph | KCD209781 | <0.02 | <0.03 | <0.10 | 47.30 | 53.49 | - | <0.02 | - | <0.02 | 0.06 | - | <0.05 | <0.08 | <0.01 | <0.02 | 100.90 |
| West | Massive Py-Sph | KCD209781 | <0.02 | <0.03 | <0.10 | 47.14 | 52.90 | - | <0.02 | - | <0.02 | <0.06 | - | <0.05 | <0.08 | <0.01 | <0.02 | 100.07 |
| West | Massive Py-Sph | KCD209781 | <0.02 | <0.03 | <0.10 | 47.07 | 53.05 | - | <0.02 | - | <0.02 | <0.06 | - | <0.05 | <0.08 | 0.02 | 0.03 | 100.23 |
| West | Massive Sph-Cp | KCD209783 | 0.03 | 0.12 | <0.10 | 46.60 | 52.90 | - | <0.02 | - | <0.02 | <0.06 | - | <0.05 | <0.08 | <0.01 | 0.02 | 99.73 |
| West | Massive Sph-Cp | KCD209783 | <0.02 | 0.38 | <0.10 | 46.87 | 53.23 | - | <0.02 | - | <0.02 | <0.06 | - | 0.08 | <0.08 | <0.01 | 0.04 | 100.63 |
| West | Massive Sph-Cp | KCD209783 | <0.02 | 0.04 | <0.10 | 46.86 | 52.66 | - | <0.02 | - | <0.02 | <0.06 | - | <0.05 | <0.08 | <0.01 | <0.02 | 99.60 |
| West | Massive Sph-Cp | KCD209783 | 0.03 | <0.03 | <0.10 | 47.11 | 54.15 | <0.07 | <0.02 | <0.08 | <0.02 | <0.06 | <0.02 | 0.27 | <0.08 | 0.02 | 0.07 | 101.67 |
| West | Massive Sph-Cp | KCD209783 | <0.02 | <0.03 | <0.10 | 47.48 | 53.62 | <0.07 | <0.02 | <0.08 | <0.02 | <0.06 | <0.02 | <0.05 | <0.08 | 0.02 | 0.04 | 101.24 |
| West | Massive Sph-Cp | KCD209783 | <0.02 | 0.26 | <0.10 | 46.75 | 52.79 | - | 0.04 | - | <0.02 | <0.06 | - | <0.05 | <0.08 | <0.01 | 0.05 | 99.93 |
| West | Massive Sph-Cp | KCD209811 | 0.08 | 0.19 | <0.10 | 47.08 | 52.94 | - | 0.05 | - | <0.02 | <0.06 | - | <0.05 | <0.08 | <0.01 | <0.02 | 100.35 |
| West | Massive Sph-Cp | KCD209811 | <0.02 | 0.03 | <0.10 | 46.70 | 52.98 | - | <0.02 | - | <0.02 | 0.24 | - | <0.05 | <0.08 | <0.01 | 0.36 | 100.33 |

## Appendix III Electron Microprobe Analysis (wt %) of Pyrrhotite in Mine D

| Lens | Ore Type | Sample # | Cu | Zn | Pb | Fe | S | Au | Ag | Hg | Sb | As | In | Se | Bi | Ni | Co | Total |
|---|---|---|---|---|---|---|---|---|---|---|---|---|---|---|---|---|---|---|
| Main | Massive Sph-Cp | 8802_10 | 0.02 | <0.03 | <0.10 | 60.49 | 40.03 | 0.10 | 0.04 | <0.08 | <0.03 | <0.05 | <0.03 | 0.08 | <0.07 | <0.01 | <0.02 | 100.75 |
| South | Massive Py-Sph | KCD209757 | <0.01 | <0.03 | <0.10 | 61.25 | 38.36 | - | 0.04 | - | <0.03 | <0.05 | - | <0.05 | <0.07 | <0.01 | <0.02 | 99.69 |
| South | Massive Py-Sph | KCD209757 | <0.01 | <0.03 | <0.10 | 61.27 | 38.64 | - | 0.04 | - | <0.03 | 0.06 | - | <0.05 | <0.07 | <0.01 | <0.02 | 100.04 |
| South | Massive Py-Sph | KCD209757 | <0.01 | 0.71 | <0.10 | 61.22 | 38.55 | - | 0.03 | - | 0.03 | <0.05 | - | <0.05 | <0.07 | <0.01 | <0.02 | 100.63 |
| South | Massive Sph-Cp | KCD209759 | 0.02 | <0.03 | <0.10 | 61.19 | 39.48 | <0.07 | <0.02 | <0.08 | <0.03 | <0.05 | <0.03 | <0.05 | <0.07 | <0.01 | <0.02 | 100.78 |
| South | Massive Sph | KCD209763 | <0.01 | <0.03 | <0.10 | 61.18 | 38.05 | - | <0.02 | - | <0.03 | <0.05 | - | <0.05 | <0.07 | <0.01 | 0.03 | 99.28 |
| South | Massive Sph | KCD209763 | <0.01 | 0.10 | <0.10 | 60.90 | 38.46 | - | 0.02 | - | <0.03 | <0.05 | - | <0.05 | <0.07 | <0.01 | <0.02 | 99.54 |
| South | Massive Sph | KCD209763 | <0.01 | 0.67 | <0.10 | 61.01 | 38.27 | - | <0.02 | - | <0.03 | <0.05 | - | <0.05 | <0.07 | <0.01 | <0.02 | 100.01 |
| South | Massive Sph | KCD209763 | 0.03 | 0.11 | <0.10 | 60.53 | 38.88 | - | <0.02 | - | <0.03 | <0.05 | - | <0.05 | <0.07 | <0.01 | <0.02 | 99.60 |
| West | Massive Py-Sph | KCD209770 | <0.01 | 0.39 | <0.10 | 61.33 | 38.04 | - | <0.02 | - | <0.03 | 0.06 | - | <0.05 | <0.07 | <0.01 | <0.02 | 99.84 |
| West | Massive Py-Sph | KCD209770 | 0.02 | 0.30 | <0.10 | 60.83 | 38.52 | - | 0.03 | - | <0.03 | <0.05 | - | <0.05 | <0.07 | <0.01 | <0.02 | 99.75 |
| West | Massive Py-Sph | KCD209770 | <0.01 | <0.03 | <0.10 | 61.19 | 38.22 | - | <0.02 | - | 0.03 | <0.05 | - | <0.05 | <0.07 | <0.01 | <0.02 | 99.46 |
| West | Massive Py-Sph | KCD209770 | <0.01 | <0.03 | <0.10 | 61.12 | 39.19 | <0.07 | <0.02 | <0.08 | <0.03 | <0.05 | <0.03 | <0.05 | <0.07 | <0.01 | <0.02 | 100.38 |
| West | Massive Py-Sph | KCD209770 | 0.02 | 0.08 | <0.10 | 61.32 | 39.35 | <0.07 | <0.02 | <0.08 | <0.03 | <0.05 | <0.03 | 0.05 | <0.07 | <0.01 | <0.02 | 100.96 |
| West | Massive Py-Sph | KCD209770 | <0.01 | 0.11 | <0.10 | 61.14 | 38.91 | 0.18 | <0.02 | <0.08 | <0.03 | <0.05 | <0.03 | 0.09 | <0.07 | <0.01 | <0.02 | 100.45 |
| Cu Str | Massive Py-Cp | KCD209773 | 0.07 | <0.03 | <0.10 | 61.41 | 38.18 | - | <0.02 | - | 0.03 | <0.05 | - | <0.05 | <0.07 | <0.01 | 0.06 | 99.77 |
| Cu Str | Massive Py-Cp | KCD209773 | 0.04 | 0.19 | <0.10 | 60.84 | 38.71 | - | <0.02 | - | <0.03 | <0.05 | - | <0.05 | <0.07 | <0.01 | 0.09 | 99.92 |
| Cu Str | Py Stringer | KCD209776 | <0.01 | 0.12 | <0.10 | 60.94 | 38.23 | - | <0.02 | - | <0.03 | 0.08 | - | <0.05 | <0.07 | <0.01 | <0.02 | 99.41 |
| Cu Str | Py Stringer | KCD209776 | <0.01 | 0.03 | <0.10 | 61.09 | 38.34 | - | 0.04 | - | <0.03 | <0.05 | - | <0.05 | <0.07 | <0.01 | <0.02 | 99.55 |
| West | Heterolithic Py | KCD209778 | <0.01 | 0.07 | <0.10 | 61.18 | 38.33 | - | 0.05 | - | <0.03 | 0.14 | - | <0.05 | <0.07 | <0.01 | <0.02 | 99.77 |
| West | Heterolithic Py | KCD209778 | 0.02 | 0.05 | <0.10 | 60.97 | 38.60 | - | <0.02 | - | <0.03 | <0.05 | - | <0.05 | <0.07 | <0.01 | <0.02 | 99.68 |
| West | Massive Py-Sph | KCD209781 | <0.01 | 0.22 | <0.10 | 61.10 | 38.59 | - | <0.02 | - | <0.03 | <0.05 | - | <0.05 | <0.07 | <0.01 | 0.02 | 99.98 |
| West | Massive Py-Sph | KCD209781 | <0.01 | 0.28 | <0.10 | 60.81 | 38.79 | - | <0.02 | - | <0.03 | <0.05 | - | <0.05 | <0.07 | <0.01 | <0.02 | 99.96 |
| West | Massive Py-Sph | KCD209781 | 0.03 | <0.03 | <0.10 | 60.83 | 38.60 | - | <0.02 | - | <0.03 | 0.07 | - | <0.05 | <0.07 | <0.01 | <0.02 | 99.55 |
| West | Massive Sph-Cp | KCD209783 | <0.01 | 1.03 | <0.10 | 60.99 | 38.31 | - | <0.02 | - | 0.04 | 0.06 | - | 0.07 | <0.07 | 0.01 | <0.02 | 100.50 |
| West | Massive Sph-Cp | KCD209783 | <0.01 | 0.78 | <0.10 | 61.00 | 38.25 | - | <0.02 | - | <0.03 | <0.05 | - | 0.06 | <0.07 | 0.03 | <0.02 | 100.15 |
| West | Massive Sph-Cp | KCD209783 | 0.02 | 0.11 | <0.10 | 61.09 | 38.07 | - | 0.09 | - | <0.03 | <0.05 | - | <0.05 | <0.07 | <0.01 | <0.02 | 99.42 |
| West | Massive Sph-Cp | KCD209783 | <0.01 | <0.03 | <0.10 | 60.97 | 39.36 | <0.07 | <0.02 | <0.08 | <0.03 | <0.05 | <0.03 | 0.09 | <0.07 | 0.02 | <0.02 | 100.45 |
| West | Massive Sph-Cp | KCD209783 | <0.01 | 0.13 | <0.10 | 60.99 | 38.89 | <0.07 | <0.02 | <0.08 | <0.03 | <0.05 | <0.03 | 0.14 | <0.07 | 0.03 | <0.02 | 100.21 |
| West | Massive Sph-Cp | KCD209783 | 0.32 | <0.03 | <0.10 | 60.79 | 39.15 | 0.12 | 0.03 | <0.08 | <0.03 | <0.05 | <0.03 | <0.05 | <0.07 | <0.01 | <0.02 | 100.46 |
| Main | Massive Sph-Cp | KCD209788 | 0.18 | 0.52 | <0.10 | 60.84 | 38.43 | - | <0.02 | - | <0.03 | <0.05 | - | <0.05 | <0.07 | <0.01 | <0.02 | 100.05 |
| Main | Massive Sph-Cp | KCD209788 | <0.01 | 0.47 | <0.10 | 60.87 | 38.58 | - | 0.02 | - | <0.03 | <0.05 | - | 0.09 | <0.07 | <0.01 | 0.04 | 100.14 |
| Main | Massive Sph-Cp | KCD209788 | <0.01 | 0.70 | <0.10 | 60.98 | 38.25 | - | <0.02 | - | <0.03 | <0.05 | - | <0.05 | <0.07 | <0.01 | 0.03 | 100.04 |
| Cu Str | Cp Stringer | KCD209790 | 0.06 | <0.03 | <0.10 | 61.29 | 38.39 | - | <0.02 | - | <0.03 | <0.05 | - | <0.05 | <0.07 | <0.01 | <0.02 | 99.80 |
| Cu Str | Cp Stringer | KCD209790 | 0.02 | <0.03 | <0.10 | 61.29 | 38.20 | - | <0.02 | - | 0.03 | <0.05 | - | <0.05 | <0.07 | <0.01 | 0.05 | 99.62 |
| Cu Str | Cp Stringer | KCD209790 | 0.16 | <0.03 | <0.10 | 61.30 | 39.58 | 0.08 | <0.02 | <0.08 | <0.03 | <0.05 | 0.03 | <0.05 | <0.07 | <0.01 | <0.02 | 101.16 |
| Cu Str | Cp Stringer | KCD209790 | 0.02 | <0.03 | <0.10 | 61.12 | 39.45 | <0.07 | <0.02 | <0.08 | <0.03 | <0.05 | <0.03 | 0.06 | <0.07 | <0.01 | 0.07 | 100.77 |

| Lens | Ore Type | Sample # | Cu | Zn | Pb | Fe | S | Au | Ag | Hg | Sb | As | In | Se | Bi | Ni | Co | Total |
|---|---|---|---|---|---|---|---|---|---|---|---|---|---|---|---|---|---|---|
| Cu Str | Cp Stringer | KCD209794 | <0.01 | <0.03 | <0.10 | 61.16 | 39.26 | <0.07 | <0.02 | <0.08 | <0.03 | <0.05 | <0.03 | <0.05 | <0.07 | 0.02 | 0.06 | 100.57 |
| Cu Str | Cp Stringer | KCD209794 | <0.01 | <0.03 | <0.10 | 61.34 | 39.39 | <0.07 | <0.02 | <0.08 | <0.03 | <0.05 | <0.03 | <0.05 | <0.07 | 0.03 | 0.06 | 100.82 |
| Cu Str | Massive Cp | KCD209797 | 0.19 | <0.03 | <0.10 | 60.58 | 37.96 | - | 0.08 | - | <0.03 | <0.05 | - | <0.05 | <0.07 | <0.01 | <0.02 | 98.86 |
| Cu Str | Massive Cp | KCD209797 | 0.05 | <0.03 | <0.10 | 61.07 | 38.04 | - | <0.02 | - | <0.03 | <0.05 | - | 0.07 | <0.07 | <0.01 | <0.02 | 99.29 |
| Cu Str | Cp Stringer | KCD209801 | <0.01 | <0.03 | <0.10 | 61.05 | 38.26 | - | <0.02 | - | <0.03 | 0.06 | - | <0.05 | <0.07 | 0.03 | 0.06 | 99.51 |
| Cu Str | Cp Stringer | KCD209801 | 0.02 | <0.03 | <0.10 | 60.69 | 38.53 | - | 0.11 | - | <0.03 | <0.05 | - | 0.07 | <0.07 | 0.02 | 0.08 | 99.53 |
| Cu Str | Cp Stringer | KCD209801 | 0.04 | 0.12 | <0.10 | 60.92 | 38.08 | - | 0.08 | - | <0.03 | <0.05 | - | <0.05 | <0.07 | 0.02 | 0.10 | 99.42 |
| Cu Str | Cp Stringer | KCD209801 | 0.04 | <0.03 | <0.10 | 60.91 | 38.39 | - | <0.02 | - | <0.03 | <0.05 | - | 0.09 | <0.07 | <0.01 | 0.06 | 99.52 |
| West | Massive Sph-Cp | KCD209807 | 0.07 | 0.08 | <0.10 | 61.03 | 38.49 | - | <0.02 | - | <0.03 | <0.05 | - | <0.05 | <0.07 | <0.01 | <0.02 | 99.72 |
| West | Massive Sph-Cp | KCD209807 | 0.06 | 0.15 | <0.10 | 61.21 | 38.71 | - | 0.10 | - | <0.03 | <0.05 | - | <0.05 | <0.07 | 0.02 | <0.02 | 100.27 |
| West | Sph-Cp Stringer | KCD209809 | 0.03 | 0.04 | <0.10 | 61.48 | 39.71 | <0.07 | <0.02 | <0.08 | <0.03 | <0.05 | <0.03 | <0.05 | <0.07 | <0.01 | <0.02 | 101.34 |
| West | Massive Sph-Cp | KCD209811 | <0.01 | 0.26 | <0.10 | 60.91 | 38.61 | - | <0.02 | - | <0.03 | <0.05 | - | <0.05 | <0.07 | <0.01 | <0.02 | 99.83 |
| West | Massive Sph-Cp | KCD209811 | <0.01 | 0.12 | <0.10 | 61.08 | 38.60 | - | <0.02 | - | <0.03 | <0.05 | - | <0.05 | <0.07 | <0.01 | <0.02 | 99.81 |
| Main | Sph Stringer | KCD209813 | <0.01 | <0.03 | <0.10 | 60.65 | 39.29 | <0.07 | <0.02 | <0.08 | <0.03 | <0.05 | <0.03 | <0.05 | <0.07 | <0.01 | <0.02 | 99.95 |
| Main | Sph Stringer | KCD209813 | <0.01 | <0.03 | <0.10 | 61.07 | 39.15 | <0.07 | <0.02 | <0.08 | <0.03 | <0.05 | <0.03 | <0.05 | <0.07 | <0.01 | <0.02 | 100.28 |

## Appendix IV Electron Microprobe Analysis (wt %) of Sphalerite in Mine D

| Lens | Ore Type | Sample # | Cu | Zn | Pb | Fe | S | Au | Ag | Hg | Sb | As | In | Se | Bi | Ni | Co | Cd | Total |
|---|---|---|---|---|---|---|---|---|---|---|---|---|---|---|---|---|---|---|---|
| Main | Massive Sph-Cp | 8802_10 | 0.04 | 61.51 | <0.10 | 4.99 | 33.69 | <0.08 | <0.02 | <0.08 | <0.03 | <0.05 | <0.03 | <0.05 | <0.07 | <0.02 | 0.02 | - | 100.29 |
| Main | Massive Sph-Cp | 8802_10 | 0.12 | 63.56 | <0.10 | 4.42 | 33.46 | 0.09 | <0.02 | <0.08 | <0.03 | <0.05 | <0.03 | <0.05 | <0.07 | <0.02 | <0.02 | - | 101.65 |
| Main | Massive Sph-Cp | 8802_10 | 0.02 | 61.53 | <0.10 | 5.29 | 33.61 | <0.08 | <0.02 | <0.08 | <0.03 | <0.05 | <0.03 | <0.05 | <0.07 | <0.02 | <0.02 | - | 100.48 |
| Main | Massive Sph-Cp | 8802_10 | 0.14 | 62.88 | <0.10 | 4.97 | 33.63 | <0.08 | <0.02 | <0.08 | <0.03 | <0.05 | <0.03 | 0.15 | <0.07 | <0.02 | <0.02 | - | 101.88 |
| Main | Massive Sph-Cp | 8802_10 | 0.14 | 61.37 | <0.10 | 5.09 | 33.76 | <0.08 | <0.02 | <0.08 | <0.03 | <0.05 | <0.03 | 0.07 | <0.07 | <0.02 | <0.02 | - | 100.48 |
| South | Massive Py-Sph | KCD209757 | 0.05 | 59.40 | <0.10 | 7.01 | 32.71 | - | <0.02 | - | <0.03 | <0.05 | - | <0.05 | 0.15 | <0.02 | <0.02 | 0.37 | 99.72 |
| South | Massive Py-Sph | KCD209757 | <0.02 | 59.77 | <0.10 | 6.24 | 33.03 | - | <0.02 | - | <0.03 | <0.05 | - | <0.05 | 0.10 | <0.02 | 0.02 | 0.25 | 99.43 |
| South | Massive Py-Sph | KCD209757 | <0.02 | 60.15 | <0.10 | 6.58 | 32.96 | - | <0.02 | - | <0.03 | 0.05 | - | <0.05 | <0.07 | <0.02 | <0.02 | 0.43 | 100.20 |
| South | Massive Sph-Cp | KCD209759 | 0.04 | 60.82 | <0.10 | 6.69 | 33.91 | <0.08 | <0.02 | <0.08 | <0.03 | <0.05 | <0.03 | <0.05 | <0.07 | <0.02 | 0.02 | - | 101.55 |
| South | Massive Sph-Cp | KCD209759 | 0.04 | 61.14 | <0.10 | 7.06 | 33.60 | <0.08 | 0.03 | <0.08 | <0.03 | <0.05 | <0.03 | 0.06 | <0.07 | <0.02 | 0.02 | - | 101.97 |
| South | Massive Sph-Cp | KCD209759 | 0.08 | 61.35 | <0.10 | 5.91 | 33.89 | <0.08 | <0.02 | <0.08 | <0.03 | <0.05 | 0.04 | <0.05 | <0.07 | <0.02 | 0.03 | - | 101.30 |
| South | Massive Sph-Cp | KCD209759 | 0.06 | 60.66 | <0.10 | 6.45 | 33.76 | <0.08 | <0.02 | <0.08 | <0.03 | <0.05 | <0.03 | <0.05 | <0.07 | <0.02 | 0.03 | - | 101.02 |
| South | Massive Sph | KCD209763 | <0.02 | 59.25 | <0.10 | 7.03 | 33.02 | - | <0.02 | - | <0.03 | <0.05 | - | <0.05 | <0.07 | <0.02 | <0.02 | 0.24 | 99.57 |
| South | Massive Sph | KCD209763 | <0.02 | 59.47 | <0.10 | 6.82 | 33.04 | - | <0.02 | - | <0.03 | <0.05 | - | <0.05 | <0.07 | <0.02 | <0.02 | 0.30 | 99.66 |
| South | Massive Sph | KCD209763 | <0.02 | 59.17 | <0.10 | 6.98 | 32.93 | - | <0.02 | - | <0.03 | <0.05 | - | <0.05 | <0.07 | 0.02 | <0.02 | 0.31 | 99.45 |
| South | Massive Sph | KCD209763 | <0.02 | 58.75 | <0.10 | 7.60 | 33.51 | - | <0.02 | - | <0.03 | <0.05 | - | <0.05 | <0.07 | <0.02 | <0.02 | 0.30 | 100.20 |
| West | Heterolithic Py | KCD209768 | 0.04 | 60.99 | <0.10 | 5.63 | 33.10 | - | 0.04 | - | <0.03 | <0.05 | - | <0.05 | <0.07 | <0.02 | <0.02 | 0.36 | 100.18 |
| West | Massive Py-Sph | KCD209770 | <0.02 | 59.42 | <0.10 | 7.41 | 33.27 | - | <0.02 | - | <0.03 | <0.05 | - | <0.05 | <0.07 | <0.02 | <0.02 | 0.31 | 100.42 |
| West | Massive Py-Sph | KCD209770 | 0.04 | 59.73 | <0.10 | 6.93 | 32.99 | - | <0.02 | - | <0.03 | <0.05 | - | <0.05 | <0.07 | <0.02 | <0.02 | 0.16 | 99.87 |
| West | Massive Py-Sph | KCD209770 | <0.02 | 60.11 | <0.10 | 6.52 | 33.38 | - | <0.02 | - | <0.03 | <0.05 | - | <0.05 | <0.07 | <0.02 | <0.02 | 0.30 | 100.32 |
| West | Massive Py-Sph | KCD209770 | 0.02 | 60.34 | <0.10 | 7.19 | 33.99 | <0.08 | <0.02 | <0.08 | <0.03 | <0.05 | <0.03 | <0.05 | <0.07 | <0.02 | <0.02 | - | 101.56 |
| West | Massive Py-Sph | KCD209770 | <0.02 | 59.65 | <0.10 | 7.04 | 33.65 | <0.08 | 0.04 | <0.08 | <0.03 | <0.05 | <0.03 | <0.05 | <0.07 | <0.02 | <0.02 | - | 100.39 |
| West | Massive Py-Sph | KCD209770 | <0.02 | 59.96 | <0.10 | 7.04 | 33.27 | - | <0.02 | - | <0.03 | <0.05 | - | <0.05 | <0.07 | <0.02 | <0.02 | 0.22 | 100.58 |
| West | Massive Py-Sph | KCD209770 | <0.02 | 60.23 | <0.10 | 7.08 | 33.29 | - | <0.02 | - | <0.03 | <0.05 | - | 0.07 | <0.07 | <0.02 | <0.02 | 0.31 | 101.01 |
| West | Massive Py-Sph | KCD209770 | <0.02 | 60.30 | <0.10 | 7.84 | 33.42 | - | <0.02 | - | <0.03 | <0.05 | - | <0.05 | <0.07 | <0.02 | <0.02 | 0.30 | 101.90 |
| West | Massive Py-Sph | KCD209770 | <0.02 | 59.98 | <0.10 | 8.01 | 33.47 | - | 0.07 | - | <0.03 | <0.05 | - | <0.05 | 0.10 | <0.02 | <0.02 | 0.26 | 101.89 |
| West | Massive Py-Sph | KCD209770 | <0.02 | 57.66 | <0.10 | 9.82 | 33.17 | - | 0.02 | - | <0.03 | <0.05 | - | <0.05 | <0.07 | <0.02 | <0.02 | 0.30 | 101.03 |
| West | Massive Py-Sph | KCD209770 | <0.02 | 57.33 | <0.10 | 10.43 | 33.34 | - | 0.04 | - | <0.03 | <0.05 | - | <0.05 | <0.07 | <0.02 | 0.03 | 0.24 | 101.42 |
| West | Massive Py-Sph | KCD209770 | 0.03 | 59.54 | <0.10 | 8.27 | 33.18 | - | <0.02 | - | <0.03 | <0.05 | - | <0.05 | <0.07 | <0.02 | <0.02 | 0.35 | 101.44 |
| West | Massive Py-Sph | KCD209770 | <0.02 | 59.84 | <0.10 | 7.60 | 33.08 | - | <0.02 | - | 0.05 | <0.05 | - | <0.05 | <0.07 | <0.02 | <0.02 | 0.16 | 100.74 |
| West | Massive Py-Sph | KCD209770 | 0.02 | 60.14 | <0.10 | 7.21 | 33.25 | - | <0.02 | - | <0.03 | <0.05 | - | <0.05 | <0.07 | <0.02 | <0.02 | 0.19 | 100.89 |
| West | Massive Py-Sph | KCD209770 | <0.02 | 59.99 | <0.10 | 7.15 | 33.21 | - | <0.02 | - | <0.03 | <0.05 | - | <0.05 | <0.07 | <0.02 | <0.02 | 0.36 | 100.75 |
| West | Massive Py-Sph | KCD209770 | <0.02 | 60.10 | <0.10 | 7.11 | 33.06 | - | <0.02 | - | 0.03 | <0.05 | - | <0.05 | <0.07 | <0.02 | <0.02 | 0.33 | 100.66 |
| West | Massive Py-Sph | KCD209770 | <0.02 | 58.85 | <0.10 | 9.30 | 33.20 | - | <0.02 | - | 0.04 | <0.05 | - | <0.05 | <0.07 | <0.02 | <0.02 | 0.34 | 101.77 |
| West | Massive Py-Sph | KCD209770 | <0.02 | 59.19 | <0.10 | 9.07 | 33.22 | - | <0.02 | - | 0.03 | <0.05 | - | 0.10 | <0.07 | <0.02 | <0.02 | 0.28 | 101.93 |
| West | Massive Py-Sph | KCD209770 | <0.02 | 59.91 | <0.10 | 8.26 | 33.20 | - | <0.02 | - | <0.03 | <0.05 | - | <0.05 | <0.07 | <0.02 | <0.02 | 0.17 | 101.55 |
| West | Massive Py-Sph | KCD209770 | 0.02 | 59.16 | <0.10 | 8.75 | 33.17 | - | <0.02 | - | <0.03 | <0.05 | - | 0.17 | 0.08 | <0.02 | <0.02 | 0.35 | 101.68 |

| Lens | Ore Type | Sample # | Cu | Zn | Pb | Fe | S | Au | Ag | Hg | Sb | As | In | Se | Bi | Ni | Co | Cd | Total |
|---|---|---|---|---|---|---|---|---|---|---|---|---|---|---|---|---|---|---|---|
| West | Massive Py-Sph | KCD209770 | 0.03 | 59.60 | <0.10 | 7.83 | 33.02 | - | <0.02 | - | <0.03 | <0.05 | - | <0.05 | <0.07 | <0.02 | <0.02 | 0.26 | 100.76 |
| West | Massive Py-Sph | KCD209770 | <0.02 | 60.67 | <0.10 | 6.75 | 33.07 | - | <0.02 | - | <0.03 | <0.05 | - | <0.05 | <0.07 | <0.02 | <0.02 | 0.29 | 100.80 |
| West | Massive Py-Sph | KCD209770 | 0.03 | 60.86 | <0.10 | 6.44 | 33.03 | - | <0.02 | - | <0.03 | <0.05 | - | <0.05 | 0.16 | <0.02 | <0.02 | 0.33 | 100.86 |
| West | Massive Py-Sph | KCD209770 | <0.02 | 60.12 | <0.10 | 7.07 | 33.11 | - | 0.03 | - | <0.03 | <0.05 | - | <0.05 | <0.07 | <0.02 | <0.02 | 0.24 | 100.61 |
| West | Massive Py-Sph | KCD209770 | <0.02 | 59.79 | <0.10 | 7.03 | 33.53 | - | <0.02 | - | <0.03 | <0.05 | - | <0.05 | <0.07 | <0.02 | <0.02 | 0.20 | 100.57 |
| West | Massive Py-Sph | KCD209770 | <0.02 | 59.84 | <0.10 | 7.10 | 33.23 | - | <0.02 | - | <0.03 | <0.05 | - | <0.05 | <0.07 | <0.02 | <0.02 | 0.29 | 100.53 |
| West | Massive Py-Sph | KCD209770 | <0.02 | 59.27 | <0.10 | 7.07 | 33.24 | - | 0.07 | - | 0.03 | <0.05 | - | <0.05 | <0.07 | <0.02 | <0.02 | 0.22 | 99.90 |
| West | Massive Py-Sph | KCD209770 | 0.02 | 58.88 | <0.10 | 8.67 | 32.94 | - | 0.08 | - | 0.03 | 0.07 | - | <0.05 | <0.07 | <0.02 | <0.02 | 0.28 | 100.99 |
| West | Massive Py-Sph | KCD209770 | <0.02 | 59.12 | <0.10 | 8.14 | 33.30 | - | 0.06 | - | 0.03 | <0.05 | - | 0.22 | <0.07 | <0.02 | <0.02 | 0.27 | 101.16 |
| West | Massive Py-Sph | KCD209770 | <0.02 | 60.16 | <0.10 | 7.36 | 33.34 | - | <0.02 | - | <0.03 | <0.05 | - | <0.05 | <0.07 | <0.02 | 0.03 | 0.32 | 101.20 |
| West | Massive Py-Sph | KCD209770 | <0.02 | 59.46 | <0.10 | 8.03 | 33.38 | - | <0.02 | - | <0.03 | <0.05 | - | <0.05 | <0.07 | <0.02 | <0.02 | 0.21 | 101.09 |
| West | Massive Py-Sph | KCD209770 | <0.02 | 59.37 | <0.10 | 7.87 | 33.26 | - | <0.02 | - | <0.03 | <0.05 | - | 0.06 | <0.07 | <0.02 | <0.02 | 0.25 | 100.88 |
| West | Massive Py-Sph | KCD209770 | 0.02 | 59.93 | <0.10 | 7.48 | 33.28 | - | 0.03 | - | <0.03 | <0.05 | - | 0.11 | <0.07 | <0.02 | <0.02 | 0.29 | 101.16 |
| West | Massive Py-Sph | KCD209770 | 0.02 | 60.54 | <0.10 | 6.58 | 33.43 | - | <0.02 | - | <0.03 | <0.05 | - | 0.14 | <0.07 | <0.02 | <0.02 | 0.31 | 101.01 |
| Cu Str | Py Stringer | KCD209776 | <0.02 | 59.72 | <0.10 | 7.03 | 33.28 | - | 0.03 | - | <0.03 | <0.05 | - | <0.05 | <0.07 | <0.02 | <0.02 | 0.19 | 100.30 |
| Cu Str | Py Stringer | KCD209776 | 0.03 | 59.89 | <0.10 | 6.62 | 33.08 | - | <0.02 | - | <0.03 | <0.05 | - | <0.05 | <0.07 | <0.02 | <0.02 | 0.18 | 99.80 |
| West | Heterolithic Py | KCD209778 | 0.12 | 60.08 | <0.10 | 6.37 | 33.16 | - | 0.17 | - | 0.06 | <0.05 | - | <0.05 | <0.07 | <0.02 | <0.02 | 0.16 | 100.12 |
| West | Heterolithic Py | KCD209778 | <0.02 | 60.21 | <0.10 | 6.39 | 32.95 | - | <0.02 | - | 0.08 | <0.05 | - | <0.05 | <0.07 | <0.02 | <0.02 | 0.14 | 99.77 |
| West | Massive Py-Sph | KCD209781 | 0.09 | 59.78 | <0.10 | 6.82 | 33.30 | - | <0.02 | - | <0.03 | <0.05 | - | <0.05 | <0.07 | <0.02 | <0.02 | 0.17 | 100.20 |
| West | Massive Py-Sph | KCD209781 | 0.06 | 59.31 | <0.10 | 6.83 | 32.95 | - | 0.04 | - | <0.03 | <0.05 | - | <0.05 | <0.07 | <0.02 | <0.02 | 0.21 | 99.43 |
| West | Massive Py-Sph | KCD209781 | 0.36 | 60.26 | <0.10 | 5.59 | 33.23 | - | <0.02 | - | <0.03 | <0.05 | - | <0.05 | <0.07 | <0.02 | <0.02 | - | 99.46 |
| West | Massive Py-Sph | KCD209781 | 0.20 | 60.24 | <0.10 | 5.40 | 32.96 | - | <0.02 | - | <0.03 | <0.05 | - | <0.05 | <0.07 | <0.02 | <0.02 | 0.11 | 98.93 |
| West | Massive Sph-Cp | KCD209783 | <0.02 | 59.19 | <0.10 | 7.15 | 32.79 | - | 0.13 | - | <0.03 | <0.05 | - | 0.10 | <0.07 | <0.02 | 0.03 | 0.35 | 99.75 |
| West | Massive Sph-Cp | KCD209783 | <0.02 | 59.24 | <0.10 | 7.00 | 33.02 | - | <0.02 | - | <0.03 | 0.07 | - | 0.08 | <0.07 | <0.02 | <0.02 | 0.36 | 99.79 |
| West | Massive Sph-Cp | KCD209783 | 0.02 | 59.79 | <0.10 | 6.59 | 32.87 | - | 0.04 | - | <0.03 | <0.05 | - | 0.09 | <0.07 | <0.02 | <0.02 | 0.25 | 99.71 |
| West | Massive Sph-Cp | KCD209783 | 0.04 | 59.30 | <0.10 | 6.94 | 32.97 | - | <0.02 | - | <0.03 | <0.05 | - | 0.05 | <0.07 | <0.02 | <0.02 | 0.34 | 99.65 |
| West | Massive Sph-Cp | KCD209783 | 0.04 | 60.30 | <0.10 | 7.32 | 33.70 | <0.08 | <0.02 | <0.08 | <0.03 | <0.05 | <0.03 | 0.22 | <0.07 | <0.02 | <0.02 | - | 101.61 |
| West | Massive Sph-Cp | KCD209783 | <0.02 | 59.82 | <0.10 | 7.17 | 33.74 | <0.08 | <0.02 | <0.08 | <0.03 | <0.05 | <0.03 | 0.13 | <0.07 | <0.02 | <0.02 | - | 100.88 |
| West | Massive Sph-Cp | KCD209783 | 0.03 | 61.23 | <0.10 | 5.79 | 33.65 | <0.08 | <0.02 | <0.08 | <0.03 | <0.05 | <0.03 | 0.07 | <0.07 | <0.02 | <0.02 | - | 100.77 |
| West | Massive Sph-Cp | KCD209783 | 0.05 | 59.43 | <0.10 | 7.07 | 33.67 | <0.08 | <0.02 | <0.08 | <0.03 | <0.05 | <0.03 | 0.08 | <0.07 | <0.02 | <0.02 | - | 100.32 |
| Main | Massive Sph-Cp | KCD209788 | 0.19 | 58.98 | <0.10 | 6.86 | 33.37 | - | 0.02 | - | <0.03 | <0.05 | - | 0.09 | <0.07 | <0.02 | 0.07 | 0.34 | 99.97 |
| Main | Massive Sph-Cp | KCD209788 | 0.06 | 58.93 | <0.10 | 7.15 | 33.03 | - | <0.02 | - | <0.03 | <0.05 | - | <0.05 | <0.07 | 0.02 | <0.02 | 0.40 | 99.64 |
| Main | Massive Sph-Cp | KCD209788 | 0.04 | 59.31 | <0.10 | 6.52 | 33.07 | - | <0.02 | - | <0.03 | 0.18 | - | <0.05 | <0.07 | <0.02 | 0.42 | 0.30 | 99.94 |
| Cu Str | Cp Stringer | KCD209790 | 0.30 | 59.70 | <0.10 | 6.33 | 32.86 | - | <0.02 | - | <0.03 | <0.05 | - | <0.05 | <0.07 | <0.02 | 0.04 | 0.45 | 99.71 |
| Cu Str | Cp Stringer | KCD209790 | 0.21 | 59.52 | <0.10 | 6.58 | 32.93 | - | <0.02 | - | 0.05 | <0.05 | - | <0.05 | <0.07 | <0.02 | 0.06 | 0.32 | 99.67 |
| Cu Str | Cp Stringer | KCD209790 | 0.23 | 60.19 | <0.10 | 6.30 | 33.63 | <0.08 | <0.02 | <0.08 | <0.03 | <0.05 | 0.25 | <0.05 | <0.07 | <0.02 | 0.06 | - | 100.66 |
| Cu Str | Cp Stringer | KCD209790 | 0.18 | 59.97 | <0.10 | 6.79 | 33.44 | <0.08 | <0.02 | <0.08 | <0.03 | <0.05 | 0.26 | <0.05 | <0.07 | <0.02 | 0.06 | - | 100.70 |
| Cu Str | Cp Stringer | KCD209794 | 0.07 | 59.59 | <0.10 | 7.22 | 33.96 | <0.08 | <0.02 | <0.08 | 0.04 | <0.05 | <0.03 | <0.05 | <0.07 | <0.02 | 0.06 | - | 100.97 |

| Lens | Ore Type | Sample # | Cu | Zn | Pb | Fe | S | Au | Ag | Hg | Sb | As | In | Se | Bi | Ni | Co | Cd | Total |
|---|---|---|---|---|---|---|---|---|---|---|---|---|---|---|---|---|---|---|---|
| Cu Str | Cp Stringer | KCD209794 | 0.16 | 58.90 | <0.10 | 7.39 | 33.71 | <0.08 | <0.02 | <0.08 | <0.03 | <0.05 | 0.04 | 0.13 | <0.07 | <0.02 | 0.07 | - | 100.40 |
| Cu Str | Cp Stringer | KCD209801 | 0.22 | 59.34 | <0.10 | 6.32 | 33.43 | - | <0.02 | - | <0.03 | 0.07 | - | <0.05 | <0.07 | <0.02 | 0.05 | 0.44 | 99.91 |
| West | Massive Sph-Cp | KCD209807 | 0.05 | 59.27 | <0.10 | 7.18 | 33.18 | - | <0.02 | - | <0.03 | <0.05 | - | 0.07 | <0.07 | <0.02 | <0.02 | 0.33 | 100.10 |
| West | Massive Sph-Cp | KCD209807 | 0.02 | 59.28 | <0.10 | 6.97 | 33.79 | - | <0.02 | - | <0.03 | <0.05 | - | 0.06 | 0.15 | <0.02 | <0.02 | 0.23 | 100.51 |
| West | Massive Sph-Cp | KCD209807 | <0.02 | 59.63 | <0.10 | 6.86 | 33.31 | - | <0.02 | - | <0.03 | <0.05 | - | 0.06 | <0.07 | <0.02 | <0.02 | 0.49 | 100.36 |
| West | Sph-Cp Stringer | KCD209809 | 0.04 | 60.89 | <0.10 | 6.56 | 33.65 | <0.08 | <0.02 | <0.08 | 0.03 | <0.05 | <0.03 | 0.08 | <0.07 | 0.02 | 0.21 | - | 101.47 |
| West | Massive Sph-Cp | KCD209811 | 0.08 | 59.25 | <0.10 | 7.01 | 33.03 | - | <0.02 | - | <0.03 | <0.05 | - | <0.05 | <0.07 | <0.02 | <0.02 | 0.26 | 99.65 |
| West | Massive Sph-Cp | KCD209811 | <0.02 | 58.97 | <0.10 | 6.92 | 33.26 | - | <0.02 | - | <0.03 | <0.05 | - | 0.13 | 0.09 | 0.03 | <0.02 | 0.19 | 99.61 |
| West | Massive Sph-Cp | KCD209811 | 0.04 | 59.47 | <0.10 | 6.90 | 33.30 | - | <0.02 | - | <0.03 | <0.05 | - | 0.11 | <0.07 | <0.02 | <0.02 | 0.18 | 100.05 |
| West | Massive Sph-Cp | KCD209811 | 0.05 | 58.91 | <0.10 | 6.99 | 33.01 | - | 0.03 | - | 0.04 | <0.05 | - | <0.05 | <0.07 | <0.02 | <0.02 | 0.24 | 99.27 |
| West | Massive Sph-Cp | KCD209811 | <0.02 | 58.36 | <0.10 | 9.14 | 33.15 | - | <0.02 | - | <0.03 | <0.05 | - | <0.05 | <0.07 | <0.02 | <0.02 | 0.23 | 100.92 |
| West | Massive Sph-Cp | KCD209811 | 0.04 | 57.22 | <0.10 | 9.73 | 32.55 | - | <0.02 | - | <0.03 | <0.05 | - | <0.05 | <0.07 | <0.02 | <0.02 | 0.19 | 99.80 |
| West | Massive Sph-Cp | KCD209811 | 0.06 | 59.40 | <0.10 | 6.69 | 32.87 | - | <0.02 | - | <0.03 | <0.05 | - | 0.12 | <0.07 | <0.02 | <0.02 | 0.23 | 99.39 |
| West | Massive Sph-Cp | KCD209811 | 0.02 | 58.15 | <0.10 | 8.63 | 33.20 | - | <0.02 | - | 0.03 | <0.05 | - | <0.05 | <0.07 | <0.02 | 0.03 | 0.25 | 100.32 |
| West | Massive Sph-Cp | KCD209811 | 0.08 | 59.69 | <0.10 | 6.91 | 33.18 | - | 0.02 | - | <0.03 | 0.06 | - | 0.09 | <0.07 | <0.02 | <0.02 | 0.22 | 100.26 |
| West | Massive Sph-Cp | KCD209811 | 0.14 | 59.22 | <0.10 | 7.09 | 33.13 | - | 0.03 | - | <0.03 | <0.05 | - | <0.05 | <0.07 | <0.02 | <0.02 | 0.28 | 99.90 |
| West | Massive Sph-Cp | KCD209811 | 0.11 | 59.31 | <0.10 | 6.94 | 33.18 | - | <0.02 | - | <0.03 | <0.05 | - | <0.05 | <0.07 | <0.02 | <0.02 | 0.12 | 99.71 |
| West | Massive Sph-Cp | KCD209811 | <0.02 | 59.29 | <0.10 | 7.11 | 32.90 | - | 0.03 | - | <0.03 | <0.05 | - | <0.05 | <0.07 | <0.02 | <0.02 | 0.20 | 99.56 |
| West | Massive Sph-Cp | KCD209811 | 0.14 | 59.38 | <0.10 | 7.06 | 33.09 | - | <0.02 | - | <0.03 | <0.05 | - | <0.05 | <0.07 | <0.02 | <0.02 | 0.27 | 99.94 |
| Main | Sph Stringer | KCD209813 | 0.02 | 60.12 | <0.10 | 6.96 | 33.93 | <0.08 | <0.02 | <0.08 | <0.03 | <0.05 | <0.03 | <0.05 | <0.07 | <0.02 | <0.02 | - | 101.09 |
| Main | Sph Stringer | KCD209813 | 0.03 | 60.63 | <0.10 | 6.66 | 34.14 | <0.08 | 0.06 | <0.08 | <0.03 | <0.05 | <0.03 | <0.05 | <0.07 | <0.02 | <0.02 | - | 101.55 |

## Appendix V Electron Microprobe Analysis (wt %) of Chalcopyrite in Mine D

| Lens | Ore Type | Sample # | Cu | Zn | Pb | Fe | S | Au | Ag | Hg | Sb | As | In | Se | Bi | Ni | Co | Total |
|---|---|---|---|---|---|---|---|---|---|---|---|---|---|---|---|---|---|---|
| Main | Massive Sph-Cp | 8802_10 | 33.92 | <0.03 | <0.10 | 30.78 | 35.33 | 0.17 | 0.24 | <0.08 | <0.03 | <0.05 | <0.03 | <0.05 | <0.07 | <0.01 | <0.02 | 100.58 |
| South | Massive Sph-Cp | KCD209759 | 33.95 | <0.03 | <0.10 | 30.78 | 35.39 | <0.07 | 0.06 | <0.08 | <0.03 | <0.05 | <0.03 | <0.05 | <0.07 | <0.01 | <0.02 | 100.25 |
| South | Massive Sph-Cp | KCD209759 | 34.01 | 0.18 | <0.10 | 30.83 | 35.25 | <0.07 | 0.03 | <0.08 | <0.03 | <0.05 | <0.03 | <0.05 | <0.07 | <0.01 | <0.02 | 100.30 |
| South | Massive Sph-Cp | KCD209759 | 33.55 | <0.03 | <0.10 | 30.89 | 35.03 | <0.07 | <0.02 | <0.08 | <0.03 | <0.05 | <0.03 | 0.12 | <0.07 | 0.02 | <0.02 | 99.69 |
| South | Massive Sph-Cp | KCD209759 | 33.88 | <0.03 | <0.10 | 31.12 | 34.96 | <0.07 | <0.02 | <0.08 | <0.03 | <0.05 | <0.03 | <0.05 | <0.07 | <0.01 | <0.02 | 99.99 |
| West | Heterolithic Py | KCD209768 | 34.02 | <0.03 | <0.10 | 30.97 | 34.89 | - | 0.07 | - | <0.03 | <0.05 | - | <0.05 | <0.07 | <0.01 | <0.02 | 100.01 |
| Cu Str | Massive Py-Cp | KCD209773 | 34.53 | <0.03 | <0.10 | 30.34 | 34.40 | - | 0.03 | - | <0.03 | <0.05 | - | <0.05 | <0.07 | <0.01 | <0.02 | 99.32 |
| Cu Str | Massive Py-Cp | KCD209773 | 33.94 | <0.03 | <0.10 | 30.95 | 34.35 | - | <0.02 | - | <0.03 | <0.05 | - | <0.05 | <0.07 | <0.01 | <0.02 | 99.27 |
| West | Heterolithic Py | KCD209778 | 34.50 | <0.03 | <0.10 | 30.82 | 34.68 | - | 0.03 | - | <0.03 | <0.05 | - | <0.05 | <0.07 | <0.01 | <0.02 | 100.06 |
| West | Massive Sph-Cp | KCD209783 | 34.01 | <0.03 | <0.10 | 30.73 | 34.61 | - | 0.05 | - | <0.03 | <0.05 | - | 0.11 | <0.07 | <0.01 | 0.03 | 99.59 |
| West | Massive Sph-Cp | KCD209783 | 34.04 | 0.96 | <0.10 | 30.01 | 34.72 | - | 0.08 | - | <0.03 | <0.05 | - | 0.14 | <0.07 | <0.01 | <0.02 | 100.05 |
| West | Massive Sph-Cp | KCD209783 | 34.29 | 0.30 | <0.10 | 30.42 | 34.57 | - | 0.12 | - | <0.03 | <0.05 | - | 0.13 | 0.10 | <0.01 | <0.02 | 99.96 |
| West | Massive Sph-Cp | KCD209783 | 33.18 | 0.04 | <0.10 | 31.22 | 35.30 | <0.07 | 0.03 | <0.08 | <0.03 | <0.05 | <0.03 | 0.05 | <0.07 | 0.02 | <0.02 | 99.86 |
| West | Massive Sph-Cp | KCD209783 | 33.36 | <0.03 | <0.10 | 30.50 | 35.06 | 0.09 | 0.04 | <0.08 | <0.03 | <0.05 | <0.03 | <0.05 | <0.07 | <0.01 | <0.02 | 99.13 |
| West | Massive Sph-Cp | KCD209783 | 33.58 | <0.03 | <0.10 | 30.87 | 35.00 | 0.07 | 0.12 | <0.08 | <0.03 | <0.05 | <0.03 | 0.08 | <0.07 | <0.01 | <0.02 | 99.75 |
| Main | Massive Sph-Cp | KCD209788 | 34.09 | 0.64 | <0.10 | 30.19 | 34.61 | - | <0.02 | - | <0.03 | <0.05 | - | 0.14 | <0.07 | <0.01 | 0.02 | 99.76 |
| Main | Massive Sph-Cp | KCD209788 | 34.01 | 0.58 | <0.10 | 30.37 | 34.38 | - | <0.02 | - | <0.03 | <0.05 | - | <0.05 | <0.07 | <0.01 | <0.02 | 99.39 |
| Cu Str | Cp Stringer | KCD209790 | 34.83 | <0.03 | <0.10 | 30.59 | 34.86 | - | <0.02 | - | <0.03 | <0.05 | - | <0.05 | <0.07 | <0.01 | <0.02 | 100.34 |
| Cu Str | Cp Stringer | KCD209790 | 34.60 | 0.06 | <0.10 | 30.37 | 34.55 | - | 0.05 | - | <0.03 | <0.05 | - | <0.05 | <0.07 | <0.01 | <0.02 | 99.72 |
| Cu Str | Cp Stringer | KCD209790 | 33.92 | <0.03 | <0.10 | 30.79 | 35.19 | <0.07 | <0.02 | <0.08 | <0.03 | <0.05 | 0.10 | <0.05 | <0.07 | <0.01 | <0.02 | 100.07 |
| Cu Str | Cp Stringer | KCD209790 | 34.01 | <0.03 | <0.10 | 30.82 | 35.21 | 0.09 | 0.03 | <0.08 | <0.03 | <0.05 | 0.03 | <0.05 | <0.07 | <0.01 | <0.02 | 100.23 |
| Cu Str | Cp Stringer | KCD209794 | 33.65 | <0.03 | <0.10 | 30.80 | 35.18 | <0.07 | 0.02 | <0.08 | <0.03 | <0.05 | 0.04 | <0.05 | <0.07 | <0.01 | <0.02 | 99.77 |
| Cu Str | Cp Stringer | KCD209794 | 33.04 | 0.13 | <0.10 | 29.72 | 35.07 | <0.07 | <0.02 | <0.08 | <0.03 | <0.05 | 0.05 | <0.05 | <0.07 | <0.01 | <0.02 | 98.09 |
| Cu Str | Cp Stringer | KCD209794 | 33.03 | <0.03 | <0.10 | 30.17 | 35.31 | 0.11 | 0.02 | <0.08 | <0.03 | <0.05 | <0.03 | <0.05 | <0.07 | 0.02 | <0.02 | 98.67 |
| Cu Str | Cp Stringer | KCD209794 | 33.80 | <0.03 | <0.10 | 30.98 | 35.42 | <0.07 | <0.02 | <0.08 | <0.03 | <0.05 | 0.05 | <0.05 | <0.07 | <0.01 | <0.02 | 100.32 |
| Cu Str | Cp Stringer | KCD209794 | 33.83 | <0.03 | <0.10 | 31.03 | 35.36 | <0.07 | <0.02 | <0.08 | <0.03 | <0.05 | <0.03 | <0.05 | <0.07 | <0.01 | <0.02 | 100.27 |
| Cu Str | Massive Cp | KCD209797 | 34.33 | <0.03 | <0.10 | 30.57 | 34.43 | - | <0.02 | - | <0.03 | <0.05 | - | <0.05 | <0.07 | <0.01 | <0.02 | 99.34 |
| Cu Str | Massive Cp | KCD209797 | 33.84 | <0.03 | <0.10 | 30.08 | 34.33 | - | <0.02 | - | <0.03 | <0.05 | - | <0.05 | 0.24 | <0.01 | <0.02 | 98.53 |
| Cu Str | Massive Cp | KCD209797 | 34.15 | <0.03 | <0.10 | 30.64 | 34.15 | - | 0.07 | - | <0.03 | <0.05 | - | <0.05 | <0.07 | <0.01 | <0.02 | 99.06 |
| Cu Str | Cp Stringer | KCD209801 | 34.23 | <0.03 | <0.10 | 30.57 | 34.32 | - | <0.02 | - | <0.03 | <0.05 | - | 0.08 | <0.07 | 0.03 | <0.02 | 99.25 |
| Cu Str | Cp Stringer | KCD209801 | 33.79 | <0.03 | <0.10 | 29.84 | 34.73 | - | <0.02 | - | <0.03 | <0.05 | - | 0.07 | <0.07 | <0.01 | 0.09 | 98.55 |
| Cu Str | Cp Stringer | KCD209801 | 34.13 | <0.03 | <0.10 | 30.41 | 34.58 | - | <0.02 | - | <0.03 | <0.05 | - | 0.16 | <0.07 | <0.01 | 0.02 | 99.37 |
| Cu Str | Cp Stringer | KCD209801 | 34.19 | <0.03 | <0.10 | 30.83 | 34.80 | - | <0.02 | - | <0.03 | <0.05 | - | <0.05 | 0.12 | 0.02 | <0.02 | 100.01 |
| West | Massive Sph-Cp | KCD209807 | 34.32 | 0.15 | <0.10 | 30.55 | 34.41 | - | 0.07 | - | <0.03 | <0.05 | - | <0.05 | <0.07 | 0.02 | <0.02 | 99.56 |
| West | Massive Sph-Cp | KCD209807 | 34.53 | 0.16 | <0.10 | 30.77 | 34.72 | - | <0.02 | - | 0.08 | 0.06 | - | <0.05 | 0.08 | <0.01 | <0.02 | 100.41 |
| West | Massive Sph-Cp | KCD209811 | 33.88 | 0.06 | <0.10 | 30.75 | 34.67 | - | 0.06 | - | <0.03 | <0.05 | - | <0.05 | <0.07 | <0.01 | <0.02 | 99.49 |
| West | Massive Sph-Cp | KCD209811 | 33.82 | 0.30 | <0.10 | 30.42 | 34.64 | - | <0.02 | - | <0.03 | <0.05 | - | <0.05 | <0.07 | <0.01 | <0.02 | 99.26 |
| West | Massive Sph-Cp | KCD209811 | 33.97 | 0.43 | <0.10 | 30.82 | 34.57 | - | 0.03 | - | <0.03 | 0.08 | - | <0.05 | <0.07 | <0.01 | <0.02 | 99.90 |
| West | Massive Sph-Cp | KCD209811 | 33.96 | 0.20 | <0.10 | 30.73 | 34.58 | - | 0.04 | - | <0.03 | <0.05 | - | <0.05 | <0.07 | <0.01 | <0.02 | 99.53 |

## Appendix VI Electron Microprobe Analysis (wt %) of Galena in Mine D

| Lens | Ore Type | Sample # | Cu | Zn | Pb | Fe | S | Au | Ag | Hg | Sb | As | In | Se | Bi | Ni | Co | Total |
|---|---|---|---|---|---|---|---|---|---|---|---|---|---|---|---|---|---|---|
| South | Massive Sph | KCD209763 | <0.03 | 0.11 | 87.09 | 0.05 | 13.47 | - | <0.03 | - | <0.03 | <0.102 | - | <0.08 | <0.26 | <0.02 | <0.02 | 100.71 |
| West | Heterolithic Py | KCD209768 | 0.14 | 0.30 | 85.48 | 0.31 | 13.35 | - | 0.73 | - | <0.03 | <0.102 | - | <0.08 | <0.26 | <0.02 | <0.02 | 100.37 |
| West | Massive Py-Sph | KCD209770 | <0.03 | 0.42 | 87.05 | 0.14 | 13.43 | - | <0.03 | - | 0.12 | <0.102 | - | 0.10 | <0.26 | <0.02 | <0.02 | 101.25 |
| West | Heterolithic Py | KCD209778 | 0.10 | <0.04 | 87.35 | 0.16 | 13.46 | - | <0.03 | - | <0.03 | <0.102 | - | <0.08 | <0.26 | 0.03 | <0.02 | 101.14 |
| West | Massive Py-Sph | KCD209781 | 0.03 | 0.14 | 86.69 | 0.88 | 13.49 | - | <0.03 | - | 0.04 | <0.102 | - | <0.08 | <0.26 | <0.02 | <0.02 | 101.28 |
| West | Massive Py-Sph | KCD209781 | <0.03 | 0.30 | 86.96 | 0.16 | 13.51 | - | <0.03 | - | <0.03 | <0.102 | - | <0.08 | <0.26 | <0.02 | <0.02 | 100.92 |
| West | Massive Py-Sph | KCD209781 | 0.57 | <0.04 | 86.65 | 0.12 | 13.44 | - | <0.03 | - | <0.03 | <0.102 | - | <0.08 | <0.26 | <0.02 | <0.02 | 100.82 |
| Cu Str | Cp Stringer | KCD209794 | 0.04 | <0.04 | 84.06 | 0.03 | 13.72 | <0.102 | <0.03 | <0.101 | <0.03 | <0.102 | <0.03 | 0.18 | <0.26 | <0.02 | <0.02 | 98.08 |
| West | Sph-Cp Stringer | KCD209809 | 0.05 | <0.04 | 81.79 | 0.36 | 11.19 | <0.102 | 0.39 | <0.101 | <0.03 | <0.102 | <0.03 | 4.54 | <0.26 | <0.02 | <0.02 | 98.33 |
| West | Massive Sph-Cp | KCD209811 | <0.03 | <0.04 | 83.68 | 1.06 | 12.97 | - | <0.03 | - | <0.03 | <0.102 | - | 0.31 | <0.26 | <0.02 | <0.02 | 98.08 |
| West | Massive Sph-Cp | KCD209811 | <0.03 | 0.14 | 86.45 | 0.05 | 13.28 | - | 0.51 | - | <0.03 | <0.102 | - | 0.30 | <0.26 | <0.02 | <0.02 | 100.75 |

## Appendix VII Electron Microprobe Analysis (wt %) of Common Trace Minerals in Mine D

| Lens | Ore Type | Sample # | Cu | Zn | Pb | Fe | S | Au | Ag | Hg | Sb | As | In | Se | Bi | Ni | Co | Sn | Mn | Total |
|---|---|---|---|---|---|---|---|---|---|---|---|---|---|---|---|---|---|---|---|---|
| *Arsenopyrite* | | | | | | | | | | | | | | | | | | | | |
| West | Massive Sph-Cp | KCD209811 | 0.02 | 0.06 | <0.09 | 34.30 | 20.62 | - | <0.02 | - | 0.49 | 42.37 | <0.03 | <0.05 | 0.07 | 0.04 | 1.68 | <0.03 | 0.03 | 99.69 |
| South | Massive Py-Sph | KCD209757 | 0.02 | <0.03 | <0.09 | 36.18 | 20.76 | - | <0.02 | - | 0.03 | 42.96 | <0.03 | <0.05 | <0.07 | <0.02 | <0.02 | <0.03 | <0.02 | 99.97 |
| West | Massive Sph-Cp | KCD209783 | 0.08 | <0.03 | <0.09 | 35.93 | 21.87 | - | <0.02 | - | 0.64 | 40.77 | <0.03 | <0.05 | <0.07 | 0.07 | 0.20 | <0.03 | <0.02 | 99.57 |
| West | Massive Sph-Cp | KCD209811 | <0.02 | <0.03 | <0.09 | 35.48 | 21.00 | - | <0.02 | - | 0.95 | 41.66 | <0.03 | <0.05 | <0.07 | <0.02 | 0.38 | <0.03 | <0.02 | 99.50 |
| *Cobaltite* | | | | | | | | | | | | | | | | | | | | |
| Main | Massive Sph-Cp | KCD209788 | <0.02 | 0.05 | <0.09 | 10.58 | 22.98 | - | <0.02 | - | <0.03 | 37.32 | <0.03 | <0.05 | <0.07 | <0.02 | 29.13 | <0.03 | <0.02 | 100.12 |
| *Tetrahedrite* | | | | | | | | | | | | | | | | | | | | |
| South | Massive Sph | KCD209763 | 17.16 | 0.78 | <0.10 | 5.96 | 21.49 | - | 29.01 | - | 26.75 | <0.04 | <0.03 | 0.09 | <0.103 | <0.02 | 0.03 | <0.03 | <0.02 | 101.31 |
| West | Massive Py-Sph | KCD209781 | 21.02 | 0.68 | <0.10 | 5.41 | 22.38 | - | 24.73 | - | 26.98 | <0.04 | <0.03 | <0.03 | <0.103 | <0.02 | <0.02 | <0.03 | <0.02 | 101.25 |
| West | Massive Py-Sph | KCD209781 | 20.36 | 0.86 | <0.10 | 5.32 | 21.89 | - | 24.98 | - | 26.52 | <0.04 | <0.03 | <0.03 | <0.103 | <0.02 | 0.02 | <0.03 | <0.02 | 100.03 |
| *Gudmundite* | | | | | | | | | | | | | | | | | | | | |
| West | Massive Py-Sph | KCD209781 | 2.16 | 14.85 | 1.56 | 21.45 | 21.05 | - | <0.07 | - | 38.58 | 0.84 | <0.03 | 0.06 | <0.103 | <0.02 | <0.02 | - | - | 100.56 |
| West | Massive Py-Sph | KCD209781 | 1.97 | 5.02 | 11.33 | 22.26 | 16.55 | - | <0.07 | - | 41.84 | 0.80 | <0.03 | 0.08 | <0.103 | <0.02 | <0.02 | - | - | 99.87 |
| *Native Silver* | | | | | | | | | | | | | | | | | | | | |
| Main | Massive Sph-Cp | 8802_10 | 0.08 | 0.17 | <0.10 | 0.78 | 0.64 | <0.10 | 98.05 | <0.10 | 0.12 | <0.07 | <0.05 | <0.06 | 0.12 | <0.02 | <0.02 | <0.03 | <0.02 | 100.12 |
| Main | Massive Sph-Cp | 8802_10 | 0.11 | <0.04 | <0.10 | 0.17 | 0.32 | <0.10 | 94.31 | <0.10 | 4.88 | 0.20 | <0.05 | <0.06 | 0.13 | <0.02 | <0.02 | - | - | 100.22 |
| West | Massive Sph-Cp | KCD209783 | <0.02 | <0.04 | <0.10 | 0.25 | 1.35 | <0.10 | 96.36 | <0.10 | 0.33 | 0.22 | <0.05 | <0.06 | <0.07 | <0.02 | <0.02 | - | - | 98.68 |
| *Native Bismuth* | | | | | | | | | | | | | | | | | | | | |
| Main | Massive Sph-Cp | 8802_10 | <0.02 | 0.04 | <0.10 | 0.02 | 0.06 | 0.14 | <0.04 | <0.10 | 0.12 | <0.07 | <0.05 | <0.06 | 98.85 | <0.02 | <0.02 | - | - | 99.31 |
| Main | Massive Sph-Cp | 8802_10 | <0.02 | 0.08 | <0.10 | 0.05 | 0.12 | <0.10 | <0.04 | <0.10 | 0.07 | <0.07 | <0.05 | <0.06 | 97.88 | <0.02 | 0.03 | - | - | 98.26 |

## Appendix VIII Electron Microprobe Analysis (wt %) of Possible Trace Minerals in Mine D

| Lens | Ore Type | Sample # | Cu | Zn | Pb | Fe | S | Au | Ag | Hg | Sb | As | In | Se | Bi | Ni | Co | Total | Possible Mineral |
|---|---|---|---|---|---|---|---|---|---|---|---|---|---|---|---|---|---|---|---|
| Main | Massive Sph-Cp | 8802_10 | 0.09 | 0.06 | <0.10 | 0.04 | 0.13 | <0.10 | 83.20 | <0.10 | 15.62 | 0.10 | <0.05 | <0.06 | 0.73 | <0.02 | <0.02 | 100.14 | *Allargentum* |
| Main | Massive Sph-Cp | 8802_10 | 11.57 | <0.04 | <0.10 | 10.99 | 12.92 | 0.22 | 48.59 | <0.10 | 9.03 | <0.07 | <0.05 | 2.22 | 6.23 | <0.02 | <0.02 | 101.76 | *Ag-Cu-Sb-Bi-Se* |
| Main | Massive Sph-Cp | 8802_10 | 0.04 | 0.05 | 21.55 | 0.02 | 9.75 | <0.10 | 18.87 | <0.10 | 0.06 | <0.07 | <0.05 | 12.92 | 36.65 | <0.02 | <0.02 | 99.91 | *Bi-Pb-Ag-Se* |
| West | Massive Py-Sph | KCD209781 | 18.96 | 28.34 | <0.10 | 18.92 | 34.22 | <0.10 | <0.04 | <0.10 | 0.04 | <0.07 | <0.05 | <0.06 | <0.07 | <0.02 | <0.02 | 100.50 | *Zn-Cu-Fe-S* |
| Cu Str | Cp Stringer | KCD209801 | 0.02 | <0.04 | 2.29 | 0.51 | 0.37 | <0.10 | <0.04 | <0.10 | <0.03 | <0.07 | <0.05 | 21.43 | 77.99 | <0.02 | 0.02 | 102.64 | *Laitakarite* |

## Appendix IX Electron Microprobe Analysis (wt %) of Siderite in Mine D

| Lens | Ore Type | Sample # | CaO | SrO | FeO | MnO | MgO | $CO_2$ | Total |
|---|---|---|---|---|---|---|---|---|---|
| West | Massive Py-Sph | KCD209770 | 0.56 | <0.03 | 57.27 | 1.01 | 2.53 | 38.90 | 100.26 |
| West | Massive Py-Sph | KCD209770 | 0.56 | <0.03 | 57.27 | 1.01 | 2.53 | 38.90 | 100.26 |
| West | Massive Py-Sph | KCD209770 | 0.54 | <0.03 | 56.89 | 1.17 | 2.21 | 38.41 | 99.22 |
| West | Massive Py-Sph | KCD209770 | 0.54 | <0.03 | 56.89 | 1.17 | 2.21 | 38.41 | 99.22 |
| Cu Str | Py Stringer | KCD209776 | 0.14 | <0.03 | 60.85 | 0.07 | 0.09 | 37.52 | 98.67 |
| Cu Str | Py Stringer | KCD209776 | 0.14 | <0.03 | 60.85 | 0.07 | 0.09 | 37.52 | 98.67 |
| West | Massive Py-Sph | KCD209781 | 0.42 | <0.03 | 55.38 | 1.60 | 2.79 | 38.29 | 98.48 |
| West | Massive Py-Sph | KCD209781 | 0.73 | <0.03 | 53.07 | 2.31 | 3.77 | 38.62 | 98.49 |
| West | Massive Py-Sph | KCD209781 | 0.45 | <0.03 | 57.29 | 1.50 | 2.11 | 38.68 | 100.03 |
| West | Massive Py-Sph | KCD209781 | 0.98 | <0.03 | 49.26 | 0.94 | 7.79 | 40.04 | 99.01 |
| West | Massive Py-Sph | KCD209781 | 0.45 | <0.03 | 53.16 | 1.41 | 4.51 | 38.71 | 98.23 |
| West | Massive Py-Sph | KCD209781 | 0.63 | <0.03 | 45.87 | 2.94 | 9.60 | 40.89 | 99.91 |
| West | Massive Py-Sph | KCD209781 | 0.29 | <0.03 | 57.05 | 0.84 | 2.71 | 38.65 | 99.54 |
| West | Massive Sph-Cp | KCD209783 | 0.55 | <0.03 | 58.11 | 0.24 | 1.98 | 38.33 | 99.20 |
| West | Massive Sph-Cp | KCD209783 | 0.55 | <0.03 | 58.11 | 0.24 | 1.98 | 38.33 | 99.20 |
| West | Massive Sph-Cp | KCD209783 | 0.26 | <0.03 | 58.26 | 0.41 | 1.78 | 38.08 | 98.78 |
| West | Massive Sph-Cp | KCD209783 | 0.26 | <0.03 | 58.26 | 0.41 | 1.78 | 38.08 | 98.78 |
| West | Massive Sph-Cp | KCD209783 | 0.65 | <0.03 | 56.02 | 2.48 | 2.22 | 38.79 | 100.15 |
| West | Massive Sph-Cp | KCD209783 | 0.65 | <0.03 | 56.02 | 2.48 | 2.22 | 38.79 | 100.15 |
| Main | Massive Sph-Cp | KCD209788 | 0.12 | <0.03 | 45.71 | 3.28 | 9.92 | 40.96 | 99.99 |
| West | Massive Sph-Cp | KCD209811 | 0.47 | <0.03 | 50.75 | 2.85 | 5.98 | 39.76 | 99.81 |
| West | Massive Sph-Cp | KCD209811 | 0.47 | <0.03 | 50.75 | 2.85 | 5.98 | 39.76 | 99.81 |
| West | Massive Sph-Cp | KCD209811 | 0.48 | <0.03 | 52.66 | 2.06 | 5.48 | 39.89 | 100.58 |
| West | Massive Sph-Cp | KCD209811 | 0.48 | <0.03 | 52.66 | 2.06 | 5.48 | 39.89 | 100.58 |

## Appendix X Electron Microprobe Analysis (wt %) of Ankerite in Mine D

| Lens | Ore Type | Sample # | CaO | SrO | FeO | MnO | MgO | $CO_2$ | Total |
|---|---|---|---|---|---|---|---|---|---|
| South | Massive Sph-Cp | KCD209759 | 27.63 | <0.03 | 17.73 | 4.20 | 7.68 | 43.54 | 100.78 |
| Cu Str | Massive Py-Cp | KCD209773 | 28.10 | <0.03 | 13.39 | 3.42 | 11.06 | 44.44 | 100.40 |
| Cu Str | Massive Py-Cp | KCD209773 | 27.62 | <0.03 | 20.36 | 2.43 | 7.04 | 43.33 | 100.78 |
| Cu Str | Cp Stringer | KCD209790 | 28.20 | <0.03 | 18.99 | 0.87 | 8.95 | 44.08 | 101.09 |
| Cu Str | Cp Stringer | KCD209790 | 28.20 | <0.03 | 18.99 | 0.87 | 8.95 | 44.08 | 101.09 |
| Cu Str | Cp Stringer | KCD209794 | 27.52 | <0.03 | 15.57 | 4.48 | 8.57 | 43.27 | 99.40 |
| Cu Str | Cp Stringer | KCD209801 | 29.46 | <0.03 | 10.15 | 0.27 | 14.67 | 45.52 | 100.07 |
| Cu Str | Cp Stringer | KCD209801 | 29.46 | <0.03 | 10.15 | 0.27 | 14.67 | 45.52 | 100.07 |
| Cu Str | Cp Stringer | KCD209801 | 28.33 | <0.03 | 13.51 | 0.63 | 12.77 | 44.83 | 100.06 |
| Cu Str | Cp Stringer | KCD209801 | 28.33 | <0.03 | 13.51 | 0.63 | 12.77 | 44.83 | 100.06 |
| Cu Str | Cp Stringer | KCD209801 | 28.15 | <0.03 | 17.15 | 0.89 | 9.90 | 43.94 | 100.01 |
| Cu Str | Cp Stringer | KCD209801 | 28.15 | <0.03 | 17.15 | 0.89 | 9.90 | 43.94 | 100.01 |
| West | Massive Sph-Cp | KCD209807 | 27.54 | <0.03 | 20.17 | 1.48 | 6.43 | 41.90 | 97.52 |
| West | Massive Sph-Cp | KCD209807 | 27.54 | <0.03 | 20.17 | 1.48 | 6.43 | 41.90 | 97.52 |
| West | Massive Sph-Cp | KCD209807 | 27.37 | <0.03 | 13.16 | 1.53 | 11.74 | 43.30 | 97.09 |
| West | Massive Sph-Cp | KCD209807 | 27.37 | <0.03 | 13.16 | 1.53 | 11.74 | 43.30 | 97.09 |
| West | Sph-Cp Stringer | KCD209809 | 28.62 | <0.03 | 7.34 | 0.76 | 17.07 | 46.06 | 99.84 |
| West | Sph-Cp Stringer | KCD209809 | 28.20 | <0.03 | 15.07 | 1.94 | 10.95 | 44.52 | 100.68 |

# Appendix XI Electron Microprobe Analysis (wt %) of Chlorite in Mine D

| Lens | Ore Type | Sample # | $SiO_2$ | $TiO_2$ | $Al_2O_3$ | FeO | MnO | MgO | CaO | $Na_2O$ | $K_2O$ | F | Cl | Total |
|---|---|---|---|---|---|---|---|---|---|---|---|---|---|---|
| South | Massive Sph-Cp | KCD209759 | 24.99 | 0.04 | 21.73 | 29.52 | 0.25 | 11.66 | 0.03 | <0.01 | <0.02 | 0.14 | <0.007 | 88.32 |
| South | Massive Sph-Cp | KCD209759 | 25.14 | 0.03 | 21.42 | 29.91 | 0.21 | 11.52 | <0.02 | <0.01 | <0.02 | 0.24 | <0.007 | 88.36 |
| South | Massive Sph-Cp | KCD209759 | 25.19 | 0.04 | 21.43 | 30.68 | 0.18 | 11.05 | <0.02 | <0.01 | <0.02 | 0.13 | 0.016 | 88.72 |
| South | Massive Sph-Cp | KCD209759 | 25.97 | 0.09 | 20.91 | 28.52 | 0.24 | 12.41 | <0.02 | <0.01 | <0.02 | 0.17 | <0.007 | 88.24 |
| South | Massive Sph-Cp | KCD209759 | 25.93 | 0.06 | 20.93 | 28.77 | 0.19 | 12.15 | <0.02 | <0.01 | <0.02 | 0.22 | <0.007 | 88.17 |
| South | Massive Sph-Cp | KCD209759 | 25.45 | 0.05 | 21.48 | 29.29 | 0.21 | 11.70 | <0.02 | <0.01 | <0.02 | 0.18 | <0.007 | 88.28 |
| West | Heterolithic Py | KCD209768 | 24.94 | 0.03 | 21.55 | 28.24 | 0.21 | 12.73 | <0.02 | 0.02 | <0.02 | <0.06 | 0.008 | 87.76 |
| West | Massive Py-Sph | KCD209770 | 21.92 | <0.03 | 22.07 | 42.92 | 0.08 | 1.51 | <0.02 | <0.01 | <0.02 | <0.06 | <0.007 | 88.51 |
| West | Massive Py-Sph | KCD209770 | 22.62 | 0.04 | 20.30 | 44.35 | 0.09 | 1.40 | <0.02 | <0.01 | <0.02 | <0.06 | 0.007 | 88.82 |
| Cu Str | Massive Py-Cp | KCD209773 | 23.57 | 0.04 | 22.67 | 35.41 | <0.03 | 7.04 | <0.02 | <0.01 | <0.02 | 0.15 | <0.007 | 88.86 |
| Cu Str | Py Stringer | KCD209776 | 23.38 | 0.08 | 20.99 | 39.22 | 0.34 | 4.22 | <0.02 | <0.01 | <0.02 | <0.06 | <0.007 | 88.27 |
| Cu Str | Py Stringer | KCD209776 | 22.83 | 0.03 | 21.70 | 39.15 | 0.37 | 4.05 | <0.02 | 0.02 | <0.02 | <0.06 | <0.007 | 88.18 |
| West | Heterolithic Py | KCD209778 | 26.44 | 0.04 | 22.23 | 21.76 | 0.16 | 16.93 | <0.02 | 0.01 | <0.02 | 0.24 | <0.007 | 87.71 |
| West | Heterolithic Py | KCD209778 | 26.17 | <0.03 | 22.51 | 21.69 | 0.15 | 16.69 | <0.02 | <0.01 | <0.02 | 0.14 | <0.007 | 87.31 |
| West | Heterolithic Py | KCD209778 | 28.18 | 0.06 | 23.73 | 20.84 | 0.14 | 14.94 | <0.02 | 0.02 | <0.02 | 0.22 | <0.007 | 88.86 |
| West | Massive Py-Sph | KCD209781 | 22.46 | <0.03 | 22.27 | 41.09 | 0.12 | 2.79 | <0.02 | <0.01 | <0.02 | <0.06 | <0.007 | 88.74 |
| West | Massive Py-Sph | KCD209781 | 23.61 | <0.03 | 19.57 | 40.30 | 0.05 | 4.94 | 0.02 | 0.02 | <0.02 | <0.06 | <0.007 | 88.51 |
| West | Massive Sph-Cp | KCD209783 | 22.32 | 0.03 | 20.43 | 41.56 | 0.13 | 3.47 | <0.02 | 0.02 | <0.02 | <0.06 | <0.007 | 87.96 |
| Main | Massive Sph-Cp | KCD209788 | 23.00 | 0.03 | 22.44 | 36.73 | 0.09 | 6.34 | <0.02 | <0.01 | <0.02 | <0.06 | <0.007 | 88.64 |
| Main | Massive Sph-Cp | KCD209788 | 23.06 | 0.03 | 21.65 | 36.92 | 0.09 | 6.02 | 0.02 | <0.01 | <0.02 | <0.06 | <0.007 | 87.81 |
| Main | Massive Sph-Cp | KCD209788 | 24.38 | 0.04 | 19.63 | 37.86 | 0.10 | 6.90 | <0.02 | 0.01 | <0.02 | <0.06 | <0.007 | 88.96 |
| Main | Massive Sph-Cp | KCD209788 | 24.04 | <0.03 | 20.47 | 36.81 | 0.07 | 6.53 | <0.02 | 0.02 | <0.02 | <0.06 | 0.008 | 87.99 |
| Main | Massive Sph-Cp | KCD209788 | 23.82 | 0.05 | 22.54 | 30.72 | 0.05 | 10.64 | <0.02 | 0.05 | <0.02 | 0.18 | <0.007 | 87.96 |
| Cu Str | Cp Stringer | KCD209790 | 24.04 | 0.04 | 22.28 | 33.16 | 0.04 | 8.49 | <0.02 | 0.02 | <0.02 | 0.10 | 0.009 | 88.13 |
| Cu Str | Cp Stringer | KCD209790 | 23.51 | 0.05 | 23.10 | 33.19 | 0.05 | 8.72 | <0.02 | <0.01 | <0.02 | 0.06 | <0.007 | 88.66 |
| Cu Str | Cp Stringer | KCD209794 | 25.01 | 0.06 | 20.78 | 31.27 | 0.27 | 10.89 | <0.02 | <0.01 | <0.02 | 0.24 | <0.007 | 88.42 |
| Cu Str | Cp Stringer | KCD209794 | 24.07 | 0.04 | 22.17 | 30.78 | 0.28 | 10.38 | <0.02 | <0.01 | <0.02 | 0.09 | <0.007 | 87.77 |
| Cu Str | Cp Stringer | KCD209794 | 24.79 | 0.06 | 21.55 | 28.52 | 0.31 | 12.90 | <0.02 | <0.01 | <0.02 | 0.35 | <0.007 | 88.34 |
| Cu Str | Cp Stringer | KCD209794 | 24.30 | 0.07 | 22.03 | 29.63 | 0.22 | 11.60 | 0.03 | <0.01 | <0.02 | 0.21 | 0.014 | 88.01 |
| Cu Str | Massive Cp | KCD209797 | 25.03 | 0.03 | 22.81 | 27.56 | 0.04 | 12.70 | 0.03 | <0.01 | <0.02 | 0.15 | <0.007 | 88.29 |
| Cu Str | Massive Cp | KCD209797 | 24.46 | 0.10 | 22.71 | 27.80 | 0.05 | 12.52 | <0.02 | <0.01 | <0.02 | <0.06 | <0.007 | 87.68 |
| Cu Str | Massive Cp | KCD209797 | 24.57 | 0.05 | 22.98 | 27.80 | 0.07 | 12.52 | <0.02 | <0.01 | <0.02 | 0.18 | <0.007 | 88.12 |
| Cu Str | Massive Cp | KCD209797 | 25.43 | 0.03 | 23.11 | 27.27 | <0.03 | 12.00 | <0.02 | 0.01 | 0.22 | 0.08 | <0.007 | 88.15 |
| Cu Str | Massive Cp | KCD209797 | 24.97 | 0.04 | 23.20 | 27.51 | 0.08 | 12.07 | 0.02 | <0.01 | 0.12 | <0.06 | <0.007 | 88.03 |
| Cu Str | Cp Stringer | KCD209801 | 23.56 | <0.03 | 23.90 | 32.34 | 0.07 | 8.32 | 0.05 | 0.02 | <0.02 | 0.06 | <0.007 | 88.32 |
| Cu Str | Cp Stringer | KCD209801 | 24.48 | 0.04 | 23.17 | 28.07 | 0.10 | 11.67 | <0.02 | <0.01 | <0.02 | 0.08 | <0.007 | 87.58 |
| Cu Str | Cp Stringer | KCD209801 | 25.16 | 0.05 | 23.57 | 28.26 | 0.08 | 11.45 | <0.02 | 0.02 | 0.18 | 0.13 | 0.008 | 88.84 |
| Cu Str | Cp Stringer | KCD209801 | 24.56 | 0.05 | 23.43 | 28.54 | 0.10 | 11.90 | 0.04 | <0.01 | <0.02 | 0.14 | <0.007 | 88.70 |
| Cu Str | Cp Stringer | KCD209801 | 24.82 | 0.07 | 23.14 | 28.35 | 0.11 | 11.67 | <0.02 | <0.01 | <0.02 | 0.12 | <0.007 | 88.26 |
| West | Sph-Cp Stringer | KCD209809 | 25.10 | 0.05 | 21.75 | 28.98 | 0.20 | 12.08 | <0.02 | <0.01 | <0.02 | 0.30 | <0.007 | 88.33 |
| West | Sph-Cp Stringer | KCD209809 | 24.83 | 0.03 | 21.92 | 29.80 | 0.18 | 11.23 | 0.03 | <0.01 | <0.02 | 0.32 | <0.007 | 88.21 |
| West | Sph-Cp Stringer | KCD209809 | 24.65 | 0.04 | 22.31 | 29.75 | 0.19 | 11.61 | <0.02 | 0.02 | <0.02 | 0.23 | <0.007 | 88.72 |
| West | Massive Sph-Cp | KCD209811 | 23.96 | 0.03 | 20.23 | 37.78 | 0.06 | 5.95 | <0.02 | 0.04 | <0.02 | <0.06 | <0.007 | 88.08 |
| West | Massive Sph-Cp | KCD209811 | 24.29 | 0.10 | 19.26 | 39.40 | 0.05 | 5.63 | <0.02 | <0.01 | <0.02 | <0.06 | 0.007 | 88.74 |
| West | Massive Sph-Cp | KCD209811 | 23.42 | 0.06 | 20.94 | 39.39 | 0.09 | 4.84 | <0.02 | 0.02 | <0.02 | <0.06 | <0.007 | 88.77 |
| Main | Sph Stringer | KCD209813 | 25.19 | 0.03 | 18.73 | 37.48 | 0.14 | 6.71 | <0.02 | <0.01 | <0.02 | 0.10 | 0.008 | 88.35 |
| Main | Sph Stringer | KCD209813 | 23.17 | <0.03 | 22.52 | 37.21 | 0.18 | 6.05 | <0.02 | <0.01 | <0.02 | <0.06 | <0.007 | 89.18 |
| Main | Sph Stringer | KCD209813 | 24.59 | 0.07 | 21.91 | 33.59 | 0.13 | 9.24 | <0.02 | 0.03 | <0.02 | 0.12 | <0.007 | 89.65 |

# Appendix XII Electron Microprobe Analysis (wt %) of Selected Silicates in Mine D

| Lens | Ore Type | Sample # | $SiO_2$ | $TiO_2$ | $Al_2O_3$ | FeO | MnO | MgO | CaO | $Na_2O$ | $K_2O$ | F | Cl | Total |
|---|---|---|---|---|---|---|---|---|---|---|---|---|---|---|
| *Sericite* | | | | | | | | | | | | | | |
| West | Heterolithic Py | KCD209768 | 48.4 | 0.24 | 32.0 | 2.07 | <0.03 | 1.72 | <0.02 | 0.22 | 10.7 | 0.50 | <0.007 | 95.73 |
| Cu Str | Py Stringer | KCD209776 | 46.9 | 0.13 | 34.1 | 2.31 | <0.03 | 0.64 | <0.02 | 0.38 | 10.7 | 0.33 | <0.007 | 95.35 |
| West | Heterolithic Py | KCD209778 | 49.3 | 0.27 | 32.5 | 1.24 | <0.03 | 1.79 | <0.02 | 0.36 | 10.8 | 0.47 | <0.007 | 96.46 |
| Cu Str | Cp Stringer | KCD209801 | 47.5 | 0.25 | 36.3 | 1.05 | <0.03 | 0.62 | <0.02 | 0.61 | 10.2 | 0.39 | 0.01 | 96.71 |
| West | Massive Sph-Cp | KCD209807 | 47.5 | 0.27 | 33.3 | 2.17 | <0.03 | 1.02 | <0.02 | 0.85 | 10.1 | 0.47 | 0.008 | 95.58 |
| *Phlogopite and Biotite* | | | | | | | | | | | | | | |
| South | Massive Py-Sph | KCD209757 | 41.1 | 0.35 | 12.2 | 13.8 | <0.03 | 18.3 | <0.02 | 0.34 | 9.24 | 4.29 | <0.007 | 97.89 |
| Main | Sph Stringer | KCD209813 | 39.6 | 0.24 | 12.8 | 20.9 | 0.08 | 13.1 | <0.02 | 0.07 | 9.70 | 3.77 | <0.007 | 98.65 |
| *Tourmaline* | | | | | | | | | | | | | | |
| Cu Str | Cp Stringer | KCD209790 | 36.8 | 0.18 | 33.0 | 9.98 | <0.03 | 4.34 | 0.13 | 1.7 | <0.02 | 0.21 | <0.006 | 86.26 |
| Cu Str | Cp Stringer | KCD209790 | 37.1 | 0.11 | 33.3 | 9.84 | 0.03 | 4.18 | 0.04 | 1.66 | <0.02 | 0.10 | <0.006 | 86.353 |
| Cu Str | Massive Cp | KCD209797 | 25.0 | 0.03 | 22.8 | 27.6 | 0.04 | 12.698 | 0.03 | <0.02 | <0.02 | 0.15 | <0.006 | 88.289 |
| Cu Str | Massive Cp | KCD209797 | 37.1 | 0.05 | 33.5 | 8.56 | <0.03 | 5.04 | 0.04 | 1.72 | <0.02 | 0.11 | <0.006 | 86.042 |
| Cu Str | Massive Cp | KCD209797 | 36.9 | 0.50 | 31.1 | 8.95 | <0.03 | 6.54 | 0.56 | 2.27 | <0.02 | 0.56 | 0.009 | 87.067 |
| *Albite* | | | | | | | | | | | | | | |
| South | Massive Sph-Cp | KCD209759 | 69.5 | <0.02 | 19.8 | 0.05 | <0.03 | <0.01 | <0.02 | 11.6 | 0.03 | <0.04 | <0.006 | 100.991 |
| West | Massive Py-Sph | KCD209770 | 68.9 | <0.02 | 19.7 | 0.05 | <0.03 | <0.01 | 0.10 | 11.6 | 0.07 | <0.04 | 0.007 | 100.493 |
| Cu Str | Massive Py-Cp | KCD209773 | 69.2 | <0.02 | 19.4 | 0.04 | <0.03 | <0.01 | 0.16 | 11.5 | 0.02 | 0.08 | <0.006 | 100.393 |
| Cu Str | Massive Py-Cp | KCD209773 | 69.5 | 0.03 | 19.5 | 0.03 | <0.03 | 0.02 | 0.15 | 11.4 | 0.04 | <0.04 | <0.006 | 100.729 |
| Cu Str | Massive Cp | KCD209797 | 68.7 | <0.02 | 19.7 | <0.03 | <0.03 | <0.01 | 0.17 | 11.5 | <0.02 | 0.05 | <0.006 | 100.18 |